Département de Géomatique Appliquée
Faculté des Lettres et Sciences Humaines
Université de Sherbrooke

Amélioration de la capabilité de modélisation et de mitigation du gel radiatif au milieu agricole

Vahid Ikani

Directeur : Richard Fournier
Codirecteur : Karem Chokmani

Thèse présentée pour l'obtention du grade de Doctorant en télédétection

Abstract:

The main objective of this study was related to radiation frost damage: (1) improving the forecasting capability of local frost, which was adapted to forecast nocturnal minimum temperature at a 30-meter resolution, using a vegetation-atmosphere energy exchange framework, and (2) proposing a new mitigation approach to protect agricultural crops during frost periods. The first advance was achieved through several specific objectives to enhance the capabilities of a meteorological spatial distribution model (Micro-Met) on four sub-models: (i) estimating local air temperature lapse rate on a daily basis (ii) modifying downward longwave equation under clear sky condition, (iii) quantifying the effects of cold air drainage on air temperature, and (iv) quantifying the forest shelter effect on wind speed. The second advance advancement was accomplished by implementing and testing a new active method based on steam cycle thermodynamic.

The first sub-model used AIRS (Atmosphere infrared sounder) air temperature profile and surface station data to estimate air temperature lapse rate on the daily and regional scale. The use of daily basis lapse rate, instead of the fixed value, allowed to present more accurate atmospheric condition. The results showed the potential of the AIRS air temperature profiles (850 hPa and 700 hPa) to estimate the temperature lapse rate.

The second sub-model used observational data associated with synoptic conditions of radiation frost to present a locally adjusted downward longwave equation. The reported root means square error (RMSE) and mean absolute error (MAE) for the current version of Micro-Met were 176.95 (Wm^{-2}) and 176.40 (Wm^{-2}) respectively, while the results of the new equation led to an RMSE and MAE of 4.90 (Wm^{-2}) and 4.00 (Wm^{-2}) respectively.

The third sub–model constituted three components: detected closed valley, estimated cold air drainage velocity, and integrated sensible heat loss and radiative cooling during the night on detected valleys. Comparison between the current Micro-Met simulation and the measured air temperature shows MAE of 1.11°C and RMSE of 1.66°C, while the comparison with the enhanced Micro-Met simulation indicated an improvement with MAE of 0.68 °C and RMSE of 1.08 °C.

The fourth sub-model was based on experimental results of wind velocity produced in a laboratory with wind-tunnel models. Three separate equations were formulated for wind velocity estimation over the windward, through the shelterbelt, and leeward areas. The results indicated a coefficient of determination (R^2) of 71% under the wind's velocity lower than $6ms^{-1}$.

The Enhanced Micro-Met version provided a new platform to power vegetation-atmosphere energy model to forecast minimum nocturnal temperature. The performance test for forecasting minimum air temperatures indicated agreement with *in-situ* measurements**.** Measurements were taken on five topographic sectors in order to assess the improved modeled prediction and led to error assessment on closed valleys (RMSE=1.34, MAE = 1.03), different parts of slopes (RMAE = 0.93, MAE = 0.73), ridges (RMSE = 1.02, MAE = 0.88), flat areas (RMSE = 0.44, MAE = 0.40), and areas close to the forest (RMSE = 0.58, MAE = 0.53).

In addition to previous specific objectives, this study proposed a new frost mitigation method based on the thermodynamics of water vapor transport from a moist source to dry sink. A vessel of warm water equipped with a Selective Inverted Sink (SIS) system was used to transport water vapor into the air, which ended up decreasing the air dryness and increasing moist entropy. This test was

carried out in an orchard. The most common mitigation method focuses on air temperature. Instead, the proposed method was based on the physical principles of moist entropy, which combined both air temperature and humidity and depicted heat content.

Overall, for this research project, a coupled model was designed to predict nocturnal minimum air temperature over hilly agricultural terrain. In particular, through improving prediction accuracy, we developed and added sub-models to estimate drops in temperature due to pooling and stagnation of cold air drainage and the effect of forest shelterbelt on wind velocity. To reduce frost effect, a new environmentally friendly active method was presented. This study served to help farmers reduce frost damages. Moreover, it can be useful for agricultural services in terms of decision-making, thereby, reducing economic damages.

Keywords: Radiation frost, Forecasting minimum air temperature, Spatial modeling, Cold air drainage, Forest shelterbelt, Air temperature lapse rate, Net radiation, Frost mitigation, Moist enthropy.

Resumè

Le gel radiatif est une des conditions météorologiques sévère affect la production agricole dans de nombreuses région du monde. Les objectives de cette étude inclut deux innovations scientifiques liées aux dégâts causés par le gel radiatif : (1) l'amélioration de la capacité de prédiction du gel local (température nocturne minimale à une résolution de 30 mètres) grâce à un modèle d'échange énergétique entre la végétation et l'atmosphère, et (2) une nouvelle méthode de diminution des risques et de protection des cultures agricoles pendant les périodes de gel.

La première innovation a été réalisée en suivant plusieurs objectifs spécifiques visant à améliorer les capacités d'un modèle de répartition spatiale météorologique (Micro-Met) via quatre sous-modèles : (i) estimation journalière du gradient thermique adiabatique de l'air, (ii) modification de l'équation de rayonnement des grandes longueurs d'onde en l'absence de nuage dans l'atmosphère, (iii) quantification des effets de l'écoulement de l'air froid sur la température de l'air, et (iv) quantifier l'effet de haies brise–vent sur la vitesse du vent. La deuxième innovation a été réalisée en mettant en œuvre et en testant une nouvelle méthode active basée sur le cycle thermodynamique. Le site d'étude se localise dans la région de Vallée de Coaticook de l'Estrie (Québec) subit les conséquences désastreuses du gel.

Le premier sous-modèle utilise une combinaison de profils de température provenant du satellite AIRS et de stations météorologiques afin d'estimer quotidiennement et régionalement le gradient thermique de l'air. L'utilisation de valeurs journalières, au lieu de valeurs fixes, permet d'estimer plus précisément les conditions atmosphériques. Les résultats ont démontré l'utilité de l'utilisation de la température de l'air obtenue par AIRS (850 hPa et 700 hPa) pour l'estimation du gradient thermique. Le second sous-modèle utilise les données associées aux conditions synoptiques du gel radiatif pour obtenir une équation du rayonnement descendant localement ajustée. Alors que l'erreur aux moindres carrés (RMSE) de Micro-Met était de 176.95 Wm^{-2} avec une erreur absolue (MAE) moyenne de 176.40 Wm^{-2}, la nouvelle équation génère une RMSE de 4.90 Wm^{-2} et une MAE de 4.00 Wm^{-2}. Le troisième sous-modèle contient trois parties :la détection des vallées fermées, l'estimation de la rapidité de drainage de l'air, et l'intégration de la perte de chaleur sensible ainsi que le refroidissement radiatif en vallée durant la nuit. La comparaison entre les simulations Micro-Met et les mesures de la température de l'air montrent une MAE de 1.11 (°C) et une RMSE de 1.66 (°C). La comparaison avec le modèle amélioré indique un gain avec une MAE de 0.68 (°C) et une RMSE de 1.08 (°C). Le quatrième sous-modèle était construit sur des résultats expérimentaux de vitesse du vent générés en laboratoire par des simulations. Trois équations ont été proposées pour estimer la vitesse du vent. Les résultats indiquent un coefficient de corrélation (R^2) de 71% pour une vitesse de vent en dessous de 6 ms^{-1}.

La version améliorée de Micro-Net fournit une nouvelle plateforme pour des modèles d'énergie végétation-atmosphère et permet de prévoir la température minimale nocturne. Les résultats des tests de prédiction de cette température minimum concordent avec les mesures in-situ. Ces mesures ont été prises dans 5 secteurs topographiques différents afin d'améliorer les modèles de prédiction et engendrent des erreurs pour des vallées fermées (RMSE = 1.34, MAE = 1.03), pour différentes pentes (RMAE = 0.93, MAE = 0.73), crêtes (RMSE = 1.02, MAE = 0.88), plaines (RMSE = 0.44, MAE = 0.40), et aux orées des forêts (RMSE = 0.58, MAE = 0.53).

En plus des objectifs spécifiques précédents, cette étude a proposé une nouvelle méthode d'atténuation du gel basée sur la thermodynamique du transport de la vapeur d'eau d'une source humide à un puits sec. Nous avons ajouté au Selective Inverse System (SIS) déjà utilisé dans le milieu, un contenant d'eau chaude à sa base pour diffuser la vapeur d'eau dans l'air ambiant. Cette opération a augmenté l'humidité de l'air ambiant et augmenté l'entropie humide. Cet essai a été réalisé dans un verger. La méthode d'atténuation la plus courante se concentre sur la température de l'air. La méthode proposée repose plutôt sur les principes physiques de l'entropie humide, qui combinait à la fois la température et l'humidité de l'air et le contenu thermique représenté.

Dans l'ensemble, pour ce projet de recherche, un modèle couplé a été conçu pour prévision la température minimale nocturne de l'air dans des terrains agricoles vallonnés. En particulier, en améliorant la précision des prévisions, nous avons élaboré et ajouté des sous-modèles pour estimer les baisses de température dues à la stagnation du drainage de l'air froid et à l'effet des brise-vent forestiers sur la vitesse du vent. Pour réduire l'effet de gel, une nouvelle méthode de mitigation active respectueuse de l'environnement a été présentée. Cette étude a le potentiel d'aider les agriculteurs à réduire les dommages causés par le gel. De plus, elle peut être utile pour les services agricoles en termes de prise de décision, réduisant ainsi les dommages économiques.

Acknowledgments:

I would like to present my sincere acknowledgement to Dr. Richard Fournier and Dr. Karem Chokmani for their support throughout my Ph.D. project. Without their contributions, my study would not have been possible. I would also express my appreciation to Caroline Turcotte from ministère de l'Agriculture, des Pêcheries et de l'Alimentation du Québec (MAPAQ). I would like to present my sincere acknowledgement to owners of Domaine Bergeville, Domaine Ives Hille, Verger Ferland, Bleuetière Mi-Vallon, Fromagerie La Station de Compton, and L'Abri Végétal. Their support was essential to establish a close connection between scientific research and practical agriculture and has been encouraging me during my research work.

Content

List of figures

List of tables

1. General introduction

The greatest agricultural risk in connection with low temperature is frost, which can cause severe damages to fruit, foliage, and plants. The danger of low temperatures in horticulture has been recognized since the beginning of farming. Thus, Romans considered the resistance to frost as an important factor when selecting species to cultivate in specific regions. They made efforts to protect crops from freezing injury nearly 2000 years ago during the first century AD (Columela, 1965). Frost is the occurrence of air temperature of 0°C or lower, measured at a height between 1.25 and 2 m above the ground within a weather shelter. Soil frost occurs when ice forms and soil may freeze. Soil frost and frozen depth can be variable and depends largly on early winter air temperature and the amount and timing of snowfall. Young vines, during establishment are particularly vulnerable to the soil frost (Snyder and Paulo de Melo-Abreu, 2005).

Based on the World Meteorological Organization (WMO), frost is one of the main disasters that limit agricultural production in many parts of the world. Damages caused by frost represent 80% of losses from climatic-related disasters (such as storm, hail, and flood) in agricultural sectors (Fig. 1.1). Consequently, frost can have serious impacts on our environment and society. In all parts of the terrestrial landmass, not including lowland tropics, frost is a cause for concern, because it affects the productivity of agricultural, horticultural and silviculture crops (Cohen, 1973; Bagdonas *et al.,* 1978).

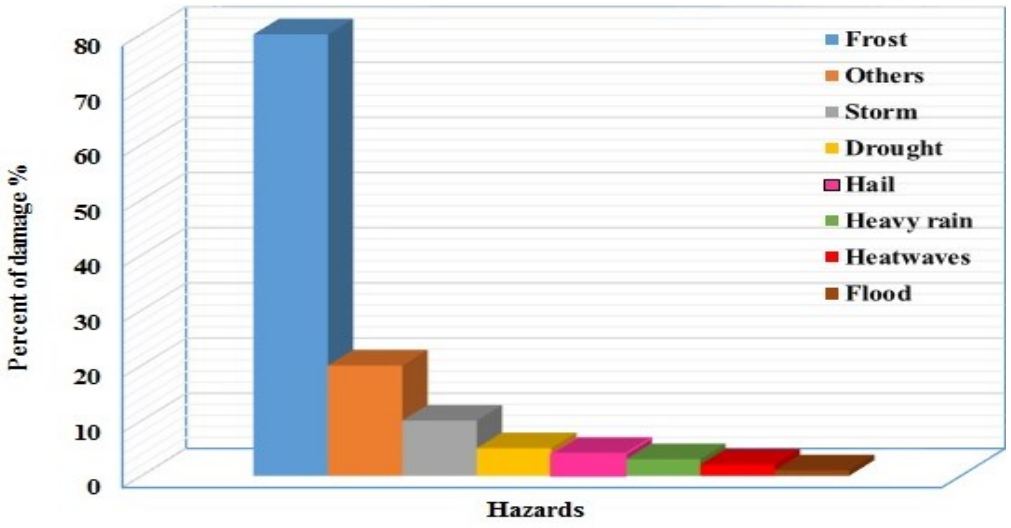

Figure 1.1 Percentage of damages due to climate-related disasters on between 2002 and 2007 (Adapted from the World Meteorological Organization (WMO) report, 2010).

Forecasts for frost nights are usually limited to minimum air temperatures (Rodrigo, 2000; Richards and Baumgarten, 2003). Knowledge of the nocturnal minimum air temperature constitutes one of the main variables during the agricultural period and can help farmers to mitigate its adverse effects on crop productivity through adequate measures. An effective implementation of any type of protection depends on a spatially accurate estimate of nocturnal minimum temperatures (Kalma *et al.*, 1992).

The sensitivity of a crop to low temperatures depends on many factors including air temperature drop. Protecting plants from the effects of critical low temperatures is generally a matter of considerable importance in agricultural and especially horticultural production of high-value fruits and vegetables. Low temperatures and frost during the growing season cause stress, which may lead to serious or irreversible damage of tissues or whole tree seedlings (Sakai and Larcher 1987; Blennow *et al.*, 1998). This significant threat to farmers and gardeners has the potential to damage plants, as well as the yield in some orchards (Gombos *et al*., 2011).

The early fall and late spring frosts usually cause damages to plants (Rosenberg *et al.*, 1983; Geiger *et al.*, 1995). In autumn, an earlier than normal frost can also destroy growing shoots or damage crops that are still in the field. However, the frost in the spring, more specifically at the end of the freezing period and at the beginning of the growing season, damages seedlings and young plants that are already at the flowering stage. Late frost in the spring can inflict a variety of damages, depending on the development stage of the plant (Vestal, 1971; Rosenberg *et al.*, 1983; Geiger *et al.*, 1995). Frost can cause a rapid decline in net photosynthesis and stomatal conductance rates. Young expanding leaves, reproductive organs, and other differentiating tree tissues are most sensitive to freezing temperatures (Taschler *et al.*, 2004).

A wide range of active and passive method exist to avoiding or reducing frost damage. Passive method, such as plant selection, site selection, appropriate use of cultural and management practices; modification of microclimate of the crop are important to avert or minimize frost damage. However, under sever frost conditions, these methods are often inadequate to protect crops Active methods are implemented just before or during a frost night to prevent ice formation within sensitive plant tissue. Wind machines, sprinkling irrigation and open-air heating are the most common active protection methods (Snyder and de Melo- Abreu, 2005; Ribeiro *et al.,* 2006).

The predicted trends in climate change, such as increasing temperature anomalies, may not altogether reduce the risk of frost. Most phenological models show that temperature rising in this

century can lead to earlier plant blossoming. In addition to the earlier start of the active vegetation period, the forecasted milder winters and early springs can multiply the risks of frost affecting buds, flowers, and fruit production (Eccel *et al*., 2008). By responding to warmer temperatures in early spring, plants face a risk of damaging fluctuations after bud break, which means that their vulnerability to low temperatures increases continuously.

1.1 Theoretical background

The earth's surface is the main energy fluxes transfer area in the lower troposphere for many atmospheric, hydrological, and biological processes. Spatial variability in the surface fluxes is responsible for spatial patterns of meteorological variables and phenomena for a range of scales (Whiteman, 1990; Madelin, 2004). Following the laws of thermodynamics, energy can be transformed, transferred or stored, but not destroyed. Thus, the constant input of energy from the environment towards earth and object surfaces must be balanced with an equal output or be stored within interacting masses. The following section examines the forms of energy fluxes that occur to balance the net surplus or deficit resulting from the energy budget.

1.1.1 Radiation and surface energy balance

There are essentially four types of energy fluxes at the surface, namely (1) net radiation (R_n) to or from the surface, (2) sensible heat fluxes (Q_H), (3) latent heat fluxes (Q_E) to or from the atmosphere, and (4) ground heat flux (Q_G) into or out of land. Net radiation may be considered an external forcing, while the sensible, latent, and ground heat fluxes constitute a response to this radiative forcing (Foken, 2008). In accordance with the principle of conservation of energy, for a unit horizontal area, the surface radiative surplus or deficit is balanced with a combination of convective exchanges to or from the atmosphere as sensible (Q_H) or latent (Q_E) heat, as well as through the conduction to or from the underlying substrate such as the soil heat flux (Q_G). From this perspective, the complete energy balance for a system corresponds to (Oke, 1987):

$$R_n = Q_H + Q_E + Q_G \quad (1.1)$$

Net radiation is usually positive during the day when the net shortwave (solar) input exceeds the net longwave (terrestrial radiative) loss; it is negative at night in the absence of solar radiation. Under clear skies at nighttime, more heat is radiated away from an orchard in the form of terrestrial radiation rather than receiving in the form of solar radiation, causing the soil temperature and consequently air temperature to drop (Snyder, 2000; Madelin, 2004). As the focus of this study is on the formation of

cold air at night, the mechanisms associated with heat loss are of primary interest. At night, the land surface loses energy through outgoing radiation, especially during clear skies. All the terms of the surface energy balance (Eq. 1.1) for land surfaces are usually negative during the evening and nighttime periods. As a result, the net radiation becomes negative in the equation for radiation balance, while the surface of the soil loses energy, due to the emission of thermal radiation. Several authors quantified these energy losses: the soil surface or that of a plant at 0°C emits radiation at about 300 Wm^{-2} or energy losses at approximately 2600000 kcal/hour. The net radiation term typically is separated into parts representing the downward shortwave radiation from the sun, reflected shortwave radiation (upward), longwave downward radiation, and finally longwave upward radiation. These terms can be sketched on a surface energy budget diagram (Fig. 1.2) where the direction of the arrow designates the direction of energy transfer. The radiation budget for any point on the surface can be expressed as:

$$Rn = Q_S + Q_{SR} + Q_{Lu} + Q_{Ld} \quad 1.2$$

where the net radiation (R_n) is calculated as the sum of the shortwave down welling radiation mainly from the sun (Q_S), the longwave down-welling infrared radiation emitted by clouds, aerosols, and gases (Q_{Ld}), the shortwave up-welling reflected (solar) radiation (Q_{SR}), and the longwave up-welling infrared (heat) radiation (Q_{Lu}). The upward shortwave radiation is governed by the magnitude of downward shortwave radiation and the proportion reflected as determined by the surface albedo (Liang *et al*., 2010). Upward longwave radiation made up of thermal radiation emitted from the surface and the portion of Q_{Ld} are reflected as determined by surface emissivity. Shortwave radiation can be divided into two types: diffuse radiation from the sky and direct solar radiation.

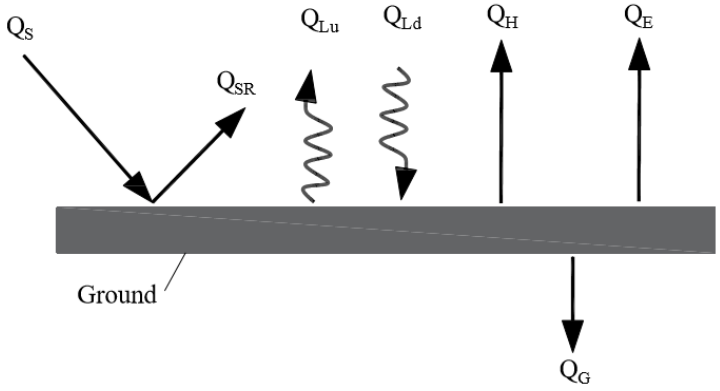

Figure 1.2 Schematics of the fluxes associated with the surface energy budget during a daytime when incoming solar radiation is present. The arrows indicate the direction of flux relative to the ground surface. Q_S is incoming solar radiation.

The loss of energy from the ground can be limited by atmospheric radiation to the earth. This limitation is of greater importance when the atmosphere has higher relative humidity. Water vapor absorbs the terrestrial radiation and reduces its escape to the space. Low-altitude cloud formations always indicate a high level of humidity in the lower levels of the atmosphere. Therefore,–during cloudiness condition, a significant fraction of the radiation emitted from the ground is absorbed in the clouds and reradiated back into the ground. Thus, clouds reduce the radiation imbalance between the upward flux from the ground and downward flux from the atmosphere. Conversely, when the atmosphere is dry and clear, the downward atmospheric radiation is less than that emitted by the earth and the energy balance is negative. The radiative and energy balances are then close to zero and the air-cooling is minimal. For example, consider the energy balance of a vegetated surface with a zero temperature for two different conditions: clear sky and cloudiness. For the clear sky, atmospheric radiation is no more than 200 Wm^{-2}. However, the terrestrial radiation (infrared radiation) is 300 Wm^{-2}. The radiative surface energy balance is -100 Wm^{-2}. Under a clear sky, more heat is lost than gained in this process. Dry air is transparent to infrared radiation, allowing energy to escape from the surface.

1.1.2 Thermal inversion phenomena

The troposphere is the atmospheric layer where on average, the air temperature decreases with increasing altitude. The change of air temperature with altitude is referred to as the air temperature lapse rate and, which will vary on any given day. During the nighttime hours, there is a net loss of longwave radiation from the surface to the sky. Sensible heat content of the soil decreases as energy is radiated away, causing the air temperature near the surface to drop. Because there is a deficit of sensible heat near the surface, there is sensible heat transfer by conduction from the air above to partially replace the surface heat loss. Therefore, the radiative cooling due to longwave radiation leads to the progressive thickening of the surface inversion layer and leading to temperature increase with altitude and the value of the lapse rate to be negative (Goplakrishnan and Shran, 1998). This phenomenon, which occurs under negative net radiation and low winds, is called a thermal inversion (Snyder and Paulo de Melo-Abreu, 2005). An inversion acts as a ceiling, preventing further upward convection, which is generally the limit for cloud development (Madelin, 2004).

1.2 Types of frost

Frost is formed through two types of physical processes: radiative or advective cooling which lead to two dominant types of frost situations, advection and radiation frosts (Tait and Zheng, 2003).

Each type is associated with different frost management strategies. Regardless, understanding the physics these two processes is critical to develop efficient frost management strategies.

Radiation frost is characterized by clear sky, no wind, and low dew point temperature. Radiation frosts occur at night and result from intense, longwave radiation cooling under calm, clear and dry atmospheric conditions. Strong surface inversions develop in the stable atmosphere associated with radiation frosts. It occurs because of heat losses in the form of radiant energy. Under a clear nighttime sky, more heat is radiated away from an orchard than it is radiated into the orchard. Consequently, the temperature drops faster near the radiating surface, causing a temperature inversion during radiation frost conditions. Energy is lost through radiation upward from the surface. It is channeled through downward radiation from the sky, conduction of heat upward through the soil, and convection of warmer air to the colder plants. Table 1.1 shows a typical nighttime energy balance for a citrus plant orchard. The values are comparable to other crops. Under a clear sky, more heat is lost than gained in this process.

Advection frost is characterized by moderate or strong cold wind (at least 2 ms^{-1} or more), below critical temperatures, which are part of large regional cold air masses. Destructive cold temperature events under advective (windy) conditions are often called freezes rather than frosts. These large-scale winds have a tendency to persist throughout the night and sometimes during the day. They may occur under cloudy or clear sky. Windy conditions do not permit thermal inversions to form although radiation losses are present. The rapid cold air movement that advects or "steals away" the heat from the plant causes damages. Advective frosts are characterized by cloudy skies, moderate to strong winds, no temperature inversion, and low humidity.

Very little can be done to protect plants against advective-type frost. Placing trees under water sprinklers is suggested as one of the few alternatives to avoid the effects of advection frost. Water transition from its liquid phase into ice lead to release the latent energy into sensible energy (334 kJ kg^{-1}). By this way, we use the energy produced by transition of water, when the air temperature is below freezing points (0°C). There are two differences between radiation and advection frosts: (i) Under radiation frost conditions, winds are normally light and temperature inversions develop as the air in contact with the cold radiating surfaces becomes chilled and heavy. However, Advection frosts often occur with strong winds. (ii) Since advection frost is caused by the passage of a cold front, it generally occurs at a regional or synoptic scale. However, radiation frost is a local phenomenon. This is why the use of spatially explicit models can help to identify the risk areas

(Ahrens, 2000). Even though both types of processes are usually present in most frost events, radiation frost is the dominant type of frost during the growing period (Snyder and Paulo de Melo-Abreu, 2005).

Table 1.1 The flux density for each of the energy transfer terms for a citrus plant orchard. Under clear skies, more heat is loss than gained (Adapted data from Bartholic *et al.*, 1974, cited in Mee, 1979).

Energy Transfer	Flux Density (Wm^{-2})
Conduction (from the soil)	+28
Convection (from the air)	+39
Downward Radiation (from the sky)	+230
Upward Radiation (from the orchard)	-315
Net Energy Loss from the crop	-18

1.3 Environmental variables linked to minimum air temperature and radiation frost

There are many factors that can affect near-surface air temperatures across regions in complex terrains. The orography, the soil and vegetation characteristics, as well as local variations in net radiation, may all play a part in determining the temperature distribution. Their relative importance will vary according to large-scale climate conditions. Many studies have reported the role of environmental variables related to frost, more specifically regarding meteorological and geographical variables. For example, Bootsma (1976) studied the minimum temperatures and risks of frost in the mountainous lands of Canada. The results indicated that the average estimated frost date occurring in valley bottoms was 34 days later in the spring and 39 days earlier in the fall compared to higher elevations. Avissar and Mahrer (1988) developed a three-dimensional model to simulate the local scale microclimate zones near ground level during radiative frost nights in non-uniform lands. Effective variables of this model included topography, vegetation, soil humidity, wind velocity and direction, and air humidity.

Field research over open areas shows that minimum temperature changes with elevation, wind velocity, and total net radiation at night (Kajfez, 1987). Nocturnal temperature varies at fine spatial scales in complex terrain, reflecting interactions of synoptic atmospheric conditions with terrain, vegetation and spatial location (Gombos *et al*., 2011). Three types of variables can influence frost damage risk and its severity: (1) meteorological variables (2) topographical variability, and (3) plant characteristics.

1.3.1 Meteorological variables

Important meteorological variables such as air humidity, cloud cover effect, wind velocity, must be considered to understand how they are connected to air temperature and frost.

Air humidity: Air humidity represents the amount of water vapor in the atmosphere and influences the surface radiation budget, consequently air temperature. Atmospheric humidity is expressed in a variety of ways, many of which have emerged from the meteorological research community. Some of the most common variables to express atmospheric humidity include dew point, specific humidity, and relative humidity. The humidity contained in the air absorbs part of the terrestrial radiation, which is then partly reemitted towards the ground. Therefore, the air humidity could then reduce the radiative deficit through an increase of atmospheric radiation during the night. In addition, the water vapor effect on the dew point temperature combined with condensation consequently releases latent heat energy. The presence of humidity limits radiative cooling, whereas dry air can enhance cooling by facilitating evaporation on soil and plant surfaces.

Cloud cover: Cloudiness is regarded as a key variable affecting the Earth's radiation balance and therefore, the difference in nocturnal cooling rates (Kidder and Essenwanger, 1995; Gustavsson, 1990). Clouds dense enough to cast a shadow on the ground emit longwave radiation like full radiators at the cloud base temperature of the water droplets or ice crystals from which they are formed. The presence of clouds increases the flux of atmospheric radiation received at the surface, because the radiation from water vapor and carbon dioxide in the lower atmosphere is supplemented by the emission from clouds in the wave band, particularly between 8 and 13 μm. For clear skies, the heat loss at the ground level is greater than during nights when the sky is partly covered. In summary, solar and terrestrial radiation depend on the amount and types of clouds.

Wind velocity: Wind velocity corresponds to another climatic variable in connection with nocturnal cooling. Wind direction determines the characteristics of air mass (temperature, humidity) on the synoptic scale. Vazart (1988) demonstrated an increased risk of frost through the advection of cold and dry air after a rainfall or snowfall (advection frost). The low speed of the wind (less than 2 ms^{-1}) is not able to enhance the mixing of the atmospheric layers and in particular, the low layers where the phenomenon of thermal inversion occurs. In the case of light winds and clear skies, the amount of turbulent heat transported downward is less than higher wind speed condition (Van de Wiel *et al*., 2012). Hence, wind speed exercises influence on air temperature differences. Strong winds prevent ground temperature inversion through genetic mixing of atmospheric layers,

but light winds can disturb cold air stagnation. During windy nights, the minimum temperature is therefore higher than during nights with light winds.

1.3.2 Effects of topographic variability, soil texture and forest

Topographic variation has a significant effect on climate on a scale of tens to hundreds of meters (Tran, 2017). The nocturnal temperature and severity of frost varies considerably with general atmospheric conditions, as well as with local differences in topography and vegetation (Richards and Baumgartner, 2003). Topography has two major effects on frost and ground-level temperature distribution: the first is tied to hill slope angle and aspect, while the second is related to local relief creating wind patterns and generation of air flow. Zinoni *et al.* (2002) conducted a climatological and orographic study to identify areas prone to frost and determine the characteristics of frost events between April 1987 and March 2000 for 161 weather stations in the Emilia-Romagna region in Italy. They determined correlations among climatic and orographic variables and defined a significant correlation between the mean minimum air temperature during the frost and the relative height from valley bottom. Moreover, a minimum temperature map was derived over New Zealand using GIS modeling and relied on factors such as ground cover, slope, elevation, latitude, and distance from the sea (Richards and Baumgarten, 2003). Their results highlighted that spatial distribution of radiation frost is closely associated with topographic patterns.

Focusing on late frost spatial modeling, the air temperature was measured using thermal infrared images during a strong thermal inversion episode in a fruit-growing area (Eccel *et al.*, 2008). Their results indicate the existence of a clear geographic pattern in the distribution of minimum air temperature. With regard to the above mentioned, several other studies have documented the importance of local topography in causing large temperature variations, assessing severity and spatial distribution of radiation frost (Tabony, 1985; Bogren and Gustavsson, 1989; Toritani, 1990; Whiteman *et al.*, 2007; Barry, 2008). All of these studies bring attention to the role of microclimate and geographical parameters related to frost risk.

As a conclusion, the severity of radiation frost varies with general atmospheric conditions, as well as local differences in topography. Primary topographic effects result from differences in hill slope angle and aspect, while secondary effects can result from the influence of terrain on mountain winds and generation of air flow effects such as cold air-drainage (Barry, 2010). Along with the changes in the topographic amplification in the valley, several factors need to be considered to determine whether or not the cold air in the valley is likely to drain.

Drainage flows are caused by the rapid cooling of the air after sunset in contact of air flow from surrounding terrain slopes. This air is negatively buoyant and pushed down the slopes towards the bottom of the valleys, following gravity. Cooling during the night caused by radiation is why cold air from mountains and slopes descends under gravity into valleys (Fohn, 2006).

The resulting horizontal buoyancy gradient drives a flow in a downslope direction, transporting air toward the valley bottom. The down-slope movement of air is referred to as katabatic wind. Local down-slope gravity flows are known by several names, particularly cold air drainage, cold air run-off, cold air stream, and cold air current (Geiger, 1965). Cold air flow, as well as *in situ* cooling, contributes to nocturnal cooling in a valley. Cold air tends to sink in the valleys; moreover, there are much lower temperatures than the corresponding free air. This phenomenon is called a "cold-air pool." The significant temperature anomalies experienced in such zones can have strong impacts on local native plant distributions, as well as horticulture and agriculture (Chung *et al.*, 2006; Hubbartet *et al.*, 2007; Bigg *et al.,* 2014).

A number of studies have contributed important knowledge about the physical processes controlling nocturnal cold air drainage. External meteorological factors that influence the magnitude of cold air drainage and nocturnal winds were identified by Barr and Orgill (1989). Physical mechanisms of heating and cooling related to cold air drainage in a single basin described (Kondo *et al.*, 1989; Konno *et al.*, 2013). Chung *et al.* (2006) presented a statistical approach to estimate the effect of cold air accumulation on local temperature variations for a small basin. The results indicate that eliminating cold air drainage in spatial estimation of nocturnal air temperature was a source of uncertainty and error. These studies and others (Dobrowski *et al.*, 2009; Lundquist and Cayan, 2007) demonstrate that cold air drainage and cold-air pool are physically interpretable processes that occur across diverse topographic areas.

Most theoretical analyses on cold air drainage flow are reduced to bare slope conditions. Cold air drainage flow also depends on the vegetation cover. For this reason, a complete model remains to be developed for cold air drainage flow by taking all the significant aspects of relief and land cover into account (Gaulden *et al.*, 2007). However, direct objective measurement and modeling of cold air pooling requires micrometeorological observations and modeling techniques that were unavailable (Lundquist *et al.*, 2008). Despite the growing awareness of influence of cold air drainage on nocturnal temperature, this phenomenon is not considered on currently interpolation methods.

In addition to local topography, soil texture plays a role in the net radiation balance and air temperature variations, because each type of soil comprises unique textural characteristics. Sandy soils warm up more rapidly in the spring than clay soils. This is due to lower heat capacity, lower thermal conductivity, and less evaporative chilling. Soil texture is defined by the relative volume of sand, silt, and clay particles. Longwave radiation emission by the surface is lower when the soil is wet and has vegetation cover. Coarse texture has poor heat capacity and therefore emits more longwave radiation than fine texture. The thermal regime of the soil can be modified by regulating incoming and outgoing radiation, as well as by changing the thermal properties of the soil (Baver *et al.*, 1972).

Mass density, specific heat, heat capacity, thermal conductivity, and thermal diffusivity are the thermal properties relevant to heat transfer through soil. These properties affect on average soil temperature or distribution of temperature in the soil. Thermal conductivity is affected by soil moisture and texture. Wet soils have higher conductivity than dry ones. Moreover, soil texture determines how quickly the soil will heat or cool. Therefore, the energy flux transmission within the soil depends on the physical properties of soil particles, their degree of compaction, and soil moisture content.

Understanding modifications to the microclimate due to wind shelters has been an active area of research for several decades (Hipsey *et al*., 2004). The influence of the forest shelterbelt on nocturnal temperatures can help formalizing to predict local frost. The primary effect of shelterbelts is the reduction in wind speed, which causes reduced air turbulence or mixing (during day and night). However, when the surface cools at night, reduced mixing causes lower minimum temperatures, compared with open areas. The sheltered zone has a modified microclimate and generally greater crop yields. The wind velocity reduction tends to decrease air and surface temperatures, partly by preventing the breakup of the atmospheric inversion (Monson, 2014).

The sheltering mechanism relies on the reduction of turbulent mixing of the cold near-surface air with warmer air aloft. Under clear conditions, this leads to a higher rate of cooling of the air in contact with the radiative cooling surface (Gustavsson *et al.*, 1998; Monson, 2014). The magnitude of temperature change in a sheltered zone may reach up to 2°C. The reduction of wind velocity in the protected areas behind a shelterbelt takes place because the shelterbelt exerts a drag force on the wind field, leading to a loss of momentum of the airflow (Plate, 1971). This results in altered microclimates in protected areas. Shelterbelts and windbreaks remain an important area of research

in field, wind tunnel and numerical studies (Rajewski, 2007). Experimental studies of wind speed and turbulence were done in laboratories with wind-tunnel models and in the field with full-scale models. Van Eimern *et al.* (1964), McNaughton (1988), and Heisler and Dewalle (1988) provided interpretations of experimental data. The effect of forest shelter on wind velocity reduction and turbulence intensity, depends on its structure such as width, length, shape (Vigiak *et al.*, 2003; Lee, 2010), and porosity (Santiago *et al*., 2007; Lampartova *et al.*, 2015). Most shelterbelt studies reported in the literature are experimentally driven, emphasizing wind-speed reduction produced by shelterbelts. Therefore, effects of the forest wind shelter are divided into two functions: directly related to the effect on wind velocity and indirectly related to air temperature due to the effect of wind velocity.

The prediction methods must add some spatial algorithms in order to account for local terrain effects. Local topography effects can result from the influence of terrain relief on wind and generation of airflow such as cold air drainage. An understanding of terrains related process such as sheltering and cold air drainage is required to improve nocturnal short-term weather predictions.

1.3.3 Plant characteristics

Plant characteristics such as the type, variety, and stage of development show that plant species differ greatly in their susceptibility to cold injury (Table 1.2). Crops are particularly prone to damage due to low temperatures during certain stages, especially flowering and early reproductive developments. During these periods, temperatures below the freezing level may damage the plants, while temperatures just above the freezing level might slow down plant growth. Frost damage occurs as water within plant cells freezes.

The air temperature at which this happens varies depending on the plant part and biochemical characteristics that change during the development of the plant. The level of tolerance to frost of a plant or the minimum air temperature at which a plant can withstand serious injury is referred to as the critical temperature (Snyder and Paulo de Melo-Abreu, 2006; Olszewski *et al.*, 2017). Protecting plants from the effects of destructive low air temperature is generally a matter of considerable importance in agriculture, especially in terms of horticultural protection of high-value fruits and vegetables.

Table 1.2 Examples of crops that may or may not resist to frost during different development stages (taken from Snyder and Paulo de Melo-Abreu, 2005).

Harmful temperature (degrees < 0°C)			
	Germination	**Flowering**	**Fruiting**
Highest resistance			
Spring wheat	9-10	1-2	2-4
Oat	8-9	1-2	2-4
Barley	7-8	1-2	2-4
Peas	7-8	2-3	3-4
Resistance			
Vetch	6-7	3-4	2-4
Beans	5-6	2-3	3-4
Sunflower	5-6	2-3	2-3
Flax	5-7	2-3	2-4
Carrots	6-7	---	---
Medium resistance			
Cabbage	5-7	2-3	6-9
Soy beans	3-4	2-3	2-3
Low resistance			
Corn	2-3	1-2	2-3
Millet	2-3	1-2	2-3
Sorghums	2-3	1-2	2-3
Potatoes	2-3	---	1-2
No resistance			
Buckwheat	1-2	1-2	0.5-2
Castor beans	1-1.5	0.5-1	2
Melon	0.5-1	0.5-1	1
Tomatoes	0-1	0-1	0-1

1.4 Frost protection methods

If economic conditions prevail, crops can sometimes be protected against frost. A wide range of passive (indirect) and active (direct) methods exist to avoid or reduce frost damage (Kalma *et al.*, 1992; Snyder and Paulo Abreu, 2005). Most of these frost protection methods are practical and effective only against radiation frost.

1.4.1 Passive methods for frost protection

Passive protection includes methods that are implemented before occurrence of radiation frost to help avoid the need for active protection. This method used well in advance before the actual freeze danger is probably the most economical and effective. The most widely employed forms of these methods include site selection, managing cold air drainage, plant selection, plant nutritional management, and bacteria control (Snyder and Paulo Abreu, 2005). The main passive method is site selection. A given farm may have one or more natural microclimates where minimum temperatures

during frost events are much warmer or colder than those in the surrounding areas. For example, under radiative cooling conditions, the earth loses heat to space and cools the adjacent layer of air. If the vineyard is on a slope, the cold, relatively dense air moves downhill (Fig. 1.3). The sinking cold air collects in low-lying areas and can create frost pockets. The vineyards in low-lying frost pockets are much more prone to frost damage, than the ones at higher elevations one. Therefore, agricultural producers should use passive protection methods such as sites selection before planting is established. In fact, good cold air drainage management and planning is an important part of freeze protection programs from the beginning.

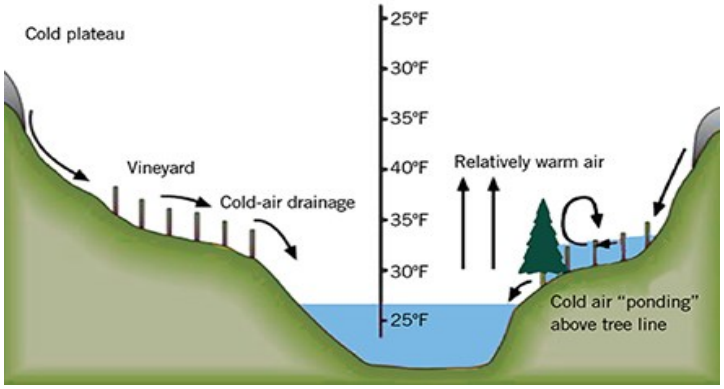

Figure 1.3 Illustration of site topography effects on air temperatures during radiative cooling. The sinking cold air collects in low-lying areas and can create frost pockets, which are much more prone to spring and fall frost damages (taken from Snyder and Paulo Abreu, 2005).

1.4.2 Active methods for frost protection

Active protection takes place just before and during a frost event, specifically after a frost warning has been issued in the weather forecast. The use of wind machines Selective inverted sink (SIS) system, open-air heating, sprinkling irrigation, and helicopters are the most common active protection methods (Fig. 1.4). The tower-less wind machine, also known as SIS system, was designed to drain cold air to prevent it from accumulating. In spite of the various methods adopted to prevent frost, the damage to plants continues to pose a problem and exert a major economic impact. Implementing frost protection at the wrong time or under the wrong conditions may sometimes be more damaging than doing nothing at all. Consequently, an efficient implementation of any type of protection depends on a spatially accurate estimate of frost. Reliable knowledge of the minimum air temperature can help farmers to mitigate its adverse effects on crop productivity by taking adequate

measures. There are methods available to protect against and to prevent frost, but they need to be implemented before the frost actually occur.

Farmer should know the nocturnal temperature variation as they occur over their land which fields are most prone to forest, so that action can be taken in these fields.

Figure 1.4 Examples of different types of active methods against frost: (a) towerless wind machine also called selective inverted sink (SIS) system; (b) open-air heating; (c) helicopters; and (d) sprinkling irrigation (taken from Snyder and Paulo de Melo-Abreu, 2005).

1.5 Forecast of minimum temperature

For efficient implementation of frost protection strategy, high resolution and accurate forecasts of minimum air temperatures are required, (Kalma *et al.*, 1992; Blennow and Persson, 1998; Prabha and Hoogenboom, 2006). Reliable forecasts are of considerable importance in the agricultural field to identify frost conditions and facilitate the implementation of protective measures (Rodrigo, 2000; Lhomme and Guilioni, 2004). Knowledge of the nocturnal minimum air temperature constitutes one of the main variables during the agricultural period and can help farmers to mitigate its adverse effects on crop productivity through adequate measures. Predictions of nocturnal minimum temperatures and warnings enable horticulturists to make good decisions in terms of frost protection (Taboni, 1985).

Forecasting the high-spatial resolution of air temperature in complex terrains represents an important scientific challenge. Current frost forecasting models only offer low spatial resolution. Studies using low-resolution climate models could not capture high-resolution interactions such as topography, vegetation cover, and cold air drainage, which are key factors of frost occurrence (Fleagle, 1950; Kalma *et al.*, 1992).

Various authors have produced a vast number of empirical formulae to predict minimum air temperature. Early methods of prediction were mainly based on statistical relations between nocturnal temperature decreases and meteorological variables (Young, 1920; Ellison, 1928). Relevant meteorological variables generally included some expression of air humidity and possibly cloud coverage. These empirical methods have only local predictive potential, but they have not really been applied to other locations (Cellier, 1993). Following Brunt's approach (1941), many simplified formulae were published based on the analytical solution of the heat conduction equation in bare soil (Jacob, 1940). However, they were developed for open areas or plains. This means that for the topographic regions with, these methods did not produce reliable predictions (Ghieliand and Eccel, 2006). Another approach adopted refers to the artificial neural network, which is empirically based and does not take into account the physical and dynamic aspects of land-atmosphere interactions or their temporal evolutions (Prabha and Hoogenboom, 2008). Other approaches based on the vegation-atmosphere energy balance designed by Shuttleworth and Wallace (1985), and upgraded by Shuttleworth and Gurney (1990), were used to predict the minimum air temperature from observations made during the sunset transition period (Lhomme and Guilin, 2004). Yet these modeling approaches do not consider the local circulations due to topography such as cold air drainage (Whiteman *et al.*, 2010).

Forecasting frost with a weather prediction model at the mesoscale reduced prediction errors when compared with earlier models. Nevertheless, numerical weather prediction (NWP) models are mostly generalized, thus the NWP data is not useful for rural areas where farming is dominant (Huth, 2004). Furthermore, Environment and climate change Canada has the responsibility to call all meteorological alerts. Frost warnings issued by Environment and climate change Canada on a regional scale (~15 km) are not presented in a format suitable to interpretation for a specific site or farm. Instead, the alerts are issued at a regional scale, for example the Coaticook area or Brome-Missisquoi area (Fig. 1.5). Conversely, the assessment of the agricultural production loss at a farm or on a local scale requires access to compatible frost information.

The existing network of weather stations does not allow sufficient spatial resolution to interpret directly frost prediction on a local scale. Yet estimating the spatial distribution of frost over a heterogeneous terrain with very few meteorological stations remains a challenge. This is more significant for agricultural purposes where knowledge of the local differences in climate within a relatively small area is mandatory. A review of the literature demonstrates that most of the spatial interpolation methods consider the distance from the reference station and the elevation (Benavides *et al*., 2007). Numerous meteorological variables are relevant to predict local frost, particularly climatological variables and local topography. The traditional methods for spatial interpolation perform poorly when used for meteorological data and existing interpolation methods often fail to predict nocturnal minimum temperature under radiation frost conditions (Chun *et al*., 2006; Dobesch *et al*., 2007).

Meteorological distribution system for high-resolution terrestrial modeling (Micro-Met) developed to produce meteorological forcing is required to run spatially distributed terrestrial models over a variety of landscapes. The model uses known relationships between meteorological variables and the surrounding landscape (primarily topography) to distribute those variables over any given landscape in computationally efficient and physically plausible ways. Station data are interpolated to a regular grid and physically based adjustments are made to the interpolated fields (Liston and Elder, 2006). Micro-Met incorporates seven sub-models to distribute the meteorological variables: air temperature, relative humidity, wind speed and direction, solar radiation, longwave radiation, surface pressure, and precipitation. To produce these spatial distributions, Micro-Met assumes that at least one value of each of the meteorological variables available for each time step, within or near the simulation site.

To create the distributed atmospheric fields, spatial interpolations are performed using the Barnes objective analysis scheme, and subsequent corrections are made to the interpolated fields using known temperature-elevation, wind-topography, humidity-cloudiness, and radiation-cloud-topography relationships. MicroMet includes a preprocessor component that first analyzes meteorological data to identify and correct potential deficiencies (e.g. values out of the ranges given in the subroutine). It then fills in any missing data segments with realistic values. The atmospheric fields are distributed using a combination of lapse rates and spatial interpolation using the Barnes objective analysis scheme.

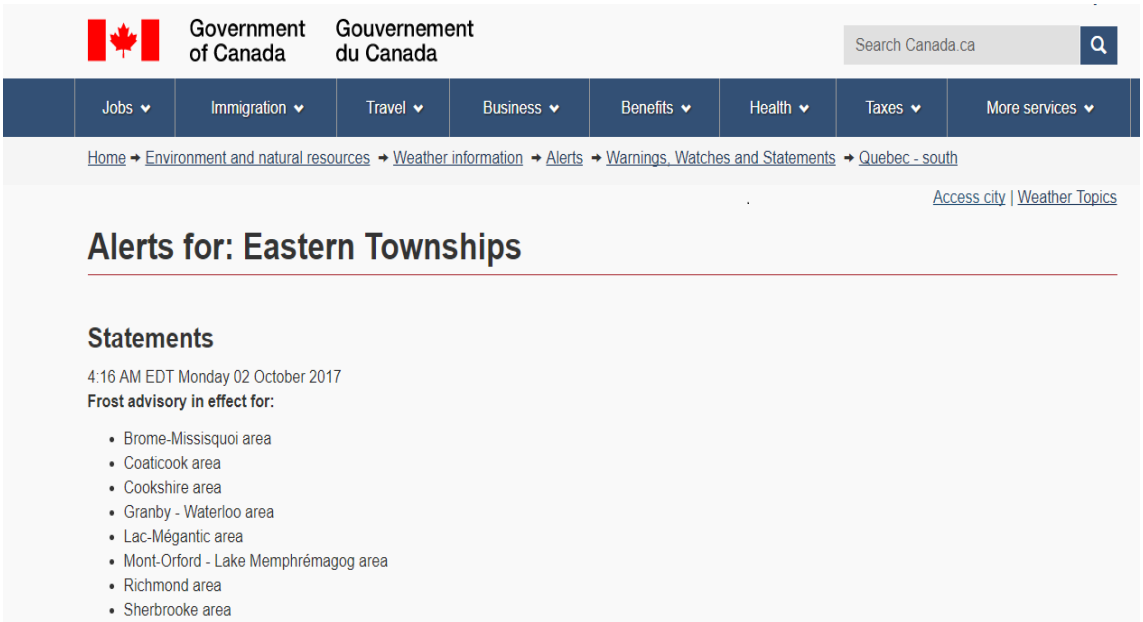

Figure 1.5 Example of a frost alert issued by Environment and climate change Canada for the Eastern Townships on a regional scale (Environment and climate change Canada, 2017).

Predictive frost models can be a tool for horticultural entities to determine the suitable conditions leading to critical temperatures (Rodrigo, 2000; Lhomme and Guilioni, 2004). The current low-spatial resolution (15 km) of minimum temperature forecasts represents a strong impetus for the development of a frost model on a fine scale (30 m). For frost prevention methods to be effective, accurate local weather information, short-term weather forecasting, and precise spatial estimates of frost are necessary.

2. Hypotheses, objectives and overview of the methodology

For efficient implementation of frost protection, accurate and high-resolution forecasts of minimum air temperatures are required (Kalma *et al.*, 1992; Blennow and Persson, 1998; Prabha and Hoogenboom, 2006). Studies using low-resolution climate models could not capture high-resolution interactions such as topography and cold air drainage, which are the key factors of frost occurrence (Fleagle, 1950; Kalma *et al.*, 1992).

Forecasting of minimum air temperature presents a number of interesting agrometeorological features. A resistance model for frost prediction (Lhomme and Guilioni, 2004) assumes a steady state regime at sunset. This type of prediction model focuses on the point-based "two-layer vegetation-atmosphere energy model" designed by Shuttleworth and Gurney (1990), an operational example of non-lagrangian model, which does not deal with the complex resolution of the non-steady-state regime.

The vegetation-atmosphere model removes the computational requirements inherent to non-steady-state numerical and analytical models to greatly simplify the overall complexity of the model and provide a potential on-site frost prediction capability (e.g. Cellier, 1993; Figuerola and Mazzeo, 1997). However, this prediction model requires many meteorological and land surface variables: air temperature, dew point, soil temperature, wind, albedo, emissivity, ground heat flux, and longwave radiation (Lhomme and Guilioni, 2004).

Meteorological networks, which can provide the necessary information, are commonly sparse in mountainous regions. Spatial interpolation techniques represent a reliable approach in order to estimate weather information for unobserved locations from nearby measurements. To run the vegetation-atmosphere model and avoid employing different interpolation methods for different variables, this research used Micro-Met model to produce high-resolution meteorological data distributions (e.g. 30-m to 1-km). Micro-Met interpolates irregularly distributed station observations to a regularly spaced grid. In addition to the station interpolations, Micro-Met employs corrections based on known temperature–elevation, wind–topography, and solar radiation–topography relationships. The resulting procedures produce much-improved oved temperature, humidity, wind, and incoming solar and longwave radiation distributions when the spatial scale of topographic variability is smaller than the distance between stations or analyses-model grid points. Nevertheless, we identified several limitations to the Micro-Met formulation and algorithm Studies on radiation frost using the Micro-Met would require enhancing the model to include the capacity to address four

considerations: air temperature lapse rate, downward longwave equation, cold air drainage and frost shelter belt.

The lapse rate of near-surface air temperature is a critical parameter for obtaining high-precision air temperature products, especially in mountainous areas. The average lapse rate values 1°C/ 100m for dry adiabatic and 0.65°C/100 m for moist adiabatic condition (Minder *et al.,* 2010) cannot distinguish the seasonal differences and atmospheric conditions related to air temperatures. The current Micro-Met system uses the general values provided by Kunkel (1989), who considered planetary spatial resolution for the northern hemisphere on a monthly mean basis (Liston and Strume, 2006). However, the monthly average values were known to be rough approximations that might not be representative of the atmospheric conditions for a particular region during a certain period (Rolland, 2003).

Downward longwave radiation is an important energy flux, for which the accurate estimation of its components is necessary for improving weather predictions (Bilbao and Miguel, 2006). Two problems were detected. First, the majority of the methods were developed empirically at specific locations and did not fare well in other locations (Crawford and Duchon, 1999; Bilbao and Miguel, 2006). Second the method used by the Micro-Met was proposed for cloudy skies, which is not associated with frost synoptic conditions (Liston and Strurm, 2006).

The main challenge in an accurate distribution of air temperature is cold air drainage and pooling that occur when cold air is drained away from the slopes. The errors made by the temperature distributed models were particularly significant in areas subject to cold-air pooling, where results of high-resolution atmospheric models were often 2 to 3°C too warm during cold pool events (Holden *et al.*, 2011). For reducing the uncertainties in the estimation of air temperature, an algorithm that adds a cold-air accumulation concept to the Micro-Met is needed.

In addition to local topography, the influence of the forest shelterbelt on wind speed poses another challenge. Most studies in this field concluded that wind-speed reduction was produced by shelterbelts. Their effects reduce wind velocity, which in turn increases the danger of frost in sheltered areas when compared with unsheltered areas. According to Lampartova *et al* (2015), a velocity below 3.6 kmh^{-1} increases considerably the risks of frost. However, Liston and Sturm (2006) distributed wind speed on the Micro-Met system using the topographically driven wind model, adjusting the speeds and directions according to topographic slope and curvature relationships. The effects of the forest shelterbelt were not integrated in the current version of Micro-Met.

Nocturnal minimum air temperature using vegetation-atmosphere energy model requires the surface temperature at sunset time, which is not available at a meteorological station. Measured values are usually very sparse in space and time (Mihalakakou, 2002). Satellite MODIS data provide this value at 13h30 local time. There is no sub-model integrated into the Micro-Met to distribute the soil temperature at target time (sunset period). In response to this lacking data , new approach needed to developed. The overall premise of this work was to improve the ability of current radiation frost models to predict local frost and propose mitigation measures to reduce the impact of frost on crop productivity.

2.1 Hypotheses and objectives

This research project was based on two working hypotheses:

i. Local circulation associated with topography was not considered in the vegetation-atmosphere energy model (Lhomme and Guilioni, 2004; Whiteman *et al.*, 2007). It is assumed that the model's accuracy in the forecasting of local minimum temperatures could be improved by adding supplemental algorithms of local circulation. We therefore speculated that it was possible to improve local minimum temperature estimates by using terrain variables that characterize factors such as topographic convergence as it can act as proxies for cold air drainage;

ii. Results obtained on methods to identify cold-air pooling in any area of complex terrain where a Digital Terrain Model (DTM) was available (e.g. Lundquist *et al.*, 2008). The scale of cold pools is frequently finer than the grid scale used for operational weather prediction models. The proposed hypothesis supposed that a 10-m resolution DTM were sufficiently accurate to represent site topography, including vegetation. More specifically, the DTM allowed quantification of the stagnation of cold air due to drainage of cold air at a resolution pertinent to agricultural management.

The overall motivation for this work was to overcome the limitations of current radiation frost models with the ultimate goal of helping to minimize the consequences of local frost on crop productivity. The observations and measurements of agrometeorological weather parameters with sufficient density in space have created monitoring systems that could be used as tools to follow developments and, when necessary to issue warnings. Therefore, the main objective of this study was to propose scientific advances in terms of two components related to the mitigation of frost damage by (i) improving the prediction capability of local frost with a new numerical model adapted to

forecast minimum temperatures at a 10-m resolution, and (ii) proposing a new mitigation approach to protect agricultural crops. These advances were accomplished by reaching two specific objectives:

1. To enhance the Micro-Met model's capabilities by taking into account four important effects, (i) the local air temperature lapse rate on a daily basis, (ii) the downward longwave radiation under clear sky conditions, (iii) the cold air drainage on the temperature drop in the depression areas, (iv) the shelter forest effect on wind speed;
2. To develop a method that extrapolates soil temperature at sunset time with inputs near the sunset.

2.2 Overview of the methodology

The radiation frost period study in this research is related to a limited period of the growing season. The usage of this period was considered because plants show a very high susceptibility to frost injury during the time when they are fully dehardened at the growing season (Rodrigo, 2000). The two-layer models developed by Shuttleworth and Wallace (1985), and Shuttleworth and Gurney (1990), were used to predict nocturnal minimum temperature. One of the key challenges in using the vegetation-atmosphere model was the limitation in availability of spatial-temporal input data. Moreover, model inputs and parameters were forced to be routinely available at various times close to the local sunset period. To extend the vegetation-atmosphere energy model across the study site, it was required the extrapolation of various meteorological variables. To overcome these problems, we proposed a methodology based on a high-resolution distribution meteorological model, remote sensing satellite data, and a weather station. The methodology was divided into four essential components as follows.

2.2.1 First component: providing meteorological data close to the sunset period

In this step, an extrapolated model designed to power energy -vegetation model. The new model was based on a formwork in Micro-Met model. Numerous algorithms were developed and added to Micro-Met to model atmospheric variables. Achieving the four specific improvements to the Micro-Met model, was required the four separate methodological steps as followed: 1. Improving atmospheric emissivity equation under clear sky conditions; 2. Estimating of the air temperature lapse rate; 3. Quantifying the effects of cold air drainage on temperature; 4. Quantifying the shelter effect on reduction of wind velocity.

2.2.2 Second component: providing soil temperature close to the sunset period

A multi-year field measurement was carried out for creating a database. The location of each of the mentioned stations was determined according to the microclimate conditions such as hilltop, mid-elevation, valley bottom, exposed, shaded ridges, and flat area. Different regression techniques were used to develop an equation to short term forecasting soil temperature. The method presented in this research, allowed using high spatial satellite soil temperature and estimating soil temperature at target hour (sunset period).

All these features were stored with two future goals: first, improving Micro-Met model to create a high-resolution meteorological distribution model; second, developing an operational model (minimum air temperature forecasting model). Enhancing the Micro-Met system offers the possibility of estimating energy fluxes over heterogeneous land surfaces and consequently, predicting nocturnal minimum temperatures over topographic terrain at a high-spatial resolution. This improvement constitutes a major development that may change the applicability to implement and protect crops against frost. Enhanced Micro-Met in comparison to current Micro-Met, provided more accurated input for the agrometeorological model such as vegetation-atmospheric energy model.

2.2.3 Third component: vegetation-atmosphere model implementation

In this regard,four methodological steps were taken: 1) Operational initialization performed with powering data input ; 2) Processing functions, fulfilling the purpose of estimating the surface albedo, emissivity, NDVI and specification of air and soil resistances; 3) Estimation radiation flux (ground heat flux and net radiation) and turbulent flux to establish the energy balance equation system; 4) Solving the energy balance equation to predict nocturnal minimal air temperature. Figure 3.1 shows diagram of the methodology procedure to predict nocturnal minimum temperatures.

2.2.4 Fourth component: presenting a new frost mitigation method

This component addressed the second main objective. Two methodological steps were taken: 1) to assess an active method, mitigating frost damage. For this purpose, SIS system was tested on two different farms during frost condition; 2) working out a new active method based on thermodynamic variable (entropy) by considering the physiographic aspects.

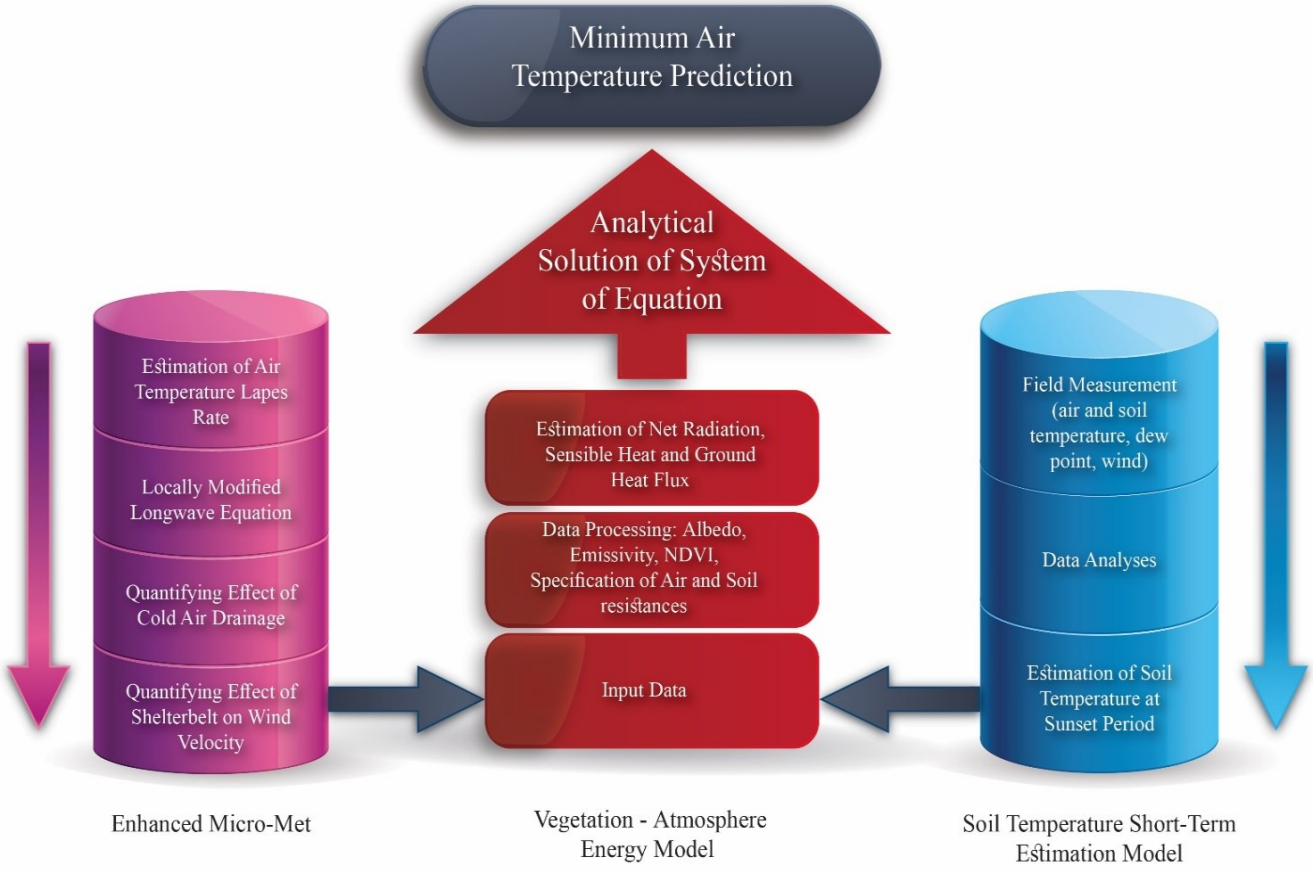

Figure 2.1 Diagram of the methodology procedure components: 1) Enhanced Micro-Met, 2) Soil temperature short –term estimation model, and 3) Vegetation-Atmosphere Energy Model to predict nocturnal minimum temperatures.

Through this methodology, it was possible to collect temporal information given by the meteorological stations, as well as spatial information provided by the satellite and field measurements. The atmospheric conditions associated with radiation frost may include clear skies, dry air, and low water vapor pressure; therefore, satellite thermal infrared observations were taken into account to gathering data. Table 2.1 presents the spectrum of the data used in this study.

Table 2.1 Description of the data used in this study.

Source	Data Description	Resolution
Meteorological Stations	Air & dew point temperature, wind velocity & direction, pressure, cloudiness (Sherbrooke, Lennoxville, Bronstone, SIREN)	Hourly
Experimental stations	Air and dew point temperatures, soil temperature and moisture at surface & 40 cm deep, wind direction & speed	10 - 20 min
Modis images	Land surface temperature, emissivity	1000 m
Landsat images	Land surface temperature, emissivity	100 m
AIRS[1]	Laps rate temperature, relative humidity at 700 hpa[2]	12 hrs, 50 km
DTM[3]	Slope, aspect, curvature, altitude	8.75 m
DSM[4]	Canopy height	2 m
Forest map	Forest type and density, land surface properties	1:20,000
Infrared camera	Thermal imagery	640×418 pixels
Soil Atlas	Soil type	1:20,000

[1] Atmospheric Infrared Sounder
[2] Hectopascal
[3] Digital Terrain Model
[4] Digital Surface Model

3. Experimental site

The study site is located in the Coaticook River valley (Compton area), the most important agricultural area in the Eastern Townships of southern Quebec, Canada (Latitude: 45°22' Longitude: 71°49'). The selected area has a significant number of agricultural lands that is primarily occupied by vineyards, orchards, blackcurrant, pear, and cherry farms. Serveral importatant commercial wineries (e.g. Demaine Bergeville, Demaine Ives Hill) and orchard (e.g. Cidrerie verger Ferland, Verger le Gros Pierre) situted in study sites. The study site was frequently affected by frost due to local topography. The local farmers suffered recurrently of economical losses due to frost damage. The area of study site is 225 km^2 and the ground elevation varies between 140 and 450 m (Fig. 3.1). There is only one standard station at the experimental site in Lennoxville that is used to gather meteorological data. To overcome this problem, several data loggers were employed to gather meteorological variables to validate the model prediction results. Their positions were determined based on the following topographic criteria: hilltop, valley bottom, exposed ridge, flat plain, etc. In addition during the reaserch two automatic stations were installed in study site to recored wind velocity (station number 20 and 14). All the research and tests were done in the commercial wineries, orchard or the other productive area situated in the study site.

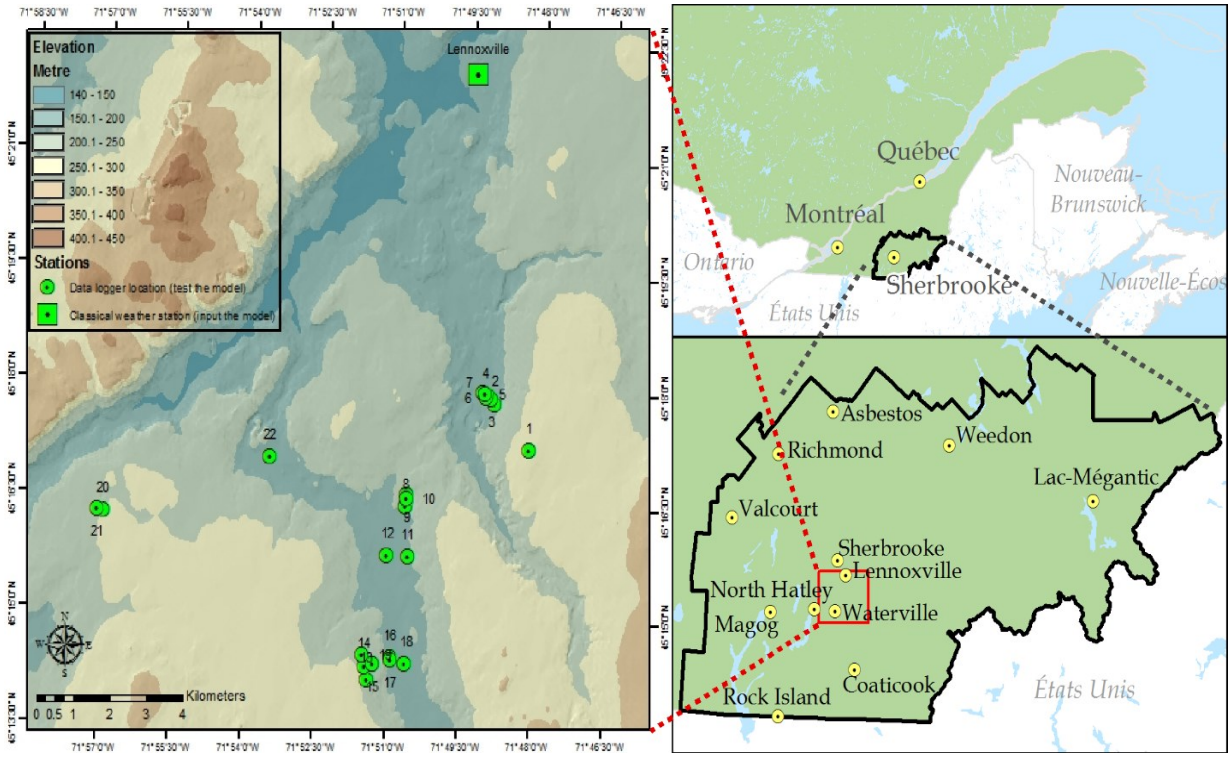

Figure 3.1 Location of the study site Coaticook River valley (Compton area). Position of weather station for the input data (square) and validation of the results (circles) are identified.

A complex topographic configuration characterizes this valley and soil texture varies with mainly loam with loam sandy on 72% of the site surface (Huguette, 2008). The land use map for the study site was based on the classification of a LandSat satellite image (Fig. 3.2) in five land use classes: Water (0.69%), Urban (7.41%), Agricultural (35.27%), Forest (53.63 %) and other (3%).

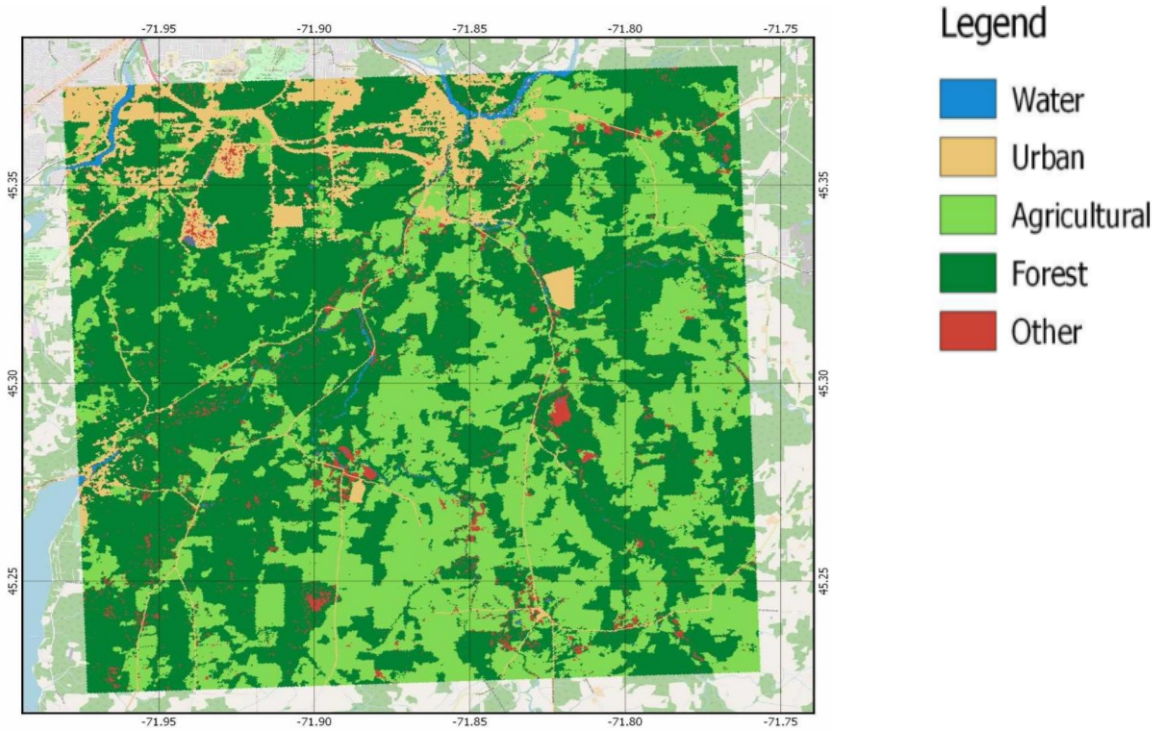

Figure 3.2 A land use map of the study site on a 225 km^2 area. Land use classes in decreasing proportion are: Forest (53.63%), Agricultural (35.27%), Urban (7.41%), Other (3%) and Water (0.69%).

Late spring frost or early fall frost may, on occasion, have a significant impact on agricultural yield in Eastern Townships (Dubois *et al.*, 1989). The damages in terms of economic costs due to frost are considerable for the Compton area. According to *La Financière agricole du Québec* (FADQ), farmers in this area often deal with reduced crop production due to frost. In agriculture, fruit (strawberry, raspberry, blueberry and apple), corn, soya, oats crop productions suffer the most from the frost. As an example, this area suffered economic losses of more than 10 million of Canadian dollars in 2000, due to the frost (FADQ, 2009).

The growing season period in this area generally starts April 25 and ends October 15. Based on the data collected over the past 30 years at the Lennoxville weather station, the minimum air temperature (-6 °C) was observed during early and late frost periods. Temperature higher than 5 °C considered as growing degree-days. Figure 3.3 presents heating degree-days and cooling degree-day

for the station in Lennoxville, based on 30 years of data (MAPAQ, 2017).

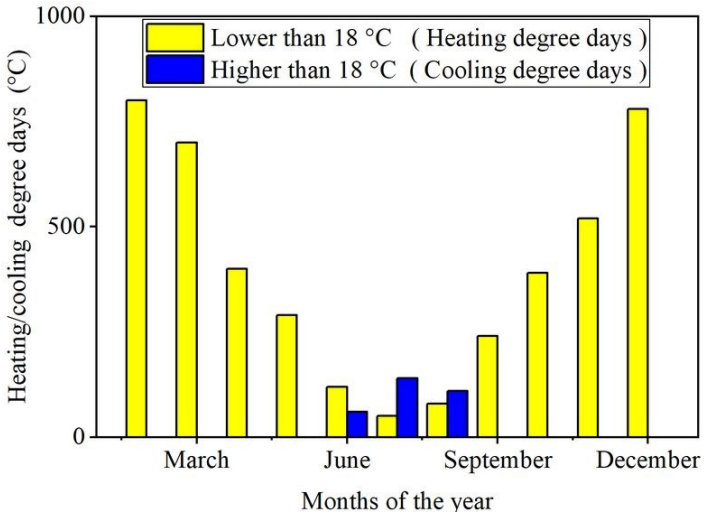

Figure 3.3 Heating degree-days (in yellow) and cooling degree-days (in blue) for the Lennoxville meteorological station based on 30 years data (taken from Ministère de l'Agriculture, des Pêcheries *et* de l'Alimentation, 2017).

Based on 11 years wind velocity direction of Lennoxville station, we derived wind rose diagrame fot two period first of May 2008 to 15 June 2017 as well as first of September 2008 to 15 October 2017. Both of windrose diagram show that dominant wind direction is south east during spring and fall frost for this area (Fig. 3.4).

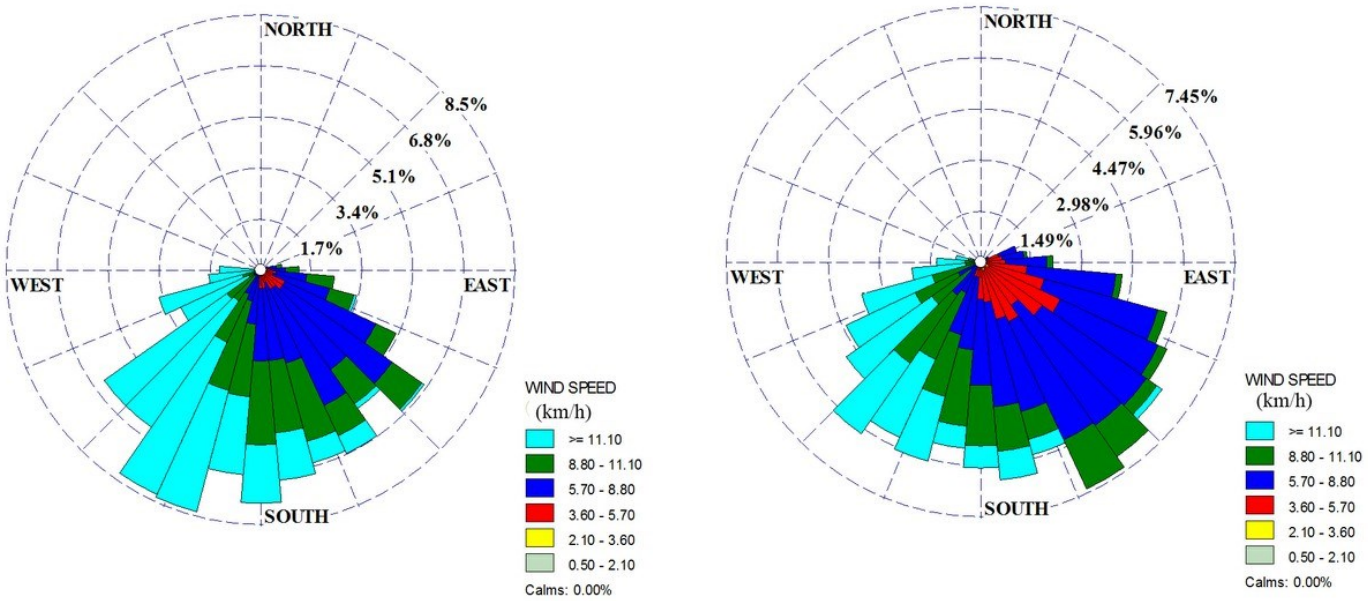

Figure 3.4 Wind rose for the study site. Left: May- June. Right: September- October.

4. Enhancement of the Micro-Met system

4.1 Introduction

Climate or meteorological information more generally is usually recorded as site-specific point information by weather stations. However, estimating the value of meteorological variables in unobserved locations requires applying interpolation techniques in combination with the available spatial data. A comparison of interpolation performances for different climate variables was difficult to find in the literature (Berndt and Haberlandt, 2018). Even if network density is known to have a strong impact on the estimation accuracy (Berndt and Haberlandt, 2018), only few studies compare the interpolation performance among different station densities (Krajewski, 1987; Goudenhoofdt and Delobbe, 2009; Nanding et al., 2015) and even fewer among different time scales (Bárdossy and Pegram, 2013; Dirks et al., 1998).

A number of models were developed to take site-specific measures to distribute them spatially for areas with important relief. The mountain microclimate simulator (MTCLIM), the Generate earth system science (GENESYS), and the meteorological distribution system for high-resolution terrestrial modeling (Micro-Met), are three models that have been used for meteorological modeling in regions with important relief. MTCLIM extrapolates meteorological variables from a point of measurement (referred to as the "base" station) to the study "site" of interest, making corrections for differences in elevation, slope, and aspect between the base station and the site. The main limitation of MTCLIM is associated with elevation and relationships between temperatures.

There is no specific algorithm to estimate temperature variation with elevation (MacDonald *et al*., 2009). GENESYS is a physically-based model for spatially estimating daily meteorological variables over complex terrain using routinely available meteorological data. It has been applied in several studies (*e.g.,* Lapp *et al*., 2005, Macdonald et *al*., 2008). However, one limitation of this model is its coarse spatial resolution (2°×2°). When increasing the resolution, the accuracy of model decreases (Daly, 2006). Moreover, GENESYS is not able to extrapolate wind speed and longwave radiation, which is necessary to study radiation frost. Meanwhile Micro-Met (Liston and Elder, 2006) produces high-resolution meteorological data distributions, *e.g.* 30 m to 1 km horizontal grid increment over a wide variety of landscapes. It utilizes weather station datasets, remote sensing observations, and/or gridded atmospheric model or analyses datasets.

Micro-Met applies known relationships between meteorological variables and the surrounding landscape to distribute the variables from point data over a continuous spatial domain containing the

stations in physically and computationally efficient ways. Micro-Met incorporates seven sub-models to distribute the meteorological variables: air temperature, relative humidity, wind speed and direction, solar radiation, longwave radiation, surface pressure, and precipitation. To produce these spatial distributions, Micro-Met assumes that at least one value of each of the meteorological variables is available for each time step, within or near, the study area. Micro-Met minimally requires air temperature, relative humidity, wind speed, and direction from a weather station, as well as data from the DTM with regard to the surrounding topography (Liston, 2006). Micro-Met has been used to distribute observed and modeled meteorological variables over complex terrain in Colorado, Wyoming, Idaho, Arctic Alaska, Svalbard, central Norway, Greenland, and Antarctica as part of a wide variety of terrestrial modeling studies (*e.g.*, Greene *et al*., 1999; Idaho (Prasad *et al.,* 2001), Wyoming (Hiemstra *et al.,* 2002), Alaska (Liston and Sturm, 2002; Liston *et al.,* 2002), Svalbard/Norway (Bruland *et al*., 2004), and the European Alps (Strasser, 2006). In addition, Micro-Met employs corrections related to known temperature elevation, wind topography, and solar radiation topography relationships.

The following descriptions summarize Micro-Met procedures implemented to adjust each meteorological variable beyond its initial spatial interpolation.

Air temperature: Extrapolating air temperature from one-point data within a horizontal regular grid was done in Micro-Met through the Barnes objective analysis scheme (Barnes, 1964, 1973; Koch *et al.*, 1983). Temperature was estimated from a Gaussian function in which the weight of a station contributes to the overall value of the grid point. The interpolation weights (w) are given by:

$$w = \exp\left[-r^2 / f(dn)\right] \qquad 4.1$$

where r is the distance between the observation and grid points, and $f(dn)$ is a filter parameter whose value defines how smooth the interpolated field will be (Listoned and Elder, 2006).

Dew point: The relatively linear behaviour of the dew point relative to the change in elevation is used for adjustments. Using a monthly varying dew point temperature lapse rate defined by Kunkel (1989) allows adjusting dew point at the station to a common reference level and then interpolate it by using Barnes scheme.

Wind speed and direction: Wind speed and direction measured by station are converted to zonal (u) and meridional (v) components that are then interpolated using the Barnes scheme. The wind direction was modified by a topographic diverting factor defined by Ryan (1977). The effects of slope and curvature on wind speed are derived using the model presented by Liston and Elder (2006).

Longwave radiation: Incoming longwave radiation is calculated while taking into account cloud cover and elevation-related variations following Iziomon *et al.* (2003). This model is valid for domains covering a wide range of elevations.

Surface pressure: In the absence of surface pressure observations (Lennoxville weather station), a time-independent atmospheric pressure distribution was taken from Wallace and Hobbs (1977).

Micro-Met is useful in a variety of applications (*e.g.*, Liston and Elder, 2006; Liston and Hiemstra, 2008). The results showed that temperature, humidity, wind, and long-wave radiation distributions are more valuable when the spatial scale of topographic variability is finer than the distance between stations or analysis-model grid points. Nevertheless, some limitations in the Micro-Met applications were recognized. Studies on radiation frost using Micro-Met would require modifying the model to include the capacity to address four considerations:

- A daily local air temperature lapse rate;
- An estimate of the incoming longwave radiation during clear sky conditions;
- The drops in temperature due to pooling and stagnation of cold air drainage;
- The effects of the forest shelterbelt on wind speed.

The first consideration on the Micro-Met model concerned a specific model to estimate downward longwave radiation. The problem lied in the fact that the algorithms currently used by of the model apply only for cloudy conditions. The algorithm was based on the equation presented by Iziomon *et al.* (2003), which did not address longwave radiation for clear sky conditions. However, clouds strongly affect this atmospheric variation (Pratia, 1995), which is part of the surface energy balance. For climatic studies and many applications such as radiation frost, the theory about clear air longwave radiation is important (Niemela *et al.*, 2001; Flerchinger *et al*., 2009). Downward longwave radiation is one of the components in nocturnal air temperature radiative cooling). This accounts for the cold air from mountains and slopes descending under gravity into valleys or basins (Fohn, 2006; Pypker, 2007).

A variety of equations can measure downward longwave radiation. (Wu *et al.,* 2012; Masiri *et al.,* 2017) provide detailed overviews of these equations. In several studies, the proposed equations were analyzed and locally adjusted using the observational data (Duarte *et al*., 2006). Since downward longwave radiation influences notably the estimation of air temperature, adding an

adjusted equation for clear sky conditions to the Micro-Met system was required. Moreover, locally adjusted equations allow estimating longwave radiation with more accuracy over a study area.

The second consideration on the Micro-Met model is tied to the air temperature lapse rate, which refers to the change in temperature with elevation. This constitutes the main difficulty in accurately interpolating air temperature in mountainous terrain (Dodson and Marks, 1997). Factors such as location, time of year, and amount of water vapor affect the atmospheric lapse rate. Dry air cools at about $10°Ckm^{-1}$, while moist air usually cools at less than $6°Ckm^{-1}$ (Bandyopadhay *et al.*, 2010). Average air temperature gradients of -0.55° (Angot, 1892), -0.60° (Dodson and Marks, 1997), or -0.65°C (Barry and Chorley, 1987) over a 100 m interval are often used when precision is not required. Employing the temperatures profile allowed detecting different atmospheric conditions, such as an inversion or atmospheric stability (Chahine *et al*., 2006; Klaes *et al*., 2007).

The existing Micro-Met model used the general values provided by Kunkel (1989), who considered a planetary spatial resolution for the northern hemisphere on a monthly mean basis (Table 4.1). However, the monthly average values were known to be rough approximations unsuitable for more precise studies (Rolland, 2003). Monthly average values of lapse rate might not be a good representation of the atmospheric conditions in a particular region during a certain period. This could cause a potential source of error (Rolland, 2003; Minder *et al.*, 2010). To calculate the lapse rate accurately, a monitoring network over an altitudinal gradient was necessary for our study. Generally, meteorological monitoring is scarce and insufficient.

A remote sensing measurement of the atmosphere could give information about the vertical distribution of atmospheric variables such as temperature (Costa *et al*., 2015). For example, the retrieval algorithm of the atmospheric infrared sounder (AIRS) was developed and gradually validated with clear and cloudy conditions (Tobin *et al*., 2006).

In summary, it was not possible to analyze different atmospheric conditions such as the inversion phenomenon to precisely estimate air temperature without obtaining real lapse rate values. Consequently, the Micro-Met system, which currently uses mean values, has to be reviewed to introduce changes to the algorithm concerning the lapse rate of air temperature.

Table 4.1 Air temperature lapse rate variations for each month of the year in the Northern Hemisphere (Kunkel, 1989) used by the Micro-Met.

	Air temperature Lapse rate (°C km^{-1})	**Month**	**Air temperature Lapse rate (°C km^{-1})**
January	4.4	July	8.1
February	4.9	August	8.1
March	7.1	September	7.7
April	7.8	October	6.8
May	8.1	November	4.5
June	8.2	December	4.7

The third consideration regarding the Micro-Met model relates to cold air drainage and cold air pooling. Both were physically interpretable processes that occurred across diverse topographic areas. They are observed on slopes as small as 1% (Soler *et al.*, 2002; Dobrowski *et al.*, 2009; Lundquist and Cayan, 2007). The errors of temperature distributed models were particularly significant in areas subject to cold-air pooling, where results of high-resolution atmospheric models are often show warmer air temperature during cold pool events. On the one hand, there is no sub-model currently in the Micro-Met model to estimate effect of cold pooling (Liston and Elder, 2006); on the other hand, the largest source of uncertainty and errors in spatial estimation of nocturnal air temperatures in topographic areas occur because of cold air drainage (Holden *et al.*, 2011). Cold air drainage and cold pools are associated with regions of frost and provide unique microclimates that influence species distributions and diversity (Wearne and Morgan, 2001). Therefore, the inclusion of a supplementary model including drainage flow and cold pool structure is necessary to allow Micro-Met to estimate drops in temperature.

The fourth and last consideration on Micro-Met model is associated with the microclimate effects of the forest shelterbelt. This concerns more specifically the reduction of wind speed, which takes place because the shelterbelt exerts a drag force on the wind field, leading to a loss of momentum of the airflow (Plate, 1971). Wind speed and direction values were modified on the Micro-Met system using the topographically driven wind model (Liston and Sturm, 1998), which adjusts the speeds and directions according to topographic slope and curvature relationships. However, the effect of the forest shelterbelt on wind speed was not examined nor integrated in the model. The sheltering mechanism relies on the reduction of turbulent mixing of the cold near-surface air with warmer air aloft. Furthermore, speed below 3.6 kmh^{-1} increases considerably the risks of frost. Taking into account these observable facts, a spatial sub-model taking in consideration sheltering had to be added to the Micro-Met system to include local terrain effects on wind speed.

4.2 Objective

The purpose of this study was to enhance the capabilities of the Micro-Met in support of the modeling done with the vegetation-atmosphere model to estimate the nocturnal surface air temperature. Four specific improvements are targeted following four considerations that have been identified as current limitations of the model, all affecting the surface air temperature:

(1) Develop a method for precise estimation of the air temperature lapse rate for the sunset period;

(2) Develop an adjusted equation for the downward longwave radiation under clear sky conditions and the wind speed;

(3) Develop a model to account for the effect of cold air drainage and cold air pooling taking into account local topography;

(4) Develop a model to estimate effects of the forest shelterbelt on wind velocity.

The significant innovative contribution of this research pertained to incorporating topographic and forest shelterbelt influences on local circulation. The proposed work will use a 10-m resolution Digital Terrain Model (DTM) and Digital Surface Model (DSM) to represent site topography, including vegetation and consequently improve the quantitative estimates of surface air temperature at the local scale. More specifically, the DTM and DSM allow the quantification of local topographic processes such as the microscale flow pattern at a resolution pertinent to agricultural management. Most studies about cold air drainage have focused on a single valley or a limited area, while our research focused on multiple valleys on a regional scale (15 km × 15 km). Results from some specific objectives compared with those from the unaltered version of Micro-Met to quantify the increase in accuracy for the aspects currently available.

4.3 Methodology

Achieving the four specific improvements to the Micro-Met model required the four separate methodological steps as followed and applied over the study area:

1. Improving atmospheric emissivity equation for clear sky conditions;
2. Estimating the air temperature lapse rate;
3. Quantifying the effects of cold air drainage on air temperature;
4. Quantifying the forest shelterbelt effect on reduction in wind velocity.

The methodology was based on temporal and spatial data provided by the weather station (Lennoxville), remote sensing (Landsat, MODIS and AIRS), *in-situ* measurements, forestry map, 10-m resolution DTM and DSM models. The analysis focused on nighttime periods (time after astronomical sunset and before sunrise) with clear sky and calm conditions, which are associated with the occurrence of radiation frost. The defining criteria for clear sky and calm conditions were a maximum of 25% cloudiness and wind speeds of less than 3.6 kmh^{-1} at the reference station (Gombos *et al.*, 2011). The results obtained following these four steps were verified and compared with *in-situ* measurements. More details about the technical framework and accuracy assessment method are provided in the following subsections.

4.3.1 Modifying atmospheric emissivity equation under clear sky conditions

The aim was to develop a locally adjusted equation for downward longwave radiation under clear sky conditions over the study area. Downward longwave radiation is described in terms of bulk emissivity and air temperature (Pratas, 1996):

$$W = \varepsilon \sigma T_a^4 \quad 4.2$$

where σ is the Stefan-Boltzmann constant (5.670373×10^{-8} Wm^{-2}), T_a is the air temperature (K), and ε is the emissivity. The most existing parameterization of the emissivity equations was based on the independent variables of air temperature and/or surface vapor pressure (Pirazzini *et al.,* 2000; Duarte *et al.,* 2006). Surface vapor pressure is symbolized by e_0 (hPa) and was estimated according to dew point temperature T_d (K), while applying the Clausius-Clapeyron equation (Rogers and Yau, 1989):

$$e_0 = 6.11exp\left[\frac{L_v}{R_v}\left(\frac{1}{273.15} - \frac{1}{T_d}\right)\right] \quad 4.3$$

where $L_v = 2.5\times10^6$ (Jkg^{-1}) corresponds to the latent heat of vaporization and $R_v = 461$ ($Jkg^{-1}K^{-1}$) to the gas constant for water vapor.

An overview of the 10 popular clear-sky emissivity parametrizations previously published is given in Table 4.2. All them were inserted in the downward longwave Equation 4.2 and locally adjusted. We employed the data recorded at an experimental station (SIRENE) at the Université de Sherbrooke that included the following variables: downward radiation, air and dew point temperatures. The period to accomplish this work covered 2014, 2015, and 2016. We selected the days that reported 0-10% cloud cover, as well as low wind velocity. We focused on wind velocity because during calm conditions, the turbulence intensity and turbulent heat exchange are relatively

small. As a result, the longwave radiation flux might change (Jaha and Mehrt, 2003; Oliphant *et al*., 2003; Steeneveld *et al.,* 2006). For this reason, only the data pertaining to clear sky observations and mean speed less than 3.6 km h^{-1} was employed to optimize the coefficient of the presented models. The longwave emissivity under clear skies was examined using data measured at 15-minute intervals during nighttime. Since there were no cloud observations at the Lennoxville station, the data for cloud cover provided by the Sherbrooke weather station was considered.

To identify the best parametric coefficients, three performance tests: the root mean square error (RMSE), the mean absolute error (MAE), and the variance account (VAF), were conducted. The results achieved allowed us to develop a locally adjusted downward longwave equation. The selected downward longwave equation was added in the Micro-Met model to overcome its limitations not only for clear sky conditions, but also for greater accuracy in terms of estimation.

Table 4.2 Emissivity (ε_0) of clear-sky parameterizations suggested by different authors based on air temperature T (K), water vapor pressure e_a (hPa), and precipitable water *w* (kgm^{-2}).

N	Authors	Equations
1	Kruk *et al.* (2010), Duarte *et al.* (2006), Sugita and Brutsaert (1993), Brutsaert (1975)	$\varepsilon_0 = 0.576\left(\frac{e_a}{T_a}\right)^{0.202}$
2	Brunt (1941), Sellers (1965)	$\varepsilon_0 = 0.605 + 0.048\sqrt{e_a}$
3	Idso (1981)	$\varepsilon_0 = 0.7 + 5.95 \times 10^{-5} e_a exp(\frac{1500}{T_a})$
4	Berdahl and Fromberg (1982)	$\varepsilon_0 = 0.741 + 0.62\left(\frac{T_{dp}}{100}\right)$
5	Prata (1996)	$\varepsilon_0 = 1 - (1 + w)exp[-(1.2 + 3w)^{0.5}]$
6	Dilley and O'Brien (1998)	$\varepsilon_0 = \frac{59.38 + 113.7(T_a/273.16)^6 + 96.96\sqrt{w/2.5}}{\sigma T_a^4}$
7	Swinbank (1963)	$\varepsilon_0 = 9.36 \times 10^{-6} T_a^2$
8	Idso and Jackson (1969)	$\varepsilon_0 = 1 - 0.261 * EXP(-7.77 \times 10^{-4}(273 - T_a)^2)$
9	Iziomon *et al.* (2003)	$\varepsilon_0 = 1 - 0.35\exp(-\frac{10e_a}{T_a})$
10	Crawford and Duchon (1999)	$\varepsilon_0 = 1.22 + 0.06\sin[(\text{month} + 2)\frac{\pi}{6}](\frac{e_a}{T_a})^{1/7}$

4.3.2 Estimation of the air temperature lapse rate

This section focuses on presenting a method to estimate the lapse rate over the study area. To obtain this variable, the temperatures had to be recorded at different altitudes and surface levels. The atmospheric infrared sounder (AIRS), a satellite-based system designed to supply data with higher vertical resolution (one kilometre) at a 50 km^2 spatial resolution, provided the vertical air temperature value. The scan geometries of AIRS and humidity sounder for Brazil (HSB), both with 1.1 degree footprints, relative to the advanced microwave sounding unit (AMSU), with a 3.3 degree footprint are illustrated in Figure 4.1. The air temperature and humidity from the AIRS could directly be retrieved at 28 different atmospheric levels (Seemann *et al*., 2003). The air temperature was reported at 28 standard pressure level between 1100 hPa and 0.1 hPa; while the moisture profile (relative humidity) was reported at 14 standard pressure level between 1100 hPa and 50 hPa (See Appendix A.1).

The air temperature retrieved from the AIRS data at 14:00 local time, as well as the ground station data, facilitated the estimation of the air temperature lapse rate. To measure the air temperature at the surface level, we used the data recorded at the sunset period at the Lennoxville station. Two points are addressed in the methodology. First, validation of AIRS values (air temperature and relative humidity); second, determination which AIRS atmospheric altitude provide more accurate air temperature and relative humidity. To this end, air temperature and relative humidity of three altitude: 925 hPa (760m), 850 hPa (1500m) and 700 hPa (3013m) from AIRS satellite retrieved.

Since Lennoxville station altitude is 188 metres (higher altitude than 1100 hPa), therefore data of 1100 hPa layer was not considered. In assessing the consistency of the retrieved values, we compared the mention retrieved altitude values against those recorded by radiosondes launched at Maniwaky upper air station (75° 59′. 31°.00′). The results allow us to select AIRS altitude data in order to estimate more accurately temperature lapse rate as well as vapor pressure coefficient.

The retrieved AIRS data over the study site and air temperature gathered at the Lennoxville station enabled us to derive the air temperature lapse rate (γ) using the following equation:

$$\gamma = {}^{\Delta T}/_{\Delta z} = \frac{(\text{Retrieved air temperature} - \text{ground based air temperature})}{\text{Vertical Distance between retrived and ground based air temperature}} \qquad 4.4\ (a)$$

where γ is lapse rate temperature (°C km^{-1}) while ΔT represents the temperature gradient between two vertical distances .

Vapor pressure coefficient is estimated using following equation:

$$\Gamma' = \frac{(\text{Retrieved dewpoint} - \text{ground based dew point})}{\text{Vertical Distance between retrived and ground based dew point}} \qquad 4.4\ (b)$$

where Γ' is dew point lapse rate (°C km^{-1}).

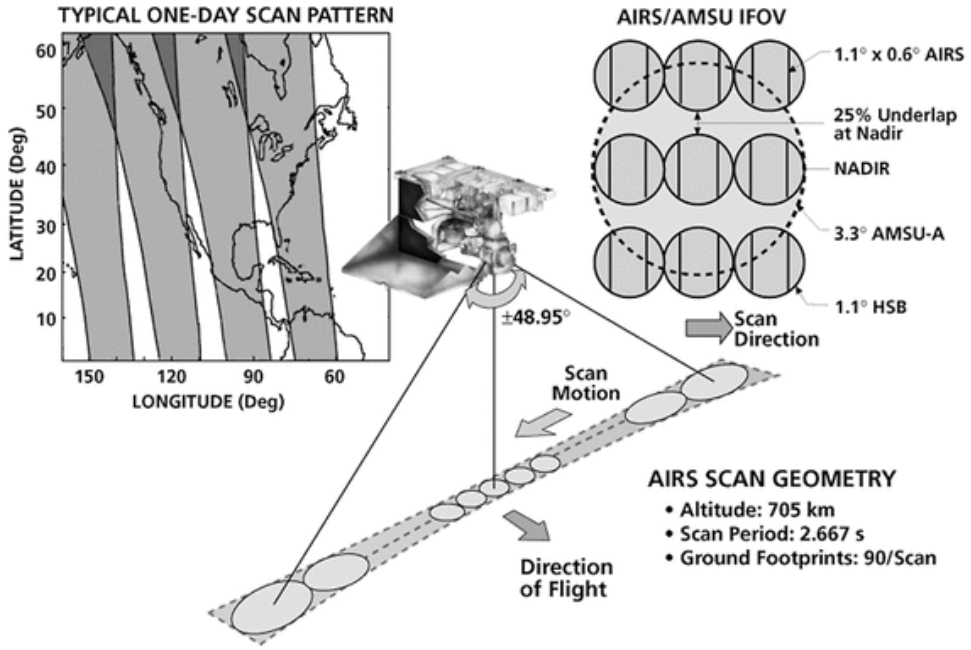

Figure 4.1 NASA illustration of scan geometry and coverage pattern for AIRS instruments on board the Aqua satellite. Image courtesy of AIRS Science Team, NASA/JPL–California Institute of Technology (GES DISC, 2016).

4.3.3 Quantifying the effects of cold air drainage on temperature

To quantify the effect of cold air drainage, it was necessary to: (A) detect and estimate the volume of the areas prone to accumulation of cold air drainage (sink, basin area or valley), (B) elaborate a new equation for the velocity of cold air drainage, and (C) quantify air temperature drop due to pooling of cold air.

A. Detecting and estimating volume of areas prone to accumulation of cold drainage

Accumulation of cold drainage was addressed in two (modules): first, detecting the areas prone to accumulation of cold air drainage (called sink pixel or valley pixel); the second estimating the volume of these areas. The first module was based on hydrological analyses performed by Jenson and Dominigue (1988) and Tarboron (1997) which enabled us to (find) the direction in which cold flows out of each pixel of the DTM. In addition, it allowed us to consider the vertical angle between the candidate pixel and each of its eight neighbours. The method was based on a 3×3 matrix applied to

the 10-meter resolution. DTM used to derive local slopes, curvatures, and percentile elevation relative to surrounding terrain.

In this section, the term “candidate pixel” applies to the pixel identified to be susceptible to accumulation of cold air drainage, whereas “neighboring pixels” are the pixels surrounding the candidate pixel, which must be compared to the slope and elevation of neighboring pixels. The pixels with slope zero and elevation equal to neighboring pixels were considered as sink pixels. Indeed, sinks correspond to pixels which have no neighbours at a lower elevation and consequently, no down-slope flow path to a neighbouring pixel. However, neighboring pixels with elevations higher or lower than the elevation of the “candidate pixel” were examined. Moreover, by establishing sink pixels with flow accumulations over a chosen threshold, it was possible to identify which pixels belonged to the drainage network. Subsequently, we determined the neighbour with the greatest down-slope angle. The pixel at the lowest altitude was considered at the base of the valley. The first ridge on each side, referred to as crest height, was recorded. The drainage area comes to an end at the first sharp curvature of each ridge**.** Figure 4.2 shows the algorithm used to detect the area prone to accumulation of cold air drainage and their volumes.

Figure 4.3 shows an example of implementation of the proposed algorithm to detect the area prone to accumulation of cold air drainage. The yellow pixels indicate the flat areas (no basin pixels, no slope pixels), the red pixels which are lower than neighboring show basin pixels which present width of the prone area floor and the other pixels shows the neighboring of the basin.

The second stage of the method focused on the estimation of volume of the areas prone to cold air accumulation. Nighttime cooling is more likely to be confined to a closed basin, because cold air is denser and tends to sink to the bottom of the basin or depression areas with no outlet (Whiteman *et al.*, 2007). For this reason, the methodology focused only on the effects of closed valleys on nocturnal temperature. The volume of valleys has considerable importance because, according to the first law of thermodynamics, an equal heat input or output into two unequal volumes of air will produce a larger temperature change in a smaller volume (Hahnenberger, 2008). After identification of the pixels associated with the accumulation of cold air drainage, the pixel at the lowest altitude was considered as the base of the valley. Using area of the base of valley, the volume was calculated for this area with height of one metre.

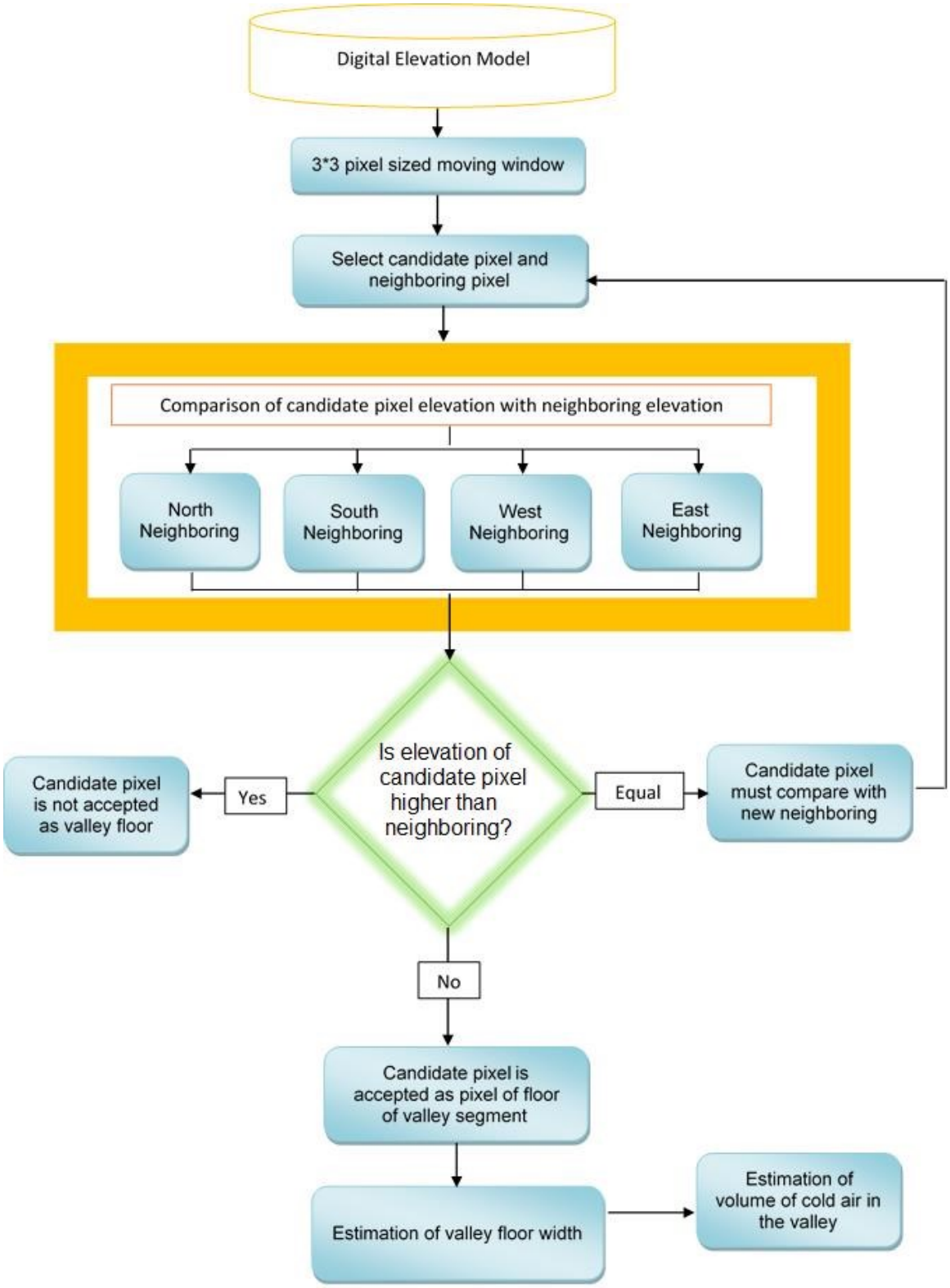

Figure 4.2 Algorithm used to detect the area prone to accumulation of cold air drainage (depression areas) and their volumes.

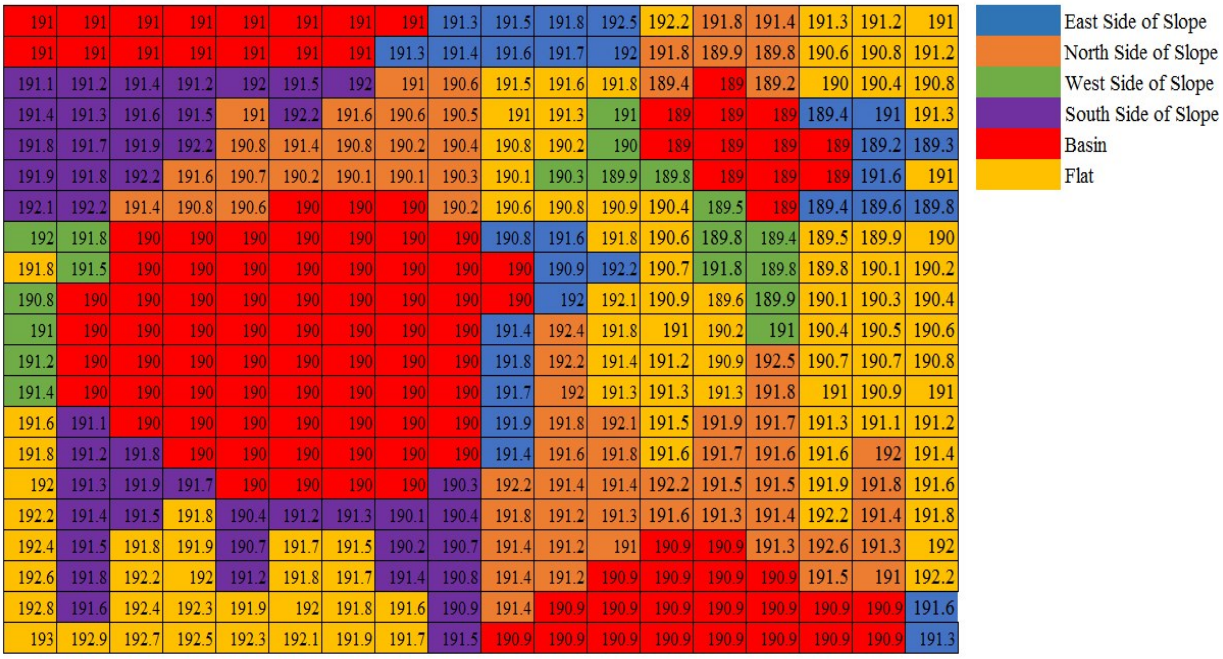

Figure 4.3 An example of implementation of the algorithm to detect area prone to accumulation cold air drainage: red pixels correspond to the basin (width) of the valley floor, yellow to the flat pixels, and other colors to slopes.

B. Elaborating of a new equation for the velocity of cold air drainage

Most theoretical analyses on cold air drainage flow are limited to bare slope conditions. Several equations were developed to estimate wind velocity associated with slope drainage (e.g. Savage *et al.*, 2008). However, the effects of land cover in terms of hydraulic friction on the velocity of cold air were not extensively considered. Cold air drainage flow also depends on the vegetation cover. For this reason, a complete model remains to be developed for cold air drainage flow by taking all the significant aspects of land cover into account (Gaulden *et al.*, 2007; Mehrt *et al.*, 2010).

We intend developing an equation to estimate the velocity, while taking into consideration vegetation cover. Toward this end, a method was defined, based on the results of two studies. The first study conducted by Wu (1999) focused on the variation of vegetation resistance with stage of submerge and unsubmerged conditions. A simplified model based on equilibrium of forces on an inclined plane with friction was developed to evaluate the drag coefficient of the vegetal element. Fig 4.4 shows force balance for uniform flow over a slope cover by vegetation. The equilibrium expressed as:

$F_G=F_D+F_S$ 4.5

where F_G is gravitational force, F_D is force exerted on the vegetation: F_S is surface friction of the surface. The magnitude of F_S is negligible compared with F_D. Therefore, gravitational force can be equated to the drag of vegetation (Fenzl, 1962).

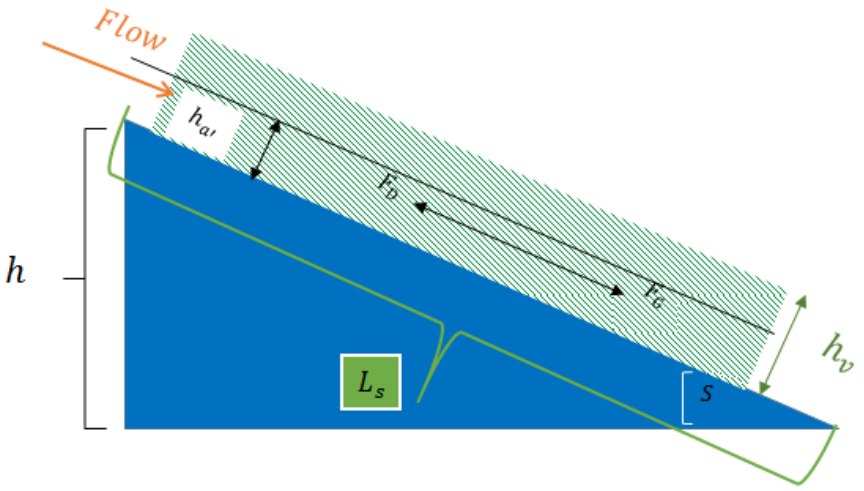

Figure 4.4 A schematics of the forces that contribute to the cold air drainage flow over a simple slope during atmospheric stability conditions F_G is gravitational force, F_D is force exerted on the vegetation; FS is surface friction of the surface. The magnitude of F_S is negligible compared with F_D.

The second study conducted by Davis (1991) developed an equation to determine moist air density. Moist air density (ρ in kg m^{-3}) can be expressed from the state equation of a non-ideal gas and the experimental conditions which results in a new equation of cold air drainage velocity by taking into account the vegetation cover:

$$\rho = \frac{PM_a}{ZRT}\left[1-\left(x_v\left(1-\frac{M_v}{M_a}\right)\right)\right] \quad 4.6$$

where P is pressure (Pa), T is the air temperature (K), x is the mole fraction of water vapor, M_a is the molar mass of dry air (Kg mol^{-1}), M_v is the molar mass of water = 18.015×10^{-3}, R is the molar gas constant = 8.31 (J mol^{-1} K^{-1}), and Z the compressibility factor.

Assessment the result is a new challenge. Measurement of cold air drainage velocity is not easily estimated from the measured variables of the existing weather stations and it requires a special methodology (Ikani *et al.,* 2016). Pfister (2016) presented a method using fiber-optic distributed temperature sensing to estimate drainage velocity. Figure (4.5.a) shows an example of a cold-air flow

and convection above the lake detected by Fiber optic. The cold-air flow came from the right-hand side of the figure and drained. However, this method is not operationally yet. The use of an ultrasonic anemometer is an alternative method (Fig.4.5.b). One main problem is to correct installation and geometric arrangement, which is not an easy task.

(a) (b)

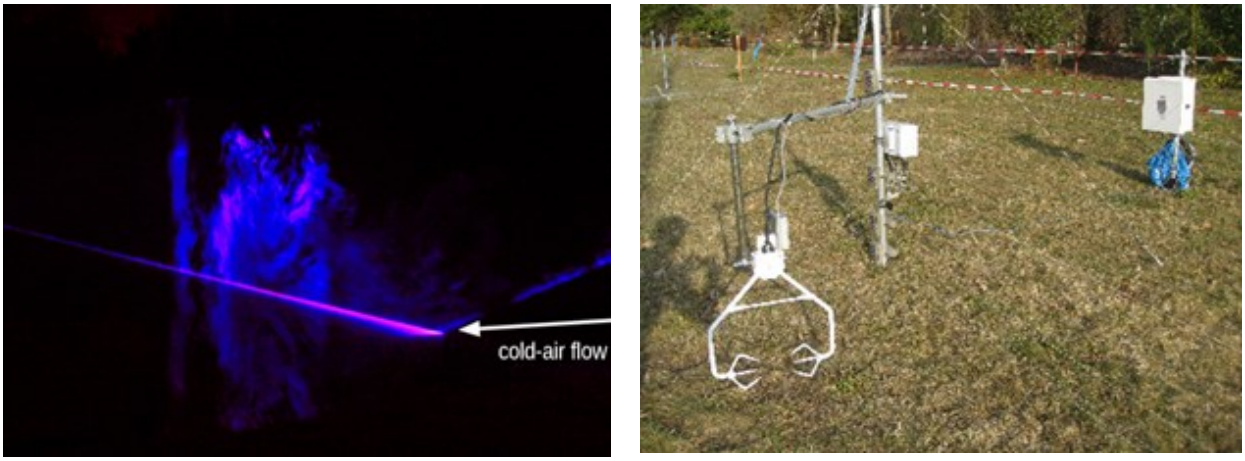

Figure 4.5 (a) an existing cold air layer with direction the white arrow is the direction of the cold air flow and shows, where the lake surface started. The cold-air flow came from the right-hand side of the picture and drained upon the lake; (b) an example of ultrasonic anemometers installation.

This part addressed the estimation of velocity of cold air drainage. We proposed a new and easy operational method that utilizes a series of thermal photographs. It was based on the theory presented by Fleagle (1950) who indicate periodic characteristic of drainage flow. Using a series of thermal photographs allows us first to visualize Fleagle theory and consequently to estimate drainage velocity. The instrument used for the observation is an infrared camera. Detection range of the instrument is -50°C - 200 with minimum temperature interval of 0.05. Each thermal image is raster scanned into a grid of 479*639 lines.

A number of thermal photography using an infrared camera were conducted particularly during calm, clear sky conditions where late radiation frosts occurred. This imagery was combined with the data from an experimental weather station. Study site was an agricultural zone (blackcurrant farm) situated on study site on 5 November 2015 (Fig. 4.6). Position of thermal camera and slope on a blackcurrant farm is presented (Fig. 4.7).

Figure 4.6 Presentation of the study area (blackcurrant farm) and the slope where thermal imagery method presented, the red circle shows the experimental station and the yellow square, the thermal infrared camera location yellow lines show field of view.

Figure 4.7 Position of infrared camera on a blackcurrant farm and the slope.

Monitoring the fluctuations of cold air mass drainage was achieved using an isothermal filtration technique applied to the series of thermal photographs to distinguish the areas with temperatures ranging between -11.5°C and -13°C. The filtration technique simply allocates a color to a range of surface temperatures. We defined three colors associated with temperature variations: black represents temperatures lower than -13°C, red indicates temperatures between -11.5°C and -13°C, and blue shows temperatures higher than -11.5°C (Fig. 4.8). A series of six thermal photographs were taken between 20:50 and 21:08 on 5 November 2015. The Figure 4.8 shows the development of the pattern of cold air over the slope between 20:50 and 21:08. At 20:50, variations in temperature on the slope were minor; however, several differences were observed later in the same day. For example, at

20:56, most of the areas on the slope were well drained. At 21:02, the temperature increased again before producing a cold airflow. The images between 21:02 and 21:08 display the temperature drops over the slope. The images exemplified that once the cold air had flowed down the slope, a short period was necessary before the next flow. The cold air drainage velocity was estimated using a temporal sequence from the thermal photographs. A temporal sequence of images enabled the documenting of variations in temperatures between lines R1 and R2 at the top and bottom of the slope respectively. Many observations of nocturnal drainage flows have indicated that surges or fluctuations are characteristic of them. While the basic mechanism for cold air drainage is fairly well understood the reason for the oscillations is not fully clear. They are mainly explained by the theory of compressional warming (Fleagle, 1950) or by modulations of the flow by gravity waves (Gryning *et al.,* 1985).

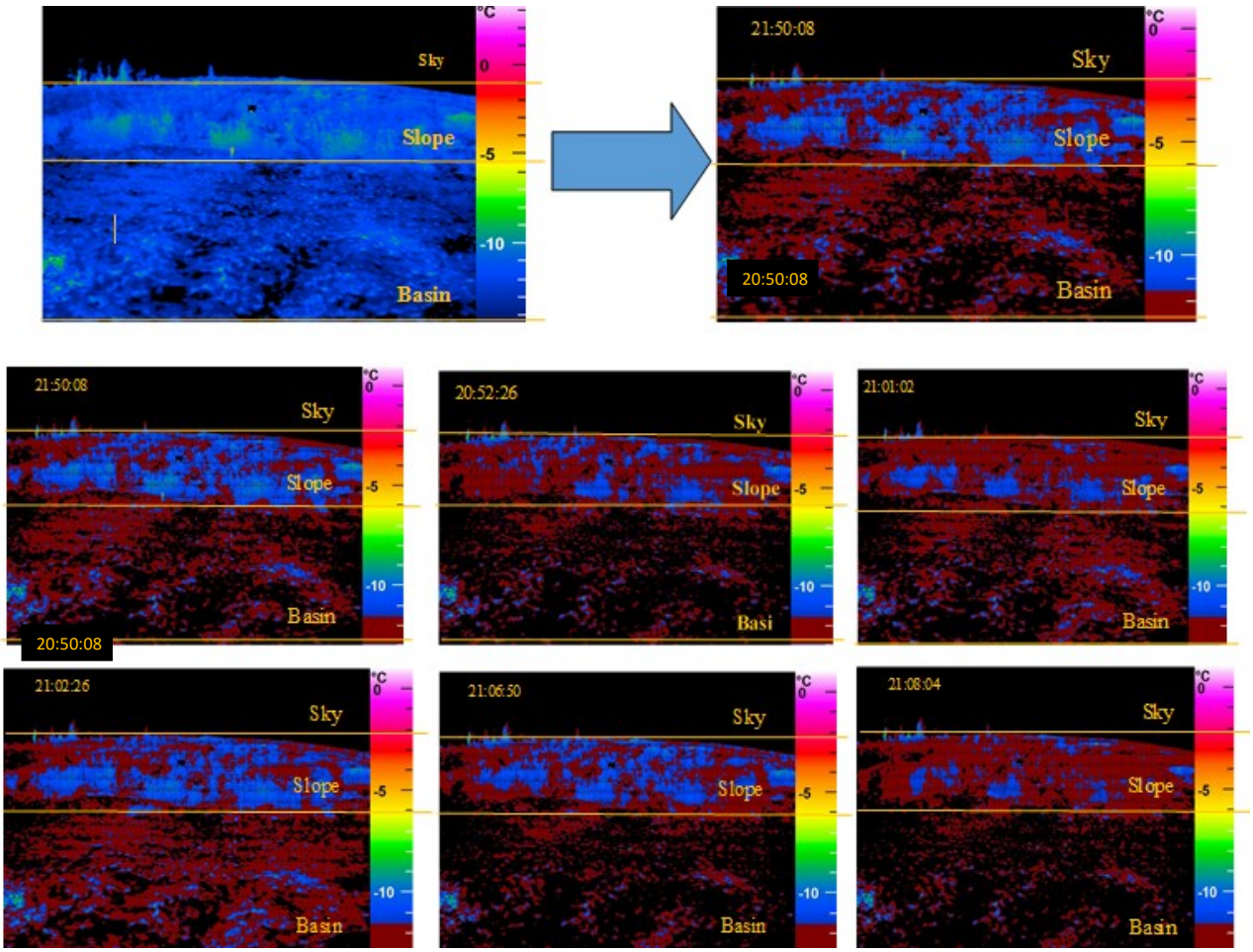

Figure 4.8 Thermal photographs with color assigned temperature range allowing to visualize the fluctuation of cold air mass drainage on a slope at six different times (labelled on the upper left corner of each image). The red area shows isothermal temperatures bet ween -11.5 °C and -13 °C.

C. Estimating air temperature drop due to pooling of cold air

In this section details of the thermodynamical framework required to derive quantify the effects of accumulation and pooling of cold air drainage on temperature presented. Here, we present details of the mathematical framework required to derive the transport.

The radiative cooling (ΔT_R) and sensible heat transfer (ΔT_{SH}) constitute the main factors to estimate the drops in temperature due to pooling of cold air. The mathematical developments required to estimate temperature drop was based on thermodynamic concepts such as those from Kondo *et al.* (1988, 1989, and 1990), De Weckker and Whiteman (2006).

The equation to estimate the drope in air temperature du to accumulation of cold air drainage (ΔT in K) is:

$$\Delta T = \Delta T_R + \Delta T_{SH} \quad 4.7$$

where ΔT_R corresponds to air cooling due to radiative flux and ΔT_{SH} to cooling due to sensible heat flux. We assumed that air temperature is horizontally uniform, except along the slope. Air cooling due to sensible expressed as follows (Kondo *et al*., 1990):

$$t_1 \overline{H} dA = C_p p V d \quad 4.8$$

$$\Delta T_{SH} = \int_0^D \frac{t_1 \bar{H}}{C_p \rho} \frac{1}{V} dA \quad 4.9$$

$$H = \frac{1}{2} c_p \rho C_H u \Delta T_{SH} \quad 4.10$$

where $\frac{t1\bar{H}}{C_\rho \rho}$ corresponds to the velocity of cold air drainage (m/s), if $\frac{t1\bar{H}}{C_\rho \rho} = u$ equation (4.9) can be reformulated as:

$$\Delta T_H = \int_0^D \frac{U dA}{V} \quad 4.11$$

where V is volume of air that occupies the region below the level (m^3) and given by:

$$V = A \times h \quad 4.12$$

where h is the elevation of the valley (m), therefore equation 4.11 can be expressed as:

$$\Delta T_H = \int_0^D \frac{U dA}{A \times h} \quad 4.13$$

$$\Delta T_H = \frac{U}{h} (\ln|A|_D - \ln|A|_0) \quad 4.14$$

In equation 4.14, A_D is the area of upper valley (m^2) and A_0 is the area of the valley bottom (m^2). Combining equations 4.8 and 4.9, and rearranging, the terms related to heat flux can be estimated as:

$$\Delta T_H = \frac{t_1 \overline{H} (\ln|A|_D - \ln|A|_0)}{h C_\rho \rho} \quad 4.15$$

where t_1 corresponds to air cooling period, C_p is the specific heat of air at constant pressure. The temporal average of sensible heat flux during the night is defined by $\overline{H}$ and can be formulated as:

$$\overline{H} = \frac{1}{2} a C_p \rho C_H u \overline{\Delta T_s} \quad 4.16$$

$$\alpha = 1 - \frac{\Delta T}{\Delta T_s} \quad 4.17$$

where ΔT is the temperature decrease of the air and ΔT_s the temperature decrease of the soil temperature:

$$\Delta T = \theta_0 - \theta \quad 4.18$$

$$\Delta T_s = \theta_0 - \theta_s \quad 4.19$$

where θ is called the potential temperature of ambient air, θ_0 is the vertical potential profile and θ_s is potential temperature of the surface which are defined as:

$$\theta = T_{air} \left(\frac{P_0}{P}\right)^{R/C_p} \quad 4.20$$

$$\theta_s = T_{surface} \left(\frac{P_0}{P}\right)^{R/C_\rho} \quad 4.21$$

$$\theta_0 = \theta_S - \theta \quad 4.22$$

where ρ is the air density (kg m^{-3}), P_0 is the air pressure at sea level 1000 (mb). $\overline{\Delta T_s}$ (Equation 4.16) is the average value of ΔT_s between the upper and bottom valleys according to the equation proposed by Kondo *et al.* (1998):

$$\overline{\Delta T_s} = \frac{\Delta T_{s(depression)} + \Delta T_{s(peak)}}{2} \quad 4.23$$

and C_H in equation 4.16 corresponds to the bulk coefficient for heat exchange and can be written as:

$$C_H \approx \frac{l_E}{h} \quad 4.24$$

where l_E is the length of the effective fetch of the parcel (m), h is the thickness of the parcel (m). Substituting equation 4.16 with 4.10, the cooling due to sensible heat exchange is expressed as:

$$\Delta T_{SH} = \int \left(\frac{1}{2} a C_p \rho C_H u \overline{\Delta T_s}\right)(C_p \rho V dA) \quad 4.25$$

$$\Delta T_{SH} = \int (1/2\ a {C_p}^2 \rho^2 C_H u \overline{\Delta T_s} V dA) \quad 4.26$$

The second energy component is radiation energy. The equation for clear skies is as follows:

$$\Delta T_R = \left(1/C_p \rho\ (L\downarrow - L\uparrow) \times t_1\right) z(°K) \quad 4.27$$

where $L\downarrow$ and $L\uparrow$ are downward and upward longwave radiations respectively and are written as follows:

$$L\downarrow = \delta\varepsilon_{atm}T^4 \quad 4.28$$

$$\mathrm{L}\uparrow = \delta\varepsilon_{\mathrm{sur}}\mathrm{T}_{\mathrm{sur}}^4 \quad 4.29$$

where equations 4.25 and 4.26 are replaced in 4.24, the radiative cooling equation can be written as:

$$\Delta T_{\mathrm{R}} = \left({}^{1}/_{C_p\rho}\,(\delta\varepsilon_{atm}T^4 - \delta\varepsilon_{sur}T_{sur}^4) \times t_1\right) z(°K) \quad 4.30$$

$$\Delta T_{\mathrm{R}} = \left({}^{\delta}/_{C_p\rho}\,(\varepsilon_{atm}T^4 - \varepsilon_{sur}T_{sur}^4) \times t_1\right) z(°K) \quad 4.31$$

where ε_{atm} is the atmospheric emissivity which was replaced by result of the first objective. According to equation 4.6 the air temperature drops due to cold air drainage is then obtained by summing the two equations 4.26 and 4.31:

$$\Delta T = \left[\left({}^{\delta}/_{C_p\rho}\,(\varepsilon_{atm}\,T^4) - \varepsilon_{sur}T_{sur}^4) \times t_1\right) z\right] + \left[\int (\tfrac{1}{2} a {C_p}^2 \rho^2 C_H u \overline{\Delta T_s}\, V dA)\right] \quad 4.32$$

Temperature cooling (ΔT) accounts from the contribution of two components: the integrated sensible heat loss (ΔT_{SH}) and cooling due to radiative cooling during the night ($\Delta \mathrm{T_R}$). Equation 4.32 was used in the cold air drainage model to estimate the drops in temperature due to pooling of cold air. In this equation ΔT present air temperature difference between valley bottom and nearby reference area due to cold air drainage. Tempeature cooling (ΔT) was added to air temperature (T_a) simulated by Micro-Met. Experimental data was confronted to those predicted by this new equation.

4.3.4 Quantifying the shelter effect on wind velocity

Quantifying the shelter effect on wind velocity is another factor that needs to be introduced in Micro-Met. Wind direction, forest canopy height, and density are the key components to quantify the sheltering effect (Read *et al.*, 1996; Van Thuyet *et al.*, 2014). The new sub-model that was integrated into the Micro-Met system included two components. The first component determines whether or not the area is relevant for a shelter effect. If a shelter effect can take place, the second component estimates the reduction in wind velocity.

The algorithm to detect the areas affected was elaborated according to the results presented by Read *et al.* (1998). Ideally, windbreaks should be located at right angles to the prevailing wind

direction. However, 45° to either side of this orientation can still provide reasonable shelter effects (Fig. 4.9).

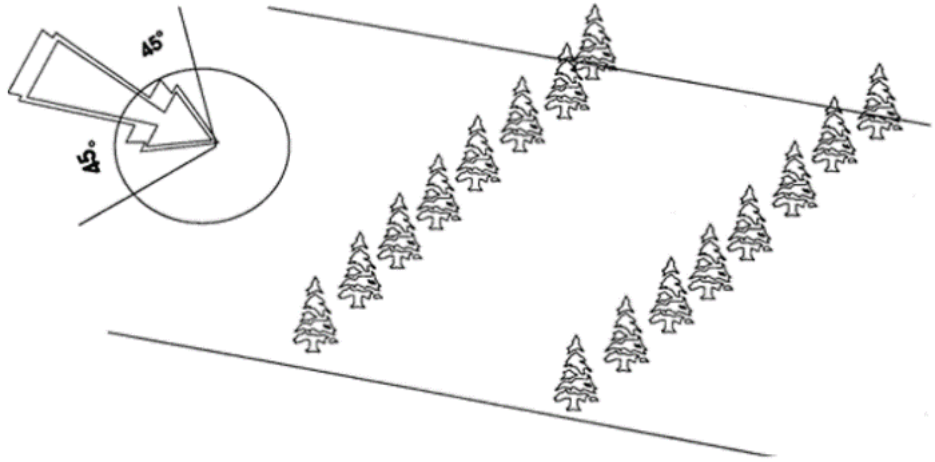

Figure 4.9 Shelter effect due to orientation of the rows of trees and the dominant wind direction (taken from Read *et al.,* 1998).

The algorithm developed to estimate reduction in wind velocity was based on the results presented by both Van Eimern *et al.* (1946) and Hanley and Kuhn (2003), who conducted wind tunnel experiments. The shelterbelt structure is characterized by the canopy heights, length and porosity (density). We noticed that shelterbelts exert an influence on the distribution of wind velocity, which is expressed in percentages of wind speed for two open areas which are called windward and leeward. Windward is defined as being in or facing the direction from which the wind is blowing; while leeward is defined as being in or facing the direction toward which the wind is blowing or being the side opposite the windward.

For example, Figure 4.10 demonstrates the effect of shelter on wind velocity for leeward and windward areas (or sides). The leeward area (right hand side of treeline in figure 4.10), whose horizontal extent was from 0 to 5 times of the treeline or shelter height (h), experienced a 50% reduction in wind velocity in comparison with the wind velocity at location 10 times from the treeline on the windward side.

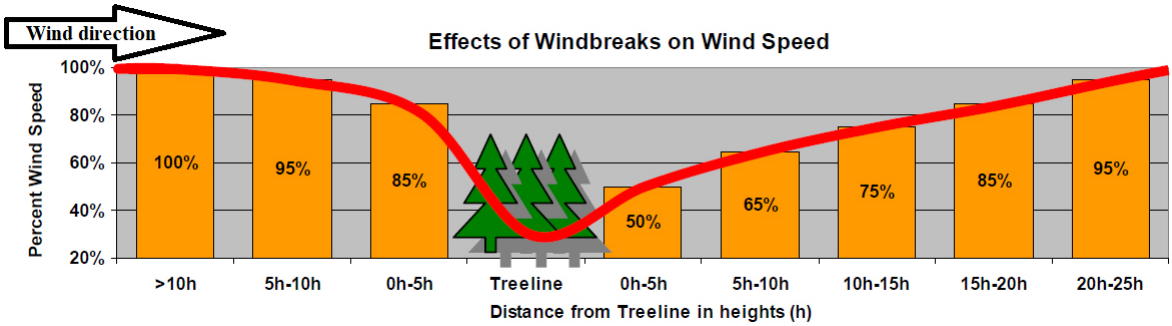

Figure 4.10 Estimated wind velocity reduction on the windward (facing the direction from which the wind blowing, left side of treeline) and leeward (facing the direction toward which the wind is blowing) right hand side of the treeline. The distances from treeline are given in units for the treeline height (h) (taken from van Eimern *et al.,* 1964).

To model wind decrease through the forest, a methodology based on the diagram presented by Nageli (1982) was defined (Fig. 4.11; blue arrow). The technical framework for wind estimation was based on curve fitting technique on three separate zones according to the height of forest as presented in Figure 4.10. Two scenarios were defined to estimate wind velocity:

Scenario 1: The wind is affected by only one forest area. In this scenario, change in wind velocity is calculated based on the flow diagram of Figure 4.10 for three zones: windward, through the forest shelterbelt, and leeward.

Scenario 2: There is a clear-cut area or a space between two forests (called forest 1 and forest 2). In this scenario, the leeward of forest 1 and windward of forest 2 were examined. Depending on the distance between the two forests, two possibilities are assumed:

A. The distance between the two forests is bigger or equal than the affected areas of the leeward of forest 1 and windward of forest 2. In this instance, we applied the algorithm to consider both forests as independent (Scenario 1);

B. The distance between the two forests is smaller than the affected areas of the leeward of forest 1 and windward of forest 2. In this case, the mean effect of both forests was considered (leeward of forest 1 and windward of forest 2). The curve fitting technique, also known as regression analysis, is used to find the best curve for a series of data points. The curve was produced a fitting equation that allowed us to find points anywhere along the curve.

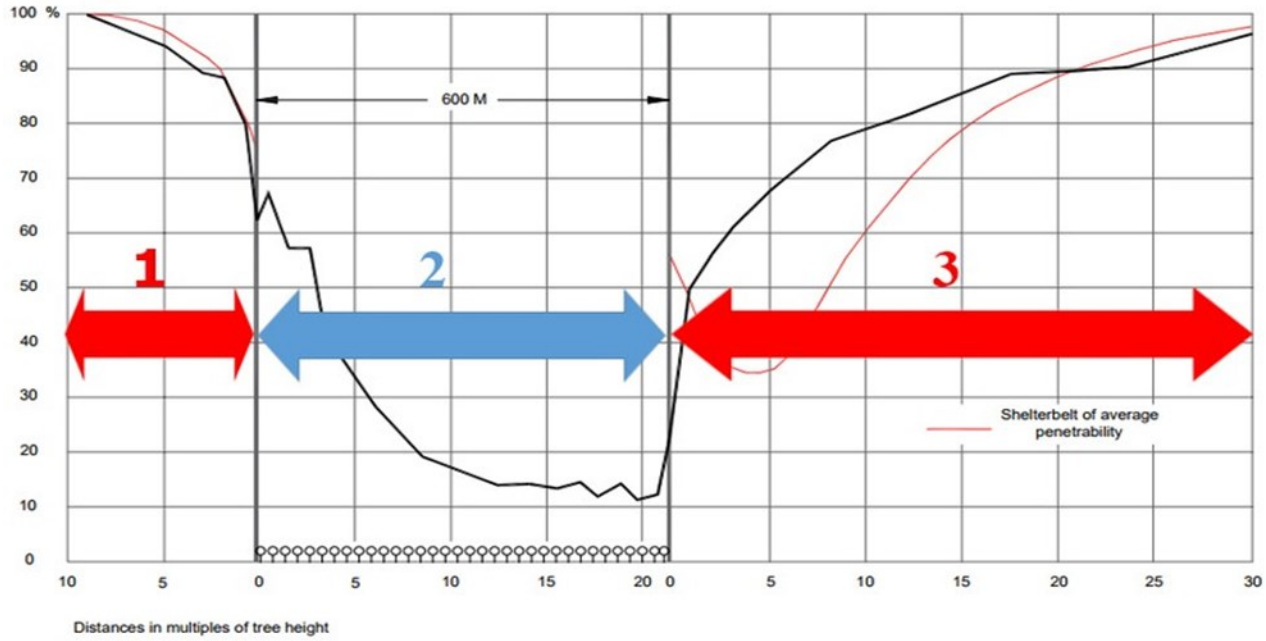

Figure 4.11 Relative wind velocities in the vicinity of a large forest and the influence of shelterbelts on the distribution of wind velocity expressed in percentages (taken from Nageli, 1982). The red arrows (1 and 3) represent windward and leeward side respectively, while the blue arrow represents the portion through the forest. The black curve shows the wind velocity change (%) and the red curve shows shelterbelt of average penetrability.

4.4 Results

4.4.1 A modified downward longwave radiation equation during clear sky conditions

The aim of this part was to present a new equation to estimate downward longwave radiation under clear skies. First, all ten emissivity models selected (Table 4.2) were integrated in Equation 4.2 and then fit to the measured values of longwave, air temperature, and dew point from the SIRENE station (Table 4.3). The data used were recorded during nighttime under clear-sky and low wind conditions. Second, we assessed the performance of the ten emissivity models by using three statistical metrics (Table 4.4): root-mean-square error (RMSE), mean absolute error (MAE), variance account for (VAF). This comparison indicates that the equation based on the one proposed by Dilley and O'Brien (1998) performed best with the lower RMSE (4.93 Wm^{-2}), MAE (4.04 Wm^{-2}), and the higher VAF (95.04 %). Therefore, it is indicated to estimate the atmospheric downward longwave emission as follows:

$$\varepsilon_0 = \frac{59.38+113.7(T_a/273.16)^6+96.96\sqrt{w/2.5}}{\sigma T_a^4} \quad 4.33$$

To formulate a final equation for a modified longwave radiation under clear sky and low wind conditions, equation 4.33 substituted with the equation 4.2 resulted in the following equation:

$$W = \sigma\left(\frac{-372.04+258.5(T_a/273.16)^{-192.94}+711.2(v/2.52)^{0.11}}{\sigma T_a^4}\right)T_a^4 \quad 4.34$$

where variable v is integrated water vapor content in kgm^{-2}. As v not commonly measured, it was estimated using the approach suggested by Prata (1996):

$$v = 46.5(e_a/T_a) \quad 4.35$$

where e_a is vapor pressure (hPa) and T_a is the atmospheric temperature (K). The new Equation 4.34 was added to the Micro-met model as an enhancement of the current version.

Table 4.3 Coefficient values for the ten emissivity equations selected to fit the measured values under cloudless and low wind conditions at the SIRENE field station on 2014, 2015 and 2016 in Sherbrooke (Canada). We selected the days that reported 0-10% cloud cover.

Equation	a	b	c	d	e	RMSE (W m^{-2})	MAE (W m^{-2})	VAF %
$\varepsilon_0 = a.T_a^b$	0.18	0.28				5.42	4.47	94.02
$\varepsilon_0 = a + b\sqrt{e_a}$	0.90	-2.25*10^{-03}				4.95	4.06	94.99
$\varepsilon_0 = a + b.e_a exp(\frac{1500}{T_a})$	0.89	2.06*10^{-6}				4.95	4.06	95.00
$\varepsilon_0 = 1 - a * exp(b * (273 - T_a)^2)$	0.11	9.0*10^{-05}				4.95	4.06	95.00
$\varepsilon_0 = a + b\left(\frac{T_{dp}}{100}\right)$	0.89	-0.01				4.99	4.07	94.93
$\varepsilon_0 = 1 - (1 + v)exp\left[-(a + b.v)^{1/2}\right]$	7.58	1.67				5.07	4.16	94.75
$\varepsilon_0 = \frac{a + b(T_a/273.16)^d + c\,(v/2.5)^e}{\sigma T_a^4}$	-372.04	258.5	711.2	-192.94	0.11	4.93	4.04	95.04
$\varepsilon_0 = a + b * \sin[(month + 2)\frac{\pi}{6}](\frac{e_a}{T_a})^{(\frac{1}{7})}$	0.92	0.10				4.96	4.06	94.99
$\varepsilon_0 = 1\_a * \exp(-\frac{b * e_a}{T_a})$	0.11	-0.72				4.95	4.06	95.00
$\varepsilon_0 = a\left(\frac{e_a}{T_a}\right)^b$	0.87	-0.01				4.96	4.06	94.99

The proposed downward longwave Equation (4.35) compared with the one of current version of Micro-Met evaluated. The reported RMSE, MAE and VAF for current version of Micro-Met of

176.95 (Wm^{-2}), 176.40 (Wm^{-2}) and 63% while the result of the new proposed equation indicated RMSE, MAE and VAF of 4.90 (Wm^{-2}), 4.00 (Wm^{-2}) and 95% respectively (Table 4.4).

Table 4.4 Statistics of downward longwave estimated using proposed Equation versus results of current version of Micro-Met.

Method	Proposed Equation (4.35)			Current version of Micro-Met		
Test	RMSE ($W\ m^{-2}$)	MAE ($W\ m^{-2}$)	VAF (%)	RMSE ($W\ m^{-2}$)	MAE ($W\ m^{-2}$)	VAF (%)
Result	4.90	4.00	95.00	177.00	176.40	63.80

4.4.2 Estimation of air temperature lapse rate

The air temperature and dew point lapse rates were obtained on a daily basis from temperatures and relative humidities recorded at different altitudes. Such data were available from AIRS data and coupled with air temperatures gathered at the Lennoxville station. Together they made possible an estimation of the lapse rate for the study site. Air temperature and relative humidity were retrieved by the AIRS at three altitude levels: 925 hPa, 850 hPa, and 700 hPa over the Maniwaki region. 21 days with clear sky and low wind condition were selected. These values were tested against air temperature and relative humidity available from the upper station in Maniwaki. The result produced coefficient of determination (R^2) of 0.74, 0.95 and 0.90 for 925 hPa, 850 hPa and 700 hPa respectively (Fig. 4.12, left colon). However, the relative humidity produced poor R^2 accuracy of 0.34, 0.12 and 0.22 for 700 hPa, 850 hPa, and 925 hPa respectively (Fig. 4.12, right colon).

Based on the above comparison, we can conclude that AIRS 850-altitude level provides the most accurate air temperature data. Therefore, the AIRS air temperature at 850 hPa level and Lennoxville station were used to estimate the air temperature lapse rate value. Since 850 hPa represent altitude of 1500 metres (5000 feet), therefore, vertical distance between 850 and ground based measurement (Δz) was 1500 m. However, the coefficient of determination of the retrieved relative humidity indicated poor accuracy. Therefore, to estimate dew point lapse rate the values of vapor pressure coefficient presented by Kunkel (1989) and used by current Micro-Met were used.

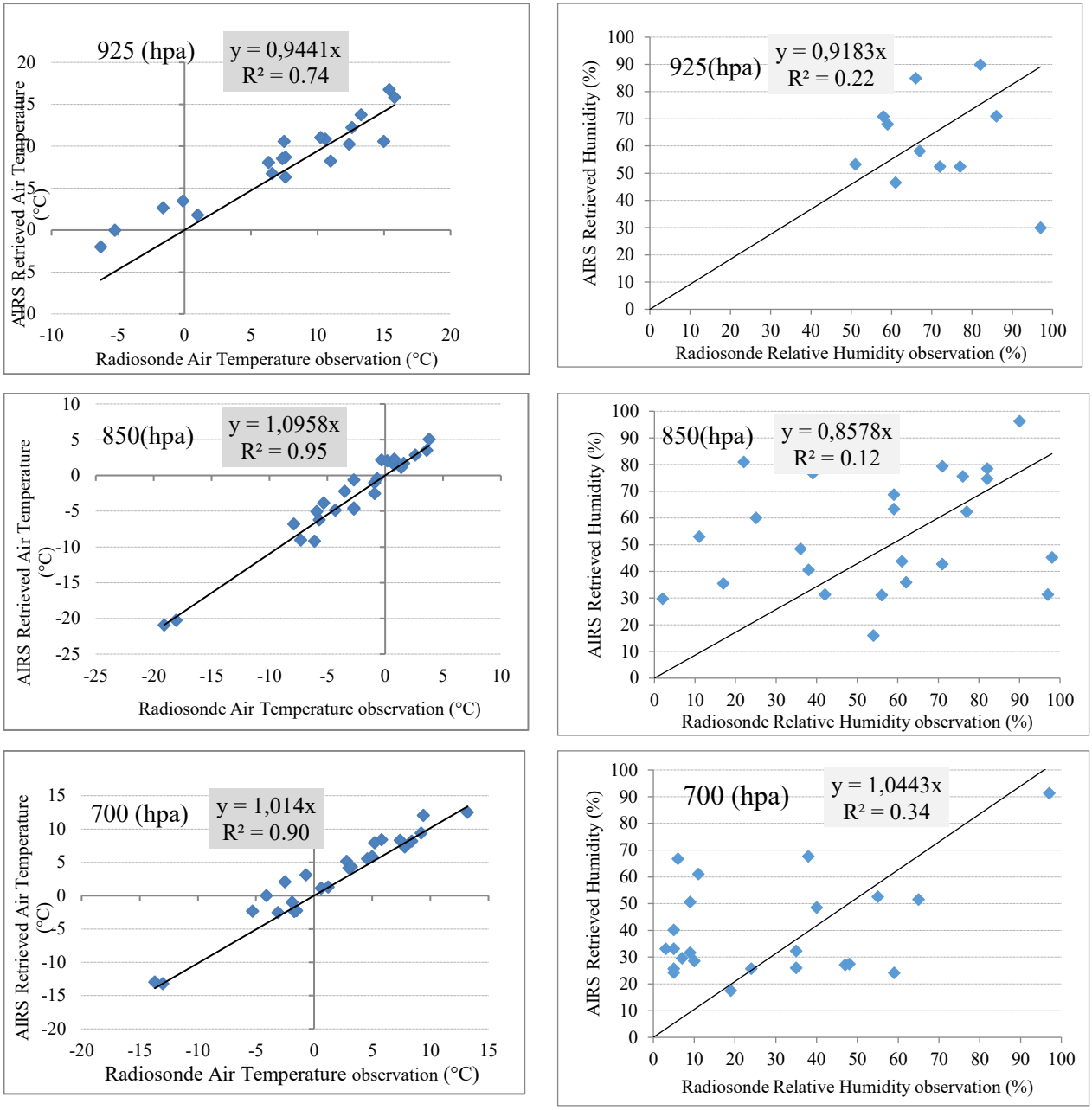

Figure 4.12 Comparison of the air temperature retrieved by AIRS versus the radiosonde observation, (a) 925 hPa, (b) 850 hPa, and (c) 700 hPa.

4.4.3 Quantifying the effects of cold air drainage on air temperature

A map for cold air pool detection was produced. The DTM was first classified according to elevation to identify the high and low areas. It was then categorized into two types of areas: closed valley presented by yellow color and no valley presented by blue color (Fig. 4.13). The map represents closed valleys at 30 m × 30 m spatial resolution using 3 × 3 moving window (DTM = 10 m).

Therefore, the implementation of the proposed algorithm on topographic map allowed us to produce a map of the valleys for the study site. These valleys were considered as reference areas to detect where cold air drainage was likely to accumulate. In the following sections numerical simulations used the valleys pixels to quantify effect of flow accumulations on nocturnal temperature.

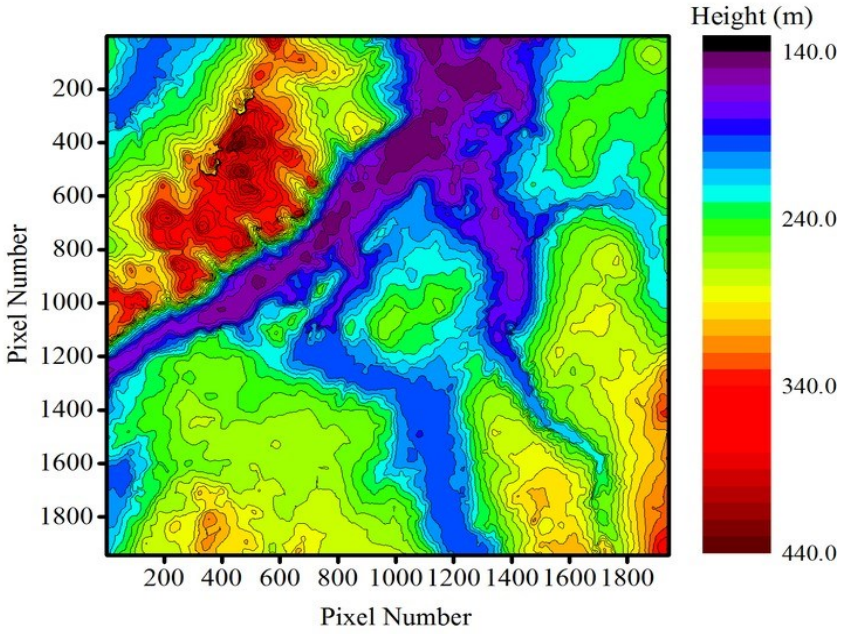

Figure 4.13 A colour representation of the Digital terrain model (DTM) of the study site with a spatial resolution of 10 m × 10 m. The low elevations are identified in blue and the high elevations in red or yellow.

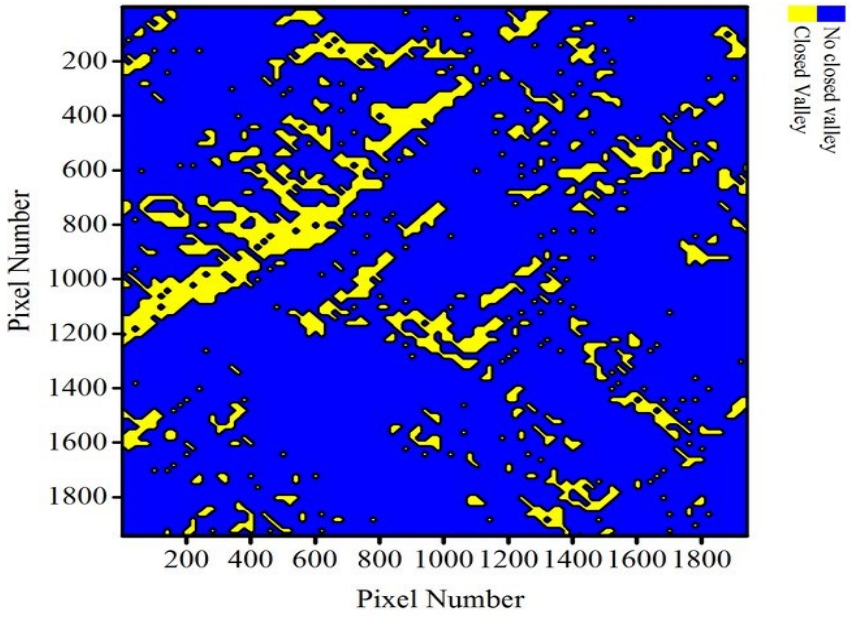

Figure 4.14 Study area divided into two categories: (1) no valley including flat areas and open valleys (blue) and (2) closed valleys (yellow shaded).

4.4.4. Estimating cold air drainage velocity

This section of the results focuses on the development of an equation to estimate the velocity of cold air drainage using infrared picture sequencing. It is considering land surface friction of a particle (air mass) on a slope during stability conditions. Figure 4.4 is used as a reference where we can see that h is the height at the top of the slope, $h_{a'}$ is the height of air mass, and h_v the vegetation height, F_D is the drag force exerted on the vegetation, F_G is the gravitational force, L_s is the slope length, s is the slope angle (for nomenclature, see Appendix 2). In the context represented by Figure 4.4, we can appreciate that on a slope area, F_d and F_G are equal (Wu *et al.*, 1999):

$$F_d = F_G \qquad 4.36$$

According to Petry and Bosmoijan (1975), flow velocity (v) inside the vegetation can be express as:

$$v = \sqrt{\frac{2gi}{C_d.m.D_s}} \qquad 4.37$$

Knowing that the air density is expressed as the ratio of the air mass over the volume:

$$\rho = \frac{m}{V} \qquad 4.38$$

We can substitule the density Equation (4.38) into Equation (4.37) for rearranging the flow velocity equation expressed by Equation (4.39)

$$v = \sqrt{\frac{2gi}{C_d.\rho V.D_s}} \qquad 4.39$$

Considering V as volume, as the surface area with width (w_s) and length (L_s):

$$V = A_s.h_{a'} \qquad 4.40$$

$$A_s = w_s.L_s \qquad 4.41$$

Air density Equation 4.6 presented by Davis (1991) can be reorganized as follows:

$$\rho = \frac{P[M_a-(x_v(M_a-M_v))]}{ZRT} \qquad 4.42$$

Substituting the air density Equation 4.40 into a reorganized flow velocity Equation 4.37 leads to:

$$v = \sqrt{\frac{2gi}{\frac{C_d.A_s.h_{a'}.P[M_a-(x_v(M_a-M_v))].D_s}{ZRT}}} \qquad 4.43$$

which can be expressed in a final equation to estimate air mass velocity or cold air drainage (ms^{-1}):

$$v = \sqrt{\frac{2gi\ ZRT}{P[M_a-(x_v(M_a-M_v))]C_d.A_s.h_{a'}.D_s}} \qquad 4.44$$

This equation is based on hydraulic concepts and consideration of land properties to produce a representation of air mass drainage velocity. This new mathematical formulation of drainage velocity quantifies the effects of cold air drainage on temperature drop (Equation 4.44). Figure 4.15 illustrates an example of the estimation of cold air drainage velocity over the study site. Equation 4.44 was applied on the map of valleys (Fig. 4.14) to derive cold air drainage velocity. Measurements were taken on 18 October 2016 at 17:00, under clear skies with synoptic winds favorable for the development of cold air drainage and accumulation of cold air in the local depression areas. The map of cold air drainage velocity was produced by applying the enhanced Micro-Met model (air temperature, humidity and air pressure models) and applying Equation 4.44. The range of air mass drainage velocity varied between 0.02 and 0.3 ms^{-1} for enclosed valleys.

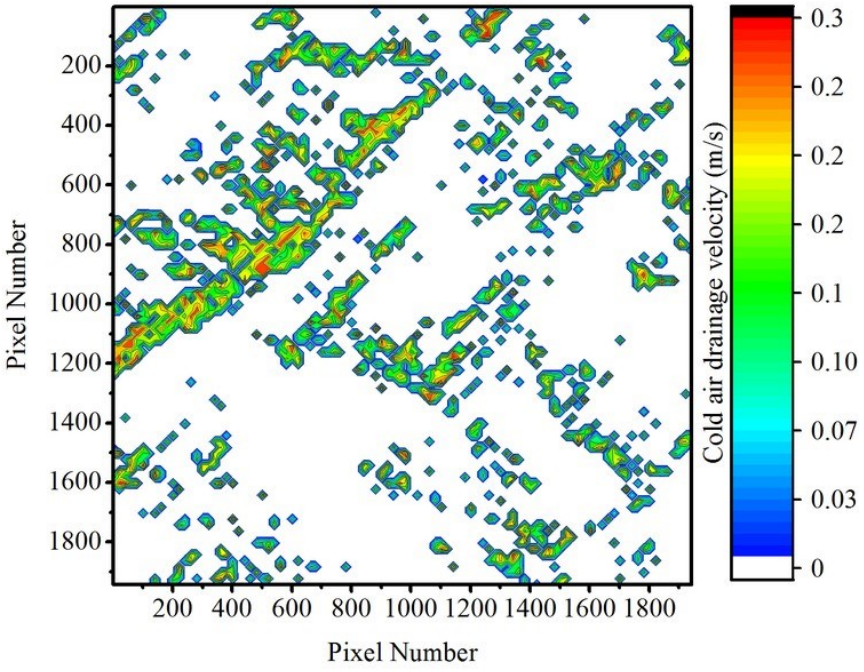

Figure 4.15 An example of applied Equation 4.44 to derive field map of the cold air drainage velocity over closed valley; 18 October 2016, at 17:00.

The air mass velocity equation was validated by comparing the results from the equation with those from the observed values. Measurement of air mass velocity is not currently possible with the existing surface weather station. We used a series of thermal photographs to estimate air mass velocity. The result was used to assess the prediction power of velocity of air mass drainage Equation 4.44. The equation was tested over an agricultural zone, more specifically on a farm located on a sloped terrain in the study site on 5 November 2015. The results of Equation 4.44 were compared with velocity of cold air mass of the series of thermal photographs. The cold air drainage velocity

was estimated using a temporal sequence from the thermal photographs to document the variations in temperatures between lines R1 and R2 at the top and bottom of the slope respectively (Fig. 4.16 right). Contrasting temperatures observed between the two lines suggest that cold air flows at intervals top and bottom of the slope, while close or identical temperatures suggest no flow. Based on the drainage flow period and distance between top and bottom of the slope (22 m), the velocity of cold air drainage was calculated is approximately 0.03 ms^{-1}, which is close to 0.02 ms^{-1}, result of the proposed equation (See Appendix A.3). The results for the cold air drainage velocity show that the thermal camera provides valuable information on the dynamics of cold air mass flow.

Figure 4.16 shows a series of temporal sampling windows with periodic sequences of temperature variations as described below:

- Between times of 308 sec and 928 sec, a temperature gradient is observed between lines R1 (top of the slope) and R2 (bottom of the slope). Accordingly, a cold air drainage can flow.
- Between times of 928 sec and 1024 sec, there is no temperature gradient between lines R1 and R2. Accordingly, no cold air drainage can flow.
- Between times of 1024 sec and 1712 sec, a temperature gradient is again observed between lines R1 and R2 that can result in flowing a cold air drainage.
- Between times of 1712 sec and 1776 sec, there is again no temperature gradient between lines R1 and R2 resulting in no cold air drainage flow.

Same sequences of temperature variations are observed for times between 1776 sec and 2640 sec with an air flow and between 2640 sec and 3024 sec with no air flow.

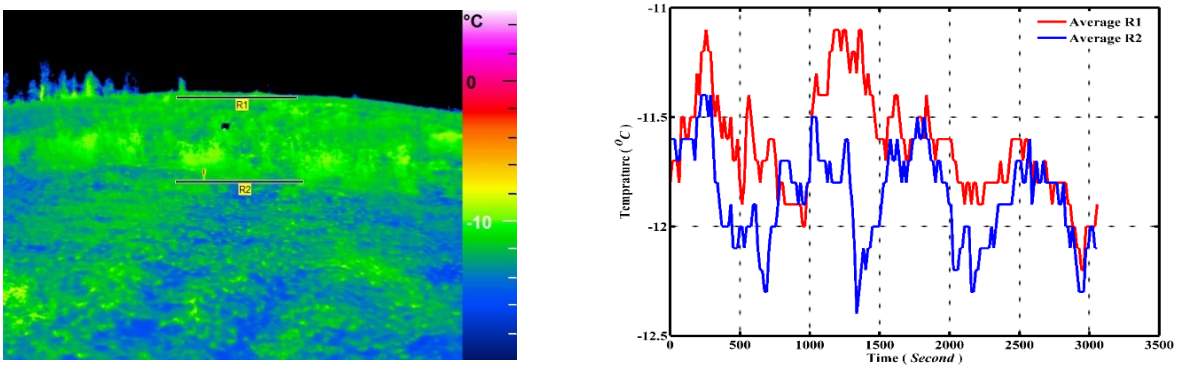

Figure 4.16 Left figure shows two parallel lines over a 22-meter distance on a slope on a farm located on a sloped terrain in the study site on 5 November 2015; right figure shows temperature time series between lines R1 and R2.

In summary, the purpose of this section is to develop a new equation to estimate cold air drainage velocity and validate it. The Equation 4.44 is based on hydraulic concepts and careful

consideration of land properties. In order to examine the competency of the new equation, the outcomes of the equation are compared to the actual infrared imagery data collected in this study. In summary, the thermal imagery approach presented in this study allows to visualize the dynamics of cold air mass. In the above approach, there are two key issues: first, visualization of periodic aspect of cold air drainage flow. Second, the use of its periodicity to estimate the velocity of cold air drainage and compared them with the theoretical results obtained by Equation 4.44.

4.4.5 Estimating temperature drops due to pooling of cold air

In this section, the results of the cold air mass drainage model were divided into two modules. The first module estimated the drops in air temperature by using Equation 4.32 over a single valley. This is somehow a restrictive application of the equation to compare the estimated values with those measure on the field. The second module applied the enhanced Micro-Met model on the whole study site to allow a comparison with the results from the current version of Micro-Met.

Module 1: This module focused on the validation of the estimated temperature drops due to the accumulation of cold air drainage by using the newly developed Equation 4.32. Towards this end, a pilot project conducted at a valley situated in the study site (Compton area) during three nights with synoptic conditions associated with frost (18-19 September 2016, 7-8 November 2017 and 8-9 November 2017). The procedures included installation of thermometers on the top and bottom of the valley and, estimation of volume and area of the valley prone to air temperature cooling and data recording from *Decagon Em50* and thermometer *Testo 174h* (Fig. 4.17). Four meteorological variables were measured at a temporal resolution of 10 minutes: air temperature, dew point, and surface temperature at the bottom as well as at the top of the valley. The nights selected for measurements were those with clear sky and calm wind. Applying Equation 4.32 produced estimated values of air temperature cooling at the bottom of the valley. Box-and-whiskers plot was produced to examine the performance of the methodology for three night separately. An average and standard deviation were calculated for both the estimated and the measured values of the three nights on a time scale starting one hour before sunset until ten hours after sunset (Fig. 4.18 and Table 4.5). Figure 4.18 display the distribution of air temperature based on standard deviation and minimum and maximum values of air temperature. The good performance of the model for the three nights. The highest difference values between the observed and estimated air temperature was 1.40 C which observed close to sunrise. While the poorest reproducing of the methodology was found for hours close to sunrise period. Statistical validation of result indicated a RMSE of 0.7 (°C), MAE of 0.5 (°C) and

VAF of 96% by considering the measured values as reference. The results indicate a RMSE of 0.7 (°C), MAE of 0.5 (°C) and VAF of 96% by considering the measured values as reference.

Figure 4.17 A photo of the test area. The instrument used was Decagon Em50 (to measure surface temperature) and thermometer (to measure air temperature) at the bottom and top of the valley.

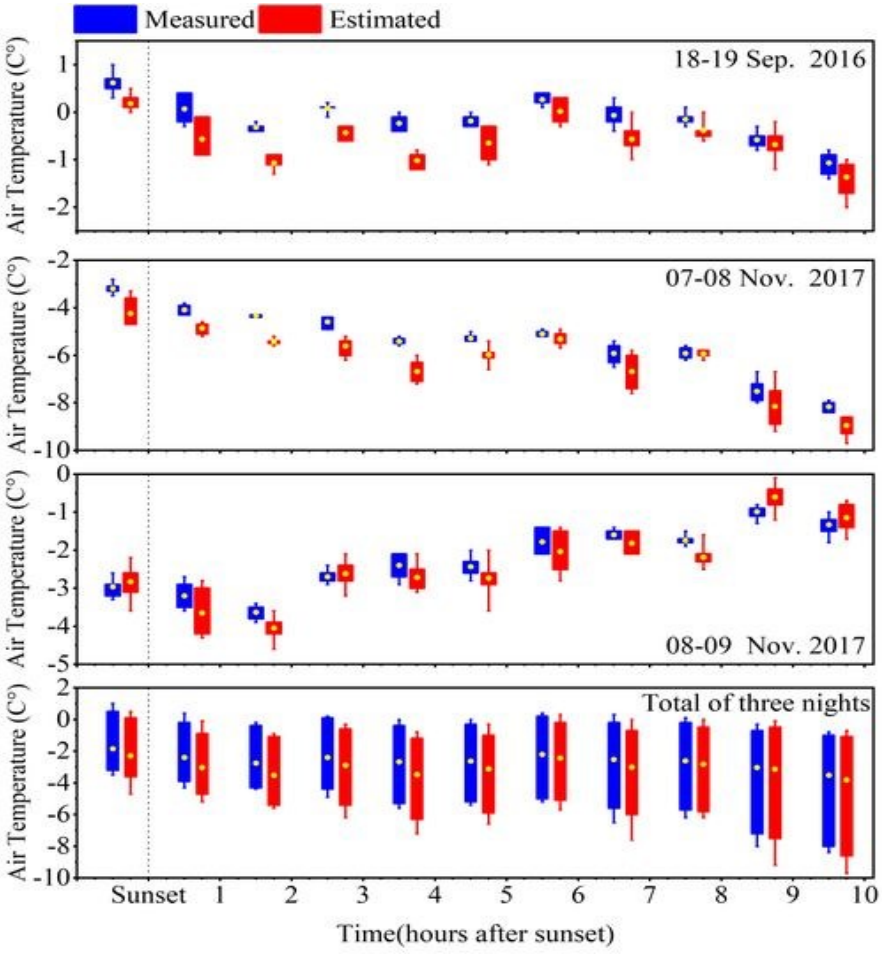

Figure 4.18 Hourly values of air temperature estimated with Equation 4.32 (red) and measured (yellow) at the bottom of the valley on three night: 18-19 September (2016), 7-8 and 8-9 November (2017). Box plots indicate maximum/minimum values at the end of the wisker, the +/- 90% values with the end of the box and the average air temperature with the dot within the box. Air temperature values were estimated and measured one hour before sunset until ten hours after sunset.

Table 4.5 Standard deviation, minimum and maximum values of measurement (Meas) and estimated (Estim) air temperature correspond to Figure 5.19. Time is presented by hour and start from one hour before sunset until ten hour after sunset.

	Hour befor sunset		**Hours after sunset**																			
	1 hour		**One**		**Two**		**Three**		**Four**		**Five**		**Six**		**Seven**		**Eight**		**Nine**		**Ten**	
	Meas	Estim	Meas	Estim	Meas	Estim	Meas	Estim	Meas	Estim	Meas	Estim	Meas	Estim	Meas	Estim	Meas	Estim	Meas	Estim	Meas	Estim
Night 18 and 19 September 2016																						
Max	1,00	0,50	0,40	-0,08	-0,20	-0,86	0,15	-0,26	0,00	-0,82	0,00	-0,32	0,40	0,26	0,30	0,03	0,05	-0.02	-0.30	-0,12	0,75	-0,73
Min	-3,50	-4,66	-4,30	-5,25	-4,40	-5,61	-4,90	-6,24	-5,60	-7,18	-5,40	-6,61	-5,20	-5,74	-6,50	-7,57	-6,20	-6,24	-8,00	-9,21	-8,40	-9,74
Sd	1,81	1,94	1,85	1,91	1,82	1,89	1,97	2,22	2,21	2,47	2,17	2,28	2,28	2,30	2,57	2,75	2,51	2,39	3,29	3,69	3,39	3,77
Night 7 and 8 November 2016																						
Max	1,00	0,50	0,40	-0,08	-0,20	-0,86	0,15	-0,26	0,00	-0,82	0,00	-0,32	0,40	0,26	0,30	0,03	0,05	-0,02	-0,30	-0,23	-0,75	-0,95
Min	0,30	-0,05	-0,25	-0,95	-0,40	-1,28	-0,10	-0,64	-0,35	-1,18	-0,30	-1,08	0,10	-0,26	-0,35	-0,96	-0,25	-0,59	-0,75	-1,16	-1,40	-2,01
Sd	0,23	0,20	0,28	0,41	0,08	0,15	0,08	0,17	0,15	0,14	0,12	0,33	0,13	0,22	0,23	0,35	0,11	0,19	0,16	0,33	0,24	0,40
Night 8 and 9 November 2016																						
Max	-2,80	-3,34	-3,80	-4,61	-4,30	-5,24	-4,40	-5,21	-5,20	-6,01	-5,00	-5,40	-4,90	-4,90	-5,40	-5,80	-5,60	-5,80	-6,70	-6,70	-7,90	-8,57
Min	-3,50	-4,66	-4,30	-5,25	-4,40	-5,61	-4,90	-6,24	-5,60	-7,18	-5,40	-6,61	-5,20	-5,74	-6,50	-7,57	-6,20	-6,24	-8,00	-9,21	-8,40	-9,74
Sd	0,24	0,59	0,21	0,26	0,05	0,13	0,24	0,39	0,15	0,45	0,16	0,39	0,13	0,29	0,43	0,71	0,23	0,16	0,49	0,96	0,21	0,46
Total of three nights																						
Max	-2,60	-2,20	-2,70	-2,84	-3,40	-3,63	-2,40	-2,13	-2,10	-2,10	-2,00	-2,00	-1,40	-1,40	-1,40	-1,50	-1,50	-1,64	-0,80	-0,12	-1,00	-0,73
Min	-3,30	-3,57	-3,60	-4,34	-3,90	-4,57	-2,90	-3,17	-2,90	-3,07	-2,80	-3,61	-2,10	-2,78	-1,70	-2,11	-1,90	-2,48	-1,30	-1,17	-1,80	-1,67
Sd	0,25	0,47	0,36	0,62	0,19	0,31	0,18	0,36	0,33	0,38	0,27	0,52	0,35	0,59	0,13	0,27	0,14	0,30	0,18	0,37	0,28	0,35

Module 2: This module applied the current version of Micro-Met and the enhanced Micro-Met. The distribution map of the air temperature at 17:00 in 18 October 2016, extracted from the current version of Micro-Met (Fig. 4.19, a), does not show the effect of cold air drainage over a closed valley. Conversely, enhanced Micro-Met map (Fig. 4.19, b) does show air temperature cooling.

(a)

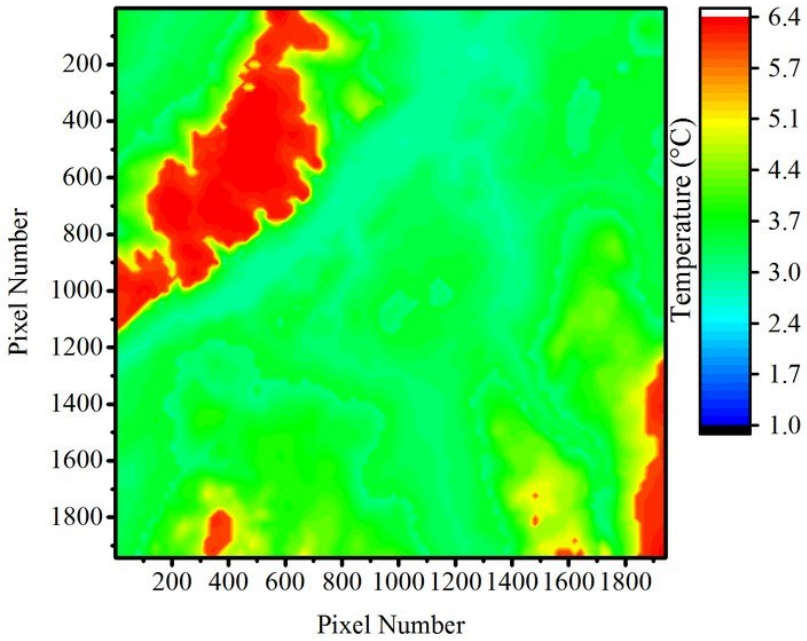

(b)

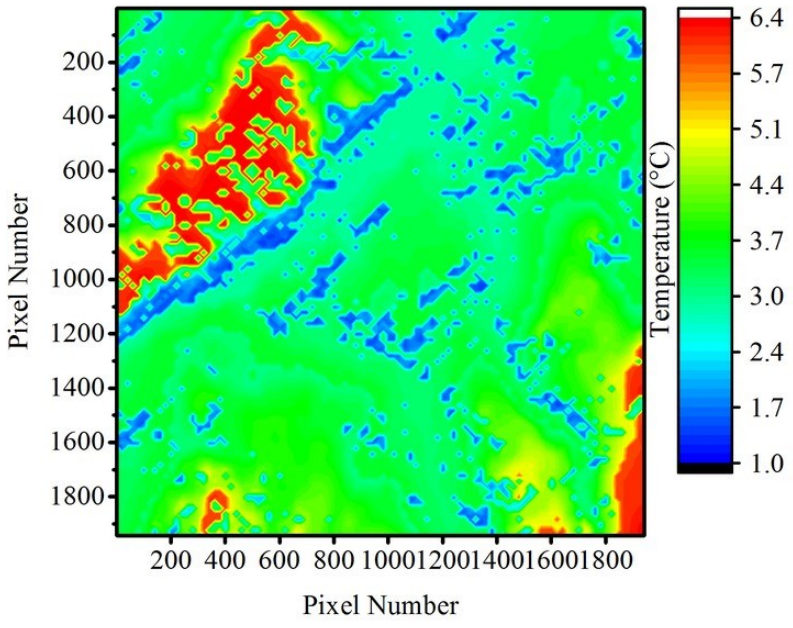

Figure 4.19 An example of distribution of air temperatures simulated by current version of Micro-Met (a) and enhanced Micro-Met (b), at 17:00, 18 October 2016.

Comparison between estimated (with enhanced Micro-Met) and the measured temperature on 15-16 September, 18-19 October 2016, and 19-20 May 2017 indicated correlation coefficient R^2 of 71% (Fig. 4.21).

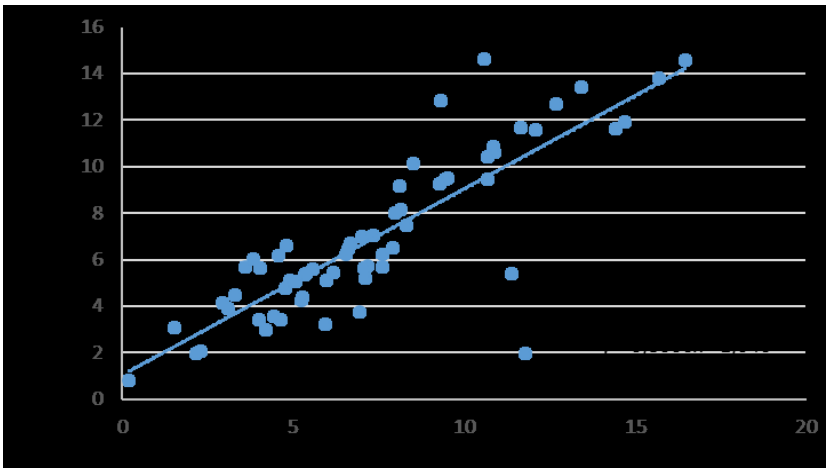

Figure 4.20 Comparison between measured and estimated (with the enhanced Micro-Met) air temperature values of a point in a low valley of the study site.

4.4.6 Quantification of the shelterbelt effect on wind velocity

The result of quantification of the shelterbelt effect on wind velocity over the study area are presented and compared with current version of Micro-Met results. We created a shelterbelt model which produced results that were then compared with those of the current Micro-Met. The selection of the most powerful curve fittings that corresponded to the profiles of wind velocity allowed to formulate three equations.

The equations allowed us to calculate the percentage of variations of wind velocity as a function of the distance from the shelterbelt and forest length (Fig. 4.21, 4.22, and 4.23). In the mentioned figures, the distance from forest shelter is measured as multiple of forest height. For the wind velocity through the forest shelterbelt, the conditions were different from the windward and leeward area. The horizontal distance was based on the percentage of the length of the shelterbelt.

Three different equations (4.45, 46, and 4.47) were applied to three different areas respectively: (1) windward, (2) over the forest shelter, and (3) leeward area regarding the wind direction.

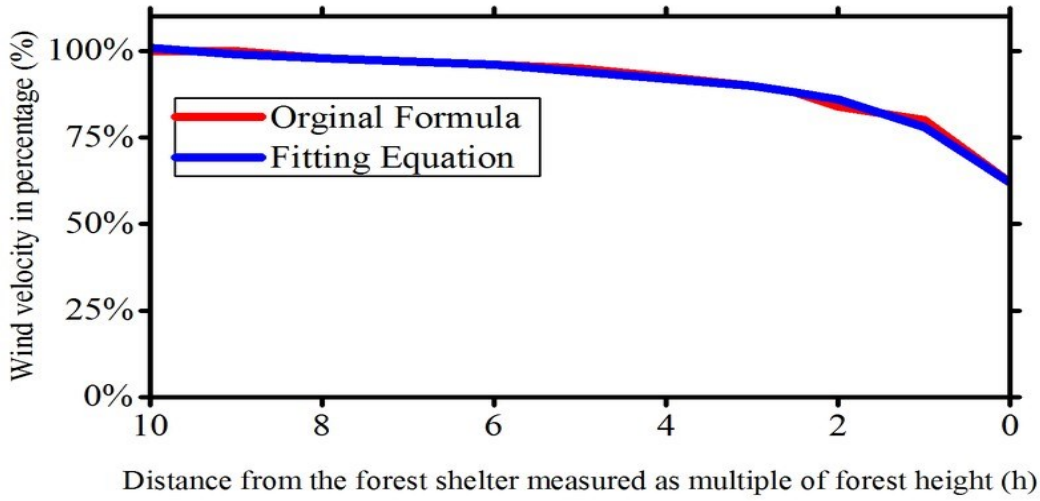

Figure 4.21 Curve fitting for the windward side. Horizontal distance from the shelterbelt expressed in tree height.

$$v_1 = (-0.2673 \times exp(0.8023 \times d)) + \left(0.8911 \times exp(-0.0122 \times d)\right) \quad 4.45$$

where v_1 is the percentage reduction in wind velocity and d is the horizontal distance from the shelterbelt.

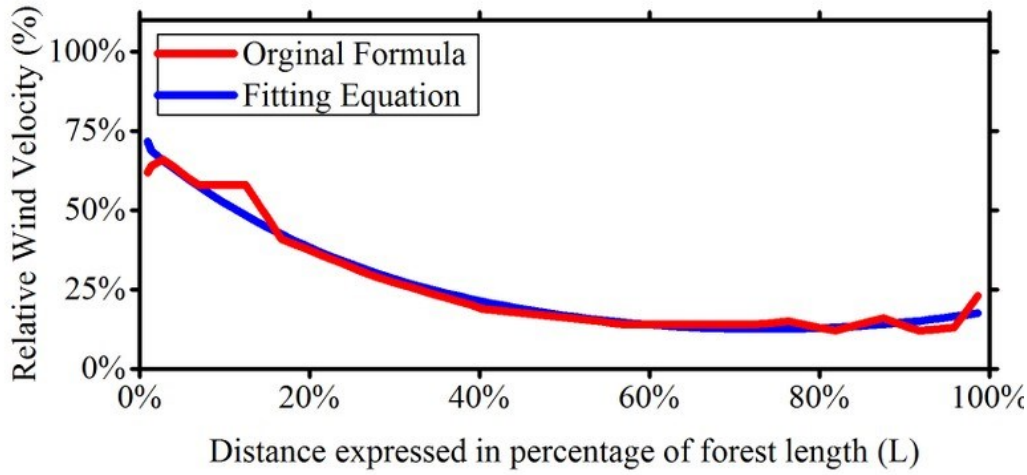

Figure 4.22 Curve fitting through the shelterbelt. Horizontal distance expressed in percentage of forest length.

$$v_2 = 0.8097 \times exp\left((-0.17) \times D\right) + \left(0.01216 \times exp(0.1158 \times D)\right) \quad 4.46$$

where v_2 is the percentage reduction in wind velocity and d is the percentage of the length of the forest shelterbelt. Depending on the direction of the wind (from left to right), the value 0% corresponded to the beginning of the forest, while 100% corresponded to the end of the forest.

To quantify the effects of the shelterbelt on wind velocity in the leeward area, the horizontal distance was defined according to tree height (Fig. 4.23).

$$v_3 = 0.8069 \times exp\big((0.005424) \times D\big) + \big((-0.5211) \times exp((-0.2463) \times D)\big) \quad 4.47$$

where v_3 is the percentage reduction in wind velocity (leeward area) and d is the horizontal distance from the forest shelter measured as multiple of forest height tree (h). Therefore, at the end of this part, three equations were developed in operation application to modeling forest shelter effect on wind velocity.

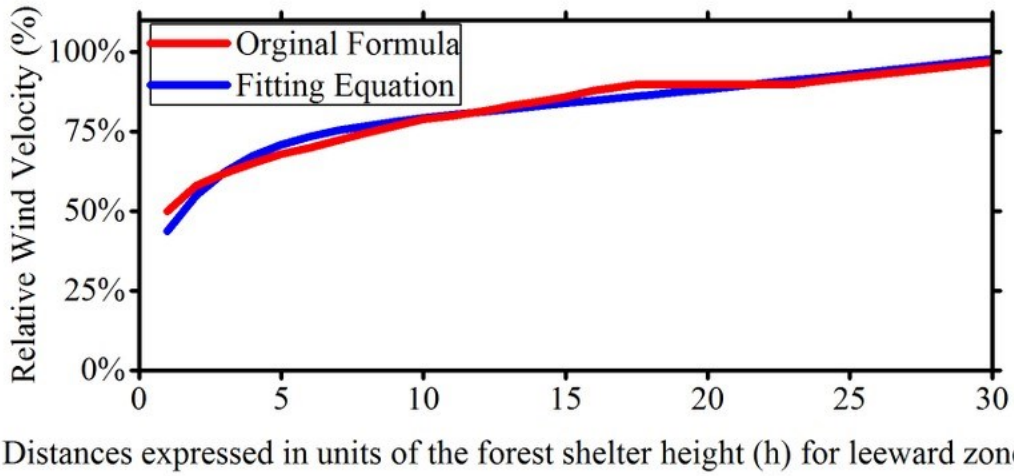

Figure 4.23 Curve fitting for the leeward area. Horizontal distance from the shelterbelt expressed in tree height.

The enhancement of the Micro-Met system through the incorporation of a shelterbelt model was evaluated using the wind data of two weather stations located in Waterville and North Hatley. The tests were carried out for 45 cases during the early and late frost periods throughout 2015, 2016, and 2017. The nights with wind speed less than 10ms^{-1} were selected. The results were acceptable, especially when the winds were low (less than 6 ms^{-1}) with RMSE = 0.98 and MAE = 0.75, VAF = 76.26% and R^2 = 0.72 (Fig. 4.24). See appendix for the values correspond to data of original formula for three area windward, over the forest and leeward.

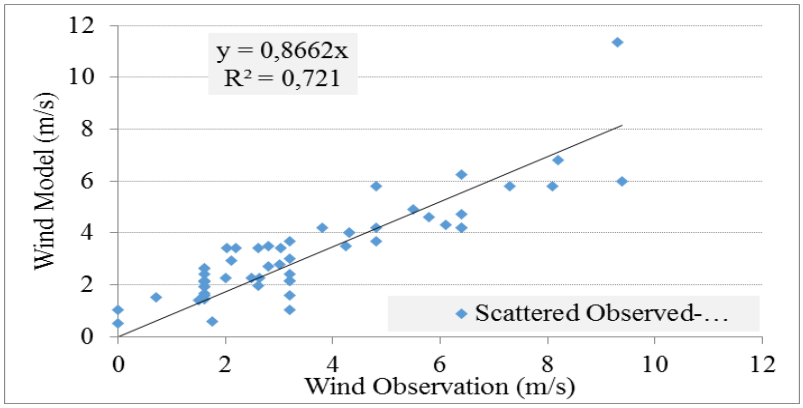

Figure 4.24 Comparison of the observed wind velocity versus those predicted using the enhanced Micro-Met model.

Examples of implementation of the current version of Micro-Met and enhanced Micro-Met model, over the study site on 15 September 2016, at 19:00 are illustrated (Fig. 4.25 (a) and Fig. 4.26 (b) respectively). Moreover, the discrepancies between current version of Micro-Met and enhanced Micro-Met regarding the effects of forest shelter was mapped (Fig. 4.26 (c)). The wind velocity recorded at the reference station (Lennoxville) on 15 September 2016, at 19:00, was 7 kmh^{-1}.

To summarize, an objective methodology was devised to developed three equations to quantify the effect of forest shelter on wind velocity. The results allowed to design a framework for the shelterbelt sub-model that was added to the current Micro-Met to quantified effect of the shelterbelt on wind velocity**.**

The shelterbelt effects reduce wind velocity, which in turn increases the risk of frost in sheltered areas when compared with unsheltered areas. According to Lampartova *et al* (2015), a velocity below 3.6 km h^{-1} increases considerably the risks of frost. Figure 4.26 is of particular interest inasmuch as it highlights areas that were more prone to nocturnal frost derived by enhanced Micro-Met and current Micro-Met respectively. Frost prone areas were defined as being characterized by wind speeds of less than 3.6 km h^{-1}.

We could therefore estimate an area of 243,387 m^2 (9 % of total areas) with a potential for a nocturnal frost due to the impact of the shelterbelt on wind velocity. Meanwhile, applying the current Micro-Met model led to 154,622 m^2 (5% of total area). It should be noted that this percentage reflected only this specific area, based on the observed synoptic wind velocity at the reference station (Lennoxville) at 19:00 with 7 km h^{-1} and a 20-degree direction. Therefore, if the direction and speed of the wind changed, the areas prone to frost would change as well.

4.5 Discussion and conclusion

To meteorological modeling over an agricultural area, access to high resolution of nocturnal air temperature constituted one of the major challenges. Consequently, the overall objective of our study was to enhance current version of Micro-Met for conditions associated with radiation frost. Micro-Met was selected because of the various possibilities it offered: it could handle large volumes of data pertaining to high resolution. Although the Micro-Met model is useful to generalize spatially some meteorological variables, it has several limitations that needed to be overcome for the purpose of this study. Micro-Met required improvements to take into account local terrain effects and local atmospheric conditions

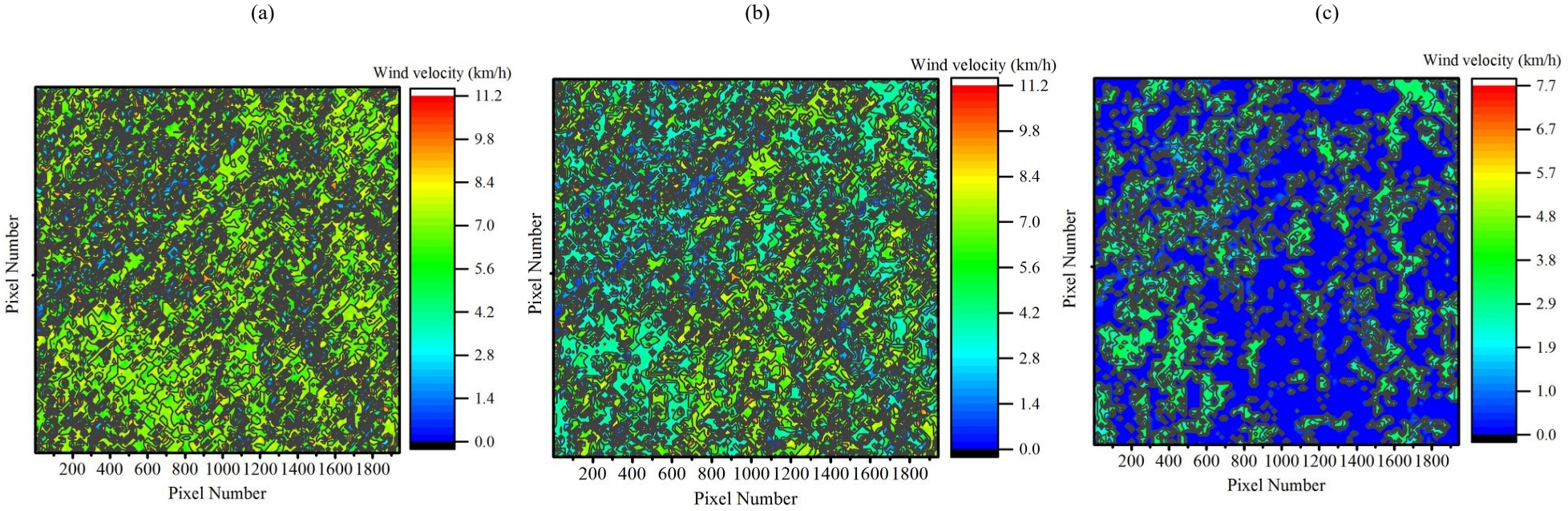

Figure 4.25 Map showing the difference between the current version of Micro-Met and the enhanced Micro-Met, which incorporated the shelterbelt sub model. The wind velocity recorded at the reference station (Lennoxville) on 15 September 2016, at 19:00, was 7 kmh^{-1} s and 20 degree direction.

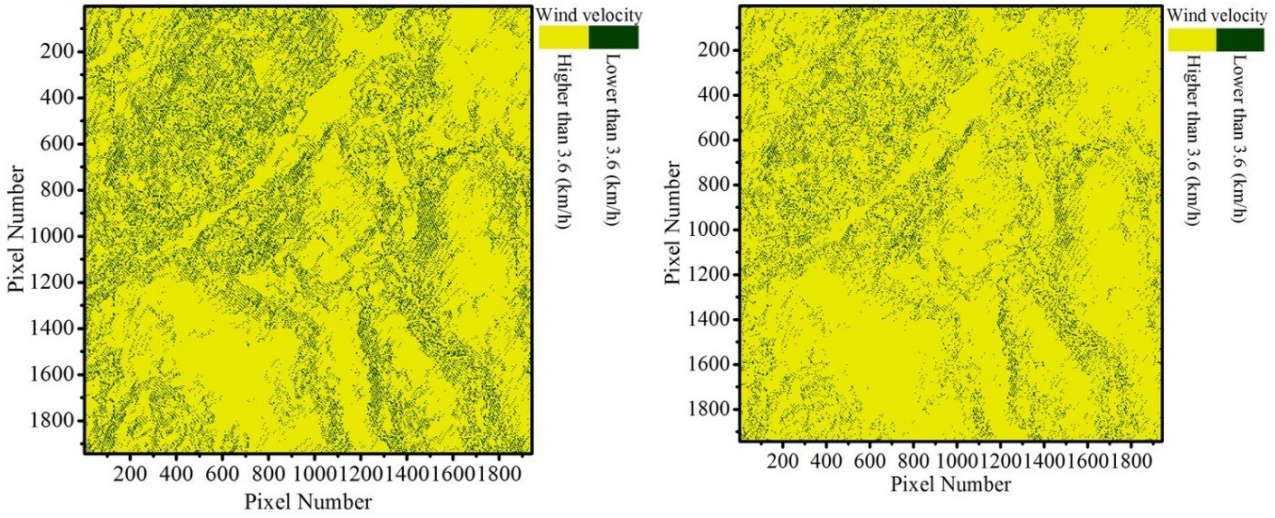

Figure 4.26 The identified areas prone to frost (in green), based on an upper limit threshold of 3.6 km/h applied to the Enhanced Micro-Met system (left) and current version on Micro-Met (right). Yellow area experienced wind velocity more than 3.6 km h-1 and green area lower than 3.6 km h^{-1}. Yellow area for Micro-Met was 154,622 m^2 while the Enhanced Micro-Met indicate 243,387 m^2.

The innovative contribution of this study involved four distinct specific objectives, developed as new sub-models, which resulted into new model capabilities added to the current version of Micro-Met model to propose an enhanced Micro-Met model: (1) the establishment of a method to determine more accurately the local air temperature lapse rate at which air cools with elevation change; (2) the development a locally adjusted downward longwave equation under clear sky condition; (3) the development of a cold air drainage model to estimate the effects of cold air drainage according to temperature drops for the depression areas, and (4) the development of a forest shelterbelt model that added the capacity to estimate the effect of forest sheltering on wind velocity for areas under that influence.

Specific objective 1(4.3.1): For the purpose of reducing the uncertainties in the estimation of downward longwave radiation with the current version of Micro-Met, a locally modified downward longwave equation was developed. This objective was accomplished by improving how the atmospheric emissivity equation calculates the downward radiation during clear skies. Lack of direct measurement at weather station was the most important limitation in this field. However, records of meteorological variables such as air temperature, dew point, precipitation are available at the classical or non classical weather station. Air emissivity is a function of water vapor pressure and air

temperature or air temperature alone. Therefore, downward longwave can be estimated using air temperature and air humidity by the emissivity model. The fitting of existing models is often subjected to local parameterization. The proposed equation to estimate downward longwave was derived by using empirical correlation adjusted to the observed data. For clear sky conditions, several studies have compared the performances of different parameterizations using recorded downward longwave (Sugita and Brutsaert 1993; Gabathuler *et al*., 2001; Flerchinger *et al*., 2009; Al-Lami *et al.,* 2017). Our study is distinctive from others, because specific synoptic conditions associated with radiation frost were selected. In addition to clear sky (which were common throughout the study), we selected low winds velocity conditions. This is important because during calm conditions, the turbulence intensity and turbulent heat exchange were relatively small. As a result, the longwave radiation flux could be changed (Oliphant *et al.*, 2003; Steeneveld *et al.*, 2006).

The comparative statistics for performance of the ten emissivity estimation equations previously published showed the better performance belonged to the equation that included perceptible water variable (RMSE (4.93 Wm^{-2}), MAE (4.04 Wm^{-2}), VAF (95.04%)). This result agreed with the results produced by Flerchinger *et al.,* (2009) and AL-Lami *et al.,* (2017) who evaluated the accuracy of atmospheric emissivity equations under clear skies. In conclusion for this specific objective, using the data from the SIRENE station allowed to validate that the modified equation estimates downward longwave more accurately than the existing algorithm in Micro-Met. The new equation was added as a sub-model in the enhanced Micro-Met. Downward longwave radiation was also a needed input of the cold air mass drainage model (third specific objective) as well as for the vegetation–atmosphere energy model (chapter 6).

Specific objective 2 (4.3.2): A new sub-model of the Enhance the Micro-Met was developed to estimate air and dew point temperature lapse rate. The lapse rate values used by the current Micro-Met model are not applicable in the presence of temperature inversions. This might be a potential source of error. This development was achieved by using simultaneously satellite data (AIRS) and ground-based meteorological data. The first obstacle was to test the AIRS data while there were no upper stations close to the study area. However, there were two upper stations in Quebec (Sept-Îles and Maniwaki). The performance of each level data was validated with a radiosonde observation of the Maniwaki upper station. The results of air temperature show reasonable agreement for two levels 850hPa with R^2= 0.95 and 700hPa with R^2= 0.90. However, lower coefficient of determination belongs to 925 hPa altitude with R^2 of 0.74. These results are in agreement with previous studies

conducted over polar regions by Jones and Standard (2012) which indicated acceptable performance of air temperature retrieved by the AIRS. Relative humidity profiles derived from the AIRS did not show acceptable agreement with the observation by radiosonde observation over Maniwaki. The coefficient of determination was very poor for estimation of relative humidity over all three levels 925 hPa, 850 hPa and 700 hPa (with R^2 of 0.22, 0.12, and 0.34 respectively). This is not in agreement with the results obtained by Gettelman *et al.* (2006) that reported a good fidelity for relative humidity retrieved by AIRS. As far as the enhancement of the Micro-Met was concerned, we did not use the relative humidity provided by the AIRS. One approach without using remote sensing data was to extrapolate air temperature based on previous observations of the environmental temperature lapse rate (Li *et al.*, 2015). However, upper meteorological records and understanding of the local air temperature lapse rate over the valley of the Coaticook area was limited.

An important limitation concerned the use of remote sensing data related to the time of satellite passage and its temporal resolution. Since the study dealt with radiation frost nights and nocturnal temperatures, the time that the satellite passed over the test site played a significant role. In addition, AIRS data do provide the required temporal measurement on a daily basis that would be needed to validate our contribution. The crossing time needed to be close to the sunset transition period; however, for Modis and AIRS satellites, it was at 14:00 (local time) with a daily temporal resolution. The MODIS could not be considered as a sounding instrument, but it had 16 infrared bands covering the spectral range from 3 μm to 14 μm, which allowed the retrieval of temperatures (Rahimzadegan and Mobasheri, 2010).

Several statistical methods are required for the temperature profile from the MODIS satellite. They usually implement the previously determined statistical relationships between the satellite radiances and the corresponding atmospheric profiles (Shiguemori *et al.*, 2004; Polyakov *et al.*, 2014). The retrieval methods remain to be optimized and validated (Rahimzadegan and Mobasheri, 2010). However, radiosondes were launched from two upper stations, far from the study site. Therefore, it is not feasible to use statistical methods. In summary, the estimation of air temperature from AIRS data with high vertical resolution at (50 km^2) spatial resolution offered an opportunity to improve regional monitoring of air temperature profiles. However, the AIRS retrievals of humidity did not agree with the radiosonde observations, which explains why we did not use the data from the AIRS.

Specific objective 3(4.3.3): The cold air drainage model allowed us to quantify the effects of the accumulation of cold air in valleys. The results of the implementation of the new drainage model illustrated that its implementation could improve the distribution of the air temperature for closed valleys. Three distinct differences can be noticed if we compared our model to others models such as those from Whiteman and McKee (1982), Whiteman (1982, 2000), Kondo *et al.* (1989), Whiteman *et al.* (1999, 2001, and 2007), Chung *et al.* 2006. As the first difference, the previous studies focused on a single valley or a limited area, while our research was applied on multiple valleys for a large area (15 km × 15 km). This allowed testing the new algorithm on valleys with different relief configurations. To resolve this limitation, we applied a new algorithm over study area using high resolution DTM. The DTM on a 10 m grid created the basis for detecting closed valleys, prone to cold air drainage. The closed valley detection method could be applied to a variety of specific locations and it is not just limited on the study site.

The second difference, while comparing with previous studies, related to the radiative cooling term. In previous studies, the radiative cooling rate is assumed constant value 0.08 Ch^{-1} (Kondo *et al.*, 1988, 1989, and 1990). However, in the proposed model a modified downward longwave equation that focused on night time period and low wind condition over the study area was developed. The third difference related to an equation for the velocity of cold air drainage. Several equations were developed for estimating wind velocity associated with slope drainage. For example, Stull (2015) proposed an equation, but it considered only the drag coefficient. Consequently, we developed an equation for cold air mass velocity on rough surface. Despite most studies for which land surface was not accounted for, our study included the effects of land cover in terms of hydraulic friction on the cold air drainage velocity. Subsequently, an important question needed to be addressed: Could the performance of this new equation be assessed? Measurements of meteorological processes such as cold air drainage flows were problematic over mountainous areas and the weather stations could not measure the velocity of cold air drainage. Therefore, to carry out a comparison, we had to adopt a new method that involved the use of thermal imagery, which allowed us to track the cold air drainage flow and pooling of cold air in low-lying areas.

Specific objective 4 (4.3.4): This objective attempted to develop a model to quantifying the effects of forest shelterbelt on wind velocity. Shelterbelts remain an important area of research in field, wind tunnel and numerical studies. The algorithm developed to estimate reduction in wind velocity was based on the results of wind tunnel experiments. However, numerical simulation forest

shelterbelt requires solution of the full turbulent Navier–Stokes equations. In addition, aerodynamic influence of a forest shelterbelt, we must have the capability of predicting the wind flow associated with the shelterbelt structure (Gromke and Ruck, 2007). The model included three separate equations were formulated for the windward, through the shelterbelt, and leeward areas. In comparison with numerical simulation forest shelterbelt which requires solution of the full turbulent Navier–Stokes equations, is easier and the result was acceptable for less than 6 ms^{-1}.

To summarize this chapter, we proposed a new framework, which we called enhanced Micro-Met to estimate air temperature at high-resolution, as well as downward longwave radiation. In this study, a fine-resolution DTM and a point-based meteorological database were integrated with the remote sensing data. This provided a platform to develop four sub-models in the enhanced Micro-Met. The consideration of land surfaces related process, such as drainage and forest shelterbelt, as well as atmospheric variables like lapse rate and longwave radiation on a local scale, constituted four advantages to enhance the Micro-Met system. Enhanced Micro-Met in comparison to current Micro-Met provided more accurate input for an agrometeorological model such as vegetation-atmospheric energy model.

5. Development of a method to predict soil temperature

5.1. Introduction

Soil temperature is an important meteorological variable that influence many of the physical, chemical and biological processes in soil and is one of the most important variables in agricultural meteorology. It influences farm activities and planning, such as date and depth of crops sowing, as well as frost protection (Ahmad *et al*., 2008). Soil temperature plays a dominant role in the growth of plants, especially during sensitive stages like germination and seedling stages. Consequently, the availability of accurate surface temperature measurements and soil temperature at various depths would allow better management of agricultural crops. Even if soil temperature is required in many ecosystem models, its observation would be spatially and temporally limited, as well as costly. Weather stations provide soil temperature only at a few specific locations. However, fluctuations in soil temperature can occur at another point close to the measurement point. Therefore, if there are few measurement points, the data collected derives from fewer sources and can provide information that is partially accurate. In locations where soil temperature measurements are sparse, the estimation of soil temperature according to other existing data poses a problem, as it strongly depends on local microclimatic conditions and soil properties (Mihalakakou, 2002; Guojie *et al*., 2016). Consequently, a method to estimate the spatial variability of soil temperature is required to set up a comprehensive database.

Soil temperature has been the subject of a variety of studies in terms of frost prediction. They focused on environmental factors, meteorological conditions, soil physical parameters, topographical variables, and other surface characteristics (Paul *et al.*, 2004; Bond-Lamberty *et al.*, 2005). Estimating soil temperature presents a difficulty near the ground surface where variations are the highest (Mihalakakou, 2002).

To accomplish this task, researchers have used various methods such as the artificial neural network (ANN) (Mihalakakou, 2002; Tabari *et al.,* 2015), wavelet transform ANN (WANN) models (Araghi *et al.*, 2017), and regression analyses (Reimer and Shaykewich, 1980; Ozturk *et al.,* 2011). These methods were used to predict soil temperatures between one and thirty days in advance at a specific meteorological station. The ANN method requires a large amount of data to produce suitable prediction values. Neural network soil temperature model is found to depend strongly on training data and cannot be used easily at locations where there is little or no observational history

(Shaogang *et al*., 2011). This limits the ability of the model to predict soil temperature on a regional scale. The WANN model presents an identical problem.

Several problems limit the development of an accurate method to predict soil temperature. The first and the most important limitation is the low spatial density of weather station which measure sol temperature. (Lehnert *et al.,* 2014). Most studies in this field used the data collected from only one station. In fact, weather stations provide point temperature measurements on a regional scale. However, most environmental models require spatially distributed soil temperature to evaluate biophysical processes (Mutiibwa *et al.*, 2015). The second limitation refers to a complex topographic configuration, which is often combined with sparse weather stations to reduce the availability of temperature measurements (Youneszadeh, 2013; Mutiibwa *et al.*, 2015). In addition, most studies on soil temperature focused on a monthly basis. However, daily or hourly measurements would be more useful for agricultural purposes (Araghi *et al.,* 2017).

The most reliable source of information would be continuously and regularly measure of surface temperature which is not easy task. In general, the models implement fragmentary timelines of soil temperature, scarce point observations or even no soil temperature field measurement at all (Lei *et al.,* 2011). A training database of meteorological variables such as soil temperature using the measured data of weather stations could improve the accuracy of estimation (Kang *et al.*, 2000). Hence, it could be advantageous to develop an operational method capable of providing short-term (hourly) estimation of soil temperature using several records that present different geographical aspects.

Most environmental models necessitate spatially distributed land soil temperature to evaluate biophysical processes. Furthermore, accurate measuring of soil temperature can be logistically difficult to accomplish due to costly field equipment. To circumvent this problem, remote sensing has the potential to supply this information at high spatial resolution. For example, the MODIS satellite provides estimation at 13:30 local standard time. To forecasting minimum temperature using vegetation-atmosphere energy model we need the soil temperature value at the sunset transition period (Lhomme and Guilioni, 2004). The main objective of this study was to develop a method that extrapolates soil temperature at a deep of 1 cm close to sunset, while using MODIS satellite data retrieved at 13:30.

5.2. Study site and available data

The study site was located in the Coaticook River Valley (Compton area), Quebec, Canada. There was no standard weather station to measure soil temperature in this area. Therefore, multi-year field measurements were conducted involving the installation of thirteen stations station taking measurement every 15 min. The data was collected in 2012, 2013, 2015, and 2017, more specifically during the spring and fall. Air temperature (°C), dew point (°C), soil humidity (m^3m^{-3}), soil temperature (°C) at a deep of 1 cm, and wind velocity (ms^{-1}) were recorded every 15 min. All variables except the wind velocity were documented at stations 1 to 11. Moreover, the wind data (speed and direction) was collected during the spring of 2015 at two stations (12 and 13), because they were equipped with an anemometer.

The location of each of the mentioned stations was determined according to microclimate conditions such as hill top, mid-elevation, valley bottom, exposed and shaded ridges, and flat area (Table 5.1, Fig. 5.1). The motivation for this particular investigation was needed for account for the soil temperature at sunset transition period as input for the vegetation–atmosphere energy model to predict nocturnal minimum temperature (chapter 6).

Table 5.1 Geographical coordinates and topographical attributes for each of the experimental stations.

St.	Latitude	Longitude	Elev.(m)	Description	Period
1	45˚13′	71˚50′	196	Valley close to river	Sep.-Oct.-Nov. 2012
2	45˚15′	71˚52′	267	Flat area	Sep.-Oct.-Nov. 2012
3	45˚13′	71˚48′	275	Open valley	Sep.-Oct.-Nov. 2012
4	45˚14′	71˚53′	276	Middle slope	Sep.-Oct.-Nov. 2012
5	45˚17′	71˚47′	280	Valley area	Sep.-Oct.-Nov. 2012
6	45˚16′	71˚54′	185	Flat area	Sep.-Oct.-Nov. 2012
7	45˚17′	71˚48′	213	Valley area	Sep.-Oct.-Nov. 2012
8	45˚17′	71˚49′	170	Middle slope	Sep.-Oct.-Nov. 2012
9	45˚13′	71˚49′	233	Middle slope	Sep.-Oct.-Nov. 2013
10	45˚16′	71˚57′	243	Valley area	May... October 2015
11	45˚16′	71˚56′	252	Flat (clear cut area)	May…October 2015
12	45˚14′	71˚51′	219	Valley area	May-Sep.-Oct. 2017
13	45˚14′	71˚50′	190	Summit	May-Sep.-Oct. 2017

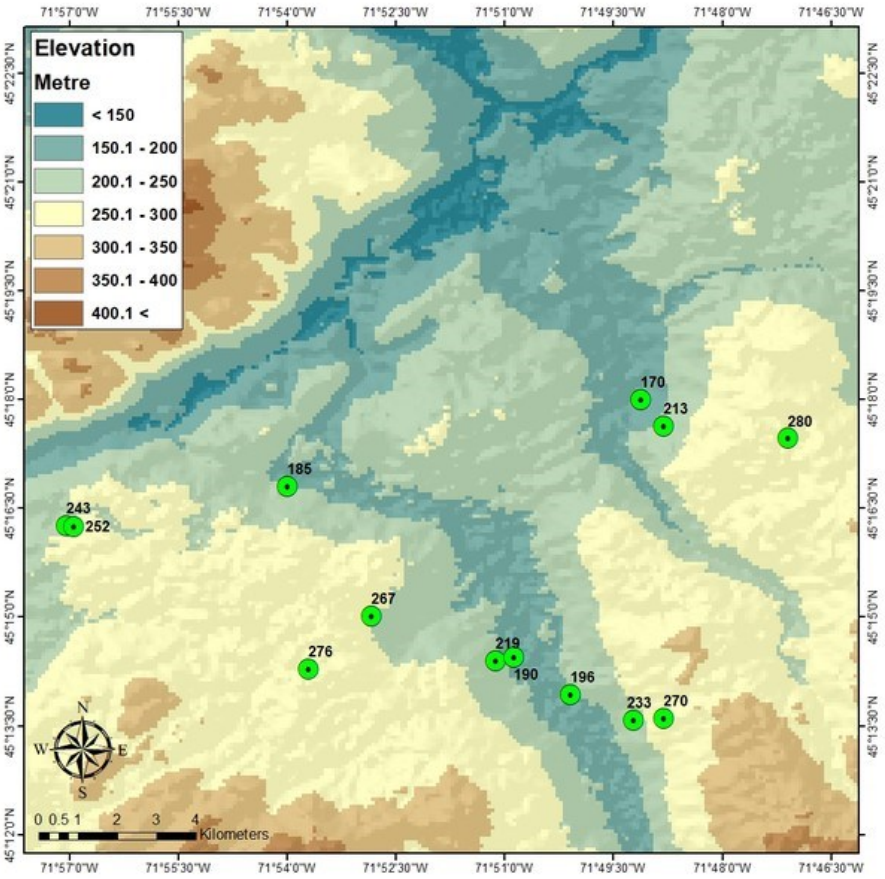

Figure 5.1 Location of the study site. The green circles show the position of the data loggers placed to measure soil and air temperatures, dew point, and wind speed. The green circles identify the location of the data loggers.

5.3 Methodology

Three methodological steps were taken to achieve the objective of this study: Toward development of a model to predict soil temperature, the first step was to establish the link between the physiographic aspects and nocturnal minimum temperature. The second step focused on model input determination. In the third step, regression method was used to develop a spatially explicit model to estimate soil temperature.

5.3.1 Spatial and temporal variability of the meteorological variables

Box and whisker plots time series were produced for the seven experimental stations (Table 5.1; stations 1-7) which had a diversified topography. Meteorological variables: air and soil temperatures, as well as dew point and soil humidity during non-frost and frost conditions were considered. Radiation frost conditions are usually associated with clear skies (defined as a maximum of 25%

cloudiness) and calm conditions (defined by wind speed of less than 3.6 kmh^{-1} at the reference station) (Gombos *et al.,* 2011). The box and whisker plot were used to show the shape of the distribution of the meteorological data, their central value, and their variability during non-frost and frost conditions. The purpose of this analysis was to select the most responsive and uncorrelated variables related to soil temperature that can serve as inputs for the soil temperature predictive mode.

5.3.2 Model input determination

The selection of the input variables constitutes one of the most important steps in the development of a predictive model, because they determine the structure of the model and value of weighted coefficient (Bilgili, 2010; Napagoda and Tilakaratne, 2012; Araghi, 2017). For this reason, the input variables must be to as independent as possible from each other. In the case of the development of a model to predict soil temperature, we selected candidate meteorological variables to assess their correlation to define a subset of relevant variables to build a predictive model. Air and soil temperatures, soil humidity, wind speed, and dew point were obtained from weather stations at two different locations. The first station was located at the bottom of the slope to serve as an example of a depression area whereas the second station was located on a flat area. The Pearson's correlation was employed for the correlation analyses.

The Pearson correlation coefficient is a statistical test that measures the relationship or association between two continuous variables. This type of analysis is based on the method of covariance, as it provides information about the magnitude of the association or correlation. The following formula calculates the Pearson *r* correlation value:

$$r = \frac{N\sum xy - \sum(x)(y)}{\sqrt{[N\sum x^2 - \sum(x^2)][N\sum y^2 - \sum(y^2)]}} \quad 5.1$$

where *r* is Pearson correlation coefficient between two variables (x and y), N is the number of observations. Coefficient values can be in the range between -1.0 and +1.0. A value of 0.0 implies no correlation between the two variables. Values range from −1 (100% negative association, or perfect inversion) to +1 (100% positive association, or perfect agreement). A value of zero indicates the absence of association. Pearson tests were used to determine the optimum input variables from those measured at the weather stations, namely soil temperature, air temperature, dew point temperature, wind speed, and relative humidity. This step in the methodology enabled us to define which variables to retain in the development of the predictive model of soil temperature.

5.3.3 Developing a short-term soil temperature predictive model

Two steps were necessary to develop a predictive model of soil temperature. The first step was to determine the best fitting model (type of degree in polynomial). Three polynomials were tested: linear, quadratic, and cubic. The dependent value, that is the soil temperature at 17:30, was made, as well as independent variables such as 30-minute intervals that began at 13:30. The results obtained in this first step allowed us to identify the type of degrees in polynomial of the predictive model. The second step involved the application of options related to regression equation. The options for regression technique modeling specified how independent variables had to be inputted.

There are different types of regression technique to control the way variables are included into the regression. We selected four types of regression techniques to input independent variables into the regression: stepwise, forward, backward, and enter (also called "forced entry"). These techniques differ in terms of type of dependent and independent variables and distribution. For example, enter (also called "forced entry") is a method of fitting regression models in which all independent variables are entered into the equation entered into the equation at the same time. Based on the input data, there were two backwards: backward (I) and backward (II). Backward (I) only considered the data at 13:30 and sunset time (17:30), while backward (II) considered the data collected for all times between 13:30 and sunset. Moreover, backward (II) used dew point and air temperature between 13:30 and 17:30. The results allowed us to identify the option that would be best adapted to estimate soil temperature.

5.3.4 Model performance evaluation

Five statistical evaluation values were used to assess the method performance: root mean square error (RMSE), mean absolute error (MAE), variance account for (VAF), standard error of the estimate (SEE), and coefficient of determination, which are all calculated as follows:

$$\mathrm{RMSE} = \sqrt{\frac{1}{n}\sum_{i=1}^{n}(Q_{io} - Q_{ie})^2} \quad 5.2$$

where Q_{io} and Q_{ie} denote the observed and estimated values.

$$\mathrm{MAE} = \frac{\sum_{i=1}^{n}(Q_{ie} - Q_{io})}{n} \quad 5.3$$

$$\mathrm{VAF} = \left[1 - \frac{\mathrm{Var}((Q_{io} - Q_{ie}))}{\mathrm{Var}(Q_{io})}\right] \times 100 \quad 5.4$$

If the VAF is 100, this represents the perfect fit.

$$\mathrm{SEE} = \sqrt{\frac{\sum(Y - Y')^2}{n}} \quad 5.5$$

where *SEE* is standard error of the estimate coefficient of Y is an actual score, Y' is a predicted score, and N is the number of pairs of scores.

The coefficient of determination (R^2) equation is as follows:

$$R^2 = \sqrt{\frac{n\sum xy-(\sum x)(\sum y)}{\sqrt{n(\sum x^2)-(\sum x)^2}\sqrt{n(\sum y^2)-(\sum y)^2}}} \quad 5.6$$

5.4 Results

5.4.1 Spatial and temporal variability of the meteorological variables

Figure 5.2 present the box plots of seven experimental stations with different topographic conditions (stations 1 to 7, Table 5.1) during non-frost (6-7 Oct. 2012) and frost weather condition (8.9 Oct. 2012) nights. The stations provide 15-min. measurements from 6 to 9 October 2012 for four measurements: air, dew point, and soil temperatures, and soil humidity. The variables measured from one hour before the sunset until sunrise period (16h-07h). The variables recorded under synoptic condition associated with frost (clear sky, low wind). Figure 5.2 shows air temperature lower 0°C for two stations (station number 2 and 4) which may be related to microtopography. During the frost condition because of low wind and calm condition, there is lower surface evaporation and soil humidity is higher in comparison with windy condition (non frost condition).

The temperature measure at one hour before sunset (16:00) until sunrise time (07:00). The plot box test indicates amount the variables, soil humidity present the lower variation during the forest condition. The coldest site during a frost night (with a minimum-recorded air temperature of -2.8°C) was located at the bottom of the slope (station 7), whereas the warmest sites (with 1.4°C) were located in the middle of the sloped and flat areas (stations 4 and 6). For stations 1, 5 and 7 located at the bottom of the valley, the ranges of air, dew point and soil temperatures were larger than which recorded at other stations on a slope or flat area. These results demonstrate that strong spatial inter-station variations of air, dew point, and soil temperature occur during the night with synoptic condition similar to frost night.

The inter-station variations in air, dew point, and soil temperatures were not marked as during the frost night. Standard deviation values are less marked during non-frost nights when compared with frost nights (Table 5.2). As another example of significant frost and non-frost differences, the most significant difference in minimum temperature between all stations was 4.8°C during frost night; while,

a difference of 0.8°C was observed for non-frost nights. It is worth mentioning that variations in soil humidity, were generally weak, even for frost nights, with the coefficient of variation (also know as relative standard deviation) being generally <~ 30%. Therefore, the results indicate the variation in the soil temperature, air temperature, dew point, was more distinct during nights with frost condition in comparison with soil humidity.

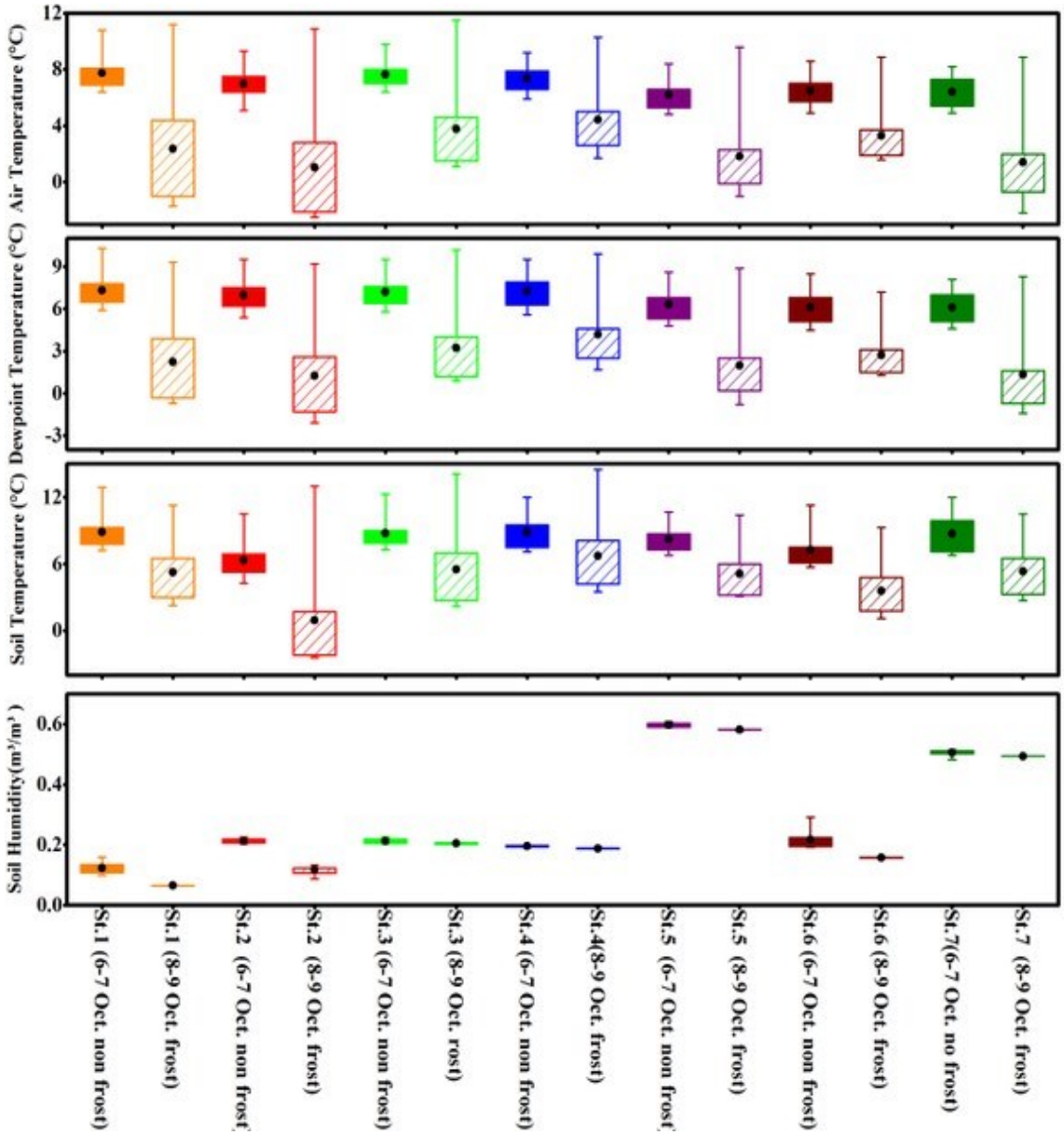

Figure 5.2 Air temperature, dew point, soil temperatures and soil humidity of the seven experimental stations during non-frost (Oct. 6-7, 2012) and frost nights (Oct. 8-9, 2012). Box plots indicate maximum/minimum values at the end of the wiskers, the +/- 90% values with the end of the box and the average air.

Table 5.2 Standard deviation of air, dew point, surface temperatures, and soil humidity for non- frost (Oct.6-7, 2012) frost nights (Oct.8, 9, 2012).

Variable / Station	Standard Deviation							
	Temperature		Dew point		Surface Temperature		Soil humidity	
	Frost	Non Frost	Frost	Non Frost	Frost	Non Frost	Frost	Non Frost
Station 1	4.04	1.35	3.17	1.35	3.08	1.72	0.019	0.001
Station 2	4.19	1.19	3.49	1.23	4.68	1.78	0.007	0.005
Station 3	3.27	1.07	2.89	1.21	3.71	1.54	0.91	0.002
Station 4	2.56	1.04	2.46	1.21	3.42	1.63	0.003	0.002
Station 5	3.10	1.09	2.90	1.13	2.42	1.23	0.006	0.002
Station 6	2.20	1.12	1.81	1.27	2.62	1.65	0.03	0.001
Station 7	2.95	1.14	2.75	1.20	2.45	1.73	0.012	0.0007

5.4.2 Data analyses and method input selection

The selection of input variables constitutes a critical step towards developing prediction models (Napagoda and Tilakaratne, 2012). The Pearson correlation test was applied to find the correlation between soil temperature and air temperature, dew point, soil humidity, wind speed and atmospheric humidity in forms of dew point and absolute humidity. According to the results, input variables were selected as independent variables to estimate soil temperature. Data of two stations, which were located on two different microclimates, were used. One was located on depression area and the other was located on flat area (stations 10 at 243m altitude and station 11 at 252m).

The Pearson correlation matrix (PCM) measures the interdependence between two variables. Table 5.3 provides the PCM of soil temperature and its correlation with air and dew point temperatures, soil moisture, absolute humidity, and wind velocity for two different stations. For both stations, a strong correlation exists between soil temperature and dew point, absolute humidity, and air temperature. Table 5.3 also indicates that air temperature has the most significant correlation with soil temperature (0.92 for flat area and 0.91 for depression area respectively). Furthermore, the PCM shows a high correlation between soil temperature and dew point. These results suggest that air temperature and dew point are primary inputs to estimate soil temperature.

Table 5.3 Correlation coefficient between variable (Air temperature, dew point temperature, soil moisture, Wind speed, and absolute humidity) with soil temperature for experimental stations located on flat and depression areas.

Variable	Time		Dew point temp		Soil hum.		Soil temp.		Absolute humidity		Wind		Air temp.	
Station	Flat	Dep	Flat	Dep	Flat	Dep	Flat	Dep	Flat	Dep	Flat	Dep	Flat	Dep
Time	1	1												
Dew point	0.04	0.05	1	1										
Soil hum.	0.10	0.10	0.29	0.22	1	1								
Soil temp.	0.09	0.09	0.92	0.91	0.08	0.02	1	1						
Abs hum.	0.03	0.03	0.98	0.98	0.18	0.12	0.92	0.91	1	1				
Wind	0.09	0.09	-0.09	-0.07	0.22	0.21	-0.09	-0.08	-0.11	-0.09	1	1		
Air temp.	0.12	0.13	0.97	0.97	0.31	0.25	0.92	0.91	0.95	0.95	0.04	0.06	1	1

Pearson test indicated that among the meteorological variables (air, dew point, soil moisture, and wind velocity), air temperature and atmospheric dew point show stronger positive relation with soil temperature. The air temperature in comparison with the soil moisture shows a 60% stronger correlation with soil temperature. The Pearson analysis presents the minimum correlation for wind velocity with soil temperature (-0.09 for flat area) and (-0.08 for depression area). Soil moisture shows weaker dependency in comparison with dew point and air temperature. Therefore, air temperature and dew point were retained for rest of the analyses.

5.4.3 Soil temperature short-term estimation method

To identify which function best fits the data, three functions (linear, non-linear quadratic and non-linear cubic) were implemented by using the field measurements. The measurements include five variables: air temperature, dew point between 13:30 and 17:00 with 60 minutes interval, maximum and average of wind speed, and soil temperature at 13:30. Table 5.4 provides the error statistics of the three functions tested. Non-linear cubic function gave the best results. However, generally the error statistics were relatively close for the three functions with only small differences between them. Therefore, the linear model was selected to develop a model to estimate soil temperature.

Table 5.4 Comparison of linear and non-linear (quadratic and cubic). The coefficient of determination (R^2), and standard error of the estimate (SEE) values do not show important difference amount the linear, quadratic and cubic.

Dependent Variables	Function models					
	Linear		Non-linear quadratic		Non-linear cubic	
	R^2	SEE	R^2	SEE	R^2	SEE
Air temperature at 13:30	0.39	2.61	0.47	2.47	0.49	2.45
Air temperature at 14:00	0.41	2.57	0.46	2.49	0.47	2.49
Air temperature at 15:00	0.56	2.32	0.58	2.21	0.60	2.17
Air temperature at 16:00	0.73	1.74	0.73	1.76	0.73	1.77
Air temperature at 17:00	0.72	1.77	0.73	1.76	0.74	1.75
Soil temperature at 13:30	0.38	2.65	0.42	2.59	0.42	2.61
Dew point at 13:30	0.46	2.46	0.50	2.39	0.53	2.36
Dew point at 14:00	0.48	2.42	0.51	2.36	0.55	2.31
Dew point at 15:00	0.52	2.32	0.52	2.33	0.53	2.34
Dew point at 16:00	0.64	2.00	0.65	2.00	0.66	2.00
Dew point at 17:00	0.59	2.14	0.60	2.15	0.65	2.02
Max wind speed	0.01	3.33	0.14	3.14	0.32	2.83
Average wind speed	0.04	3.29	0.18	3.07	0.25	2.97

The results of implementation of four types of regression techniques stepwise, forward backward, and enter are presented in Figure 5.3 (a, b, c and d respectively). The coefficient of determination of step wise technique (R^2=0.64) shows the lowest value (Fig. 5.3 a) in comparison with the other techniques. The results for the stepwise and forward options were very similar. For this reason, just the stepwise technic was presented. In addition, the soil temperature employed by Backward (I) technique indicate coefficient of determination R^2=0.77 (Fig.5.3 b) while Backward (II) show R^2= 0.79 (Fig.5.3 c). The enter technique showed the highest coefficient of determination: R^2=0.78 (Fig.5.3 d). The equation of different methods and nomenclature presented in Table 5.5 and 5.6.

(a)

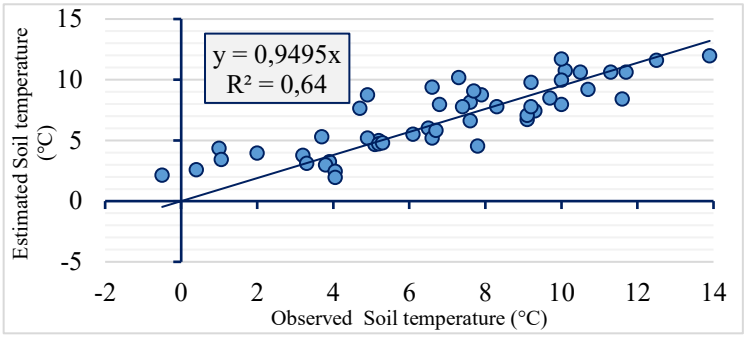

(b)

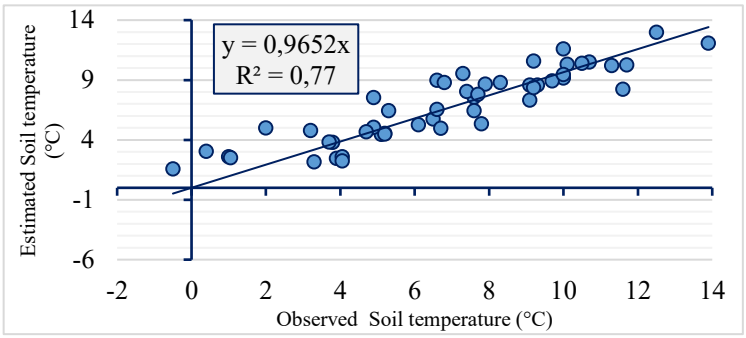

(c)

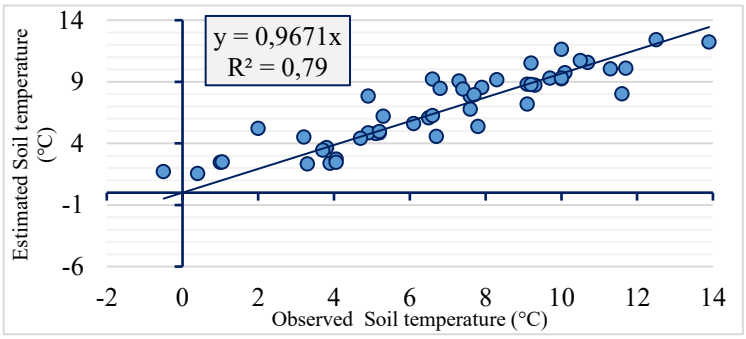

(d)

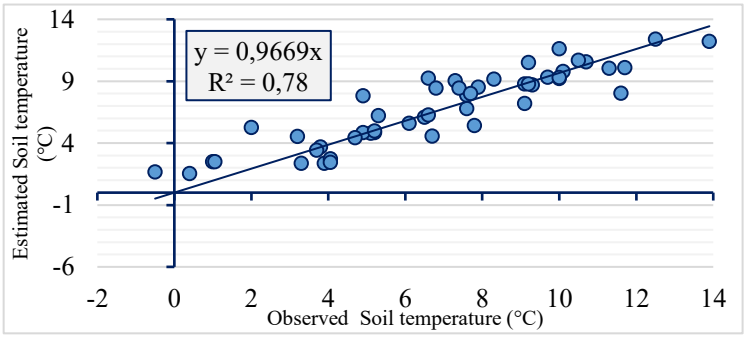

Figure 5.3 The observed and estimated soil temperature values (a) stepwise (and forward), (b) backward (I), (c) backward (II), (d) enter technics.

Table 5.5 selected methods and their mathematical functions in estimating soil temperatures at sunset time. For the nomenclature, see Table 5.7.

Method name	Input variables	Mathematical function
Linear-Backward(I)	Air, Dew point, and Soil temperature	$S=3.044+0.817a_1+-1.655a_2+1.012a_4+0.224S1+0.767d2+-0.395d4$
Linear-Enter	Air, Dew point, and Soil temperature	$S=2.644+1.173a_1+1.927a_2+0.018a_3+0.365a4+0.645a_5+0.241S1+0.375d_1+0.97d_2+0.111d_3+0.087d_4+-0.543d_5$
Linear-Backward(II)	Air, Dew point, and Soil temperature	$S=3.059+0.877a_1+-1.719a_2+0.499a_4+0.546a_5+0.233S_1+0.799d_2+0.46d_5$
Linear-Stepwise&Forward	Air temperature	$S=2.283+0.647a_4$

Table 5.6 Nomenclature of different equations presented in Table 5.5.

a_1= Air temperature at 13:30	d_1= Dew point at 13:30	S_1=soil temperature at 13:30
a_2= Air temperature at 14:00	d_2= Dew point at 14:00	S=soil temperature estimate
a_3= Air temperature at 15:00	d_3= Dew point at 15:00	--
a_4= Air temperature at 16:00	d_4= Air temperature at 16:00	--
a_5= Air temperature at 17:00	d_5= Dew point at 17:00	--

5.4.4 Assessing the performance of prediction methods

Measured and estimated soil temperatures were compared with experimental field results to validate the accuracy of the current method. The performances of the methods were evaluated using the root mean square error (RMSE), the mean absolute error (MAE), the variance account (VAF), standard error of the estimate (SEE), and coefficient of determination (R^2). The results are summarized for each method in Table 5.7. Results demonstrate that the stepwise and forward method reflects a significant difference compared to the three other methods, which showed no noticeable differences. Equation derived by stepwise include minimum variable (air temperature), but statistical performance test shows better result for the other equations. Although the Enter method delivered the best performance, the backward method (I) was selected because it required less input and show close performance to Enter method. The following equation describes the backward method (I):

$$S=3.044+0.817a_1+-1.655a_2+1.012a_4+0.224S_1+0.767d_2+-0.395d_4 \quad 5.7$$

In this equation, a_1 corresponds to air temperature at 13:30, a_2 to air temperature at 14:00, a_4 to air temperature at 16:00, S_1 to soil temperature retrieved by MODIS at 13:30 local time, d_2 to dew point at 14:00, and d_4 to dew point at 16:00.

Table 5.7 Statistical performance indices for different methods.

Method	Input variables	RMSE	MAE	VAF	R^2	SEE
Linear-Enter	Air tem. Dew point, Soil tem.	1.39	1.08	78.20	0.81	1.54
Linear-Backward(I)	Air tem. Dew point, Soil tem.	1.40	1.10	77.61	0.82	1.53
Linear-Backward (II)	Air tem. Dew point,	1.43	1.15	76.52	0.81	1.54
Linear-Stepwise& Forward	Air temperature	1.71	1.40	62.61	0.64	1.75

5.5 Discussion and conclusion

Soil temperature represents a critical agricultural and environmental variable. Despite its importance, measured values are usually very sparse in space and time. Even though soil temperature estimation was previously studied by other researchers, the intent of this study was to develop a method to estimate soil temperature close to the sunset transition period. To this end, a multi-year field measurement was carried out for creating a database. The data recorded during this study served to implement two strategies. First, potential input variables for network methods were selected based on the Pearson correlation matrix. Second, methods with different combinations of input variables were tested. The most important set of input variables were selected based on estimation accuracy.

The results of Pearson coefficient tests indicated that the correlation between soil and air temperatures was the highest. Bond-Lamberty et al. (2005) and Mutiibwa et al. (2015) presented similar results. While there was a strong relationship between soil and air temperature, the two temperatures have different physical meanings, magnitudes, and responses to atmospheric conditions. The results also show that correlation between soil temperature and dew point, and absolute humidity was higher than soil humidity and wind speed. The results imply that atmospheric humidity was more important than soil humidity and wind speed. Bilgili (2010) presented the same results with regard to soil humidity. It should be noted that the Pearson coefficient test indicated that in depression area correlation of air temperature and soil temperature were higher in comparison with flat area. In addition, the physiographical analysis showed that during frost nights and non-frost nights, soil humidity variations were not as significant as dew point, as well as air and soil temperatures.

The results of fitting polynomial model demonstrate that there was no notable difference among the linear, quadratic and cubic models. The linear approach corresponded to the observed

diurnal course of soil temperature presented by Foken (2008), which implied that the daily cycle of the soil temperature was the first order of a sinusoid function. Close value among cubic, non-linear and linear led to selected linear functions for the estimation method. Therefore, soil temperature variations could be written as a linear function of the selected meteorological variables. The implementation of different linear regression technics showed the best performance for the Enter technic. However, the Backward (I) technique denoted the performance closest to the Enter technic. The Backward (I) technique was selected to estimate soil temperature, because this function needed less input in comparison to the Enter techniques.

In the course of this study, we encountered two major limitations. First, the measurement of data represented a problem, because the surface-based network of weather stations could not satisfy the requirements of the climate research community. There is no regular soil temperature measurement. Soil temperature measurements were spatially and temporally irregular which, in turn, restricted their spatial estimation, especially on a regional scale. In locations where soil temperature measurements were sparse, estimating soil temperature accurately according to other existing data became problematic, as it depended on local microclimatic conditions. This led to an insufficient amount of data. The study area was typical of a general situation where a low number of weather stations strongly limited the spatially explicit estimation of soil temperature. This enabled us to establish a database that reflected diverse microclimatic conditions in this area. To overcome this limitation, we installed a network of temporal weather stations. In addition, this study focused on frost conditions, more specifically meteorological conditions associated with radiation frost events. This reduced the amount of data at locations where there is little observational history. For this reason, we had to collect data several years period during which we were able to observe various events associated with radiation frost. The measurement of wind velocity was the second limitation to overcome. Among the 13 temporal stations installed over the study site, only two were equipped with an anemometer. To record more precise field measurements, an anemometer should have been positioned at each temporal station. As a result, we were only able to perform Pearson statistical analyses based on the data that included wind velocity for two stations.

Most of the research conducted so far focused on prediction of soil temperature, from a daily up to a monthly basis. Moreover, most studies employed the data recorded at only one station to develop a method that could estimate soil temperature in a specific area (Tabari *et al.,* 2015; Araghi *et al.,* 2017). However, in the field of agro meteorology short-term soil temperature

estimation is required to forecasting nocturnal minimum temperature. To add to the existing research, we carried out a study that would be more comprehensive in terms of microclimate conditions, because we used multiple stations located in different topographic aspects such as valleys and slopes. Since soil temperature varies depending on climate conditions, this multi-point algorithm enabled us to perform a more detailed microclimate analysis for establishing an equation between soil temperature and other atmospheric variables. As different microclimatic conditions had been considered, it was possible to improve the estimation of soil temperature on a regional scale. We presented a method for estimation on limited inputs associated with air temperature, dew point and soil temperature at 13:30. Many methods for soil estimation are complex, because they require an extensive range of input variables (Li *et al.*, 2011).

The method developed in the context of this study depended solely on the available data at specific times. In addition, the capability of using satellite data made this method suitable for spatial applications on a regional scale. It should be noted that soil temperature depends on a number of variables such as location, net radiation at the surface, soil texture, moisture content, and ground cover. These parameters were not considered in this study.

Finally, the method presented in this research, allow us to use high spatial satellite soil temperature to estimate soil temperature at target hours. In addition to result of performance test selected equation employed air and dew point at the hour between 13h30 and sunset transition period. Therefore in addition to air temperature this equation considered air humidity. Therefore, using atmospheric variable may improve accurate prediction. Successful prediction of soil temperature may lead to reducing time, costs, and equipment maintenance, all of which are necessary for on-site monitoring. Therefore, efficient methods to calculate soil temperature at remote locations from several monitoring stations are essential. Despite current limitations due to the lack of ground observations in the study area, major advances can be expected. This will require more investigation of soil temperature estimation, combination and comparison of modeling and observational data sets, as well as additional numerical and field experiments.

6. Modifications of the vegetation-atmosphere energy model to forecast nocturnal minimal air temperature

For efficient implementation of frost protection strategy, high resolution and accurate forecasts of minimum air temperatures are required, (Kalma *et al.*, 1992; Blennow and Persson, 1998; Prabha and Hoogenboom, 2006). Farmer should know the nocturnal temperature variation as they occur over their land which fields are most prone to forest, so that action can be taken in these fields. Predicting minimum temperatures may be approached by using different models. Early methods of frost prediction were mainly based on physical–analytical approach was developed by Brunt (1941). However, these methods were developed for open areas, but in regions with irregular topography, the same applications encounter greater difficulties (Ghielmi and Eccel, 2006; Asakura *et al.,* 2011). Another approach is the use of the Artificial Neural Network (ANN). One of its limitations is that it is empirically based and does not take into account the physical and dynamical aspects of land-atmosphere interactions or their temporal evolutions explicitly (Prabha and Hoogenboom, 2008). The Numerical Weather Prediction (NWP) models are regarded as other methods to predict minimum temperature. However, the NWP was not made for specific agricultural regions; thus, its data was not very useful for local assessment in rural areas (Huth, 2004; Eccel *et al.*, 2007).

The approaches based on energy balance approach such as vegetation-atmosphere energy have been used to predict the air temperature from previous observations (Lhomme and Guilini, 2004). This kind of the prediction model is based on the transfer of sensible and latent heat and ground heat flux. Sensible and latent heat fluxes by definition should strictly be defined within the Lagrangian framework, of which the theories were developed for surface energy models (Raupach 1987, 1989a, 1989b; Warland and Thurtell, 2000). These models remain somewhat complex and difficult for local implementation (Lhomme and Guilioni 2004). However, numerous vegetation-atmosphere models use the simpler K theory to parameterize the sensible and latent heat fluxes via conceptual resistances, rather than turbulent quantities (Monteith 1975; Shuttleworth 1976; Shuttleworth and Wallace, 1985; Cleugh and Dunin, 1995; Zhang *et al.*, 1995).

The point-based "two-layer vegetation-atmosphere energy model" designed by Shuttleworth and Gurney (1990) is an operational example of nonlagragian model, which does not deal with the complex resolution of the non-steady-state regime. It is based on a static representation of the soil-plant-atmosphere system and assumed to reflect the conditions reached at the end of the night, when minimum temperatures usually occur. One limitation is that the model required many meteorological

and land surface variables (Lhomme and Guilioni, 2004). Another possible limitation is associated with ground heat flux that is difficult to measure. Moreover, estimating the ground heat flux for regional scale is time consuming and logistically expensive (Zhu *et al.*, 2014). In order to obtain the ground heat flux over a regional scale, various empirical methods based on remote sensing data have been recommended. However, the ground heat flux cannot be estimated only by satellite measurements.

Another limitation of layer vegetation-atmosphere model concerned topographic effects. On the one hand, most mountain slopes experience nocturnal drainage flow on clear nights with weak synoptic winds. On the other hand, the vegetation-atmosphere model does not have a specific algorithm to quantify the effects of cold air drainage (Whiteman, 2007). Moreover, the model is a point-based model. However, the heterogeneity of land surface makes single-point surface measurements less representative of the surrounding areas. Therefore, to develop a prediction model on a regional scale, a structured approach had to be adopted, allowing us to represent the heterogeneous surface, as well as the transfer of the current point-based model into a grid-based model.

Simulations with the enhanced Micro-Met model could provide more accurate inputs to overcome the limitations of the vegetation-atmosphere model. We hypothesized that the combination of the enhanced Micro-Met simulation data and remote sensing offered the possibility to derive the local distribution of energy fluxes over heterogeneous land surfaces close to the sunset period. To explore this hypothesis, the main objective of this study was to modify and integrate the vegetation-atmosphere energy model with the enhanced Micro-Met to develop its predictive capability of minimum air temperature near the ground.

6.1 Description of the vegetation-atmosphere energy model

The two-layer vegetation-atmosphere energy model developed by Shuttleworth and Wallace (1985) and Shuttleworth and Gurney (1990) constitutes the basis for minimum temperature prediction in this study. The model used the method of resistance according to Ohm's law. In this method, depending on which quantity the flux refers to, the potential difference corresponds to the proper parameter. Thus, when the flux of heat is considered, the potential difference refers to temperature difference. Similarly, for the electrical analogue shown in Figure 6.1, the differences in vapor pressure and temperature across the resistance can be written in terms of the relevant resistance and flux

(Schulz *et al.*, 1998). Consequently, sensible heat (H) and latent heat (λE) fluxes between canopy air space and canopy (r_{ac}), or canopy air space and ground (r_{as}), or canopy air space and reference height (r_{aa}), can be estimated. The vegetation-atmosphere model uses the meteorological data at sunset period to predict air and soil temperatures resulting from radiative cooling. The energy fluxes directly affect the changes in temperature (Heinemann and Martsolf, 1988). Therefore, the energy balance equations lead us to estimating minimum nocturnal air and soil temperatures. The surface energy balance is expressed as:

$$\mathrm{R_n} - \mathrm{G} = \mathrm{H} + (\mathrm{LE}) \qquad 6.1$$

where R_n is the net radiation (Wm^{-2}), *G* is the ground heat flux (Wm^{-2}), *H* is the sensible heat flux (Wm^{-2}), and LE is the latent heat flux (Wm^{-2}), λ corresponds to the latent heat of vaporization and *E*, to the actual evapotranspiration. The basic principle underlying two-layer models is that the two sources of water vapor and heat are superimposed; hence, heat and water vapor enter or leave the bottom layer only via the top one. The total flux of sensible heat flux emanating from the whole surface corresponds to the sum of the fluxes emanating from each layer (soil and vegetation):

$$\mathrm{H} = \mathrm{H_s} + \mathrm{H_v} \qquad 6.2$$

H_s and H_v are soil and vegetation sensible heat fluxes respectively, and are expressed as:

$$H_s = \rho C_p \frac{(T_s - T_a)}{r_{a_s}} + \rho C_p \frac{(T_v - T_a)}{r_{a_v}} \qquad 6.3$$

where r_{as} r_{av} are soil surface resistance and leaf stomata resistance, T_s represents the soil temperature, T_a the air temperature, and T_v the vegetation temperature. The transfer of latent heat flux can also be formulated as:

$$\lambda E_s = \left(\frac{\rho c_p}{\gamma}\right)\left(\frac{e_* - e_0}{r_{as}}\right) \qquad 6.4$$

$$\lambda E_c = \left(\frac{\rho c_p}{\gamma}\right)\left(\frac{e_* - e_0}{r_{ac}}\right) \qquad 6.5$$

$$LE = LE_s + LE_v = \frac{\rho C_p}{\gamma} \cdot \frac{e_0 - e_a}{r_{aa}} \qquad 6.6$$

where r_{aa}, r_{as} and r_{ac} represent aerodynamic resistance, soil surface resistance, and leaf stomata resistance respectively (for more details, see Appendix C), the ground heat flux (G) is derived from the heat diffusion equation as follows:

$$\mathrm{G} = \mathrm{h}(\mathrm{T_s} - \mathrm{T_{sd}}) \qquad 6.7$$

where *h* is the heat transfer coefficient, T_s the soil temperature, and T_{sd} is the soil temperature at the reference depth (z_d). The net radiation (R_n) can be calculated with the following equation:

$$R_n = G + H + LE \quad (6.8)$$

where G is ground heat flux (Wm^{-2}), H is sensible heat flux (Wm^{-2}), and LE is latent heat flux (Wm^{-2}). The analytical solution of the system of energy equations allows us to predict nocturnal minimum temperatures of soil and air (Lhomme and Guilioni, 2004).

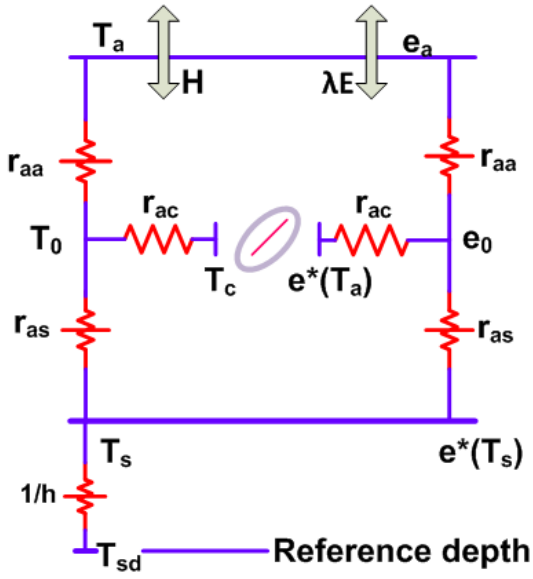

Figure 6.1 Schematic diagram and potential-resistance network for the one-dimension two-layer representation of energy transfers within and above the canopy (see nomenclature in table E1 of Appendix E for definition of the symbols).

6.2 Methodology

To carry out the main objective, a methodology based on the vegetation-atmosphere energy model was adopted. It employed a combination of three data sources: classical weather station, remote sensing (MODIS and Landsat), and enhanced Micro-Met simulation data. The weather station in Lennoxville provided point meteorological variables. The station data used for spatially distributed and development gridded data sets by enhanced Micro-Met. The satellite data served to derive surface temperature as well as input data for the land surface albedo model.

Enhanced Micro-Met model provided data-regressed simulations of the meteorological data, which were then transferred into short-term soil temperature model, surface albedo model, and vegetation-atmosphere energy model. Three methodological steps were taken in this study to address the main objective. Initialization was the first step performed regarding the function of powering the input data. Processing functions represented the second step, which fulfilled the purpose of estimating the land surface albedo, ground heat flux, latent heat flux, sensible heat flux, and net radiation at

sunset to establish the energy balance equation system. Finally, the implementation and output of the model consisted in solving the energy balance equation to predict nocturnal minimum air temperature. We employed a combination of three data sources: classical weather station, remote sensing (MODIS and Landsat), and enhanced Micro-Met simulation data. The weather station in Lennoxville provided point meteorological variables. The station data used for spatially distrusted and development gridded data sets by enhanced Micro-Met model. The satellite data served to derive surface temperature as well as input data for the land surface albedo model.

Enhanced Micro-Met model provided data-regressed simulations of the meteorological data, which were then transferred into short-term soil temperature model, surface albedo model, and vegetation-atmosphere energy model. This methodology enabled us to improve the representation of the fluxes associated with heterogeneous surfaces characteristic of the study area and facilitated the transformation of the current point-based model into a practical grid-based model. Figure 6.2 shows the flow diagram of the modified vegetation-atmosphere energy model to predict minimum temperature. Flow diagram of the procedure of employed the vegetation-atmosphere energy model to predict nocturnal minimum temperatures near the surface.

6.2.1 Initialization

The initialization involved inputting data for the sunset transition period. Enhanced Micro-Met provided distributed data points of the following atmospheric variables: air temperature, dew point, wind velocity, air pressure, and longwave radiation for vegetation-atmosphere model. Drops in temperature due to pooling of cold air and the shelterbelt effects on wind velocity and precise estimation of longwave downward radiation, were considered to increase the accuracy of the initialization component. We employed the Eco-Forest model, DTM, and DSM to extract the land cover and canopy height, both of which then served to estimate the air and soil resistances. To have access to soil temperature close to the sunset period, was estimated using equation short-term forecasting model presented in chapter 5 was employed.

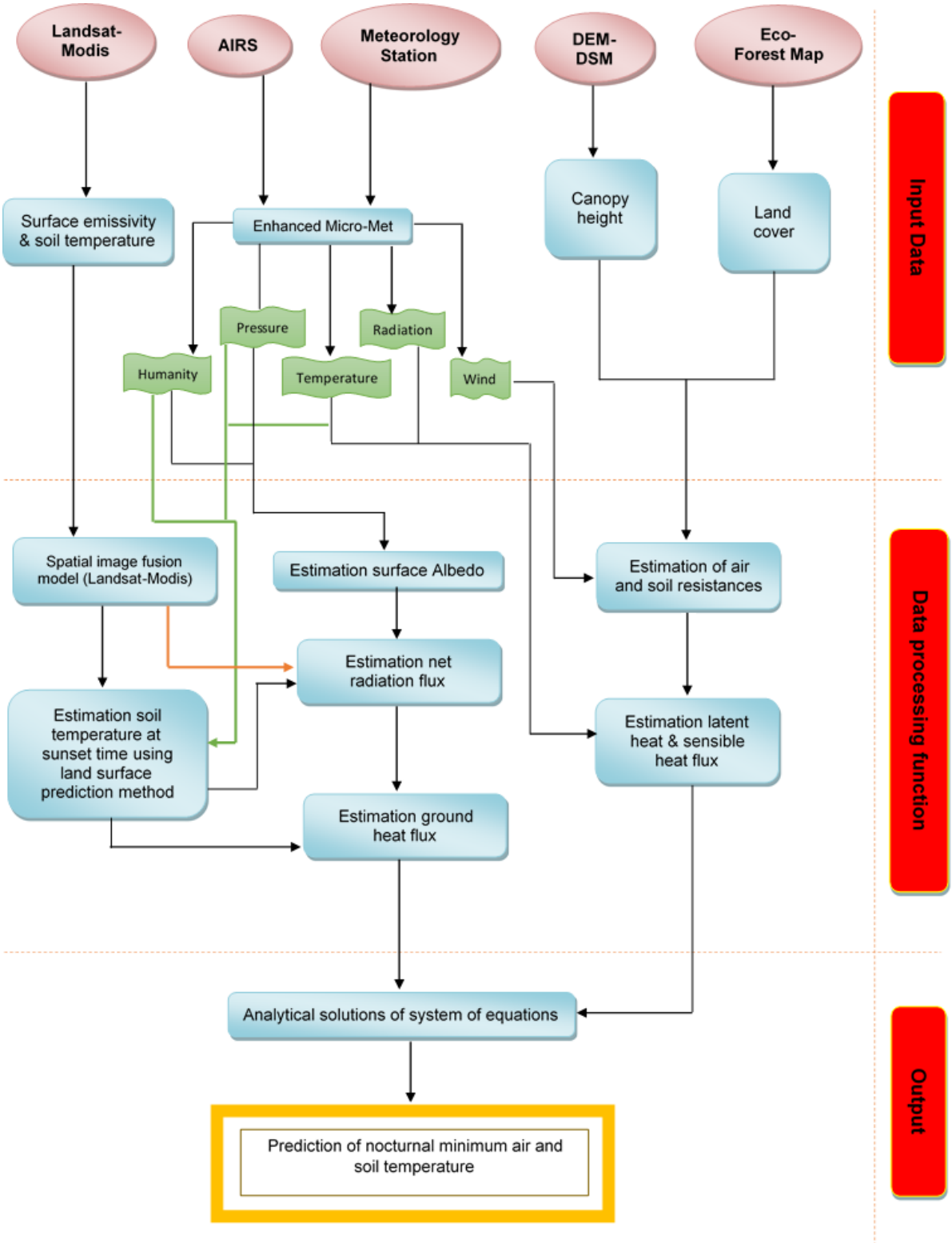

Figure 6.2 Flow diagram of the procedure of employed the vegetation-atmosphere energy model to predict nocturnal minimum temperatures.

6.2.2 Processing functions

The components relating to processing functions were divided into two modules as follows:

Module 1: Estimation of the surface albedo.

Module 2: Estimation of the latent heat flux, sensible heat flux, and ground heat flux.

Module 1: Estimation of the surface albedo

The surface albedo is a variable defined as the ratio of the solar radiation reflected from earth's surface to the solar radiation incident upon it (Liang et *al*., 2013). It differs depending on land surface covers, as well as atmospheric conditions. We employed the method presented by Tasumi *et al*. (2007) to estimate the surface albedo. Toward this aim, Landsat satellite data and enhanced Micro Met model were used. The modeling of the surface albedo included three steps: (a) estimation of the at-satellite bidirectional reflectance; (b) estimation of the at-surface reflectance; and (c) integration of the weighting function.

a. Estimation of the at-satellite bidirectional reflectance

Assuming the absence of an atmosphere for the band 1-5 and band 7 of the Landsat:

$$p_{t,b} = \frac{E_{out(band)}}{E_{in(band)}} \quad 6.9$$

where E_{out} is the out-going energy at the top of the atmosphere and E_{in} the in-coming energy within the band (1-5 and 7), which were estimated using the following equation (Allen, 1996):

$$E_{in(band)} = G_{sc(band)} \times \cos\theta \times dr \quad 6.10$$

where G_{sc} is to the solar constant (Wm^{-2}), θ is the solar incident angle calculated from the following equation (Tasumi *et al.*, 2003):

$$\cos(\theta) = \sin(\delta)\sin(\phi)\cos(s) - \sin(\delta)\cos(\phi)\sin(s)\cos(\gamma) + \cos(\delta)\cos(\phi)\cos(s)\cos(\omega) + \cos(\delta)\sin(\phi)\sin(s)\cos(\gamma)\cos(\omega) + \cos(\delta)\sin(s)\sin(\gamma)\sin(\omega) \quad 6.11$$

where δ = declination of the earth (positive in summer in the northern hemisphere); ϕ = latitude of pixel 9 positive for the northern hemisphere and negative for the southern hemisphere; s = surface slope, where s = 0 for horizontal and s = π/2 radiations for the vertical downward slope (s is always positive and represents the downward slope in any direction). γ = surface is the aspect angle, where γ = 0 for slope oriented due south, γ = - π/2 radians for slopes oriented due east, γ = +π/2 radians for slopes oriented due west, and γ = ±π radians for slopes oriented due north. Parameter ω is the hour

angle, where ω = 0 is the solar noon, ω is negative in the morning, and ω is positive in the afternoon. All trigonometric functions are in radians.

$$\delta = 0.409sin(\frac{2\pi}{365}J - 1.39) \quad 6.12$$

The term *dr* is defined as *1/de-s*, where *de-s* is the relative distance between the earth and the sun in astronomical units. It was computed using the following equation (Allen *et al.*, 1998):

$$dr = 1 + 0.0033 \times \cos\langle J\frac{2\pi}{365}\rangle \quad 6.13$$

where *J* symbolizes the number of days in the year between 1 (January 1) and 365 or 366 (December 31), and the angle (J × 2π/365) is in radians. The output energy at the top of the atmosphere was estimated using the equation presented by Allen (1996):

$$\mathrm{E_{out(band)}} = \langle \mathrm{a} + (\mathrm{b} - \mathrm{a}) \times \frac{\mathrm{DN}}{255}\rangle \pi \quad 6.14$$

where *a* and *b* are constant values and *DN* a digital number.

b. Estimation of the at-surface reflectance

This estimation was conducted for band b as follows (Tasumi *et al*., 2007):

$$p_{s,b} = \frac{R_{in,s,b}}{R_{out,s,b}} = \frac{p_{t,b} - p_{a,b}}{\tau_{in,b} \times \tau_{out,b}} \quad 6.15$$

where $R_{in,s,b}$ and $R_{out,s,b}$, ($Wm^{-2}m^{-1}$) are at-surface hemispherical incoming and reflected radiances, $\tau_{in,b}$ is the effective narrowband transmittance for incoming solar radiation, and $\tau_{out,b}$ is the effective narrowband transmittance for shortwave radiation reflected from the surface. $\tau_{out,b}$ and $\tau_{out,b}$ account for the attenuation of both beams and diffuse the radiation. $p_{a,b}$ is an atmospheric path reflectance for band b that represents the solar radiation backscattered by the atmosphere to the satellite. Parameters $\tau_{in,b}$ and $\tau_{out,b}$ account for the attenuation of both beams and diffuse the radiation. They were calculated using individually derived equations for each band of the satellite (Allen, 2007). $p_{a,b}$ was estimated for each band as a function of transmittance, which was expressed as $\tau_{in,b}\ and\ \tau_{out,b}$ (Tasumi *et al.*, 2007):

$$\tau_{in,b} = C_1 exp\left[\frac{C_2 \times P_{air}}{K_t \times \cos\theta_h} - \frac{C_3 \times W + C_4}{\cos\theta_h}\right] + C_5 \quad 6.16\ (a)$$

$$\tau_{out,b} = C_1 exp\left[\frac{C_2 \times P_{air}}{K_t} - \frac{C_3 \times W + C_4}{1}\right] + C_5 \quad 6.16\ (b)$$

where P_{air} is the atmospheric pressure (kPa), θ_h is the solar zenith angle for the horizontal surface and was calculated as follows:

$$\cos\theta_{hor} = sin(\delta)sin(\phi) + cos(\delta)\,cos(\phi)cos(\omega) \quad 6.17$$

W is the water in the atmosphere (mm) using the equation derived for North America by Garrison and Adler (1990):

$$W = 0.14e_aP_{air} + 2.1 \quad 6.18$$

where e_a is the water vapor pressure (mm). $C_1 - C_5$ are fitted satellite-dependent constants, *te* is the horizontal surface orientation, all of which were used even for the application in mountain terrains to properly estimate relative atmospheric thickness. $P_{air}/\cos\theta_h$ is the surrogate for the atmospheric mass and optical path length (Tasumi *et al.*, 2007). Water vapor pressure in equation 6.18 can be computed using air temperature and dew point according to the Clausius-Clapeyron equation:

$$e_a(mb) = 6.11exp\left[\frac{L_v}{R_v}\left(\frac{1}{273.15} - \frac{1}{T(K)}\right)\right] \quad 6.19$$

where Lv is the latent heat of vaporization ($2.5*10^6$ J kg^{-1}), Rv is the gas constant for water vapor (461 Jkg^{-1}), T_0= 273 K and Td is the dew point temperature

c. Integration of the weighting function

The broadband surface albedo was calculated from the multiband satellite data. The weighting function allowed us to integrate the band reflectance within the short-wave spectrum (Starks *et al.*, 1991).

$$\alpha = \sum_{b=1}^{7}\left[P_{s,b}W_b\right] \quad 6.20$$

where α is the surface albedo, W_b is the weighting coefficient that represents the fraction of the at-surface solar radiation occurring within the spectral range represented by a specific band, and *b* is the number of integrated satellite bands.

Module 2: Estimation of the sensible heat flux, latent heat flux, and ground heat flux

The latent heat flux and sensible heat flux were estimated using the modified version of the Shuttleworth and Wallace (1985) vegetation-atmosphere energy model. The equations are described in terms of resistances by applying Ohm's law to analogue electrical network (Equations 6.3 and 6.6), where the energy fluxes were functions of the aerodynamic resistance and surface resistance (see Appendix E).

The next step involved estimating ground heat flux (G). There are numerous schemes for estimation of the ground heat flux that include different complexities; ranging from simple empirical relations to more sophisticated numerical parameterizations (Wang and Zeid, 2012). The most techniques for measuring or modeling of this flux provide point estimate; therefore, would not be appropriate for vegetation-atmosphere energy model. In order to estimate ground heat flux for study site (15km×15km) we focused on remote sensing data. However, ground heat flux cannot be estimated directly from satellite measurements. Many empirical methods have been developed to derive regional ground heat flux using remote sensing data. Most of them emphasize on the development of the relationship between the ratio of ground heat flux and net radiation (Verhoef *et al.*, 2012; Li *et al.*, 2017). The selected methodology employed the following relation by Bastiaanssen (Equation 6.21), where the ground flux is expressed as a function in terms of the land surface albedo, normal difference vegetation index, and surface temperature:

$$G = \left[\frac{(T_s - 273.15)}{a}(0.0038\alpha + 0.0074\alpha^2)(1 - 0.98NDVI^2)\right]R_n \quad 6.21$$

where Rn is net radiation flux, Ts is soil temperature, NDVI is Normal difference vegetation Index, and α albedo, all of which served to make an estimation over the study site as follows:

Net radiation (R_n) was calculated based on land surface radiation:

$$R_n = (1 - \alpha)\, R_s + \varepsilon\, \sigma(T_a - T_s) \quad 6.22$$

where R_s corresponds to the downward short-wave radiation, also known as the total solar radiation and can be expressed as:

$$R_s = \left(\frac{1}{\rho}\right)^2 I_0 \cos\theta\, \tau_b = R_0 \tau_b \cos\theta \quad 6.23$$

where I_0 is the solar constant, R_0 is the vertical incidence of the solar radiation on top of the atmosphere, θ is the sun zenith angle on the slope, τ_b is the direct atmospheric transmittance, $\left(\frac{1}{\rho}\right)^2$ is the revised coefficient of the sun-earth distance, α is the surface albedo, ε is the emissivity, σ is the Stefan-Boltzmann constant ($5.678*10^{-8}$ Wm^2k^{-4}); T_s is the surface temperature and T_a is air temperature. The surface temperature was estimated in three steps. First, we retrieved the surface temperature from the MODIS satellite (13:30 local time). The second involved, estimating the soil temperature during the sunset period, and this was achieved with the equation proposed in chapter 5.

6.2.3 Model implementation and output

This component focused on the implementation of the model using the analytical solutions of the system of equations presented by (Lhomme and Guilioni, 2004). Depending on the meteorological conditions, there were two cases: with dew deposition and without dew deposition. Consequently, there were two different cases of model implementation: (a) an analytical solution to the system of equations without dew deposition and (b) an analytical solution to the system of equations with dew (or rime) deposition. Complete details of the solutions are provided in Appendixes D and E. Predictions of nocturnal minimum air temperature and soil temperature were outputs in this component.

6.3 Results

In this section, we presented an example of applying the model over the study site on 18 November 2016. The distribution maps of the surface albedo, ground heat flux and nocturnal minimum temperature forecast (main objective) on the night of 18-19 November was demonstrated. The satellite data and simulations of enhanced Micro-Met allowed us to produce the distribution maps of the net radiation and ground heat flux at a high-spatial resolution, with respect to topography and land cover.

6.3.1 Estimation of the surface albedo

The integration of Landsat and enhanced Micro-Met simulation data were used to produce the distribution albedo (%) map (Fig. 6.3). The enhanced Micro-Met model provided a distribution map of air temperature, dew point and air pressure. In this respect, Lennoxville constituted the reference station, while the AIRS satellite data was used to estimate the air temperature lapse rate. Before running the surface albedo model over the study site, the model was validated using correspondence *in situ* measurements. An automatic weather station, SIRENE (Université de Sherbrooke), measured the incoming and reflected shortwave radiation. The satellite derived albedos were compared to albedos derived from these radiation measurements for the time the satellite passed over the station area (10:30).

The satellite-derived pixels were averaged over a square of 3×3 pixels. The 21 Landsat images were taken during cloudless days in the spring (May) or autumn (September-October). The simulated albedos were compared to ground measurements at the SIRENE station for the time the satellite passed over the station area. MAE of 0.05% was found. RMSE of 0.64% and VAF of 71.02%. On

average, the satellite-derived albedos exceeded the measured surface albedo by 6%, with standard deviation of 0.66. This modeling approach was used to obtain map of surface albedo at 30 m resolution which used to estimate ground heat flux. Figure 6.3 shows an example of distributed map surface albedo over study site in November 2016. The map of albedo was used in vegetation-atmosphere model to produce map of net radiation and consequently nocturnal minimum air temperature.

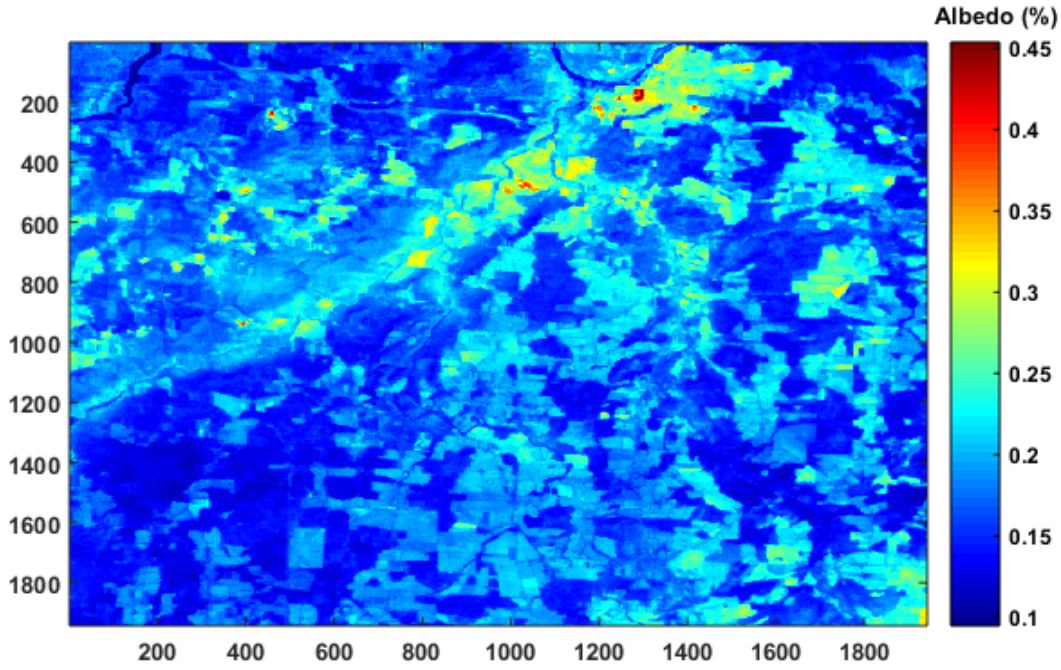

Figure 6.3 Distribution map of the surface albedo at a 30-m spatial resolution over the study site, using the data from the Landsat images and enhanced Micro-Met simulations (November 2016).

6.3.2 Estimation of the ground heat flux

The regional ground heat flux can not directly be estimated from satellite observations. It was calculated as an indirect variable through net radiation, and surface albedo values. First, net radiation was estimated using land surface radiation (Eq. 6.22). To this end, the satellite data, simulations of the Enhanced Micro-Met model and Lennoxville station were used. Figures 6.4 and 6.5 illustrate the net radiation and ground heat flux maps respectively derived on 18 November 2016, over the study site. Satellite remote sensing, weather station combined to simulations of the Enhanced Micro-Met model provide a potential to estimate the net radiation over the study site.

(a)

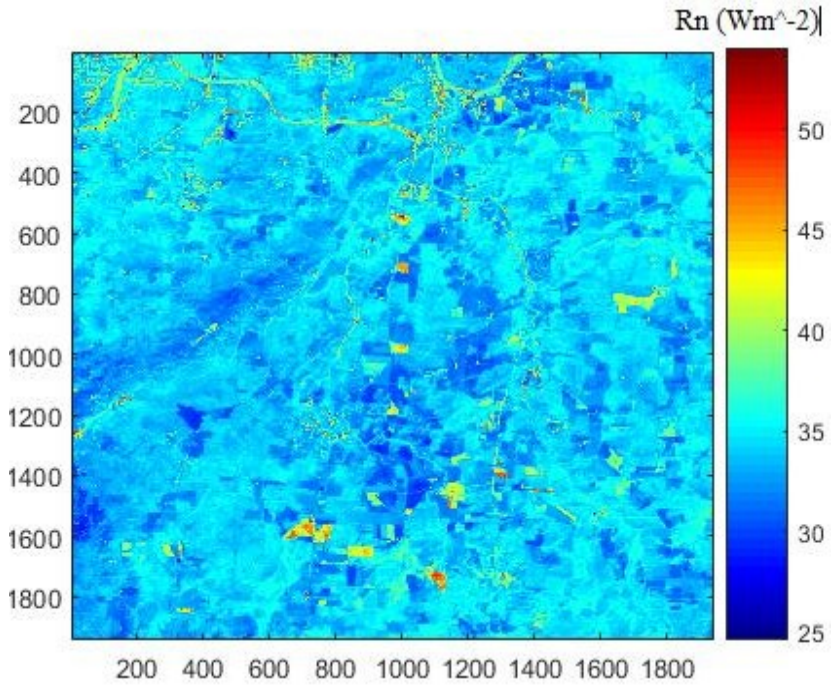

(b)

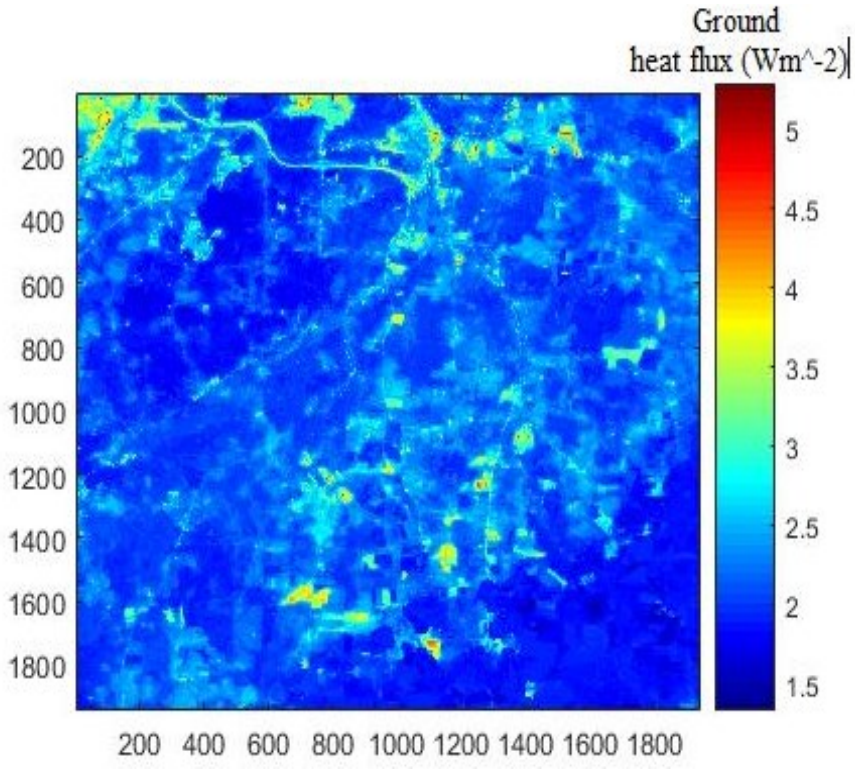

Figure 6.4 Fig. (a) Shows distribution map of the net radiation flux at 17h00, 18 November 2016; and (b) ground heat flux, at 17:00, 18 November 2016 over the study site.

6.3.3 Prediction of nocturnal minimum air temperatures

This section addressed the main objective of the study: prediction of nocturnal minimum air temperatures over the study site. The method used to modify the vegetation-atmosphere energy model incorporated the reference station, satellite data, and simulations of the enhanced Micro-Met model. The enhanced Micro-Met provided meteorological variables such as air temperature, air pressure, dew point, and effects of the shelterbelt on wind velocity at the sunset period with quantifications of cold air drainage on air temperature. The challenging question is how happened to cold air drainage during the night whether the cold air drainage flow all the night or not. Toward monitoring and verifying the dynamic process of cold air drainage, the time series temperatures at the top and bottom of the slope for two nights 27-28 and 29-30 May 2016 are presented in Figure 6.5. It should be noted that both nights were experienced the synoptic condition associated with radiation frost. The figure illustrated that after reaching the minimum temperature, the oscillation aspect of the cold air drainage flow was vanishing. This means that there was no cold air drainage flow between the top and the bottom of the slope once the minimum temperature had been reached. The effects of the accumulation of cold air lasted throughout the night until the air temperature reach at the maximum of minimum values. Therefore, the results suggest that cold air drainage model could be applied on the prediction minimum temperature. Therefore, the cold air drainage applied twice. The first time was at sunset to generate more accurate input data for the vegetation-atmosphere energy model. The second time, we applied it on the forecasting results of the vegetation-atmosphere energy model.

Figure 6.6 (a, b) show examples of the minimum temperature prediction over the study site (night of 18-19 November 2016). Figure 6.6 (a) show the result of vegetation-atmosphere model while figure 6.6 (b) shows the results after applying the cold air derange sub-model on Figure 6.6 (a), we employed the cold air drainage sub-model just for closed valleys.

From these findings, we implemented the cold air drainage model onto the results of the prediction model using predicted minimum air and soil temperatures. The statistical test showed an improvement in the prediction value. The improved test show RMSE = 1.34 (˚C) and MAE = 1.01 (˚C). Using the minimum air and soil temperatures predicted by the vegetation-atmosphere energy model, we employed the cold air drainage model to obtain results only for valleys. The new results indicated better prediction values for these areas (Fig. 6.6, b).

(a)

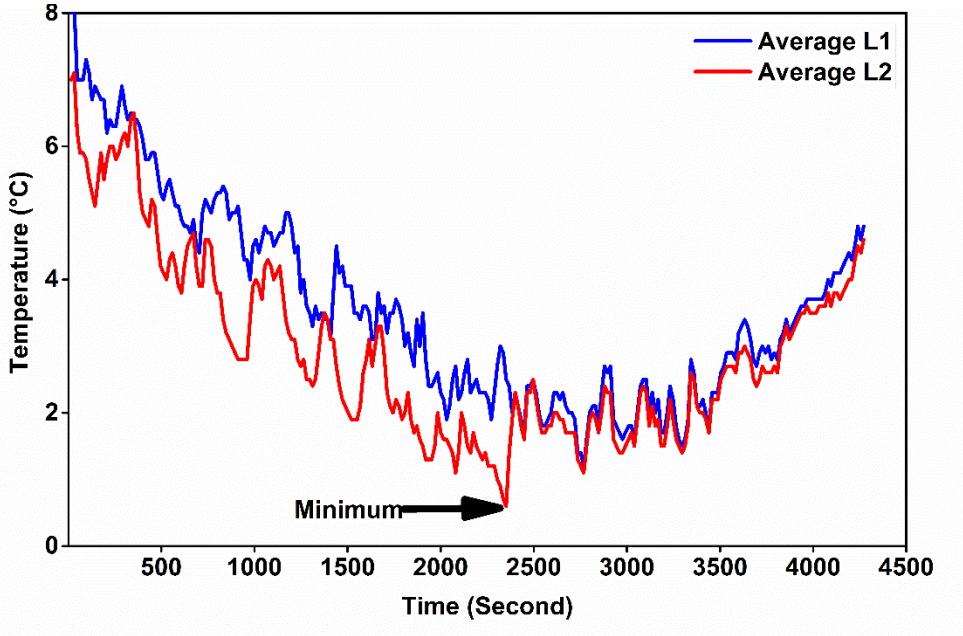

(b)

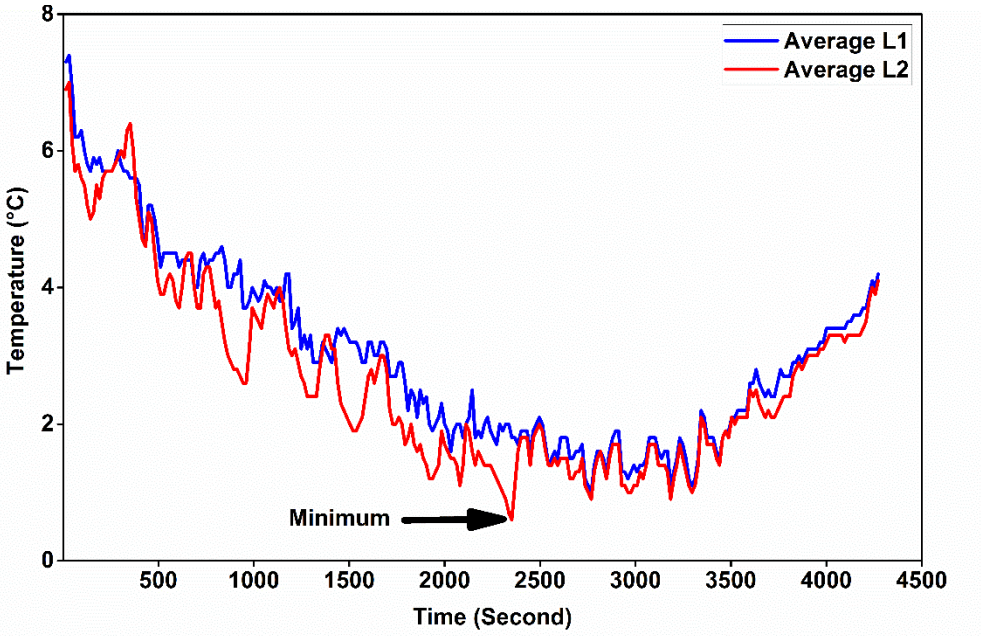

Figure 6.5 Time series of air temperatures recorded with an infrared camera on upper (L1) and bottom slope (L2) on 27-28 May 2016 (a) and 29-30 May 2016 (b). These figures show there were no periodic oscillations subsequent to minimum temperature point.

(a)

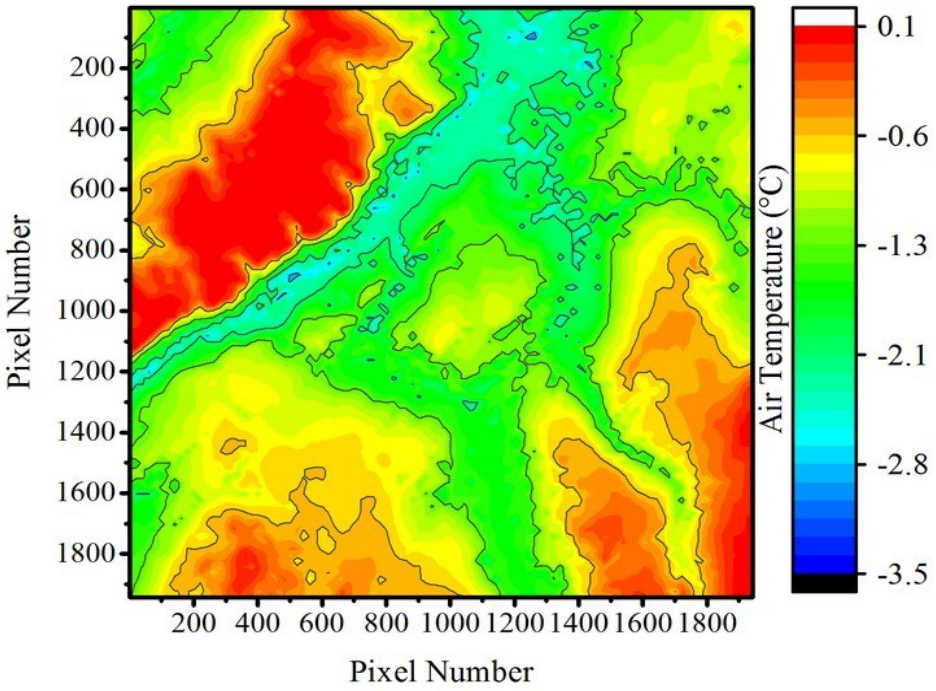

(b)

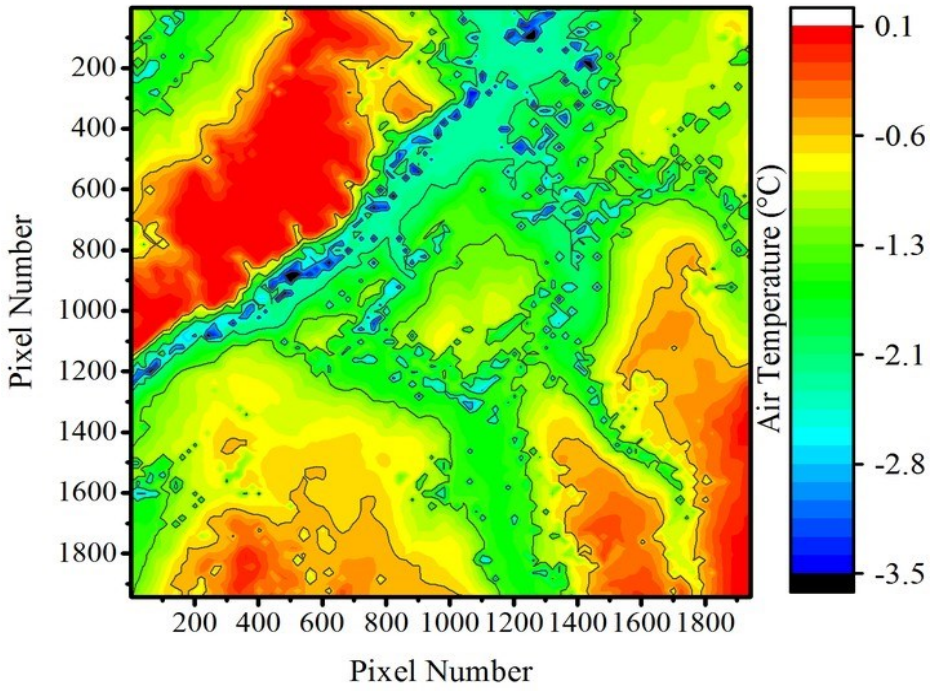

Figure 6.6 (a) Spatial distribution of the prediction of nocturnal minimum temperature (°C) over the study site (November 18-19, 2016). (b) Spatial distribution over after appling cold air drainage model on prediction map.

6.3.4 Performance of the model

The minimum temperatures predicted by the vegetation-atmosphere energy model were compared to the data collected on the study site. Measurements were taken on five topographic sectors to assess the vegetation-atmosphere prediction result on closed valleys, different parts of slopes , flat areas, areas close to the forest (between 2 and 4 times the heights of the trees), ridges, different parts of slopes.

For the closed valley, there are two categories, the assessment based on vegetation-atmosphere model (before using sub-model), and assessment based on applying cold air drainage sub-model on result of vegetation-atmosphere model (after using sub- model). The results before applying cold air drainage model show overestimation of the minimum temperature in comparison with the measured values (RMSE =1.45, MAE = 1.14, SEE = 0.76). However, the statistical test showed an improvement in the prediction value after applying the sub-model. (RMSE =1.04, MAE =0.75, SEE = 0.92). Concerning flat areas, measurements were conducted in areas far from the forest. In comparison with other areas, we observed better results (RMSE = 0.44, MAE = 0.40, SEE =0.43). This could be explained by the minimum topographic effects on air-cooling in these areas, such as the advection effect caused by winds and no accumulation of cold air. With respect to slopes, the measurements were performed far from the forest. We selected different parts of slopes: upper, middle, and bottom. The prediction results indicated higher air temperatures in comparison with measurements (RMSE = 0.93, MAE = 0.73, SEE = 0.62). This could be justified by the thermal belt formation on the slopes, which was not discussed during the process for the enhancement of the Micro-Met system. The error observed for ridges was higher than flat areas and slopes (RMSE = 1.03, MAE = 0.88, SEE = 0.85). This may be due to the effect of wind advection over ridges where there was no shelterbelt, cold air drainage, or stagnation of cold air. As for areas close to the forest, the prediction of minimum temperatures showed an overestimation (RMSE = 0.58, MAE = 0.53, SEE = 0.58). It should be noted that the enhanced Micro-Met could not calculate the effects of the forest shelterbelt on temperatures. The shelterbelt model estimated only the effects of the shelterbelt on wind velocity.

Table 6.1 Performance test for forecasting minimum air temperatures based on different aspects.

Test \ Location	Valley		Flat	Close to forest	Ridge	Slope
	Applying drainage model on Mcro-Met	Appling drainage model on result of vegatation-atmosphere model				
RMSE (˚C)	1.45	1.04	0.44	0.58	1.03	0.93
MAE (˚C)	1.14	0.75	0.40	0.53	0.88	0.73
SEE (˚C)	0.76	0.92	0.43	0.58	0.85	0.62

6.4 Discussion and conclusion

In this study, the two-layer model developed by Shuttleworth and Wallace (1985), and Shuttleworth and Gurney (1990), was used to predict nocturnal minimum temperature. This model presented an advantage: it did not deal with the rather complex resolution of the non-steady-state regime that most of the physical models to solve numerically or analytically. The model was based on a static representation of the vegetation-atmosphere system, which reflects nocturnal minimum temperatures. Using two models: enhancement Micro-Met and vegetation-atmospheric model allow to predict nocturnal minimum temperature over the study site. The performance test for forecasting minimum air temperatures indicated agreement with *in-situ* measurement values**.** Measurements were taken on five topographic sectors to assess the improved modeled prediction and led to error assessment on closed valleys different parts of slopes ridges, flat areas and areas close to the forest.

It should be noted that there were no generally acceptable methodologies to compare spatial distributed models with point-based models. Therefore, we could not compare our results with those presented by Lhomme and Guilioni (2004) and Lyons *et al.* (2009). In comparison with mentioned studies there were four improvements. First, we included a cold air drainage model, an effect that had not been taken into account by vegetation-atmosphere energy models (Whiteman, 2007). Second, we introduced the shelterbelt effect on wind velocity for better accuracy with regard to prone areas. Third, since one of the problems with this kind of prediction model referred to downward longwave radiation (Lhomme and Guilioni, 2004; Lyons *et al.*, 2009), a locally adjusted equation was derived, evaluated, and integrated into the vegetation-atmosphere model. Finally, we developed an equation for short-term forecasting of soil temperature instead of using a mean nocturnal value of soil temperature from the previous night.

One of the key challenges in using the vegetation-atmosphere model was the limited availability of spatial-temporal input data. Moreover, model inputs and parameters had to be routinely available at various times close to the local sunset period. This was difficult to achieve at our study site for two reasons: the need for characterisation of soil and land surface properties on a local scale, and the limited availability of accurate spatial measurements. To extend the vegetation-atmosphere energy model across the study site required the extrapolation of various meteorological variables. To overcome these problems, we proposed a methodology based on a high-resolution distribution meteorological model (Enhanced Micro-Met), remote sensing satellite data, and a meteorological station (Lennoxville). Providing soil temperature near the sunset period constituted yet another challenge. However, the use of this model to predict minimum temperatures with input near the sunset period was necessary. To meet this requirement, we developed an equation using the MODIS data and ran a simulation of the enhanced Micro-Met (chapter 5).

High-resolution thermal imagery was used to characterize flow dynamic of cold air drainage. A new method to visualize and estimate cold air drainage was developed. Results from this method indicated that there was no cold air drainage flow between the top and the bottom of the slope once the minimum temperature had been reached. From these findings, we implemented the cold air drainage model for the second time onto the results of the forecasting model using predicted minimum air and soil temperatures. The statistical tests showed an improvement in the forecasting values over the valleys incomparison before applying cold air drainage model for the second time (RMSE = 0.41, MAE = 0.39, SEE = 0.16).

The amount of different variables regarding the estimation of the ground heat flux over the study site posed a challenge. On the one hand, most techniques used for measuring provided point estimates. In addition to local topography, land cover influences the response of the surface to the energy flux. Any variation in albedo can lead to differences in surface temperature by affecting the reflection of solar radiation away from the land surface and therefore, contributing to atmospheric heating or cooling. The values for albedo were typical daily average values. Moreover, it was important to recognize that the reflection coefficient for solar radiation could change from place to place, even if the vegetation cover was the same (Shuttleworth, 2012). For example, using typical surface albedo values for a variety of ground surfaces caused an underestimation of minimum temperatures after modifying the vegetation-atmosphere energy model. The results indicated that derived satellite values of the surface albedo and emissivity increased the accuracy with regard to the

prediction of minimum air temperatures. This agreed with previous results produced by Wollenweber (1995) who indicated that the albedo could have an important impact on energy fluxes. An accurate calculation of the net radiation and ground heat flux required ascertaining the surface albedo of the study site. Any error in albedo propagated through the retrieved algorithm of the vegetation-atmosphere energy model could affect the final estimation of minimum temperatures. This demonstrates that the vegetation-atmosphere energy model that was based on the energy transfer needed an accurate albedo at specific times in the year, constituting an important input.

In conclusion, the integration of remote sensing, the data from the Lennoxville station, and the enhancement of the Micro-Met model enabled us to estimate the energy fluxes on a daily basis during the sunset period and consequently, to predict minimum air temperatures. The use of various data sources improved the representation of the energy fluxes associated with heterogeneous surfaces related to the study area, as well as the transfer of the point-based vegetation-atmosphere energy model into a more practical grid-based model.

7. Improvement of the method for the effectiveness of frost protection

7.1 Introduction

Cost effective frost protection is important in many fruit growing areas to increase the production despite climate fluctuations and extremes. The fruit producer may avoid using low elevation land areas with high frost risks, but which might otherwise be suitable for example for grapevines. However, grapevines are grown in areas in which a degree of frost risk is accepted, but may require large investments in frost prevention and protection measures (Wilson, 2001).

To prevent or reduce frost damage, an expansive range of passive and active methods such as heaters, wind machines, sprinkling irrigation, and unmanned helicopters were developed. Orchard heaters and wind machines constitute major disadvantages such as high costs and pollution. Irrigation systems involve greater risks of not protecting from frost damage (Ghaemi *et al*., 2009).

Passive methods under severe frost conditions are often inadequate to protect crops. Although, different protection methods may reduce frost damages, their applications and the influence of the microclimate on their efficiency are not well known and documented (Battany, 2012). There are no perfect solutions against the frost in the agricultural field, as the problem is much more complex than it may appear.

Different active protection methods may reduce frost damages, but their applications may complicate. Adopting frost protection measures incorrectly at the wrong time or under inappropriate conditions may be more damaging than doing nothing at all (Snyder and Melo-Abreu, 2005). The selective inverted sink (SIS) system, also known as the towerless wind machine or upward-blowing wind machine, constitutes a new active frost protection system (Fig. 7.1).

The SIS system has been increasingly adopted worldwide due to its low investment costs. The operational noise level is much lower than conventional wind machines and helicopters. Several countries such as the USA and Canada currently use it. The SIS system requires less power and consumes less fuel per hour. It is portable, easy to maintain, and does not need permanent installations. It was designed to modify the inversion layer by draining the coldest air, expelling it upwards to the higher and warmer strata where it is dispersed (Hu *et al*., 2018).

Based on a literature review, we found some paradoxal analyses with regard to the efficiency of the SIS system. For example, Splenger (2015) indicated that the SIS system pulls cool air from the ground in the areas most prone to frost and directs it upward more than one kilometer. However,

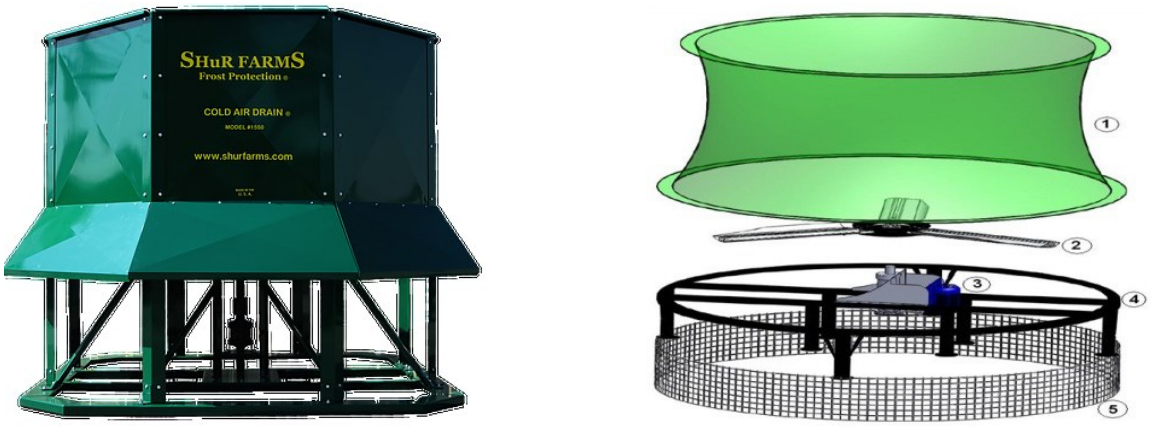

Figure 7.1 Left: selective inverse sink (SIS) system or upward-blowing wind machine. Right: Parts of upward-blowing wind machine; 1.Fan chimney, 2.Fan kit, 3.engine, 4.construction 5.Protection cage (taken from Vardar and Taskin, 2014).

Battany (2012) demonstrated that with the use of the smoke tracking method, the air reached a 25-m height and then tended to slowly settledown. Vardar and Taskin (2014) performed an experiment in a peach orchard, showing that the temperature difference between the two points of lower and higher elevation areas was reduced when the SIS system was operating in the orchard. However, there was no information about the meteorological conditions during the onset of the SIS system. Their analysis did not compare the air temperature gradients for the rest of the night while the SIS system was inactive.

Yazdanpanah and Stigter (2010) used the SIS system in an almond orchard. An increase in temperature (0.5 to 2.8°C) due to the SIS system operation system was reported. However, the analysis did not compare the air temperature patterns for nights when the wind machine was not used (Battany, 2012). In addition, as the SIS system itself does not generate heat, there was no discussion about the reason for this 2°C increase in the almond orchard.

It should be noted that the interactions of the SIS system with some topoclimate effects such as cold air drainage and inversion strength were not well stated. Using an SIS system was not proven to be as effective or decrease the damage. The quantitative relationships of the protection level and the location of the SIS system remain unknown. The SIS system was recently used in the Eastern Townships farms and in our study site. It was questioned whether or not this method of protection was appropriate and cost effective for this region (MAPAQ, 2013).

Its potential in our study site had been uncertain due to lack of meteorological assessment. Consequently, this study had two distinct but interrelated main objectives. First, we aimed to validate

the capability of the SIS against radiation frost during different micro-topographic conditions. We hypothesized that the high-resolution network provided more accurate and valuable spatial pattern of the minimum air temperature.

The second objective was to propose and test a new low cost, effective and environmentally acceptable frost protection method. We presumed that air temperature was not an appropriate indicator of heat content and that applying the protection method based on air temperature was not sufficient. We supported the application of moist entropy which combined both air temperature, humidity and depicted heat content. However, the application of frost protection methods and the influence of the microclimate are not well documented (Battany, 2012).

7.2 Methodology

The methodology was divided in two modules. The first module focused on first objective: SIS evaluation, while the second oriented to the second objective: presenting a new active method against frost. The measurements introduced in the first module were obtained through meteorological field campaigns. The experiments were carried out in an orchard (Cidrerie Verger Ferland) and a commercial wine vineyard (Le Domaine Bergeville). In both orchards, the farmers observed frost damage. Nocturnal temperature variations were analysed with the data of a 20 and 50-meter network that encompassed 53 and 30 data loggers respectively (Fig. 7.2 and Fig. 7.3). The air temperature was recorded with a frequency of ten and thirty minutes in a synchronous mode of operation. The diameter of the SIS system was 2.39 m. The SIS system worked at a 540-rpm speed. The measurements presented in this paper were obtained during meteorological field campaigns in the study site in autumn 2014 and 2015.

In the second module, we presented, installed and tested a new active method that was combined the SIS system and a warm water reservoir to elucidate the second objective. The new method was proposed to use the “forced convection”. Forced convection was provided by an external force generated by SIS system when it is operating (with 540 rpm speed). The system used this force to transfer a maximum of water vapor into the air in order to decrease the air dryness (Fig.7.4). In this method we considered the thermodynamic transformations of water vapor during moist convection and derived the corresponding changes of entropy presented. The theoretical framework of thermodynamics of this innovation method was based on the moist entropy and steam cycle presented by Pauluis (2010).

Figure 7.2 Left: Field measurement area of an orchard (Cidrerie Verger Ferland). Right: Observational network where black points represent the locations of the 53 data loggers to measure air temperature.

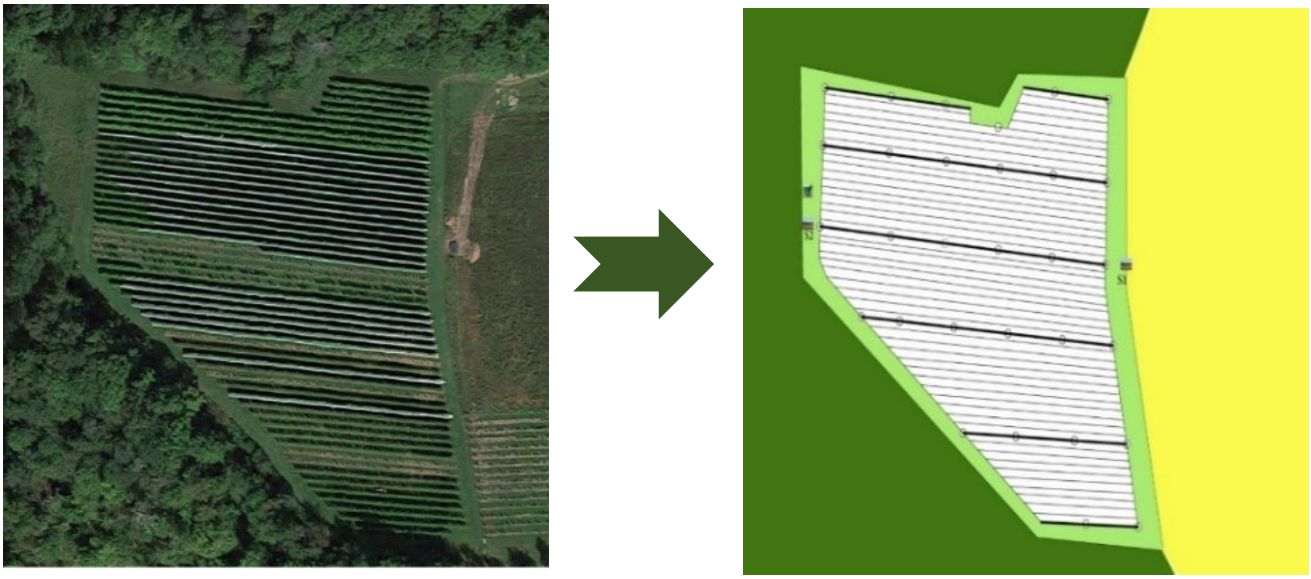

Figure 7.3 Left: Field measurement area of vineyard (Le Domaine Bergeville) situated in study site. Right: observational network where circles represent the locations of the 30 data loggers to measure air temperature.

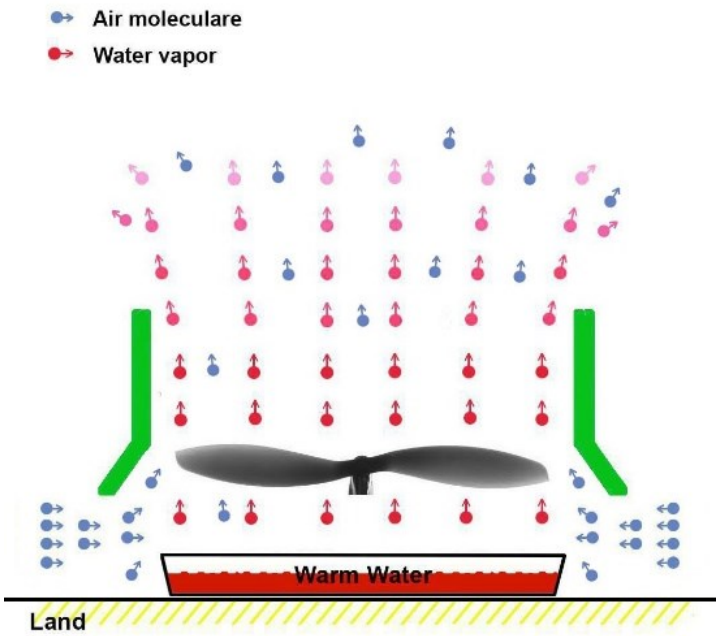

Figure 7.4 Schematic representation of forced convection provided by combined SIS system (worked at a 540-rpm speed). The red color show hot water reservoir.

7.2.1 Theoretical framework

Internal energy, enthalpy and entropy are the key factor to study thermodynamic properties of the moist atmosphere, because they correspond to the first (internal energy and enthalpy) and second (entropy) laws of thermodynamics. Clausius' formulation of the second law can be written as:

$$\Delta S = \frac{Q}{T} + \Delta S_m \qquad 7.1$$

where ΔS (J/K) is the entropy change associated with a physical transformation, Q is the external heating, and T is the temperature of the system and ΔS_m is irreversible entropy production. Entropy arises directly from the Carnot cycle. During a thermodynamic process, the temperature T of an object changes as heat Q is applied or extracted. A more correct definition of the entropy S is the differential form that accounts for this variation. For heating or cooling of any system (gas, liquid or solid) at constant pressure from an initial temperature T_0 to a final temperature T, the entropy change is

$$\Delta S = nC_p ln\frac{T}{T_0} \qquad 7.2$$

where n provided that the constant-pressure molar heat capacity (or specific heat) C_P is constant and that no phase transition occurs in this temperature interval.

The second law of thermodynamics does not deal with the equation for the entropy budget quantitatively. In fact, the equation for moist entropy is another form of the energy equation (or the first law of thermodynamics plus the empirical formulas for down gradient transport phenomena). In this direction, the energy equation is rewritten with moist entropy in the place of temperature, yielding to an equation for moist entropy.

Moist entropy represents only the contribution from moist air that consists of dry air, water vapor. The entropy per unit mass of moist air is defined by

$$S = (1 - q_t)\left(C_{pd} lnT - R_d lnp_d\right) + q_t C_l lnT + \frac{q_v L_v}{T} - q_v R_v lnH \qquad 7.3$$

In this expression q_t is mixing ratio, for water vapor, C_{pd} is the specific heat at constant pressure of dry air, C_l is the specific heat of liquid water, T is the temperature, q_v is the specific humidity, L_v is latent heat of vaporization, $R_d \, and \, R_v$ are the gas constants of dry air and water vapor, pd is the partial pressure of dry air, and H is the relative humidity. The new method is based on thermodynamic cycle, the steam cycle, presented by Pauluis (2010).

A steam cycle generates mechanical work by transporting water vapor from warm moist source to dry cold sink and arise air entropy. Thermodynamic system is composed of the steam engine and two reservoirs that act as the warm source and cold sink for the cycle (Fig.7.5). Using warm water allows us to treat the exchange of water vapor as internal processes and to take into account the internal entropy production by diffusion.

The warm reservoir contains liquid water at T_{in} partial pressure of water vapor e_{in}, and the cold reservoir contains air at T_{out} and partial pressure of water vapor e_{up}. A mass of water vapor Δr_T evaporates adiabatically in the warm reservoir and then is injected during the moistening stage of the steam cycle. The cycle expands moist air to T_{out} and water vapor is then diffused from the cycle to the cold reservoir. Therefore, water vapor is transferred from the warm source to the cold sink.

The change in entropy (J/K) is the inverse of the temperature integrated over the change in heat transfer. For heating or cooling of any system (gas, liquid or solid) at constant pressure from an initial temperature T_0 to a final temperature T_f, the entropy changes. This behavior is directly related to the fact that the convective heat transport is mostly due to the latent heat transport (Pauluis and Held, 2002).

To conclude, the methodology was based on a thermodynamic steam cycle. The steam cycle is a heat engine that transports latent heat energy from a warm source associated with the evaporation

of water to a dryer area. We can state that a steam cycle transports water vapor from a moist source to a dry sink.

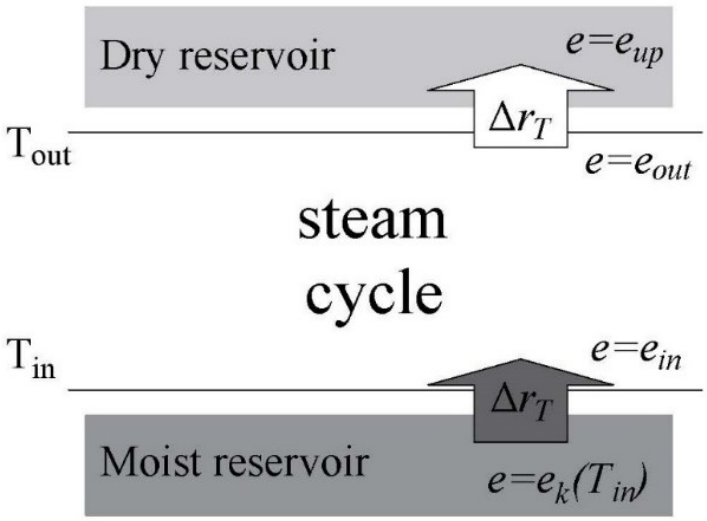

Figure 7.5 Schematic representation of thermodynamic system. A given amount of water vapor transfer Δr_T from moist reservoir to steam cycle temperature at warm temperature Tin .The cycle then carries this water vapor to a lower temperature Tout where it is diffused into dry reservoir (from Pauluis (2011)).

7.2.2 Implementation process

We installed a reservoir under the SIS system and a water tank and to prepare heated water to 25˚C (Fig.7.6). Two tethered balloon probes were used for observation during the test. One of the balloons was close to the new method locations (called SIS point) and another was 35 m far from test point (called reference point). The probe consisted of a temperature-humidity sensor. Temperature and dew point were monitored at 18 m above the ground.

The experiment was conducted during night of May 13-14 May 2015. The moist entropy (at 18 m) calculated and presented for Reference point and SIS point during periods when the SIS system is operating. The aim of this module was to calculate and compare the moist entropy at two different points using observational data and Equation 7.1.

Figure 7.6 Selective inverted sink (SIS) system and water warm tank.

7.3 Results

7.3.1 Observational evidence of the effects of the SIS system on air temperature

The spatial-temporal influence of the SIS system on air temperature was evaluated by deriving isothermal map of temperature distribution before, during, and after the operation of the SIS system. Figure 7.6 illustrates the temperature patterns during the frost night. The SIS system was started at 21:06; however, after 60 minutes, more precisely at 22:06, there was no effective evidence. The development of lower temperature was observed. In addition, the SIS system was tested at the centre of the orchard, but the results were not better than the others.

Figures 7.7 and 7.8 illustrate the temperature patterns during the SIS test for two different locations on a vineyard (night of 28-29 October 2013 and night of 16-17 November 2013). In the figures, the SIS system sign shows the location of the SIS system and the strikethrough sign indicates “no SIS system operating”. Finally, the normal sign means “SIS system operating”. Visual examination of isothermal maps did not indicate any evidence of an SIS system effect.

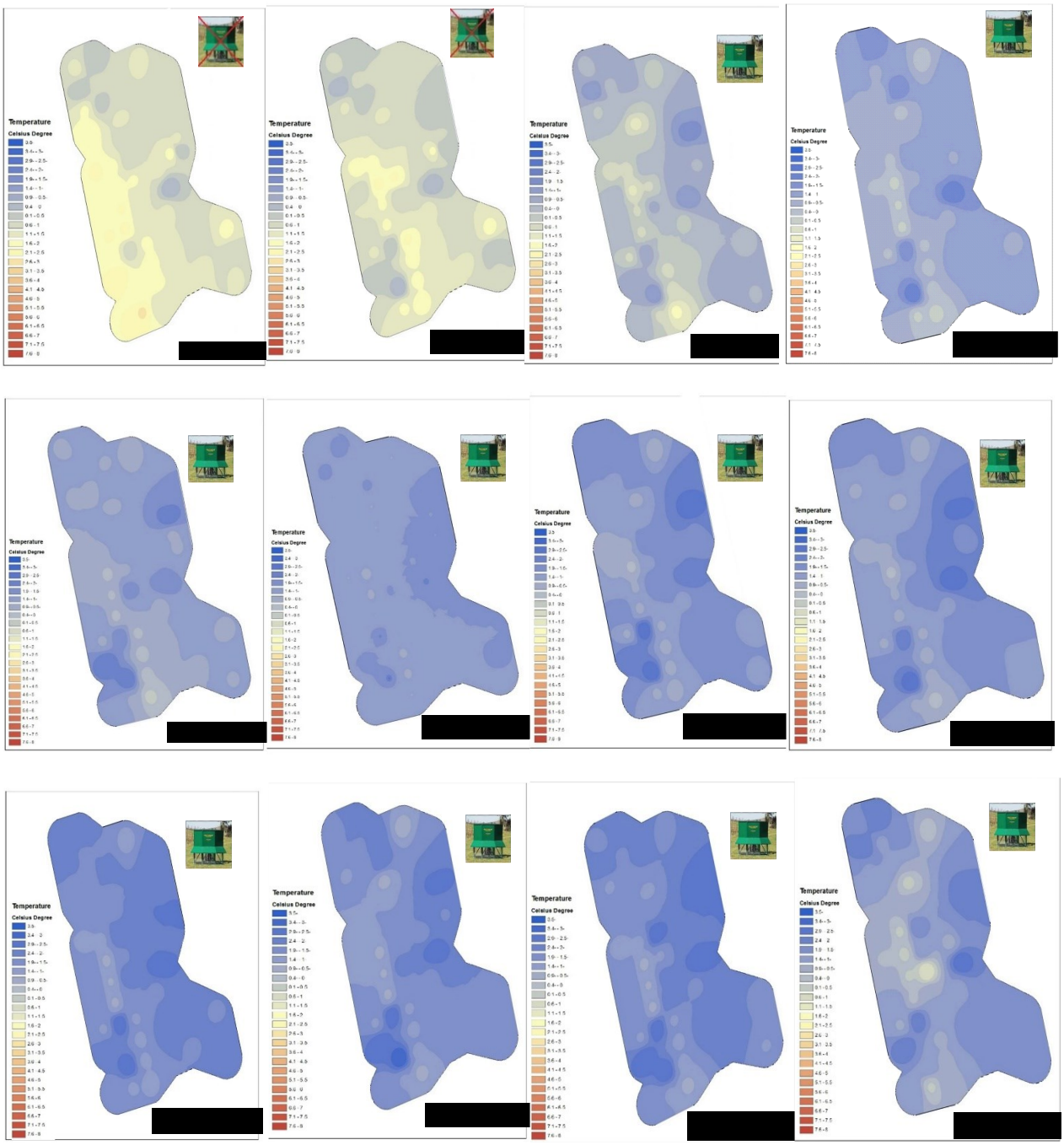

Figure 7.7 Air temperature patterns during the night of 29-30 September 2014 (Cidrerie Verger Ferland). The SIS system sign shows the location of the SIS system; strikethrough sign means “no SIS system operating” and normal sign means “SIS system operating”.

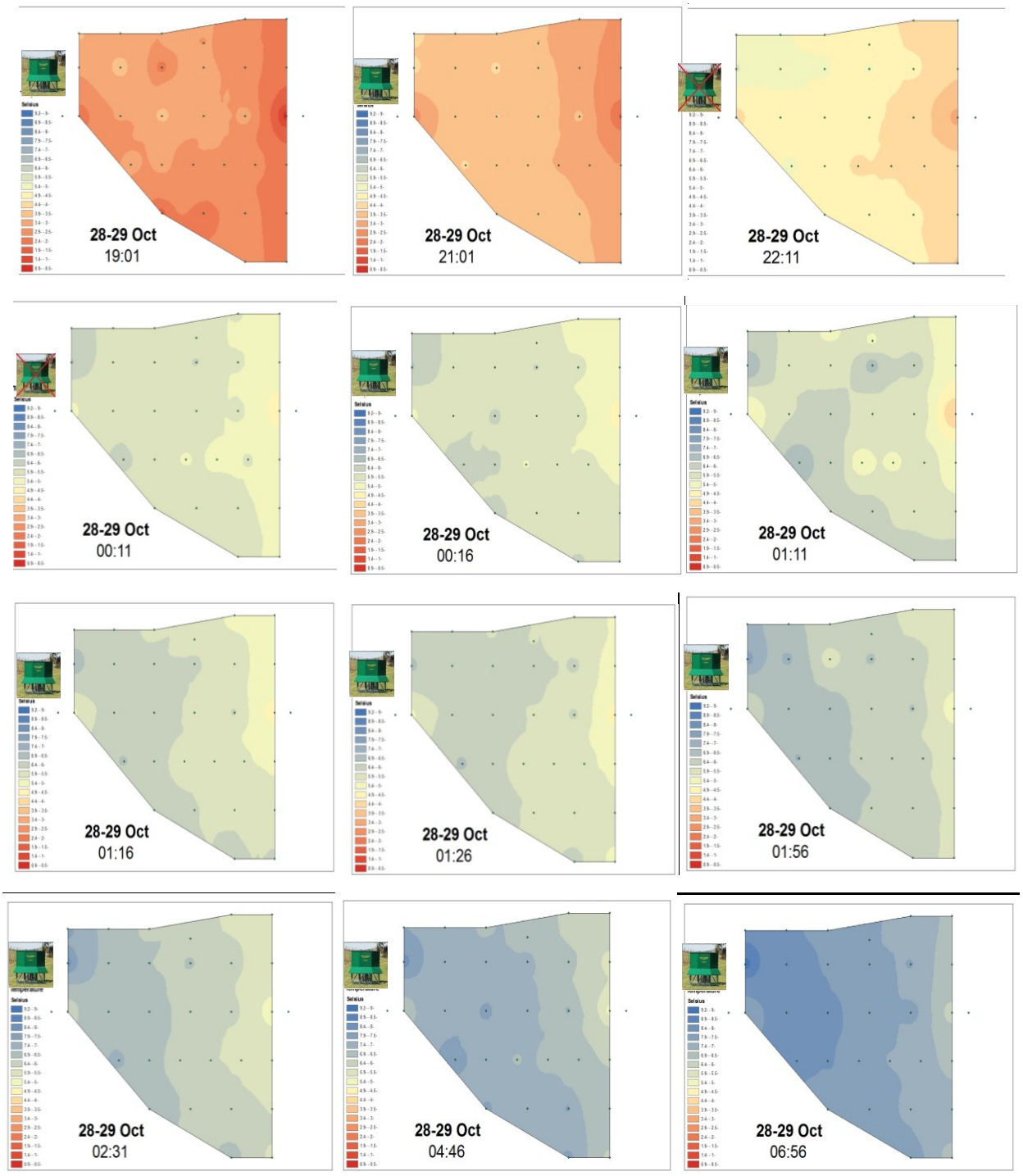

Figure 7.8 Air temperature pattern during SIS applying night of 28-29 October 2013 (Le Domaine Bergeville). SIS sign show location of SIS; strikethrough sign means 'no SIS operating' and normal sign means 'SIS operates.

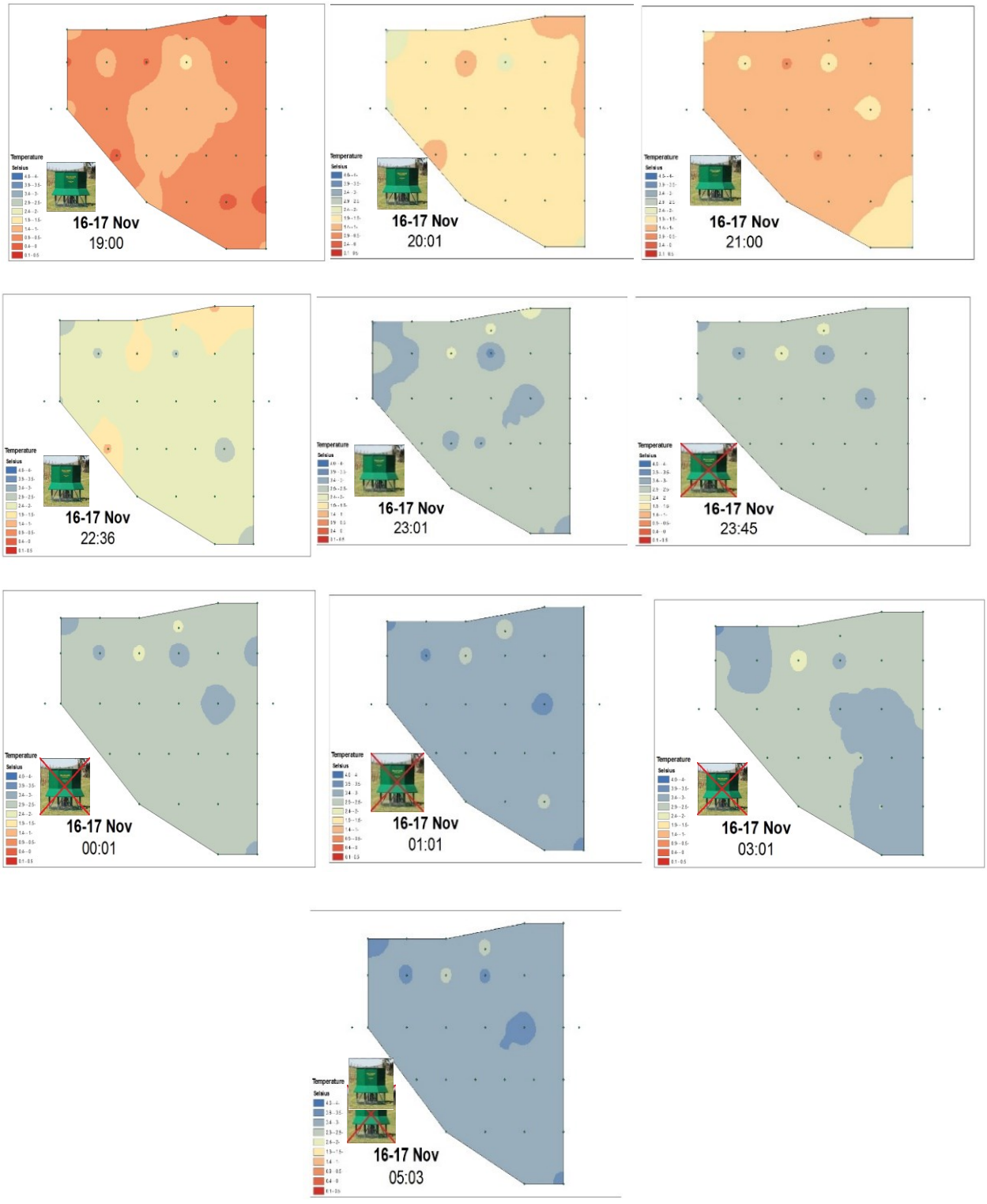

Figure 7.9 Air temperature patterns during the night of 16-17 November 2013 (Le Domaine Bergeville). The SIS system sign shows the location of the SIS system; strikethrough sign means "no SIS system operating" and normal sign means "SIS system operating".

7.3.2 Results for the implementation of the new method

We performed a test using a hot water reservoir and the SIS system. On the one hand, we observed that the area where the SIS was installed, an area prone to frost, was not affected. On the other hand, frost phenomenon occurred over the reference area. A comparison between air temperature, specific humidity, and entropy at the Reference point and Test point at 18 m and 2 m are presented (Fig.7.9).

The air temperature close to the test point (where the SIS was installed) was higher than that at the reference point (e.g. 02:15). The air temperature at the reference point was 0˚C, while at the Test point it was 4.5˚C with higher specific humidity and entropy. The moist entropy calculated at an 18-m altitude was higher above the Test point in comparison with the Reference point, indicating that the contribution of moisture to the magnitude of entropy was greater around the Test point.

7.4 Discussion and conclusion

The utility assessment of the SIS system was done under different microclimate conditions. The key challenge in this field was to determine to which extent the temperature had changed when SIS system and comparing it to the location without one. To overcome this problem, we used high-resolution monitoring grid points. Increasing the resolution when necessary to inspect the role of the SIS on temperature. The results of the experimental study did not provide conclusive observational evidence that the SIS had impartial efficiency on nocturnal cooling. Operating the SIS had no noticeable effect in increasing air temperature. On the one hand, this result was in agreement with Battany (2012) who indicated that the SIS had no net effect on air temperature. On the other hand, it contradicted Domoto (2006), Hokmabady *et al*. (2007), Yazdanpanah and Stigter (2011) who found an increase in air temperature due to the operation of the SIS system.

The fact that there is little academic published research in this field constituted a limitation. Only a few articles related to the performance evaluation of the SIS or other protection methods were published. Most reports by companies look into the SIS (e.g. SHuR FARMS Frost Protection), but the academic results were based on the single point data recorded (e.g. Yazdanpanah and Stigter, 2011; Vardar and Taskin, 2014). In our research, the spatial-temporal influence of wind machines on air temperatures was evaluated using high-resolution isotherm maps. This set-up enabled us to cover small scale variations associated with the air-cooling process and air disturbance, which were produced during the SIS system operation.

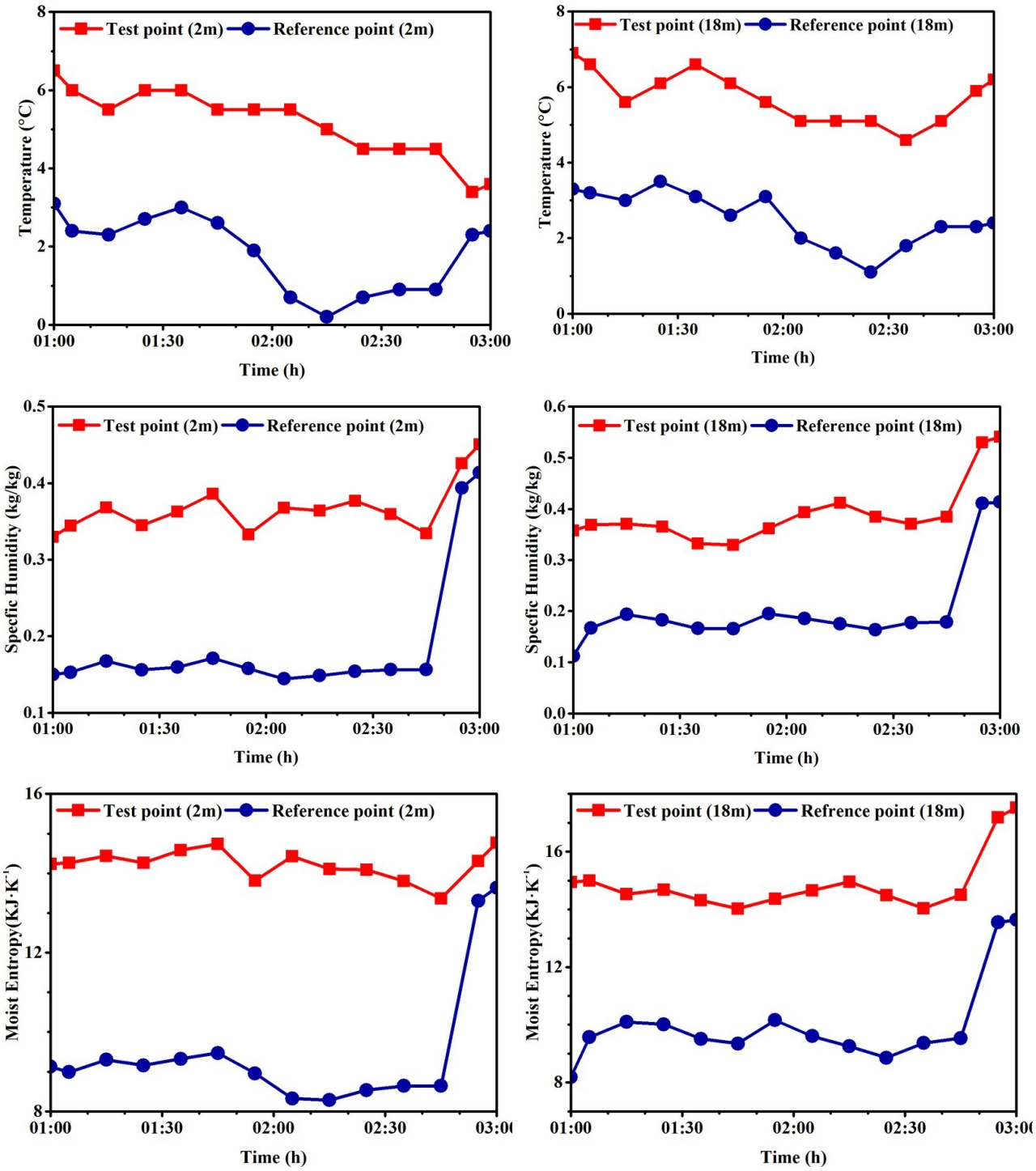

Figure 7.10 Air temperature, specific humidity and moist entropy at 2m and 18m for two points: Reference point and Test point (14 May 2015) Cidrerie Verger Ferland.

The differences between the present study and previous ones in this field were the following:

- We assessed the effects of the SIS system using a high-resolution gridded temperature data set;
- We tested the SIS system in different topographic locations;
- We started the SIS system at different times (e.g. before sunset, after sunset, before inversion formation, after inversion formation, etc.). Considering these conditions, we measured the nocturnal cooling rate during selected frost nights according to cloudiness and wind speed.

To explain why the SIS system was not efficient, we tried to derive the airflow it produced. An observation experience of the SIS system airflow patterns was conducted in the orchard. Using smoke during the SIS operation showed that a minor part of its exhausted flux came from the horizontal direction. It might be due to the roughness of the land surface. In contrast, a major part of the flux came from the upper layer around the SIS system, which behaved like a funnel (Fig.7.10). The measurements with a portable anemometer showed that the wind speed in the funnel direction (23 ms^{-1}) was approximately 4 times greater than the wind speed in the horizontal direction (6 ms^{-1}). These findings explained the fact that the SIS system was unable to remove a sufficient amount of cold air or stagnant air, while a very small volume of cold air accumulated on the depression or sink area could move.

.

Figure 7.11 Derivation of the airflow produced by the SIS system. The figure show that a minor part of the SIS system exhausted flux was from horizontal direction (small horizon sign) and major part of the flux was from the upper layer around the SIS system, which behaves like a funnel (ground sign).

The purpose of the second objective was to introduce and implement a new frost protection method. A combined SIS system warm water operated like a heat engine that transport heat from warm source associated with evaporation of water to a colder energy sink. The most common method against the frost which focuses on air temperature. Instead, the proposed method is based on the physical principles of moist entropy, which combined both air temperature and humidity and depicted heat content. Indeed, instead of air temperature increasing we oriented toward heat energy increasing. The result show that the area where we increased the energy, an area prone to frost, was not affected.

The results of implementation the proposed method during frost condition shows an increasing of specific humidity, moist entropy and air temperature compared with the other point. The temperature difference between two points was in the range between 1 and 3.5 ˚C. Furtheremore, the results indicate that with increasing moist entropy, air temperature variation was decreased. This new environmentally friendly method has the potential to provide a useful alternative to several frost protection methods such as heaters and fires.

This study highlighted the importance of high-resolution measurements in the agrometeorological field. Using high-resolution climatic research keys helped us to understand the microclimates and improve the frost protection systems. Fine resolution is needed to fully represent the farm prone area and evaluation site.

8. Conclusion

Forecasting the high-spatial resolution of air temperature in complex terrains represents an important scientific challenge. Understanding the spatial extent and timing of frost is important for horticulture, and viticulture due to the potential for crop damage. Since crops are sensitive to low temperatures during the growing season, the minimum temperature constitutes a key meteorological variable that is helpful to predict frost. This study presents two models based on a vegetation-atmosphere energy framework and a meteorological distribution system for high-resolution terrestrial modeling (Micro-Met). The spatial distribution of the nocturnal minimum temperature in an agricultural area was estimated using a combination of two models.

This last chapter is divided into three sections. The first section is dedicated to the achievement of research objectives and innovative contributions. The second section focuses on results. The last section highlights the implications of the research and areas of future work based on the findings.

8.1 Achievement of research objectives and innovative contributions

The aim of this study was to propose scientific advances in two strategic areas related to the mitigation of frost damage: first, improving the prediction capability of local frost with a numerical model adapted to forecast minimum temperatures and second, assessing the performance of an active protection method and proposing a new one. To achieve the main objectives, three specific objectives were accomplished:

1. To develop a method that extrapolates soil temperature at sunset;
2. To enhance the capabilities of a meteorological spatial distribution model (Micro-Met) on four sub-models: (i) quantifying the effects of cold air drainage on air temperature, (ii) quantifying the forest shelter effect on wind speed, (iii) estimating the local air temperature lapse rate on a daily basis, and (iv) modifying a downward longwave equation under clear sky condition;
3. To assess an active method against radiation frost and propose a new system to reduce frost damage.

The first specific objective was achieved by conducting multiyear measurements. Their purpose was to create a database in order to develop a method to estimate soil temperatures close to sunset. The vegetation-atmosphere energy model required the surface temperature at sunset, but this information was unavailable from neither the Lennoxville meteorological station nor the MODIS

satellite data, which only provided this value at 13h30. Using a stepwise regression model, enhanced Micro-Met, and the data from the satellite MODIS collected at 13h30 enabled us to develop a method to calculate the soil temperature at this time. The use of multiple stations in different topographic aspects, such as valleys, slopes, and ridges offered an advantage. Since the soil temperature variation depended on climate conditions, this methodology allowed us to perform a more detailed microclimate condition and establish an equation between soil temperature and other atmospheric variables: air temperature and dew point. Although most research focused on monthly or daily mean values of soil temperature, not prioritizing the time of input data, our model concentrated on short-term (hourly) forecasting for a specific area.

The second specific objective to enhance the capabilities of a meteorological spatial distribution model (Micro-Met) included four considerations. The first was to estimate the air temperature lapse rate instead of using fixed values provided by the current version of Micro-Met. The lapse rate is a critical variable to find the variations of air temperature, especially in mountainous areas. The daily lapse rate was estimated based on the AIRS air temperature profile and a ground-based meteorological station (Lennoxville). Since the best performance (between three levels of 925 hPa, 850 hPa, and 700 hPa) was 850 hPa, it should be noted that the result for relative humidity was not acceptable. Despite the fact that most spatial distribution models used a fixed lapse rate value, this study estimated daily lapse rate. This key distinction of our model allowed us to monitor more accurate atmospheric conditions such as the inversion phenomenon.

The second consideration on the current version of Micro-Met concerned a sub-model to estimate downward longwave radiation under clear skies. An improved emissivity model was derived to modify a downward longwave equation, which was adapted to the study site using data from the SIRENE experimental station (Université de Sherbrooke). The comparative statistics of ten emissivity equations previously published showed that the equation that included the atmospheric water vapor content performed best. In comparison with other studies, the improved equation considered two atmospheric conditions: clear skies and low wind velocity, both of which are associated with synoptic conditions of frost occurrence. The performance test indicated a significant improvement to estimate longwave radiation.

The key question, which was addressed through the third sub-model, the third consideration, was quantifying the drops in temperature due to the stagnation of cold air drainage in closed valleys. The sub-model constituted two components: i) detecting and estimation of closed valley volume, and

ii) estimating cold air drainage velocity. Most of the research centred on single valleys or limited areas. However, our research focused on multiple valleys with various volumes over the study site (15km × 15km). An operational method was presented to detect and estimate volume of the closed valleys where cold air was stagnant. The DTM on a 10 m grid created the basis for detecting closed valleys. The method was not limited to the study site and could be applied to other regions. The effects of land cover in terms of hydraulic friction on the velocity of cold air were not extensively examined. Most formulas considered bare soil conditions. This is why we developed a formula to estimate the velocity of cold air drainage.

The last consideration, involving the fourth sub-model, had the purpose of providing more accurate wind velocity for areas affected by the forest shelterbelt. The shelterbelt model was incorporated into the Micro-Met system to power the vegetation-atmosphere energy model. Based on experimental results produced in a laboratory with wind-tunnel models, three separate equations for estimation of wind velocity over windward, leeward and through the forest areas were developed. In comparison with numerical methods, there were less mathematical processes. A numerical simulation of a forest shelterbelt requires the complex full turbulent Navier-Stokes equations. In addition, to model the aerodynamics of a forest shelterbelt, we must have the capability to predict the wind flow associated with the shelterbelt structure. Both methods, simulation and wind tunnel experiment results, are difficult to assess. Our model indicated recommend acceptable values for wind velocity lower than 6 ms^{-1}.

The synthesis of the second specific objective integrated with the Micro-Met system led to the production of an improved version, the enhanced Micro-Met, which covered terrains related processes (cold air drainage and shelterbelt), as well as atmospheric variables (downward longwave and air temperature lapse rate), important in terms of air temperature forecasting. The enhanced Micro-Met provided a platform to power the vegetation-atmospheric energy model and allowed us to transfer the point-based structure of the vegetation-atmosphere model into grid-points one. Moreover, the two models tackled limited availability of spatial-temporal input data, and characterisation of soil and land surface properties on a local scale model inputs and variables had to be routinely available at the local sunset period.

In addition to the previous specific objectives, this study evaluated an active frost method. An assessment of the SIS system was done in different topographic locations. Observations presented by the air temperature distribution maps did not show evidence that the SIS system had impartial

efficiency on nocturnal cooling. Moreover, a new frost mitigation method based on thermodynamic of water vapor transport from a moist source to dry sink was proposed. A vessel of warm water equipped with a selective inverted sink (SIS) system was used to transport water vapor into the air, which ended up decreasing air dryness and increasing moist entropy. The most common mitigation method focuses on air temperature change by movement of air (such as helicopter or wind machine). Instead, the proposed method was based on moist entropy, which depicted heat content. The second step involved a new active method based on using forced convection produced by the SIS system increasing water vapor. In this approach, we considered the thermodynamic transformations of water during moist convection and derived the corresponding changes of moist entropy, while increasing latent heat.

8.2 Summary of results

The results demonstrated a potential of the AIRS air temperature profile to improve the regional scale (1 km - 100 km) monitoring of temperature profiles where there were no upper weather stations. However, the AIRS retrievals of humidity did not agree with the radiosonde observations. The combination of the Enhanced Micro-Met simulation data and remote sensing offered the possibility to derive the local distribution of energy fluxes over heterogeneous land surfaces close to the sunset period.

The performance assessment of the applied cold air drainage model demonstrated that the prediction results for the closed valleys had improved. This result was in agreement with the first hypothesis: by taking into account the local air circulation due to terrain feature vegetation -atmosphere model's accuracy in the prediction of local minimum temperatures could be improved. The cold air drainage was applied twice. The first time was at sunset to generate more accurate input data for the vegetation-atmosphere energy model. We then applied it to the forecasting results.

The improvements to the modeling capabilities required the use of several data sets: data from a weather station, a fine-resolution (10 m) Digital Terrain Model and a Digital Surface Model, and remote sensing data (Landsat, Modis, AIRS, and high-resolution thermal camera). The scale of cold pools is frequently finer than the grid scale used for operational weather prediction models. This study presented an automatic algorithm to detect at high resolution the areas where cold air drainage accumulated. Increasing the resolution allowed us to represent local circulation and its role on

minimum temperature differences. Therefore, the high-spatial resolution DTM and high-quality DTM were necessary to quantify precisely the effects of cold air drainage and consequently nocturnal air temperature prediction. This result was in agreement with the second hypothesis which assumed DEM at high resolution 10m is adequate to represent effect of cold air accumulation on air temperature.

The results showed that high-resolution thermal imagery was a powerful tool to characterize the dynamics of cold air drainage. A new method for visualizing and estimating cold air drainage was developed. Results from this method indicated that there was no cold air drainage flow between the top and bottom of the slope once the minimum temperature had been reached. This type of information is new because it is not available on existing observation networks.

In the field of frost protection, temperature needs to be supplemented with additional metrics for an agro-meteorological application such as frost. The results present an environmentally friendly method based on increasing the entropy budget. This active method has the potential to provide a useful alternative to some frost protection methods such as heaters and fires. This study highlighted the importance of high-resolution measurements in the agro-meteorological field. High-resolution features make it possible to detect areas prone to frost.

8.3 Research implications and future study

The implications of this research are of foremost interest to the prediction of minimum temperatures of agricultural terrains, especially regarding improved frost warnings. An accurate system to predict air temperatures at local resolutions can potentially reduce frost damages, because it provides farmers with the opportunity to prepare for frost events. Such a system would be useful to supply site-specific warnings of frost risks of much higher resolutions than those issued by Environment Canada. In this respect, the local minimum nocturnal temperature maps represent an important tool for land use planning and farm/crop management in agriculture and horticulture. The maps may be used by Quebec authorities to develop frost risk protection plans in the regions prone to risk. Moreover, we may eventually arrive at a proper assessment of the quality of spatial data and environmental models to determine the accuracy of the information derived from them.

The results of this study open doors to further research based on diagnostic and prognostic modelling more specifically over the region with complex topographic configuration. Enhanced Micro-Met model gives opportunity to improve climatological diagnostic analysis as well as to

develop meteorological inputs to high resolution hydrological, ecological and air quality models. The gridded meteorological data are one of the key inputs to theses models.

There are many further steps desirable to continue and extend this work. Further work is required to integrate more topographic aspect like geometric of the valley. This allow us to improve the cold air drainage model over open valies. We would benefit from a deeper understanding of the land-atmosphere processes that govern the cooling of air temperature, which in turn would help to better predict local frost events. For further research, it would be recommended to extend this work toward road meteorology field; for example, forecasting radiation fog and icing on roads. The couple vegetation-atmosphere energy model and Micro-Met model is an operational model to forecast dew formation on the land surface. Moreover, increasing the Digital Terrain Model could be another possibility in terms of research. Using a more precise model allowed us to gain a deeper understanding of the topographic processes that govern the cooling of air temperature, which in turn helped to better predict local frost events.

9. References

Ahmad, R., Arshad, M., Khalid, A., Zahir, Z.A. and Mahmood. T., 2008. Effect of compost enriched with N and L-tryptophan on soil and maize. Agronomy for sustainable development, 28, pp. 299-305.

Ahrens, C.D., 2000. Meteorology Today: An Introduction to Weather, Climate, and the Environment. Thomson Higher Education, USA, pp. 537.

AL-Lami, A.M., AL-Salihi, A.M. and AL-Timimi, Y.K., 2017. Parameterization of the Downward Long Wave Radiation under Clear-sky Condition in Baghdad, Iraq. Asian Journal of Applied Sciences. 10, pp.10-17.

Araghi, Mousavi Baygi, M., Adamowski, J., Martinez, Ch. and van der Ploeg, M., 2017. Forecasting Soil Temperature Based on Surface Air Temperature Using Wavelet-Artificial Neural Network. Meteorological Applications, 24, pp. 603-611.

Avissar R. and Mahrer Y., 1988. Mapping frost sensivite areas at a three-dimensional localscale numerical model, part II. Comparison with observation. J. Appl. Meteor., 61, pp. 414-46.

Aumann, H.H., Chahine, M.T., Gautier, C., Goldberg, M.D., Kalnay, E., McMillin, L.M., Revercomb, H., Rosenkranz, P.W., Smith, W.L., Staelin, D.H., Strow, L.L., and Susskind, J., 2003. AIRS/AMSU/HSB on the Aquamission: Design, science objectives, data products, and processing systems, IEEE Trans. Geosci. Remote Sensing, 41, pp. 253–264.

Bagdonas, A., Georg, J.C. and Gerber, J.F., 1978. Techniques of frost prediction and methods of frost and cold protection. WMO Technical note, p. 57.

Bárdossy, A., Pegram, G., 2013. Interpolation of precipitation under topographic influence at different time scales. Water. Resour. Res., pp. 4545-4565.

Barnes, S., 1964. A technique for maximizing details in numerical weather map analysis. J. Appl. Meteor., 9, pp. 396-409.

Bartholic, J.F., Halsey, L.H. and Biggs, R.H., 1974. Effects of UV radiation on agricultural productivity, Third Conference on CIAP, US.Washangton D.C, pp. 498-504.

Barr, S., and Orgill M M., 1989. Influence of external meteorology on nocturnal valley drainage winds. J. Appl. Meteor., 28, pp**.** 497–517.

Barry R.G., 2010. Mountain weather and climate. Cambridge University Press, Cambridge, UK. Pp.506.

Barry, R.G., and Chorley, R.J., 1987. Atmosphere, Weather and Climate, 5th ed. Routledge, pp. 448.

Battany, M., 2012. Climate Change in CA: Vineyard Cultural Practices, presented at the California Department of Food and Agriculture Climate Change Adaptation Consortium, 28, Modesto, CA.

Baver, L.D., Gardner, W.H. and Gardner, W.R. 1972. The thermal regime of soils. Soil physics. John Wiley. pp. 253-280.

Berndt C., and Haberlandt U., 2018. Spatial interpolation of climate variables in northern Germany influence of temporal resolution and network density. Contents lists available at ScienceDirect. J. Hydrology., 15, pp.184-202.

Benavides, R., Montes, F., Rubio, A., and Osoro, K., 2007. Geostatistical modeling of air temperature in a mountainous region of Northern Spain. Agricultural and Forest Meteorology, 146, pp. 173-188.

Bilgili, M., 2010. Prediction of soil temperature using regression and artificial neural network models. Meteorol. Atmos. Phys. 110, pp. 59–70.

Blennow, K., Persson, P., 1998. Modeling local-scale frost variations using mobile temperature measurement with a GIS, Agricultural and Forest Meteorology, 89, pp. 59-71.

Bogren, J., and Gustavsson, T., 1989. Modeling of local climate for prediction of road slipperiness. Phys. Geogr., 10, pp. 147–164.

Bond-Lamberty B., Wang C. and Gower S.T., 2005. Spatiotemporal measurement and modeling of boreal forest soil temperatures. Agricultural and Forest Meteorology, 131, pp. 27- 40.

Bootma, A., 1976. Estimating minimum temperature and climatological freeze risk in hilly terrain Agricultural and Forest Meteorology, 16, pp. 425-443.

Bruland, O., G. E. Liston, J. Vonk, and A. Killingtveit, 2004. Modeling the snow distribution at two high-Arctic sites at Svalbard, Norway, and at a sub-Arctic site in central Norway. Nordic Hydrol, 35, pp.191–208.

Brunt D., 1941. Physical and dynamicac meteorology. Cambridge University Press, NewYork, 428

Cellier, P., 1993. An operational model for predicting minimum temperatures near the soil surface under clear sky conditions. J. Appl. Meteor, 32, pp. 871–883.

Chahine, M.T., Pagano, T.S., Aumann, H.H., Atlas, R., Barnet, C., Blaisdell, J., Gautier, C., 2006. AIRS: Improving weather forecasting and providing new data on greenhouse gases. Bull. Am. Meteorol. Soc., 87, pp. 911- 926.

Chen T., Yen M., Hsieh J. and Arritt R., 1999. Diurnal and seasonal variations of the rainfall measu red by the automatic rainfall and meteorological telemetry system in Taiwan. Bull. Am. Meteorol., Soc. 80. pp. 2299–2312.

Chung, U., Seo, H., Hwang, K.H., Hwang, B.S., 2006. Minimum temperature mapping over complex terrain by estimating cold air accumulation potential. Agricultural and Forest Meteorology, 137, pp. 15–24.

Cohen, S.B., 1973. Oxford World Atlas. Oxford University Press. United Kingdom. Davies, R.J. 1987. Trees and weeds: weed control for successful tree establishment. Forestry Commission Handbook, UK 2.

Columela, L.J.M., 1965. 1st Century AD. De re rustica. English Edition, On Agriculture. Harvard University Press, Cambridge.

Costa, M.J., Obregón, M.A., Pereira, S., Salgueiro, V., Potes, M., Couto, F.T., Salgado, R., Bortoli, D. and Silva, A.M., 2015. Analysis of atmospheric vertical profiles in the presence of desert dust aerosols. IOP Conference Series. Earth and Environmental Science, 28, pp.1-9.

Crawford T.M. and Duchon C.E., 1999. An improved parameterization for estimating effective atmospheric emissivity for use in calculating daytime downwelling longwave radiation. J. Appl. Meteor, 38, pp. 474–480.

Daly, C., 2006. Guidelines for assessing the suitability of spatial climate data sets. International J. Climatology 26, pp. 707–721.

Davis, R.E., 1991. A synoptic climatological analysis of winter visibility trends in themideastem United States. Atmos. Envimn, 258, pp.165-175.

De Wekker, S.F.J. and Whiteman. D., 2006. On time scale of nocturnal boundary layer cooling in valleys and basins and over plains. J. Appl. Meteor., 45, pp. 813–820.

Diak, G.R., Bland, W.L., Mecikalski, J. and Anderson, M.C., 2000. Satellite-based estimates of longwave radiation for agricultural applications. Agricultural and Forest Meteorology, 82, pp.219–226.

Dilley, A.C. and D.M., O'Brien, 1998. Estimating downward clear sky long-wave irradiance at the surface from screen temperature and precipitable water. Quart. J. Roy. Meteor. Soc., 124, pp. 1391–1401.

Dobesch, H.P., Dumolard & Dryas, I. Eds. 2007. Spatial interpolation for climate data: the use of GIS in climatology and meteorology Geographical Information Systems. Series. London: ISTE ltd.

Dobrowski S.Z., Abatzoglou J.T., Greenberg J.A. and Schladow S.G., 2009. How much influence does landscape-scale physiography have on air temperature in a mountain environment, Agricultural and Forest Meteorology, 149, pp.1751–1758.

Dodson, R. and Marks, D., 1997. Daily air temperature interpolated at high spatial resolution over a large mountainous region, Climate research, 8, pp.1-20.

Duarte, H. F., N. L. Dias, and S. R. Maggiotto., 2006. Assessing daytime downward longwave radiation estimates for clear and cloudy skies in southern Brazil. Agricultural and Forest Meteorology, 139, pp. 171 – 181.

Eccel E., Arman G., Zottele F. and Gioli B., 2008. Il telerilamento all' infrarosso termico per la mappatura delle temperature minime ad elevato dettaglio territorial. (Thermal infrared remote sensing for high-resolution minimum temperature mapping) Italian Journal of Agrometeorology, 13, pp. 52-61.

Ellison, E.S., 1928. A critique on the construction and use of minimum temperature formulas. Mon. Wea. Rev., 56, pp. 485-495.

Fenzl, R.N., 1962. Hydraulic resistance of broad shallow vegetated channels. Ph.D. Thesis. University of California, Davis CA, USA.

Figuerola P.J. and Mazzeo N.A., 1997. An analytical model for the prediction of nocturnal and dawn surface temperatures under calm, clear sky conditions. Agricultural and Forest Meteorology, 85, pp. 229-237.

Fleagle, R.G., 1950. A theory of air drainage, Journal of Meteorology, 7, pp. 227–232.

Flerchinger, G.N., Xaio, W., Marks, D., Sauer, T.J., and Yu, Q., 2009. Comparison of algorithms for incoming atmospheric long-wave radiation, Water Resour. Res., 45, pp1-13.

Foken, T., 2008. The energy balance closure problem. Ecol. Appl., 18. pp. 1351-1367.

Gabathuler, Marty, M., C.A. and Hanselmann, K.W., 2001. Parameterization of incoming longwave radiation in high-mountain environments. Phys. Geogr., 22, pp. 99–114.

Geiger, R., Aron, R.H. and Todhunter, P., 2009. The climate near the ground. Rowman &Littlffield., INC, pp. 620.

Gettleman, A. and Collins, W.D., 2006. Climatology of upper-tropospheric relative humidity from the Atmospheric Infrared Sounder and implications for climate. J. Climate., 19, pp.6104–6121.

Ghielmi, L. and Eccel, E., 2006. Descriptive Models and Artificial Neural Networks for Spring Frost Prediction in an Agricultural Mountain Area. Computers and Electronics in Agriculture, 54, pp.101-114.

Gombos, B., Koles, P., Montvajszki, M., 2011. Spatial differences of night temperature in hilly regions and its horticultural importance, Agriculture and environment, 3, pp.102-109.

Goudenhoofdt, E. Delobbe L., 2009. Evaluation of radar-gauge merging methods for quantitative precipitation estimates. Hydrol. Earth Syst. Sci., pp. 195-203.

Greene, E. M., Liston G.E., and Pielke Sr.R.A., 1999. Simulation of above treeline snowdrift formation using a numerical snow-transport model. Cold Reg. Sci. Technol., 30, pp.135-144.

Gribanov, K.G. and Zakharov, V.I., 2004. Neural network solution for temperature profile retrieval from infrared spectra with high spectral resolution. Atmospheric Science Letters, 5, pp. 1-11.

Gromke, C. and Ruck, B., 2007. Influence of trees on the dispersion of pollutants in an urban street canyon-experimental investigation of the flow and concentration field. Atmospheric Environment, 41. pp. 3302-3387.

Gryning, S.E., Mahrt, L. and Larsen, S., 1985. Oscillating nocturnal slope flow in a coastal valley, Tellus, Series A, 37, pp. 196-203.

Gustavsson, T., Karlsson, M., Bogren, J. and Lindqvist, S., 1998. Development of temperature patterns during clear nights. J. Applied Meteorology, 37. pp. 559-571.

Gustavsson, T., 1995. A study of air and road temperature variation during clear wind nights. Int. J. Climatology., 15, pp. 919-932.

Guojie. H., Zhao. L. and Xiaodong, W.U., 2016. An analytical model for estimating soil temperature profiles on the Qinghai-Tibet Plateau of China, Journal of Arid Land, 8, pp. 232-240.

Hahnenberger, M., 2008. Topographic effects on nighttime cooling in a basin and plain atmosphere. University of Utah. pp. 85.

Hanley, D.P. and Kuhn. G., 2003. Trees against the wind. Washington State University, Oregon State University, University of Idaho. p. 47.

Heinemann P.H. and Martsolf J.D., 1988. Prediction of Cooling of a Nocturnal Environment Using Two Atmospheric Models. Climatology Lab, Fruit Crops Department, University of Florida, Gainesville, Florida .pp. 473-481.

Heisler, G., M. and Dewalled, D.R., 1988. Effects of windbreaks structure on wind flow. Agric. Ecosytem Environ, 22, pp. 41-69.

Hiemstra, C.A., G. E. Liston, and W.A. Reiners., 2002. Snow redistribution by wind and interactions with vegetation at upper treeline in the Medicine Bow Mountains, Wyoming, USA. Arct. Antarct. Alp. Res., 34, pp.262–273.

Hipsey, M.R., Antenucci, J.P., Brookes J.D., Burch M.D., Regel, R., H. and Linden, L., 2004. A three dimensional model of Cryptosporidiumdynamics in lakes and reservoirs: A new tool for risk management, International journal of river basin management, 2, pp. 185 –197.

Holden, Z., Crimmins, A., Cushman, S., 2011. Empirical modeling of spatial and temporal variation in warm season nocturnal air temperatures in two North Idaho mountain ranges. Agricultural and Forest Meteorology, 151, pp. 261-269.

Hubbart, J.A., Link, T.E., Gravelle J.A. and Elliot, W.J., 2007. Timber harvest impact on water yield in the continental/maritime hydroclimate region of the U.S. Journal of forestry, 53, pp. 169-180.

Huguette. M., 2008. De l'énergie en granules: un potentiel, 71^{e} congrès de l'ordre des agronomes du Québec.

Iijima, Y., and Shinoda, M., 1998. Formation of a cold air lake during the warm season in a small hollow in Mt. Inakodake, Yatsugatake Range (in Japanese with English abstract). Geogr. Rev. Japan, 71, pp. 559-572.

Iziomon, M.G., Mayer, H. and Matzarakis, A., 2003. Downward atmospheric longwave irradiance under clear and cloudy skies: Measurement and parameterization. J. Atmos. Sol.-Terr. Phys., 65, pp. 1107-1116.

Jacobs, W.C., 1940. A comparison of upper soil temperatures and shelter temperatures. Bull. Amer. Meteor. Society, 21, pp. 181-183.

Jenson, S. and Domingue, J., 1988. Extracting Topographic Structure from Digital Elevation Data for Geographic Information System Analysis. Photogrammetric Engineering and Remote Sensing, 54, pp. 1593-1600.

Jones, T.A., and Stensrud, D.J., 2012. Assimilation of AIRS temperature and mixing ratio profiles using an ensemble Kalman filter approach for convective-scale forecasts. Wea. Forecasting, 27, pp. 541-564.

Kajfez, B.L., 1989. Early autumn frost in upper Carniola Slovenia (Yugoslavia), Zbornik Biotecknіske Univerez, 53, pp. 19-26.

Kalma, J.D., Laughlin, G.P., Caprio, J.M. and Hamer, P.J.C., 1992. The Bioclimatology of Frost, Its Occurrence, Impact and Protection. Springer, Berlin, pp.144.

Kang S. Kim, Lee S. and Oh, D., 2000. Predicting spatial and temporal patterns of soil temperature based on topography, surface cover and air temperature S. Forest ecology and management, 136, pp. 173-184.

Kidder, S.Q., and O.M. Essenwanger, 1995. The effect of clouds and wind on the difference in nocturnal cooling rates between urban and rural areas. J. Appl. Meteor., 34, pp. 2440–2448.

Kiefer, M.T. and Zhong, S., 2013. The effect of sidewall forest canopies on the formation of cold-airpools - A numerical study.J. Geophys. Res. Atmos., pp. 118.126.

Kim H. and Yun SH., 2011. Evaluation of potential reference genes for quantitative RT-PCR analysis in Fusarium graminearum under different culture conditions. Plant Pathol J. 27. pp. 301–309.

Koch, S.E., DesJardins, M. and Kocin, P.J., 1983. An interactive Barnes objective map analysis scheme for use with satellite and conventional data. J. Climate Appl. Meteor., 22, pp. 1487-1503.

Kondo, J., Okusa, N., 1990. A Simple Numerical Prediction Model of Nocturnal Cooling in a Basin with Various Topographic Parameters. J. Appl. Meteor., 29, pp.604-618.

Kondo, J., Sato, T., 1989. A simple model of drainage flow on a slope. Band layer Meteor., 43, pp. 103–123.

Kondo, J., Kuwagata, T., 1989. Heat Budget Analysis of Nocturnal Cooling and Daytime Heating in a Basin. Jouarnal of Atmospheric sience, 46, pp.169-180.

Krajewski, W.F., 1987. Cokriging radar-rainfall and rain gage data**.** J. Geophys. Res.–Atmos., 92, pp. 9571-9580.

Kunkel, K.E., 1989: Simple procedures for extrapolation of humidity variables in the mountainous western United States. J. Climate, 2. pp. 656–669.

Lampartova, I., Schneider, J., Vyskot, I., Rajnoch, M. and Litschmann, T., 2015. Impact of protective shelterbelt microclimate characteristics. Ekológia (Bratislava), 34, pp. 101–110.

Lapp, S., Byrne, J., Townshend, I. and Kienzle, S., 2005. Climate warming impacts on snowpack accumulation in an alpine watershed. International J. Climatology, 25. pp. 521-536.

Laughlin J.P. and Kamal J.D., 1990. Frost Risk mapping for landscape Planning: A methodology. Theoretical and applied climatology, 42, pp. 41-51.

Lee, L.F. and Liu X., 2010. Specification and estimation of social interaction models with network structures. Econometrics Journal, 13, pp. 145–176.

Lehnert, M., 2015. Factors affecting soil temperature as limits of spatial interpretation and simulation of soil temperature. Acta Universitatis Palackianae Olomucensis–Geographica, 45, pp. 5-21.

Liang, S., K. Wang, X. Zhang, and M. Wild., 2010. Review on estimation of land surface radiation and energy budgets from ground measurement, remote sensing and model simulations. J. Selected topics in applied earth observations and remote sensing, 3, pp. 225-240.

Liston, G.E. and Elder, K., 2006. A Meteorological Distribution System for High-Resolution Terrestrial Modeling. J. Hydrometeor., 7. pp. 217-234.

Lhomme, J.P. and Guilioni, L., 2004. A simple model for minimum crop temperature forecasting during nocturnal cooling, Agricultural and Forest Meteorology, 123, pp, 55-68.

Liston, G.E., and Hiemstra.C. 2008. A simple data assimilation system for complex snow distributions. J. Hydrometeor., 9, pp.989-1004.

Liston, G.E., McFadden. J., Sturm. M., 2002. Modeled changes in arctic tundra snow, energy, and moisture fluxes due to increased shrubs. Global Change Biol., 8, pp. 17-32.

Liston, G.E., and Sturm. M., 2002. Winter precipitation patterns in arctic Alaska determined from a blowing-snow model and snow-depth observations. J. Hydrometeor., 3, 646-659.

Liston, G.E. and Sturm, M., 1998. A snow-transport model for complex terrain. Journal of Glaciology, 44, pp. 498-516.

Lundquist, J.D. and Huggett, B., 2008. Evergreen trees as inexpensive radiation shields for temperature sensors, Water Resour. Res., 44. pp. 1-5.

Lundquist, J.D. and Cayan D.R., 2007. Surface temperature patterns in complex terrain: Daily variations and long-term change in the central Sierra Nevada, J. Geophys. Res., 112, pp.1-15.

Lio, Y., and Key, J., 2003. Detection and Analysis of Clear-Sky, Low-Level Atmospheric Temperature Inversions with MODIS, American Meteorological Society, 12, pp. 1727-1737.

Oliphant, A.J., Spronken-Smith R.A., Sturman, A.P. and Owens, I.F., 2003. Spatial variability of surface radiation fluxes in mountainous terrain. J. Appl. Meteor., 42, pp.113–128.

Ma, Y., Su, Z., Li, Z.L., Koike, T. and Menenti M., 2002. Determination of regional net radiation and soil heat flux over a heterogeneous landscape of the Tibetan Plateau Hydrol. Process, pp. 2963-2971.

Ma, Y., Zhong, L., Wang, B., Ma, W., Chen, X. and Li, M., 2011. Determination of land surface heat over heterogeneous landscape of the Tibetan Plateau by using the MODIS and in situ data. Atmos. Chem. Phys., 11, pp. 10461–10469.

Madelin M., 2006. L'al´ea gelif printanier dans le vignoble marnais en Champagne. Modélisation spatiale à une échelle fine des ´ecoulements de l'air et des températures minimales. These de doctorat, Université de Paris VII, pp. 347.

McNaughton, S.J., 1986. On plants and herbivores.Am. Nat., 128, pp. 765–70.

Madlin M. and Beltrando G., 2005. **S**patial interpolation based mapping of the spring frost hazard in the Champagne vineyards. Meteorological Application, 12. pp. 51-56.

Marjus, N., 2010. Estimating daily land surface temperatures in mountainous environments by reconstructed MODIS LST data. Remote sensing, 2. pp. 333-353.

Martz L.W. and Garbrecht J., 1992. Numerical definition of drainage network, subcatchment areas from digital elevation models. Computers, Geosciences, 18. pp. 747 – 761.

Mihalakakou G., 2002. On estimating soil surface temperature profiles. Energy Build, 34. pp. 251–259.

Minder, J.R., Mote, P.W. and Lundquist, J.D., 2010. Surface temperature lapse rates over complex terrain: Lessons from the Cascade Mountains, J. Geophys. Res. Atmos., 115.pp. 1-13.

Mutiibwa, D., Vavrus S.J., McAfee S.A. and Albright, T.P., 2015: Recent spatiotemporal patterns in temperature extremes across conterminous United States. J. Geophys. Res. Atmos., 120, pp. 7378–7392.

Nanding, N., Rico-Ramirez, M.A., Han D., 2015. Comparison of different radar-raingauge rainfall merging techniques. J. Hydroinform., pp. 422-445.

Napagoda. N., A.D. and Tilakaratne. C.D., 2012. Artificial Neural Network Approach for Modeling of Soil Temperature. Sri Lankan Journal of Applied Statistics, 13, pp. 39-59.

Niemelä P., Chapin F.S., Danell K. and Bryant J.P., 2001. Herbivory-mediated responses of selected boreal forests to climate change. Climate Change, 48, pp. 427-440.

Oke, T.R., 1987. Boundary layer climates, Psychology Press, Science, pp.435.

Oliphant, A.J., Spronken-Smith R.A., Sturman, A.P. and Owens, I.F., 2003. Spatial variability of surface radiation fluxes in mountainous terrain. J. Appl. Meteor., 42, pp.113-128.

Ozturk, C., Karaboga, D. and Gorkemli, B., 2011. Probabilistic dynamic deployment of wireless sensor networks by artificial bee colony algorithm. Sensor, 11. pp. 6056- 6065.

Pauluis, O., 2011, Water Vapor and Mechanical Work: A Comparison of Carnot and Steam Cycles. J. The Atmospheric Sciences, 68, pp.91-102.

Pauluis, O. and Held, I.M., 2002. Entropy Budget of an Atmosphere in Radiative–Convective Equilibrium. Part I: Maximum Work and Frictional Dissipation. J. The Atmospheric Sciences, 59, pp. 125-139.

Paul, F., Huggel, C. and Kaab, A., 2004. Combining satellite multispectral image data and a digital elevation model for mapping of debris-covered glaciers. Remote sensing of environment, 89, pp. 510–518.

Pirazzini, R., M. Nardino, A. Orsini, F. Calzolari, T. Georgiadis, and V. Levizzani., 2000. Parameterisation of the downward longwave radiation from clear and cloudy skies at NyÅlesund. International Radiation Symposium, Russia.

Plate, E.J., 1971. The Aerodynamics of Shelterbelts, J. Agricultural meteorology, 8, pp. 203–222.

Polyakov, A.V., Timofeev, Yu. M. and Virolainen, Ya. A., 2014. Using neural networks in the temperature and humidity sounding of the atmosphere, Atmos. Ocean. Phys. 50, pp.330–336.

Prabha, T. and Hoogenboom, G., 2008. Evaluation of weather research and forecasting model for two frost events. Computers and electronics in agriculture, 64, pp. 234-247.

Prata A.J., 1996. A new long-wave formula for estimating downward clear-sky radiation at the surface. Q. J. R. Meteorol. Soc., 122, pp. 1127–1151.

Prasad, R., D.G. Tarboton, G.E. Liston, C.H. Luce, and M.S. Seyfried., 2001. Testing a blowing snow model against distributed snow measurements at Upper Sheep Creek, Idaho, USA. Water Resour. Res, 37, pp. 1341–1357.

Rahimzadegan, M., and Mobasheri M.R., 2010. An Attempt for Improving MODIS Atmospheric Temperature Profiles Products in Clear Sky. Meteorological Application, 18, pp.181-187.

Reimeri. A and Shayekewichz C., 1980. Estimation of Manitoba soil temperature from atmospheric meteorological measurement. Canadian Journal Soil Sociality, 60, pp. 299-309.

Richards K. and Baumgarten M., 2003. Towards Topoclimatic Maps of frost and frost Risk for Scotland New Zealand, 15th Annual Colloquium of the Spatial Information Research Centre. University of Otago, New Zealand.

Richard, L., Paulo de Melo-Abreu, J., 2005. Frost protection: fundamentals, practice, and economics. Food and Agriculture Organization of the United Nations, pp.126.

Rivest D. and Vezina A., 2015. Maize yield patterns on the leeward side of tree windbreaks are site-specific and depend on rainfall conditions in eastern Canada. Agroforestry Systems, 89, pp. 237-246.

Rodrigo J., 2000. Spring frosts in deciduous fruit trees morphological damage and flower hardiness. Sci. Hortic., 85, pp. 155–173.

Rogers, R.R. and Yau, M.K., 1989. A Short Course in Clouds Physics.Pergamon Press, pp. 290.

Rolland, C., 2003 Spatial and Seasonal Variations of Air Temperature Lapse Rates in Alpine Regions, Journal of Climate, Vol 16, pp. 1032-1046.

Rosenberg, M.J., Blad, L.B. and Verma, B. SH., 1985. Microclimate the biological environment. John wiley & sons, pp. 528.

Roger, R. and Yau, M., 1989. A short course in cloud physics, third Edition, Butterworth-Heinemann, pp. 306.

Ryan, B.C., 1977: A mathematical model for diagnosis and prediction of surface winds in mountainous terrain. J. Appl. Meteorol., 16, pp. 571-584.

Sakai, A. and Larcher, W., 1987. Frost Survival of Plants. Responses and Adaptation to Freezing Stress. Ecological Studies, 62, Springer, Berlin.

Santiago, J.L., Martin, F., Cuerva, A., Bezdenejnykh, N., and SanzAndres, A., 2007. Experimental and numerical study of wind flow behind windbreaks. Atmos. Environ., 41, pp. 6406–6420.

Savage, K., Davidson, E., and Richardson, A.D., 2008. A conceptual and practical approach to data quality and analysis procedures for high-frequency soil respiration measurements. Functional Ecology, 22, pp. 1000-1007.

Seemann, S.W., Li, J., Gumley, L.E. and Menzel, W.P., 2003. Operational retrieval of atmospheric temperature, moisture, and ozone from MODIS infrared radiances. J. Appl. Meteorol., 42, pp. 1072-1091.

Shannon E. Brown, Kurt S. Pregitzer, David D. Reed, and Andrew J. Burton. 2000, Predicting daily mean soil temperature from Daily mean air temperature in Four Northern Hardwood Forest Stands, Forest Scinece., 46, pp. 297-301.

Shaogang, L., John, L.D., Zhengfu, B. and Njoroge, W., 2011. Improved soil temperature modeling. Environmental Earth Sciences, 6, pp.1123-1130.

Shuttleworth, W.J., Wallace, J.S., 1985. Evaporation from sparse crops an energy combination theory. Quart. J. Royal Meteorol. Soc., 111, pp. 839-855.

Shuttleworth, W.J. and Gurney, R.J., 1990. The theoretical relationship between foliage temperature and canopy resistance in sparse crops. Quart. J. Royal Meteorol. Soc., 116, pp.497-519.

Santanello, J.A. and. Friedl M.A., 2003. Diurnal covariation in soil heat flux and net radiation. J. Appl. Meteorol., 42, pp. 851-862.

Snyder R.L., and Paulo de Melo-Abreu, J., 2005. Frost protection: fundamentals, practice and economics. Vol. 1. Food and Agriculture Organization of the United Nations. pp. 223.

Steeneveld, G.J., van de Wiel, B.J.H. and Holtslag, A.A.M., 2006. Modeling the Arctic Nocturnal Stable Boundary Layer and its Coupling to the Surface. Boundary Layer Meteorology, 118. pp. 357-378.

Sugita, M. and Brutsaert, W., 1993. Cloud effect in the estimation of instantaneous downward longwave radiation, Water. Resour. Res., 29, pp.599-605.

Tabari H., Marofi, S. and Sabziparvar A.A., 2010. Estimation of daily pan evaporation using artificial neural network and multivariate non-linear regression. Irrig. Sci., 28, pp. 399–406

Tabari, H., Taye, M.T., and Willems, P., 2015. Water availability changein central Belgium for the late 21st century. Global Planet.Change, 131, pp. 115–123.

Tabony, R.C., 1985. Relations between minimum temperature and topography in Great Britain, Journal of Climatology, 5, pp. 503-520.

Tait, A. and Zheng, X., 2003. Mapping Frost Occurrence Using Satellite Data. J. Appl. Meteor., 42, pp.193- 203.

Tarboron, G.D., 1997. A new method for the determination of flow directions and upslope areas in grid digital elevation models. Water Resources Research, pp. 309-319.

Taschler, D., Beikircher B. and Neuner. G., 2004. Frost resistance and ice nucleation in leaves of five woody timberline species measured in situ during shoot expansion. Tree Physiol., 24, pp. 331–337.

Young, F.D., 1920. Forecasting minimum temperatures in Oregon and California. Mon.Wea. Rev., 16, Supplement, pp. 53-60.

Yue, Li., Zhenzhong Z., Lin Z. and Shilong P., 2015. Spatial patterns of climatological temperature lapse rate in mainland China: A multi-time-scale investigation. Journal of geophysical research, 120, pp. 2661-2675.

Van de Wiel, B.J.H., A.F. Moene, and H.J.J. Jonker, 2012. The cessation of continuous turbulence as precursor of the very stable nocturnal boundary layer. J. Atmos. Sci., 69, 3097-3115.

Van Eimern, J., Karschon, R., Razmova, L.A. and Robertson. G.W., 1964. Windbreaks and shelterbelts. World Meteorol. Organ. Tech. Notes., 59, pp. 188.

Van Thuyet, D., Van Do, T., Sato, T. and Thai Hung, T., 2014. Effects of species and shelterbelt structure on wind speed reduction in shelter. Agroforestry Systems, 88, pp. 237-244.

Vazart V., 1988 : Les gelées de printemps de 1885 - 1986 dans le vignoble champenois : historique et conséquences, relations avec la production de raisin. Thèse de doctorat, Université de Reims Champagne-Ardenne.

Vestal C.K.,1971. First and last occurrences of low temperature during the cold season. Monthly Weather Review, 99, pp. 650-652.

Vigiak O., Sterk G., Warren A. and Hagen L.J., 2003. Spatial modeling of wind speed around windbreaks. Catena, 52, pp. 273-288.

Wallace, J.M. and P.V. Hobbs., 2006. Atmospheric Science - An Introductory Survey. London. Academic Press. pp. 505.

Wang H. and Takle, E.S. 1997. Momentum budget and shelter mechanism of boundary-layer flow near a shelterbelt. Boundary Layer Meteorology, 82, pp. 417- 435.

Wang H., Takle, E.S. and Shen J. 2001. Shelterbelts and windbreaks: mathematical modeling and computer simulations of turbulent flows, Annual Review of Fluid Mechanics, 33, pp. 549.

Wang, Z.H. and Bou-Zeid, E., 2012. A novel approach for the estimation of soil ground heat flux. Agricultural and Forest Meteorology, 155, pp. 214-221.

Wearne, L.J. and Morgan, J.W., 2001. Recent forest encroachment into subalpine grasslands near Mount Ho- tham, Victoria, Australia. Arctic, Antarctic, and Alpine Research, 33, pp. 369–377

Whiteman, C.D., Hoch, S.W., Lehner, M. and Haiden T., 2010. Nocturnal cold air intrusions into Arizona's Meteor Crater: Observational evidence and conceptual model. J. Appl. Meteor., 49, pp. 1894-1905.

Whiteman, C.D., De Wekker, S.F.J. and Haiden, T., 2007. Effect of dewfall and frost fall on nighttime cooling in a small, closed basin. J. Appl. Meteor., 46, pp.3-13.

Whiteman, C.D., 1990. Observations of thermally developed wind systems in mountainous terrain. Atmospheric Processes over Complex Terrain. Amer. Meteor. Soc., 45, pp. 5- 42.

Wu, M.S., Chang, C.Y., Chang, R.W., and Chang, K.C., 2012. Early return of augmented wave reflection impairs left ventricular relaxation in aged Fisher. Exp. Gerontol., 47, pp. 680- 686.

Wu, S., Wong, H.K. and Lüdmann, T., 1999. Gravity-driven sedimentation on the northwestern continental slope of the South China Sea: results from high-resolution seismic data and piston cores. Chinese Journal of Oceanology and Limnology, 17, pp. 155-169.

Zinoni, F., Antolini, G., Campisi, T., Marietto, V., and Rossi, F., 2002. Characterisation of Emilia-Romagna region in relation with late frost risk. Physics and Chemistry of the Earth, 27, pp.1091-1101.

Appendix A.1. AIRS Standard Pressure Levels (Taken from GES DISC, 2016)

Index	PressStd, (hpa) air temperature	PressureStd, (hpa) relative humidity
1	1100.0	1100.0
2	1000.0	1000.0
3	925.0	925.0
4	850.0	850.0
5	700.0	700.0
6	600.0	600.0
7	500.0	500.0
8	400.0	400.0
9	300.0	300.0
10	250.0	250.0
11	200.0	200.0
12	150.0	150.0
13	100.0	100.0
14	70.0	70.0
15	50.0	50.0
16	30.0	
17	20.0	
18	15.0	
19	10.0	
20	7.0	
21	5.0	
22	3.0	
23	2.0	
24	1.5	
25	1.0	
26	0.5	
27	0.2	
28	0.1	

Appendix A.2. Wind speed variation as a function of distance from a windbreak and windbreak structure on the windward and leeward sides of a forest shelter taken from Hanley and Kuhn (2003).

Open wind speed 32.19 Km/h. Conifer 40% - 60% density					
H distance from windbreak	5H	10H	15H	20H	30H
Km per hour	9.66	16.09	19.31	24.14	30.58
% of open wind speed	30%	50%	60%	75%	95%
Open wind speed 32.19 Km/h. Multi-row 60% - 80% density					
H distance from windbreak	5H	10H	15H	20H	30H
Km per hour	8.05	11,26	20.92	27.36	30.58
% of open wind speed	25%	35%	65%	85%	95%
Open wind speed 32.19 Km/h. Solid fence 100% density					
H distance from windbreak	5H	10H	15H	20H	30H
Km per hour	8.05	22.53	28.97	30.58	32.19
% of open wind speed	25%	70%	90%	95%	100%

Appendix A.3. Nomenclature of cold air drainage velocity equation

	Parameters	Value	Unit	Description
1	F_D			Drag Force Exerted on the Vegetation
2	F_G			Gravitational Force
3	v		$^{m}/_{s}$	Wind Speed in the 0.15 height of the surface in vegetation
4	g	9.8	m / s^2	Gravitational Acceleration
5	i			Channel slope
6	C_d			Drag coefficient
7	m		kg	Mass of air between surface and 0.15 height in vegetation
8	D_s		m	Diameter of the cylindrical elements
9	ρ		$^{kg}/_{m^3}$	Density of air between surface and 0.15 height in vegetation
10	V	120	m^3	Volume of air between surface and 0.15 height in vegetation
11	A_s	800	m^2	Cross sectional area
12	$h_{a'}$	0.15	m	Height of air between surface and 0.15 height in vegetation
13	W_s	40	m	Slope Width
14	L_s	20	m	Slope Length
15	h	8	m	Slope Height
16	P		Pa	Ambient pressure
17	M_a	28.9635×10^{-3}	$^{kg}/_{mol}$	Molar mass of dry air
18	Z			Compressibility factor of air
19	R	8.314510	$^{J}/_{mol.K}$	Molar ideal gas constant
20	T		K	Ambiant temperature in Kelvin
21	x_v			The mole fraction of water vapor
22	M_v	18.015×10^{-3}	$^{kg}/_{mol}$	Molar mass of water vapor
23	α	1.00062		
24	β	3.14×10^{-8}		
25	γ	5.67×10^{-7}		
26	R	8.314510	$^{J}/_{mol.K}$	Molar ideal gas constant
27	A	1.2378847×10^{-5}	$^{1}/_{K^2}$	
28	B	$-1.9121316 \times 10^{-2}$	$^{1}/_{K}$	
29	C	33.93711047		
30	D	-6.3431645×10^{3}	K	
31	a_0	1.58123×10^{-6}	$^{K}/_{Pa}$	
32	a_1	-2.9331×10^{-8}	$^{1}/_{Pa}$	
33	a_2	1.1043×10^{-10}	$^{1}/_{K.Pa}$	
34	b_0	5.707×10^{-6}	$^{K}/_{Pa}$	
35	b_1	-2.051×10^{-8}	$^{1}/_{Pa}$	
36	c_0	1.989810^{-4}	$^{K}/_{Pa}$	
37	c_1	-0.000002376	$^{1}/_{Pa}$	
38	d	1.83×10^{-11}	$^{K^2}/_{Pa^2}$	
39	e	-0.765×10^{-8}	$^{K^2}/_{Pa^2}$	
40	P_{sv}		Pa	Saturation vapor pressure at ambient temperature
41	f_{pt}			Enhancement factor at ambient temperature and pressure

Appendix A.4 Estimation of cold air drainage velocity using proposed equation

Time	F_{G2}	F_τ	F_s	FD	Ro	C_d	λ	h_v	W_s	L_s	v m/s
17h	3602.92	2758.45	6038.77	322.60	1.343735	2.5	0.95	0.4	40	20	0.022
18h	3613.06	2766.21	6055.75	323.51	1.347514	2.5	0.95	0.4	40	20	0.023
19h	3618.52	2770.39	6064.90	324.00	1.34955	2.5	0.95	0.4	40	20	0.024
20h	3625.27	2775.55	6076.21	324.61	1.352067	2.5	0.95	0.4	40	20	0.024

List of parameters and variables were used to estimate cold air dranage velocity (Equation 4.32)

Parameter	Value	Unit	Parammeter	Value	Unit
g	9.8	ms^{-2}	Ma	18.02	g/mol
H_valley	15	m	Mv	28.964	g/mol
L_valley	20	m	Saturation vapor pressure	3.625139	hPa
Slope bed (i)	1.133893		Saturation vapor pressure	-0.25282	
R	8.31451		Partial water vapor pressure	0.725028	
Ds	40		Psv	362.3	
T	266.16	k	Fpt	1.0038	
Rh	20		The mole fraction of water vapor (xv)	0.0007	
P	1150	hpa	cd	2.5	
P	1.134962	atm	As	400	
Z	0.999236		ha	0.1	m

$$v = \sqrt{\frac{2gi\ ZRT}{P\left[M_a - \left(x_v(M_a - M_v)\right)\right]C_d.A_s.h_a.D_s}}$$

$$v = \sqrt{\frac{2 \times (9.8 \times 1.133893 \times 0.999128 \times 8.31451 \times 266.16)}{1150 \times [28.964 - (0.0007 \times (28.964 - 18.02))]2.5 \times 400 \times 0.1 \times 40}}$$

$$v = \sqrt{\frac{49144.6}{82928152.6}}$$

$$v = \sqrt{0.0006}$$

$$v = 0.0245\ ms^{-1}$$

Appendix A.5. Estimation temperature drop due to cold air drainage accumulation

15 September 2016

Time	17:10	18:10	19:10	20:10	21:10	22:10	23:10	0:10	1:10	2:10	3:10	4:10	5:10	6:10
Basin Air Temperature (K)	273.35	271.95	271.25	271.35	271.35	272.05	271.35	270.85	270.55	270.15	269.25	270.75	270.95	270.65
Basin Surface Temperature (K)	277.05	276.65	276.25	275.85	275.95	276.15	275.95	275.75	275.75	275.45	275.05	275.35	275.55	275.55
Top Air Temperature (K)	272.95	271.55	270.95	271.05	271.09	271.87	271.25	271.15	270.95	270.75	269.85	271.45	271.65	271.55
Top Surface Temperature (K)	276.53	276.13	275.86	275.46	275.61	275.92	275.82	276.14	276.27	276.23	275.83	276.26	276.46	276.72
Basin Air Potential Temperature (K)	271.38	274.13	269.27	273.52	273.52	274.23	269.42	273.05	272.77	268.17	271.44	273.03	273.26	272.93
Basin Surface Potential Temperature	275.05	278.87	274.23	278.06	278.16	278.36	273.99	277.99	278.02	273.44	277.28	277.67	277.90	277.87
Top Air Potential Temperature	270.98	273.72	268.97	273.22	273.26	274.05	269.32	273.35	273.18	268.77	272.04	273.74	273.96	273.84
Top Surface Potential Temperature	274.54	278.34	273.84	277.67	277.82	278.13	273.86	278.38	278.54	274.21	278.07	278.59	278.81	279.05
Basin Vertical Potential	3.67	4.74	4.96	4.54	4.64	4.13	4.57	4.94	5.24	5.26	5.85	4.64	4.64	4.94
Top Vertical Potential	3.55	4.62	4.87	4.45	4.56	4.08	4.54	5.03	5.36	5.44	6.03	4.85	4.85	5.21
Basin Δt	-267.71	-269.39	-264.30	-268.99	-268.89	-270.10	-264.85	-268.11	-267.53	-262.91	-265.59	-268.39	-268.62	-267.99
Basin ΔT_s	-271.38	-274.13	-269.27	-273.52	-273.52	-274.23	-269.42	-273.05	-272.77	-268.17	-271.44	-273.03	-273.26	-272.93
Top Δt	-267.43	-269.11	-264.09	-268.78	-268.70	-269.97	-264.78	-268.32	-267.81	-263.33	-266.01	-268.89	-269.11	-268.62
Top ΔT_s	-270.98	-273.72	-268.97	-273.22	-273.26	-274.05	-269.32	-273.35	-273.18	-268.77	-272.04	-273.74	-273.96	-273.84
a	0.01	0.02	0.02	0.02	0.02	0.02	0.02	0.02	0.02	0.02	0.02	0.02	0.02	0.02
$\overline{\Delta T_s}$	-271.18	-273.93	-269.12	-273.37	-273.39	-274.14	-269.37	-273.20	-272.97	-268.47	-271.74	-273.38	-273.61	-273.38
U (m/s)	0.026	0.026	0.026	0.026	0.026	0.026	0.026	0.026	0.026	0.026	0.026	0.026	0.026	0.026
$\overline{H}$	-0.87	-1.15	-1.17	-1.10	-1.13	-1.01	-1.08	-1.20	-1.27	-1.24	-1.42	-1.13	-1.13	-1.20
ΔT_H (K)	-0.20	-0.28	-0.30	-0.30	-0.32	-0.30	-0.34	0.00	-0.02	-0.03	-0.06	-0.06	-0.08	-0.10
ΔT_R (K)	-0.16	-0.08	0.00	0.08	0.16	0.24	0.32	0.40	0.48	0.56	0.64	0.72	0.80	0.88
ΔT (K)	-0.36	-0.36	-0.30	-0.22	-0.16	-0.06	-0.02	0.40	0.46	0.53	0.58	0.66	0.72	0.78

7-8 November 2017

Time	Pressure	Top Air Temperature (K)	Top Surface Temperature (K)	Basin Air Temperature (K)	Basin Surface Temperature (K)	Top Air Potential Temperature (k)	Top Surface Potential Temperature (k)	Basin Air Potential Temperature (K)	Basin Surface Potential Temperature (k)	Top Vertical Potential	Basin Vertical Potential	Top ΔT_s	Basin ΔT_s	$\overline{\Delta T_s}$	U (m/s)	$\bar{H}$	ΔT_H (K)	ΔT_R (K)	ΔT (K)	Real ΔT (K)	Difference between real and model ΔT
2017-11-07 16:50	996.8	270.8	279.2	272.3	273.4	271.0	279.4	272.5	273.6	8.4	1.1	-271.0	-272.5	-271.7	0.2540	-382.1	-2.218	2.140	-0.078	0.6	0.7
2017-11-07 17:00	996.8	270.4	279.2	271.7	273.4	270.6	279.4	271.9	273.6	8.8	1.7	-270.6	-271.9	-271.2	0.2538	-300.2	-2.153	2.114	-0.038	0.5	0.5
2017-11-07 17:10	996.8	270.1	278.2	271.2	273.3	270.3	278.4	271.4	273.5	8.1	2.1	-270.3	-271.4	-270.8	0.2536	-250.3	-2.120	2.105	-0.015	0.3	0.3
2017-11-07 17:20	996.8	269.9	278.2	270.9	273.2	270.1	278.4	271.1	273.4	8.3	2.3	-270.1	-271.1	-270.6	0.2535	-218.3	-2.100	2.098	-0.002	0	0.0
2017-11-07 17:30	996.8	269.9	278.2	270.9	273.1	270.1	278.4	271.1	273.3	8.3	2.2	-270.1	-271.1	-270.6	0.2535	-203.8	-2.100	2.098	-0.002	0.8	0.8
2017-11-07 17:40	996.8	270.0	278.2	270.1	273.0	270.2	278.4	270.3	273.2	8.2	2.9	-270.2	-270.3	-270.2	0.2536	-197.0	-2.071	2.058	-0.013	0.3	0.3
2017-11-07 17:50	996.8	269.7	278.2	269.8	272.9	269.9	278.4	270.0	273.1	8.5	3.1	-269.9	-270.0	-269.9	0.2534	-169.5	-2.044	2.049	0.005	-0.2	-0.2
2017-11-07 18:00	996.8	269.4	278.2	270.0	272.9	269.6	278.4	270.2	273.1	8.8	2.9	-269.6	-270.2	-269.9	0.2533	-147.5	-2.043	2.065	0.022	0.1	0.1
2017-11-07 18:10	996.8	269.3	278.2	269.9	272.7	269.5	278.4	270.1	272.9	8.9	2.8	-269.5	-270.1	-269.8	0.2532	-136.1	-2.030	2.057	0.026	0.2	0.2
2017-11-07 18:20	996.8	269.2	278.2	269.7	272.7	269.4	278.4	269.9	272.9	9.0	3.0	-269.4	-269.9	-269.6	0.2532	-126.1	-2.019	2.049	0.030	0.2	0.2
2017-11-07 18:30	996.8	269.0	278.2	269.5	272.7	269.2	278.4	269.7	272.9	9.2	3.2	-269.2	-269.7	-269.4	0.2531	-114.4	-2.001	2.038	0.037	0	0.0
2017-11-07 18:40	996.8	268.9	278.2	269.5	272.6	269.1	278.4	269.7	272.8	9.3	3.1	-269.1	-269.7	-269.4	0.2531	-106.6	-2.001	2.043	0.042	-0.1	-0.1
2017-11-07 18:50	996.8	268.9	278.2	269.6	272.5	269.1	278.4	269.8	272.7	9.3	2.9	-269.1	-269.8	-269.4	0.2531	-102.0	-2.005	2.047	0.042	-0.1	-0.1
2017-11-07 19:00	996.8	268.9	278.2	269.7	272.4	269.1	278.4	269.9	272.6	9.3	2.7	-269.1	-269.9	-269.5	0.2531	-97.7	-2.008	2.050	0.042	0	0.0
2017-11-07 19:10	1006	268.9	278.2	269.7	272.4	268.4	277.7	269.2	271.9	9.3	2.7	-268.4	-269.2	-268.8	0.2519	-93.8	-2.010	2.053	0.043	0.1	0.1
2017-11-07 19:20	1006	268.8	277.2	269.6	272.4	268.3	276.7	269.1	271.9	8.4	2.8	-268.3	-269.1	-268.7	0.2518	-88.2	-1.999	2.044	0.045	-0.2	-0.2
2017-11-07 19:30	1006	268.9	277.2	269.8	272.3	268.4	276.7	269.3	271.8	8.3	2.5	-268.4	-269.3	-268.8	0.2519	-86.9	-2.015	2.058	0.043	0.2	0.2
2017-11-07 19:40	1007	268.9	277.2	269.6	272.3	268.3	276.6	269.0	271.7	8.3	2.7	-268.3	-269.0	-268.7	0.2518	-83.8	-2.004	2.046	0.042	-0.1	-0.1
2017-11-07 19:50	1007	268.8	277.2	269.7	272.3	268.2	276.6	269.1	271.7	8.4	2.6	-268.2	-269.1	-268.7	0.2518	-79.1	-2.007	2.053	0.046	0.1	0.1
2017-11-07 20:00	1007	268.8	277.2	269.6	272.3	268.2	276.6	269.0	271.7	8.4	2.7	-268.2	-269.0	-268.6	0.2518	-76.4	-2.003	2.049	0.046	0.2	0.2
2017-11-07 20:10	1007	268.7	277.2	269.4	272.2	268.1	276.6	268.8	271.6	8.5	2.8	-268.1	-268.8	-268.5	0.2517	-72.3	-1.991	2.039	0.048	0	0.0
2017-11-07 20:20	1007	268.8	277.2	269.4	272.2	268.2	276.6	268.8	271.6	8.4	2.8	-268.2	-268.8	-268.5	0.2518	-71.6	-1.995	2.040	0.045	0	0.0
2017-11-07 20:30	1007	268.7	277.2	269.4	272.1	268.1	276.6	268.8	271.5	8.5	2.7	-268.1	-268.8	-268.5	0.2517	-67.9	-1.991	2.040	0.048	0.1	0.1
2017-11-07 20:40	1007	268.3	277.2	269.3	272.0	267.7	276.6	268.7	271.4	8.9	2.7	-267.7	-268.7	-268.2	0.2515	-60.5	-1.975	2.035	0.061	0.2	0.1
2017-11-07 20:50	1007	268.3	277.2	269.1	272.0	267.7	276.6	268.5	271.4	8.9	2.9	-267.7	-268.5	-268.1	0.2515	-58.8	-1.965	2.025	0.060	-0.2	-0.3

Time	Pressure	Top Air Temperature	Top Surface Temperature	Basin Air Temperature	Basin Surface Temperature	Top Air Potential	Top Surface Potential	Basin Air Potential	Basin Surface Potential	Top Vertical Potential	Basin Vertical Potential	Top ΔT_s	Basin ΔT_s	$\overline{\Delta T_s}$	U (m/s)	$\bar{H}$	ΔT_H (K)	ΔT_R (K)	ΔT (K)	Real ΔT (K)	Difference between real
2017-11-07 21:00	1007	267.9	277.2	269.3	272.0	267.3	276.6	268.7	271.4	9.3	2.7	-267.3	-268.7	-268.0	0.2513	-52.9	-1.964	2.035	0.072	0.4	0.3
2017-11-07 21:10	1007	267.7	277.2	268.9	271.9	267.1	276.6	268.3	271.3	9.5	3.0	-267.1	-268.3	-267.7	0.2512	-49.6	-1.941	2.015	0.074	0.2	0.1
2017-11-07 21:20	1007	267.7	277.2	268.7	271.9	267.1	276.6	268.1	271.3	9.5	3.2	-267.1	-268.1	-267.6	0.2512	-48.3	-1.935	2.009	0.074	0.3	0.2
2017-11-07 21:30	1007	267.6	277.2	268.4	271.9	267.0	276.6	267.8	271.3	9.6	3.5	-267.0	-267.8	-267.4	0.2511	-46.2	-1.921	1.995	0.075	-0.1	-0.2
2017-11-07 21:40	1007	267.8	277.2	268.5	271.8	267.2	276.6	267.9	271.2	9.4	3.3	-267.2	-267.9	-267.5	0.2512	-46.7	-1.930	2.000	0.070	-0.1	-0.2
2017-11-07 21:50	1007	268.0	277.2	268.6	271.8	267.4	276.6	268.0	271.2	9.2	3.2	-267.4	-268.0	-267.7	0.2513	-47.3	-1.939	2.005	0.066	0.2	0.1
2017-11-07 22:00	1007	267.9	277.2	268.4	271.8	267.3	276.6	267.8	271.2	9.3	3.4	-267.3	-267.8	-267.5	0.2513	-45.3	-1.928	1.996	0.068	-0.3	-0.4
2017-11-07 22:10	1008	267.8	277.2	268.7	271.8	267.2	276.5	268.1	271.2	9.4	3.1	-267.2	-268.1	-267.6	0.2512	-43.4	-1.938	2.009	0.071	0.2	0.1
2017-11-07 22:20	1007	268.0	277.2	268.5	271.8	267.4	276.6	267.9	271.2	9.2	3.3	-267.4	-267.9	-267.6	0.2513	-44.1	-1.935	2.000	0.065	0	-0.1
2017-11-07 22:30	1007	268.2	276.2	268.5	271.8	267.6	275.6	267.9	271.2	8.0	3.3	-267.6	-267.9	-267.7	0.2514	-44.8	-1.940	2.000	0.060	0.2	0.1
2017-11-07 22:40	1007	267.8	276.2	268.3	271.7	267.2	275.6	267.7	271.1	8.4	3.4	-267.2	-267.7	-267.4	0.2512	-40.6	-1.922	1.991	0.070	0.1	0.0
2017-11-07 22:50	1008	267.8	276.2	268.2	271.7	267.2	275.5	267.6	271.1	8.4	3.5	-267.2	-267.6	-267.4	0.2512	-39.7	-1.918	1.987	0.069	-0.1	-0.2
2017-11-07 23:00	1007	268.1	276.2	268.3	271.6	267.5	275.6	267.7	271.0	8.1	3.3	-267.5	-267.7	-267.6	0.2514	-41.2	-1.930	1.991	0.062	0	-0.1
2017-11-07 23:10	1008	268.3	276.2	268.3	271.6	267.7	275.5	267.7	271.0	7.9	3.3	-267.7	-267.7	-267.7	0.2514	-42.0	-1.935	1.991	0.056	0	-0.1
2017-11-07 23:20	1008	268.2	276.2	268.3	271.6	267.6	275.5	267.7	271.0	8.0	3.3	-267.6	-267.7	-267.6	0.2514	-40.3	-1.932	1.991	0.059	-0.1	-0.2
2017-11-07 23:30	1008	268.0	276.2	268.4	271.6	267.4	275.5	267.8	271.0	8.2	3.2	-267.4	-267.8	-267.6	0.2513	-38.0	-1.931	1.996	0.065	0.2	0.1
2017-11-07 23:40	1008	268.0	276.2	268.2	271.6	267.4	275.5	267.6	271.0	8.2	3.4	-267.4	-267.6	-267.5	0.2513	-37.3	-1.923	1.987	0.064	0.1	0.0
2017-11-07 23:50	1008	268.0	276.2	268.1	271.5	267.4	275.5	267.5	270.9	8.2	3.4	-267.4	-267.5	-267.4	0.2513	-36.6	-1.919	1.983	0.064	0	-0.1
2017-11-08 0:00	1008	267.8	276.2	268.1	271.5	267.2	275.5	267.5	270.9	8.4	3.4	-267.2	-267.5	-267.3	0.2512	-34.6	-1.914	1.983	0.069	0.4	0.3
2017-11-08 0:10	1008	266.9	276.2	267.7	271.5	266.3	275.5	267.1	270.9	9.3	3.8	-266.3	-267.1	-266.7	0.2508	-29.1	-1.880	1.966	0.085	0.2	0.1
2017-11-08 0:20	1008	266.7	276.2	267.5	271.4	266.1	275.5	266.9	270.8	9.5	3.9	-266.1	-266.9	-266.5	0.2507	-27.7	-1.869	1.957	0.088	-0.2	-0.3
2017-11-08 0:30	1008	267.2	276.2	267.7	271.4	266.6	275.5	267.1	270.8	9.0	3.7	-266.6	-267.1	-266.8	0.2509	-29.5	-1.886	1.966	0.080	-0.2	-0.3
2017-11-08 0:40	1008	267.6	276.2	267.9	271.4	267.0	275.5	267.3	270.8	8.6	3.5	-267.0	-267.3	-267.1	0.2511	-31.1	-1.902	1.974	0.072	-0.3	-0.4
2017-11-08 0:50	1007	267.5	276.2	268.2	271.3	266.9	275.6	267.6	270.7	8.7	3.1	-266.9	-267.6	-267.2	0.2511	-30.0	-1.911	1.987	0.076	0.3	0.2
2017-11-08 1:00	1007	267.6	276.2	267.9	271.3	267.0	275.6	267.3	270.7	8.6	3.4	-267.0	-267.3	-267.1	0.2511	-30.0	-1.902	1.974	0.072	0.3	0.2
2017-11-08 1:10	1008	267.5	276.2	267.6	271.3	266.9	275.5	267.0	270.7	8.7	3.7	-266.9	-267.0	-266.9	0.2510	-29.0	-1.888	1.961	0.073	0.3	0.2
2017-11-08 1:20	1008	267.3	276.2	267.3	271.3	266.7	275.5	266.7	270.7	8.9	4.0	-266.7	-266.7	-266.7	0.2509	-27.6	-1.872	1.948	0.076	0.1	0.0
2017-11-08 1:30	1008	267.1	276.2	267.2	271.2	266.5	275.5	266.6	270.6	9.1	4.0	-266.5	-266.6	-266.5	0.2508	-26.2	-1.864	1.944	0.080	0.1	0.0
2017-11-08 1:40	1008	267.2	276.2	267.1	271.2	266.6	275.5	266.5	270.6	9.0	4.1	-266.6	-266.5	-266.5	0.2509	-26.3	-1.863	1.940	0.077	0.4	0.3
2017-11-08 1:50	1008	267.0	276.2	266.7	271.2	266.4	275.5	266.1	270.6	9.2	4.5	-266.4	-266.1	-266.2	0.2508	-25.0	-1.840	1.919	0.079	0.2	0.1

Time	Pressure	Top Air Temperature	Top Surface Temperature	Basin Air Temperature	Basin Surface Temperature	Top Air Potential	Top Surface Potential	Basin Air Potential	Basin Surface Potential	Top Vertical Potential	Basin Vertical Potential	Top ΔT_s	Basin ΔT_s	$\overline{\Delta T_s}$	U (m/s)	$\bar{H}$	ΔT_H (K)	ΔT_R (K)	ΔT (K)	Real ΔT (K)	Difference between real
2017-11-08 2:00	1008	266.5	276.2	266.5	271.2	265.9	275.5	265.9	270.6	9.7	4.7	-265.9	-265.9	-265.9	0.2506	-22.8	-1.826	1.912	0.087	0.3	0.2
2017-11-08 2:10	1008	266.0	276.2	266.2	271.2	265.4	275.5	265.6	270.6	9.7	5.0	-265.4	-265.6	-265.5	0.2503	-20.9	-1.805	1.898	0.093	0.4	0.3
2017-11-08 2:20	1008	265.6	276.2	265.8	271.2	265.0	275.5	265.2	270.6	9.8	5.4	-265.0	-265.2	-265.1	0.2501	-19.5	-1.785	1.881	0.096	-0.6	-0.7
2017-11-08 2:30	1008	265.5	276.2	266.4	271.2	264.9	275.5	265.8	270.6	9.0	4.8	-264.9	-265.8	-265.3	0.2501	-19.0	-1.810	1.910	0.100	0.5	0.4
2017-11-08 2:40	1007	265.3	276.2	265.9	271.1	264.7	275.6	265.3	270.5	9.0	5.2	-264.7	-265.3	-265.0	0.2500	-18.2	-1.786	1.886	0.100	-0.2	-0.3
2017-11-08 2:50	1007	265.2	276.2	266.1	271.1	264.6	275.6	265.5	270.5	8.3	5.0	-264.6	-265.5	-265.0	0.2500	-17.8	-1.795	1.898	0.102	0.3	0.2
2017-11-08 3:00	1007	265.3	276.2	265.8	271.1	264.7	275.6	265.2	270.5	8.4	5.3	-264.7	-265.2	-264.9	0.2500	-17.7	-1.782	1.882	0.100	0	-0.1
2017-11-08 3:10	1007	265.2	276.2	265.8	271.1	264.6	275.6	265.2	270.5	9.3	5.3	-264.6	-265.2	-264.9	0.2500	-17.3	-1.780	1.880	0.101	0.3	0.2
2017-11-08 3:20	1007	265.1	275.2	265.5	271.1	264.5	274.6	264.9	270.5	9.4	5.6	-264.5	-264.9	-264.7	0.2500	-16.8	-1.770	1.871	0.101	0.1	0.0
2017-11-08 3:30	1007	265.0	275.2	265.4	271.1	264.4	274.6	264.8	270.5	9.4	5.7	-264.4	-264.8	-264.6	0.2499	-16.4	-1.764	1.865	0.101	-0.1	-0.2
2017-11-08 3:40	1007	264.8	275.2	265.5	271.1	264.2	274.6	264.9	270.5	9.3	5.6	-264.2	-264.9	-264.5	0.2498	-15.8	-1.767	1.871	0.104	-0.3	-0.4
2017-11-08 3:50	1007	264.8	275.2	265.8	271.1	264.2	274.6	265.2	270.5	9.5	5.3	-264.2	-265.2	-264.7	0.2498	-15.6	-1.780	1.885	0.105	-0.2	-0.3
2017-11-08 4:00	1008	264.6	275.2	266.0	271.1	264.0	274.5	265.4	270.5	9.5	5.1	-264.0	-265.4	-264.7	0.2497	-15.0	-1.786	1.894	0.108	0.3	0.2
2017-11-08 4:10	1008	264.7	275.2	265.7	271.1	264.1	274.5	265.1	270.5	9.7	5.4	-264.1	-265.1	-264.6	0.2497	-15.0	-1.774	1.879	0.106	0.1	0.0
2017-11-08 4:20	1008	264.8	275.2	265.6	271.1	264.2	274.5	265.0	270.5	9.6	5.5	-264.2	-265.0	-264.6	0.2498	-15.0	-1.771	1.875	0.104	0.4	0.3
2017-11-08 4:30	1008	264.8	275.2	265.2	271.2	264.2	274.5	264.6	270.6	9.2	6.0	-264.2	-264.6	-264.4	0.2498	-14.8	-1.754	1.857	0.102	-0.5	-0.6
2017-11-08 4:40	1008	264.7	275.2	265.7	271.3	264.1	274.5	265.1	270.7	8.9	5.6	-264.1	-265.1	-264.6	0.2497	-14.5	-1.774	1.880	0.106	0.2	0.1
2017-11-08 4:50	1008	264.5	275.2	265.5	271.3	263.9	274.5	264.9	270.7	8.9	5.8	-263.9	-264.9	-264.4	0.2496	-14.0	-1.763	1.870	0.107	0	-0.1
2017-11-08 5:00	1008	264.3	275.2	265.5	271.5	263.7	274.5	264.9	270.9	9.2	6.0	-263.7	-264.9	-264.3	0.2495	-13.5	-1.760	1.868	0.108	0.1	0.0
2017-11-08 5:10	1008	264.1	275.2	265.4	271.7	263.4	274.5	264.7	271.0	9.7	6.3	-263.4	-264.7	-264.1	0.2494	-13.0	-1.759	1.868	0.110	-0.5	-0.6
2017-11-08 5:20	1008	264.6	275.2	265.9	271.9	264.0	274.5	265.3	271.3	9.8	6.0	-264.0	-265.3	-264.6	0.2497	-13.6	-1.782	1.889	0.108	-0.3	-0.4
2017-11-08 5:30	1008	265.4	275.2	266.2	272.2	264.8	274.5	265.6	271.6	9.8	6.0	-264.8	-265.6	-265.2	0.2500	-14.9	-1.801	1.902	0.100	0.1	0.0
2017-11-08 5:40	1008	266.2	275.2	266.1	272.6	265.6	274.5	265.5	272.0	9.0	6.5	-265.6	-265.5	-265.5	0.2504	-16.4	-1.808	1.898	0.090	-0.1	-0.2
2017-11-08 5:50	1008	266.4	275.2	266.2	272.9	265.7	274.5	265.5	272.2	8.8	6.7	-265.7	-265.5	-265.6	0.2505	-16.7	-1.815	1.902	0.087	-0.3	-0.4
2017-11-08 6:00	1008	266.5	275.2	266.5	273.1	265.8	274.5	265.8	272.4	8.7	6.6	-265.8	-265.8	-265.8	0.2505	-16.7	-1.828	1.915	0.087	0	-0.1
2017-11-08 6:10	1008	266.5	275.2	266.5	273.2	265.8	274.5	265.8	272.5	8.7	6.7	-265.8	-265.8	-265.8	0.2505	-16.5	-1.828	1.915	0.087	0.6	0.5
2017-11-08 6:20	1008	265.6	275.2	265.9	273.4	264.9	274.5	265.2	272.7	9.6	7.5	-264.9	-265.2	-265.1	0.2501	-14.4	-1.791	1.888	0.097	0.5	0.4
2017-11-08 6:30	1008	265.7	275.2	265.4	273.5	265.0	274.5	264.7	272.8	9.5	8.1	-265.0	-264.7	-264.9	0.2501	-14.5	-1.772	1.865	0.093	0.1	0.0
2017-11-08 6:40	1009	265.5	275.2	265.3	273.8	264.8	274.5	264.6	273.1	9.7	8.5	-264.8	-264.6	-264.7	0.2500	-13.9	-1.767	1.862	0.095	-0.3	-0.4
2017-11-08 6:50	1008	266.5	275.2	265.6	274.1	265.8	274.5	264.9	273.4	8.7	8.5	-265.8	-264.9	-265.4	0.2505	-15.8	-1.794	1.877	0.083	-0.2	-0.3

8-9 November 2017

Time	17:10	18:10	19:10	20:10	21:10	22:10	23:10	0:10	1:10	2:10	3:10	4:10	5:10	6:10
Basin Air Temperature (K)	273.35	271.95	271.25	271.35	271.35	272.05	271.35	270.85	270.55	270.15	269.25	270.75	270.95	270.65
Basin Surface Temperature (K)	277.05	276.65	276.25	275.85	275.95	276.15	275.95	275.75	275.75	275.45	275.05	275.35	275.55	275.55
Top Air Temperature (K)	272.95	271.55	270.95	271.05	271.09	271.87	271.25	271.15	270.95	270.75	269.85	271.45	271.65	271.55
Top Surface Temperature (K)	276.53	276.13	275.86	275.46	275.61	275.92	275.82	276.14	276.27	276.23	275.83	276.26	276.46	276.72
Basin Air Potential Temperature (K)	271.38	274.13	269.27	273.52	273.52	274.23	269.42	273.05	272.77	268.17	271.44	273.03	273.26	272.93
Basin Surface Potential Temperature	275.05	278.87	274.23	278.06	278.16	278.36	273.99	277.99	278.02	273.44	277.28	277.67	277.90	277.87
Top Air Potential Temperature	270.98	273.72	268.97	273.22	273.26	274.05	269.32	273.35	273.18	268.77	272.04	273.74	273.96	273.84
Top Surface Potential Temperature	274.54	278.34	273.84	277.67	277.82	278.13	273.86	278.38	278.54	274.21	278.07	278.59	278.81	279.05
Basin Vertical Potential	3.67	4.74	4.96	4.54	4.64	4.13	4.57	4.94	5.24	5.26	5.85	4.64	4.64	4.94
Top Vertical Potential	3.55	4.62	4.87	4.45	4.56	4.08	4.54	5.03	5.36	5.44	6.03	4.85	4.85	5.21
Basin Δt	-267.71	-269.39	-264.30	-268.99	-268.89	-270.10	-264.85	-268.11	-267.53	-262.91	-265.59	-268.39	-268.62	-267.99
Basin ΔT_s	-271.38	-274.13	-269.27	-273.52	-273.52	-274.23	-269.42	-273.05	-272.77	-268.17	-271.44	-273.03	-273.26	-272.93
Top Δt	-267.43	-269.11	-264.09	-268.78	-268.70	-269.97	-264.78	-268.32	-267.81	-263.33	-266.01	-268.89	-269.11	-268.62
Top ΔT_s	-270.98	-273.72	-268.97	-273.22	-273.26	-274.05	-269.32	-273.35	-273.18	-268.77	-272.04	-273.74	-273.96	-273.84
a	0.01	0.02	0.02	0.02	0.02	0.02	0.02	0.02	0.02	0.02	0.02	0.02	0.02	0.02
$\overline{\Delta T_s}$	-271.18	-273.93	-269.12	-273.37	-273.39	-274.14	-269.37	-273.20	-272.97	-268.47	-271.74	-273.38	-273.61	-273.38
U (m/s)	0.026	0.026	0.026	0.026	0.026	0.026	0.026	0.026	0.026	0.026	0.026	0.026	0.026	0.026
$\bar{H}$	-0.87	-1.15	-1.17	-1.10	-1.13	-1.01	-1.08	-1.20	-1.27	-1.24	-1.42	-1.13	-1.13	-1.20
ΔT_H (K)	-0.20	-0.28	-0.30	-0.30	-0.32	-0.30	-0.34	0.00	-0.02	-0.03	-0.06	-0.06	-0.08	-0.10
ΔT_R (K)	-0.16	-0.08	0.00	0.08	0.16	0.24	0.32	0.40	0.48	0.56	0.64	0.72	0.80	0.88
ΔT (K)	-0.36	-0.36	-0.30	-0.22	-0.16	-0.06	-0.02	0.40	0.46	0.53	0.58	0.66	0.72	0.78

Appendix A.6 Extrapolated values for three areas : Windward, over the forest and Leeward areas based on distance and percentage of wind speed

Windward area			Over the forest			Leeward area		
Distance	**Percentage of wind speed**	**Formula**	**Distance**	**Percentage of speed**	**Formula**	**Distance**	**Percentage of wind speed**	**Formula**
10	100	100.7	**1**	68	69.7	**1**	40	40.4
9	100	99.4	**2**	58	59.2	**2**	50	56.5
5	95	94.2	**3**	58	50.3	**3**	58	60.8
3	90	90	**4**	42	43	**4**	62	64.5
2.5	88	88.3	**5**	35	36.8	**5**	68	67.8
1	80	78.2	**6**	28	31.6	**8**	78	75.4
0	62	62.4	**10**	18	18.7	**10**	80	79.1
			13	15	14.4	**12.5**	82	82.7
			14	15	13.6	**15**	85	85.5
			16	14	13.1	**17.5**	90	87.8
			17	16	13.2	**18**	90	88.3
			18	13	13.6	**19**	90	89
			19	16	14.2	**20**	90	89.8
			20	12	15	**21**	90	90.5
			22	14	17.5	**22**	90	91.2
			25	25	23.1	**23**	90	91.8
						25	92	93
						30	95	95.8

Appendix B.1 Spectral range of a specific band of Landsat

Table B.1

Band / Constant	Band 1	Band 2	Band 3	Band 4	Band 5	Band 7
G_{sc}	1970	1843	1555	1047	227.1	80.53
a	-6.2	-6.4	-5	-5.1	-1	-0.35
b	191.6	196.5	152.9	157.4	31.06	10.8

Table B.2

Band / Parameter	Band 1	Band 2	Band 3	Band 4	Band 5	Band 7
C1	0.987	2.319	0.951	0.375	0.234	0.365
C2	-0.00071	-0.00016	-0.0033	-0.00048	-0.00101	-0.00097
C3	0.000036	0.0000105	0.00028	0.005018	0.004336	0.004296
C4	0.088	0.0437	0.0875	0.1355	0.056	0.0155
C5	0.0789	-1.2697	0.1014	0.6621	0.7757	0.639
$p_{a,b}$	0.0726	0.0597	0.0344	0.0193	0.018	0.0152

Table B.3

Band / Parameter	Band 1	Band 2	Band 3	Band 4	Band 5	Band 7
W_b	0.254	0.149	0.147	0.311	0.102	0.036

Table B.4

	F_{G2}	F_τ	F_s	FD	Ro	C_d	λ	h_v	W_s	L_s	v
17h	3602.929	2758.453	6038.772	322.6096	1.343735	2.5	0.95	0.4	40	20	0.0224
18h	3613.062	2766.211	6055.756	323.517	1.347514	2.5	0.95	0.4	40	20	0.0235
19h	3618.52	2770.39	6064.904	324.0057	1.34955	2.5	0.95	0.4	40	20	0.0241
20h	3625.27	2775.558	6076.217	324.6101	1.352067	2.5	0.95	0.4	40	20	0.0249

Appendix C. Specification of air and soil resistances

*The aerodynamic resistance r_{aa} is calculated by means of the classical formula that takes into account the stability correction functions for wind and temperature (Brutsaert,1982), as follows. See Nomenclature (page 20) for definition of the symbol.

$$r_{aa} = \frac{1}{k^2 u_a}\left[\ln\left(\frac{z_r - d}{z_0}\right) - \Psi_h(z_r)\right] \times \left[\ln\left(\frac{z_r - d}{z_0}\right) - \Psi_m(z_r)\right] \quad \text{C. 1}$$

and Ψh and Ψm are the integral correction functions, respectively, for heat and momentum. During nocturnal cooling, the regime is stable (Lhomme and Guilioni, 2004)

* Air resistances (r_{ac}) within the canopy are calculated using the formulations proposed by Choudhury and Monteith (1988):

$$r_{ac} = \frac{\alpha_w [w_1 / u(z_h)]^{0.5}}{4\alpha_0 L_0 [1 - exp(-\alpha_w/2)]} \quad \text{C. 2}$$

Where w is the leaf width, L_0, leaf Area index and α_w and α_0 are two constant $u(z_h)$

$$u(z_h) = \frac{u_a[ln[z_h - d/z_0] - \Psi_m(z_h)]}{ln[z_r - d/z_0] - \Psi_m(z_r)} \quad \text{C. 3}$$

*The aerodynamic resistance between the substrate and the source height of the whole canopy is defined as integral of the reciprocal of eddy diffusivity over the height range (Choudhury and Monteith, 1988) as follow:

$$r_{as} = \frac{z_h \exp(a_w)}{a_w k(z_h)} \times \left\{\exp\left[\frac{-a_w z_{0s}}{z_h}\right] - \exp\left[\frac{-a_w (d + z_0)}{z_h}\right]\right\} \quad \text{C. 4}$$

where $K(z_h)$ is the value of eddy diffusivity at canopy height is calculated as follows:

$$K(z_h) = \frac{k^2 u_a (z_h - d)}{[\ln[z_r - d/z_0] - \Psi_m(z_r)]} \quad \text{C. 5}$$

Appendix D. Model implementation when dew or rime deposit does not occur

The three unknowns (T_o, T_c, T_s) are the solutions of the following system:

$$T_0 = \frac{T_a/r_{aa}+T_C/r_{ac}+T_s/r_{as}}{G_a} \quad \text{D. 1}$$

where G_a defined as $$G_a = \frac{1}{r_{aa}} + \frac{1}{r_{ac}} + \frac{1}{r_{as}} \quad \text{D. 2}$$

soil surface temperature is given by:

$$T_s = \frac{\left[fQ(r_{as}+2r_{ac})+\rho c_p\right]\left[G_a(hT_{sd}+(1-f)S)+\rho c_p T_a/(r_{aa}r_{as})\right]+\left[fG_aQ+\rho c_p/(r_{aa}r_{as})\right]\left[S(fr_{ac}+(f-1)r_{as})-hr_{as}T_{sd}\right]}{\left[fQ(r_{as}+2r_{ac})+\rho c_p\right]\left[G_a(h+Q)+\rho c_p(1/r_{aa}+1/r_{ac})/r_{as}\right]+\left[fG_aQ+\rho c_p/(r_{ac}r_{as})\right]\left[Q(fr_{ac}+r_{as})-hr_{as}+\rho c_p\right]} \quad \text{D. 3}$$

where

$$Q=4\varepsilon\sigma T_a^4 \qquad S=\varepsilon\,(R_a+3\sigma T_a^4) \quad \text{D. 4}$$

Ra (eq.C-4) is atmospheric long way radiation was estimated using the formula proposed by Brutsaert (1982) which involves an atmospheric emissivity (ε_a) as follows:

$$R_a = \varepsilon_a \sigma T_a^4 \qquad \varepsilon_a = \mu\left(e_a/T_a\right)^{1/7} \quad \text{D. 5}$$

μ is empirical coefficient; T_a is air temperature (estimated as discussed in second component) e_a is vapor pressure (Pa).

Vapor pressure is estimated using equation (Wallace and Hobbs, 2006):

$$T_d = \frac{243.5\ln(e_a/6.112)}{17.67-\ln(e_a/6.112)} \quad \text{D. 6}$$

Finally, crop temperature (T_c) equation is:

$$T_c = \frac{Ts\left[Q(fr_{ac}+r_{as})+hr_{as}+pc_p\right]+S\left[(r_{as}+r_{ac})-r_{as}\right]-hr_{as}T_{sd}}{fQ(r_{as}+2r_{ac})+pc_p} \quad \text{D. 7}$$

Appendix E. Model implementation when dew or rime deposits occur

The four unknowns (T_c, T_s, T_0, and e_0) are the solutions of the following system:

$$(1-f)\varepsilon R_a + \varepsilon\sigma\left(T_c^4 - T_s^4\right) - h\left(T_s - T_{sd}\right) = \rho c_p\left[\frac{T_s - T_0}{r_{as}} + \frac{e\times(T_s) - e_0}{\gamma r_{as}}\right] \quad \text{E. 1}$$

$$f\varepsilon\left[R_a + \sigma\left(T_s^4 - 2T_c^4\right)\right] = \frac{\rho c_p\left[(T_c - T_0) + \left(e\times(T_c) - e_0\right)/\gamma\right]}{r_{ac}} \quad \text{E. 2}$$

$$T_0 = \frac{T_a/r_{aa} + T_c/r_{ac} + T_s/r_{as}}{G_a} \quad \text{E. 3}$$

$$e_0 = \frac{e_a/r_{aa} + e\times(T_c)/r_{ac} + e\times(T_s)/r_{as}}{G_a}$$

Replacing T_0 and e_0 in Eqs. (E.1) and (E.2) with their expressions Esq. (E.3) and (E.4) and using Eqs.

$$\begin{cases} AT_s + BT_c = C \\ A'T_s + B'T_c = C' \end{cases} \quad \text{E. 4}$$

$$A = \rho c_p\left(1 + \frac{s}{\gamma}\right)\left[\frac{1 - 1/(G_a r_{as})}{r_{as}}\right] + h + Q \quad \text{E. 5}$$

$$B = -fQ - \rho c_p\,\frac{1 + (s/\gamma)}{G_a r_{ac} r_{as}} \quad \text{E. 6}$$

$$C = (1-f)S + hT_{sd} - \left(\frac{\rho c_p}{r_{as}}\right)\times\left\{\left[\frac{e\times(T_a)}{\gamma}\right]\left[1 - \frac{1/r_{ac} + 1/r_{as}}{G_a}\right] - \frac{e_a/\gamma}{G_a r_{aa}}\right. \quad \text{E. 7}$$
$$\left. + T_a\left[\frac{(s/\gamma)(1/r_{ac} + 1/r_{as})}{G_a} - \frac{s}{\gamma} - \frac{1}{G_a r_{aa}}\right]\right\}$$

$$A' = fQ + \rho c_p\left(\frac{1 + s/\gamma}{G_a r_{ac} r_{as}}\right) \quad \text{E. 8}$$

$$B' = -2fQ + \frac{\rho c_p}{r_{ac}}\left(1 + \frac{s}{\gamma}\right)\left(1 - \frac{1}{G_a r_{ac}}\right) \quad \text{E. 9}$$

$$C' = -fS + \left(\frac{\rho c_p}{r_{ac}}\right)\times\left\{\left(\frac{e\times(T_a)}{\gamma}\right)\left(1 - \frac{1/r_{ac} + 1/r_{as}}{G_a}\right) - \frac{e_a/\gamma}{G_a r_{aa}} - T_a\left[\frac{1}{G_a r_{aa}} + \left(\frac{s}{\gamma}\right)\left[1 + \frac{1/r_{ac} + 1/r_{as}}{G_a}\right]\right]\right\} \quad \text{E. 10}$$

$$T_c = \frac{AC' - A'C}{AB' - A'B} \quad \text{E. 11}$$

$$T_c = \frac{B'C - BC'}{AB' - A'B} \qquad \text{E. 12}$$

The coefficients of this system are expressed as:

Table E.1 Nomenclature

Nomenclature	
d	Zero plan displacement height (m)
f	Fraction area covered with vegetation
h	Soil exchange coefficient defined as k_T/z_d ($Wm^{-2}k^{-1}$)
k	Von karman's constant
L_0	Leaf area index (m^2m^{-2})
T_r	Radiometric surface temperature (K°)
T_{sd}	Soil temperature at a reference depth (K°)
W_1	Leaf width (m)
z_h	Canopy height (m)
z_r	Reference height in the air (m)
z_0	Canopy roughness length (m)
z_{0s}	Roughness length of the substrate (m)
α_0	Constant coefficient
α_w	Constant coefficient
ε	Crop and soil emissivity
$K(z_h)$	The value of eddy diffusivity at canopy height
Ψ_h	Integral correction function for heat
Ψm	Integral correction function for momentom

Appendix F. Estimation of moist entropy of new method presented against frost

Time	Pressure (mb)	Air Temp ,2m (c°), Refrence	Air Temp , 18m (c°),Refrence	Air Temp ,2m (c°),Test Point	Air Temp ,18m (c°),Test point	Specific Humidity ,2m,Refrence	Specific Humidity, 18m,Refrence	Specific Humidity 2m,Test point	Specific Humidity, 18m,Test point	Moist Entropy ,2m (J/K) Refrence	Moist Entropy ,18m (J/K) Refrence	Moist Entropy ,2m (J/K) Test point	Moist Entropy, 18m (J/K) Test point
1:05	1033.9	3.1	3.3	6.5	6.9	0.1	0.1	0.3	0.4	9.1	8.2	14.2	14.9
1:15	1034.4	2.4	3.2	6.0	6.6	0.2	0.2	0.3	0.4	9.0	9.6	14.3	15.0
1:25	1034.0	2.3	3.0	5.5	5.6	0.2	0.2	0.4	0.4	9.3	10.1	14.4	14.5
1:35	1034.1	2.7	3.5	6.0	6.1	0.2	0.2	0.3	0.4	9.2	10.0	14.3	14.7
1:45	1034.5	3.0	3.1	6.0	6.6	0.2	0.2	0.4	0.3	9.3	9.5	14.6	14.3
1:55	1034.6	2.6	2.6	5.5	6.1	0.2	0.2	0.4	0.3	9.5	9.3	14.7	14.0
2:05	1034.1	1.9	3.1	5.5	5.6	0.2	0.2	0.3	0.4	9.0	10.2	13.8	14.4
2:15	1034.7	0.7	2.0	5.5	5.1	0.1	0.2	0.4	0.4	8.3	9.6	14.4	14.7
2:25	1034.9	0.2	1.6	5.0	5.1	0.1	0.2	0.4	0.4	8.3	9.3	14.1	15.0
2:35	1035.4	0.7	1.1	4.5	5.1	0.2	0.2	0.4	0.4	8.5	8.9	14.1	14.5
2:45	1035.2	0.9	1.8	4.5	4.6	0.2	0.2	0.4	0.4	8.6	9.4	13.8	14.0
2:55	1035.3	0.9	2.3	4.5	5.1	0.2	0.2	0.3	0.4	8.6	9.5	13.4	14.5